Multi-resolution time-domain modelling technique and its applications in electromagnetic band gap enhanced antennas

Wang, Xiaojing

Multi-Resolution Time-Domain Modelling Technique and Its Applications in Electromagnetic Band Gap Enhanced Antennas

Xiaojing Wang

A Thesis Submitted in Partial Fulfilment of the Requirements

for the Degree of

Doctor of Philosophy

School of Electronic Engineering and Computer Science

March, 2010

To my family and friends

Abstract

Newly emerged Electromagnetic Band Gap (EBG) structures possess multiple frequency bands that prohibit wave propagation and such stop bands are basically determined by the periodicity of the structure. Such desirable features make EBG hybrid antenna an interesting topic. Traditional full-wave techniques lack the efficiency to fully cope with the complexity of these hybrid structures, since the periodical elements are often much smaller in size than the accompanying antenna components.

The Haar wavelet based Multi-Resolution Time Domain (MRTD) technique provides improved numerical resolution over the conventional Finite-Difference Time-Domain (FDTD) method, as well as simplicity in formulation. One-dimensional, two-dimensional and three-dimensional level-one codes are developed to assist the numerical modelling of the hybrid EBG antennas. An explicit form of Perfectly Matched Layer (PML) configuration is proposed, proved and presented. As a generic approach, its extensions suit every single level of Haar wavelet functions. A source expansion scheme is proposed thereafter.

The concept of a multi-band multi-layer EBG hybrid antenna is presented. The theoretical prediction of antenna resonances is achieved through an effective medium model. It has been verified via numerical simulations and measurements. The 3D MRTD code is later applied to simulate such a structure.

In addition, EBG enhanced circularly polarized photonic patch antennas have been studied. It is demonstrated that split-resonant rings (SRRs) and the like in EBG antennas can lead to antenna gain enhancement, backward radiation reduction and harmonic suppression.

Furthermore, a circularly polarized two-by-two antenna array with spiral EBG elements is presented. The spiral element with ground via is more compact in size than the traditional mushroom structure, which is proven very efficient in blocking unwanted surface wave. Hence it reduces the mutual coupling of the array antenna significantly.

Acknowledgements

The author is grateful to his supervisors, Prof. Yang Hao from Department of Electronic Engineering and Prof. Cho-Ho Chu from School of Mathematical Science, for their guidance during the PhD study.

Also, the author would like to express his gratitude to the following individuals and institutions for their generous help:

Dr. Yan Zhao from Queen Mary, for sharing his FDTD code for comparison purposes. Dr. Chin-Pang Liu and Dr. Chin Hsiu Chuang from University College London, and other joint project members (Mr. Simon Tse and Prof. Clive Parini from Queen Mary; Dr. Tabassam Ismail and Prof. Alwyn Seeds from University College London; Mr. P. G. Huggard from Rutherford Appleton Laboratory) for their collaborative efforts in the joint experiments and publications. Mr. Yoonjae Lee from Queen Mary, for the helpful discussions on various technical topics. Mr. John Dupuy from Queen Mary, for his help in manufacturing the antenna samples.

The financial privilege from the Westfield Trust Scholarship under the college title (Queen Mary and Westfield College) is gratefully acknowledged. This thesis serves the purpose of summarizing the author's research work, therefore fulfills the financial obligation to the this institution.

List of Publications

1. Xiaojing Wang, Yang Hao, "Dual-band operation of an electromagnetic band-gap patch antenna", Microwave and Optical Technology Letters. Volume 49, Issue 10, Date: October 2007, Pages: 2454-2458

2. Xiaojing Wang, Yang Hao, Peter S. Hall, "Dual-band Resonances of a Patch Antenna on UC-EBG Substrate," The Proceeding of Asia Pacific Microwave Conference 2005 (APMC 2005), DECEMBER 2005 (IEEE Xplore indexed)

3. Xiaojing Wang, Yang Hao, "Multi-layer Uni-planar EBG Antenna and Its Dual-band Realization", The Proceeding of UK National URSI Symposium 2006, July 2006

4. Xiaojing Wang, Simon Tse, Yang Hao, Clive Parini; Chin-Pang Liu, Chin-Hsiu Chuang, Tabassam Ismail, Alwyn Seeds; Peter Huggard, "AN EBG ANTENNA WITH INTEGRATED OPTICAL TRANSDUCER", The Second European Conference on Antennas and Propagation (EuCAP 2007), Edinburgh, UK, Nov. 2007 (IEEE Xplore indexed under Eucap 2007)

5. Xiaojing Wang, Yang Hao, Cho-Ho Chu, "Stability Comparison between Multi-Resolution Time-Domain (MRTD) and Finite Difference Time-Domain (FDTD) Techniques", Loughborough Antennas and Propagation Conference 2008 (LAPC 2008), March 2008 (IEEE Xplore indexed)

6. Xiaojing Wang, Yang Hao, Cho-Ho Chu, "PERFECT MATCHING LAYER FOR HAAR WAVELET BASED MULTI-RESOLUTION TIME-DOMAIN TECHNIQUE", IET Seventh International Conference on Computation in Electromagnetics (CEM 2008), Brighton, UK, April 2008

7. Xiaojing Wang, Yang Hao, "A Perfect Matching Layer for Haar Wavelet Based Multi-Resolution Time-Domain Technique", IEEE International Symposium on Antennas and Propagation 2008 (APS 2008), San Diego, USA, July 2008 (IEEE Xplore indexed)

8. Simon Tse, Xiaojing Wang, Yang Hao, Clive Parini; Chin-Pang Liu, Chin-Hsiu Chuang, Tabassam Ismail, Alwyn Seeds; Peter Huggard, "An EBG Enhancement to Patch

Array Antenna with Integrated Optical Transducer", 19th International Conference on Applied Electromagnetics and Communications (ICECom 2007), Dubrovnik, Croatia, Sep. 2007 (IEEE Xplore indexed)

9. C. H. Chuang, C. P. Liu, T. Ismail, X. J. Wang, S. W. H. Tse, Y. Hao, C. Parini, P. G. Huggard, A. B. Krysa, J. S. Roberts, and A. J. Seeds, "Integrated Photonic Electromagnetic Band Gap Antenna with InGaAs/AlInGaAs Multiple Quantum Well Asymmetric Fabry-Perot Modulator", IEEE International Topical Meeting on Microwave Photonics (MWP2007), Victoria BC, Canada, Oct. 2007 (IEEE Xplore indexed)

10. C.H. Chuang, C.P. Liu, T.Ismail, X. Wang, Y. Hao, C. Parini, P. G. Huggard, A.B. Krysa, J.S. Roberts and A. J. Seeds, "Integrated Photonic Electromagnetic Band Gap Antenna with Asymmetric Fabry-Perot Modulator transmitting IEEE 802.11a in Wireless-Over-Fiber system", Journal of Lightwave Technology, VOL 26, NO. 15, pp. 2671-2678 August 2008

Contents

List of Abbreviation

1D: One-dimensional

2D: Two-dimensional

3D: Three-dimensional

ABC: Absorbing Boundary Condition

AFPM: Asymmetric Fabry-Perot Modulator

CDF: Cohen-Daubechies-Feauveau function

CPU: Central Processing Unit

EBG: Electromagnetic Band Gap structure

EM: Electromagnetic

FDTD: Finite-Difference Time-Domain

FFT: Fast Fourier Transformation

FSS: Frequency-Selective Surface

MQW: Multiple Quantum-Well

MRTD: Multi-Resolution Time-Domain Technique

PBC: Periodic Boundary Condition

PBG: Photonic Band Gap Structure

PEC: Perfect Electric Conductor

PMC: Perfect Magnetic Conductor

PML: Perfect Matching Layer

RIS: Reactive Impedance Surface

S-MRTD: Scaling function based MRTD

SRR: Split Ring Resonator

TE: Transverse Electric

TM: Transverse Magnetic

W-MRTD: Wavelet function based MRTD

List of Figures

Chapter 1

Introduction

1.1 Overview

This thesis consists of two major pieces of work: the code development of a Haar wavelet based Multi-Resolution Time-Domain (MRTD) technique and the design of a multi-layered Electromagnetic Band Gap (EBG) antenna and several photonic EBG antennas. Later the MRTD is implemented to simulate the multi-layer EBG antenna. Several papers based on these research have been published or submitted during the course of this PhD. The work not only facilitates the author's own understanding of electromagnetics but also lays the foundation of a comprehensive numerical simulator for the group's future research.

The mathematical development of the wavelet theory and its engineering applications represents noticeably one of the pivotal interdisciplinary areas in 20th century. In 1910, Hungarian mathematician Alfréd Haar proposed the staircase approximation of an arbitrary function, using piecewise constants, which were later named the Haar wavelets [1]. Since then, many variations of the wavelets, as well as many applications of them have been developed. The introduction of the wavelet transform into electronic engineering, especially in image engineering applications in the 1990s marked one of the recent major advancements.

Almost at the same time, the multi-resolution technique derived from the wavelet transform, emerged in electromagnetics. Katehi *et. al.* [2] first introduced the MRTD

technique based on the Battle-Lemarie wavelets. Later, many other wavelet bases were used, yielding many kinds of MRTD schemes and Wavelet-Galerkin Methods or hybrid methods that combines wavelet basis with conventional numerical techniques.

Among all the MRTD iterations, the one based on the Haar wavelets is the most concise in terms of algorithm programmability, due to the orthogonality of the Haar wavelets and their compact support, which will be explained in later chapters. The Haar based MRTD provides reasonable numerical resolution as well as simplicity in formulation, which is partially why we developed this to model the EBG structures.

The newly emerged Electromagnetic Band Gap (EBG) structures possess multiple frequency bands that prohibit wave propagation and such stop bands are basically determined by the periodicity of the structure, in either material characteristics or the layout sequence of materials. Because of this periodicity, the structures themselves are traditionally simulated using the unit-cell approach, where a unit cell (the part that duplicates along the periodicity direction) of the structure is analysed with the assumption that it can be infinitely duplicated. This is somewhat unrealistic for a practical application such as a EBG antenna. The structure size will always be finite, and there will always be interactions between the EBG elements and other components in the structure.

A full-wave simulation is therefore essential to estimate the performance of such hybrid structures. Traditional full-wave techniques lack the efficiency to cope with the complexity of such structures. The EBG periodical elements are often much smaller in size than the accompanying components such as the radiating patch on our proposed EBG antennas. The fine detail of the structure often requires a $1/20$ or even $1/100$ ratio of the mesh size comparing to the operating wavelength λ, in order to have an accurate prediction, while the overall structure can have dimensions as large as tens of λ. Such a vast contrast between the mesh size and the overall structure means that huge computational resources are required if any traditional full-wave simulators are to be employed to account for a reasonable numerical resolution and accuracy. One of the advantages of the level-1 Haar based MRTD is that it consumes equal or less memory comparing to the conventional Finite-Difference Time-Domain (FDTD) technique, while doubling the resolution (more detail explained in chapter 4).

The EBG structures and their unique characteristics have led to many applications in microwave engineering, especially in antennas. A dual-band double layer EBG antenna was developed, measured and reported. The idea is a first of its kind, which reveals the multi-resonance capability of a patch antenna (or rather a microstrip cavity) utilizing not only the aforementioned stopbands but also the passbands of the EBG substrates.

The photonic antenna concept captured the advantage of both the EBG enhanced antenna and the integrated photonic modulator (the AFPM device, Asymmetric Fabry-Perot Modulator). It can be used in radio-over-fiber communications, which in turn will make the distributions of multiple wireless services including GSM/UMTS, TETRA and WLAN via installed optical fibers in an indoor environment a reality. The photonic antennas can be used as the interface between the installed fiber infrastructure and wireless service users in such indoor scenarios. The novel AFPM is employed as an electrical/optical transducer, performing both optical intensity modulation and photodetection in a single device. Our contribution in this joint project are the EBG enhanced antennas that host the AFPM devices. The EBG single antenna reduces the backward radiation from the device, while on the other hand the EBG structure improved the isolation between ports on the array antenna and made the overall 4- element structure much more compact.

In all, this thesis covers the major parts of my PhD work. The intrinsic Perfectly Matched Layer (or Perfect Matching Layer, PML) and source expansion for Haar wavelet based MRTD, the development of the 3D MRTD code, their applications in a hybrid EBG antenna as well as the proposed EBG antennas themselves mark the novelty of this thesis.

1.2 Objectives of the Thesis

There are a few objectives that the author would like to achieve by writing up this thesis:

1. To demonstrate the superiority and discuss the tradeoffs of the Haar based MRTD technique over the conventional FDTD method.

2. To report the concept and development of the EBG hybrid antennas.

3. To demonstrate basic features of the MRTD numerical code, in its one-dimensional, two-dimensional and three-dimensional applications.

1.3 Organization of the Thesis

In order to achieve the objectives aforementioned, this thesis is organized as follows.

Chapter 1 provides a general overview of the author's works, reveals the aims and structure of the thesis.

Chapter 2 elaborates the background information and the literature on theories and applications of EBG structures. It also briefly introduces the traditional FDTD method, since it will be used as a reference algorithm to compare simulation results.

The wavelet function upon which the general MRTD method based is introduced in Chapter 3. Variations based on different types of wavelets are also explained. The mathematical derivations reveal the advantages and potential drawbacks of the algorithm.

Chapter 4 describes the Haar wavelet based MRTD technique in detail. It also includes a proposal of intrinsic MRTD PML in its explicit form, as well as a source expansion schemes in two-dimensional and three-dimensional configurations.

In Chapter 5, several EBG enhanced antennas are designed, simulated and reported. The measurements verified that the antennas possess improved performance on top of the initial design requirements.

Chapter 6 further demonstrates the numerical simulation of the multi-layer EBG antenna using the proposed Haar MRTD algorithm.

Finally, Chapter 7 discusses the outcome of the research by drawing conclusions and proposing future work.

Chapter 2

Introduction to EBG Structures

2.1 Introduction

The Electromagnetic Bandgap (EBG) structures are recognized as a sub-category of metamaterials, based on their characteristic periodicity. Metamaterials [3] are artificial materials engineered to provide properties that may not be readily available in nature. They have the potential to control and manipulate wave propagation in a manner that eludes conventional materials, because of their periodic nature that can either be small-scale or resonant. Their use may enable us to create highly directional antennas, enhance the performance of small antennas [4] by making them appear as though the electrical lengths were much larger, and design highly integrated transceiver systems that can be packaged in a limited space [5]. Although the practical applications of metamaterials are currently limited by their loss characteristics and operational bandwidths, it is essential to develop efficient modelling tools to quantify and represent the characteristics of metamaterials and their behavior, especially when they form an integral part of complex electromagnetic systems.

In particular, the traditional 'unit-cell' analysis may not be valid for truncated periodic structures. In addition, when devices such as antennas are placed closed to EBG structures, it is necessary to account for the interaction between antennas and EBGs, in a numerically rigorous manner. This is particularly important since analytical models exist

only for a very small class of periodic structures, consequently, there is often a tendency to attempt to simplify the original problems by making gross approximations to reduce their complexy. However, this often involves sacrificing the accuracy to the point that may make the results totally erroneous, and the performance predictions misleading [6].

Being less numerically dispersive [2] and less memory intensive over conventional methods, the MRTD technique was deemed a good fit for analysing hybrid EBG antennas. It will be further clarified in later chapters. The general theory and applications of EBG structures are described below.

2.2 Basic theory of EBG structures and the "unit cell" approach

In general, many of the artificial Electromagnetic (EM) materials can be classified as metamaterials, such as Left-Handed Materials (LHM), Electromagnetic Bandgap (EBG) structures, and Photonic Bandgap (PBG) structures [8]. Among the metamaterials, the EBG structure is of particularly growing interest. It inherits the name of "bandgap" material from the PBG in photonics, while EBG is mostly operating in microwave spectrum. There are many different types of EBG structures, with the typical common periodic aspect. EBG structures have multiple frequency bands that prohibit wave propagation and such stop bands are basically determined by the periodicity of the structure.

For example, a typical transmission coefficient chart of an EBG structure with plane wave incident is shown in Fig 2.1. The pass bands and stop bands are corresponding to those in Fig 2.2. With the existence of k (wave number) at each frequency, the pass bands allow the incident wave to propagate through the structure and radiate. At the frequencies for which k does not exist, no propagation mode is allowed; the incident wave will be reflected and scattered at the interface. These frequencies are characterized as stop bands or bandgaps.

Periodic planar structures, such as a mushroom structure illustrated in Figs. 2.3 and 2.4, are more compact than the 3D structures such as a woodpile structure and an array of dielectric holes [10]. As it turns out, planar EBG structures are popular in antenna applications, which makes them the priority in research. The mushroom structure has two

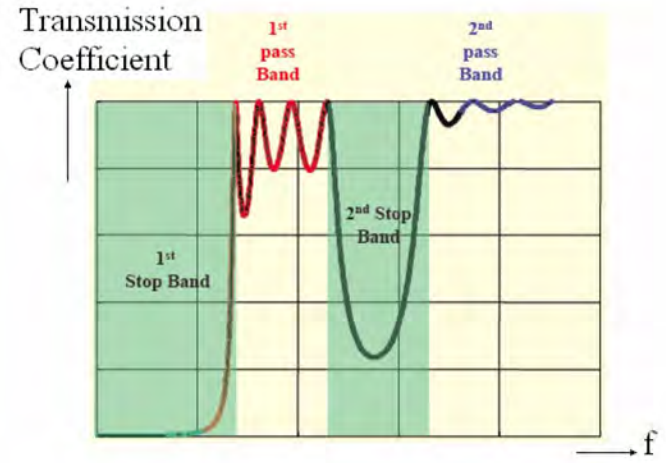

Figure 2.1: Typical EBG structure transmission chart [18]

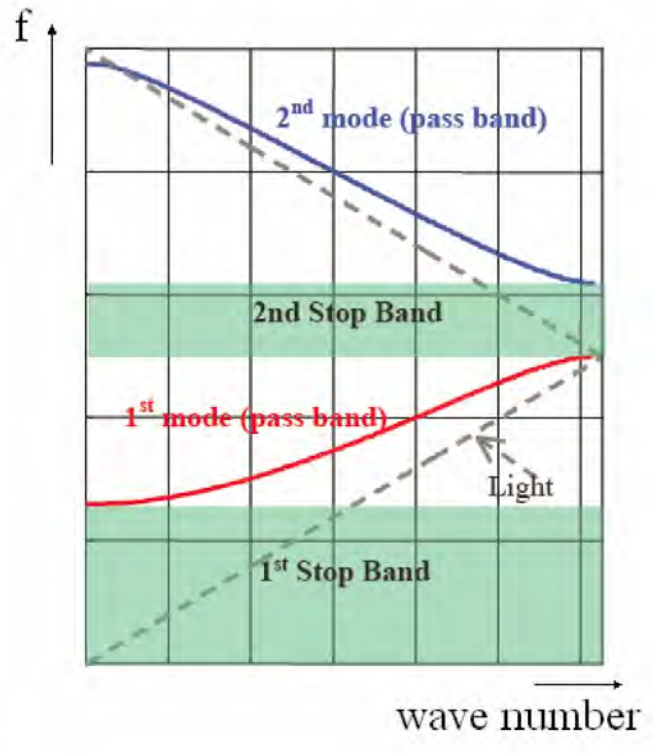

Figure 2.2: Typical propagation modes chart [18]

bandgap features, to suppress the surface wave and to reflect the normal incident wave in-phase [10]. When the planar EBG structure is used as a reflector, it is also called a High Impedance Surface (HIS) or a Reactive Impedance Surface (RIS). Within the bandgap, the wave cannot propagate; the surface behaves as having a large impedance at this frequency range, hence the HIS name.

The typical mushroom structure and many other planar EBG structures have a Perfect Electrical Conductor (PEC) ground plane at the bottom. This results in total energy reflection from the ground plane, hence a transmission chart like the one shown in Fig 2.1 is no longer available. Instead, a reflection chart is used for modelling and investigating the bandgap performance. A typical reflection phase chart of an EBG structure is shown in Fig 2.5.

In Fig 2.5, the blue curve represents the reflection phase at an observation point close to the surface when a plane wave normally incidence (perpendicular to the surface) on the EBG structure that with a PEC ground at the bottom. The frequency corresponding to the cross 0 degree point indicates the bandgap centre frequency.

A handful of periodic structures can be analysed theoretically. As for the mushroom EBG structure, it can be analysed using its equivalent circuit. Sievenpiper [9] presented some initial in-depth detail of the equivalent circuit theory of the hexagonal shaped mushroom structure. A modified locally resonant cavity cell (LRCC) model for square mushroom patches was introduced in [11]. Its equivalent circuit is shown in Fig 2.6.

The following formulas can be used to calculate the bandgap frequency of EBG structures in the LRCC model. [11]

$$C = \frac{\varepsilon_0(1+\varepsilon_r)W}{\pi}\cosh^{-1}(\frac{W+g}{g}) \tag{2.1}$$

$$L = \mu_0 h \tag{2.2}$$

$$\omega_0 = \frac{1}{\sqrt{LC}} \tag{2.3}$$

where C is the capacitance due to the gap between the EBG patches. L is the inductance resulting from the current flowing along the vias to the ground plane. ε_0 and μ_0 are the permittivity and permeability of the free space. W, g and h are the width of the patch,

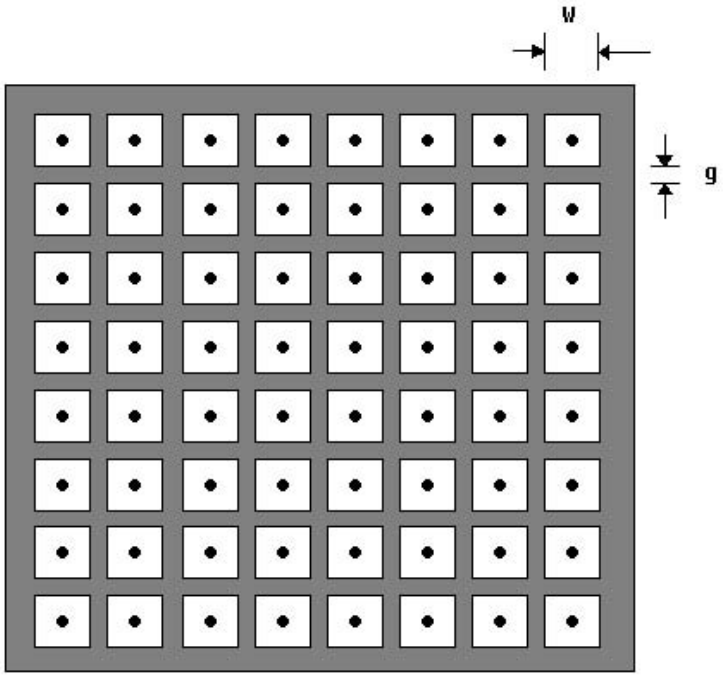

Figure 2.3: Mushroom Structure on a dielectric slab (top view), reproduced from [9]

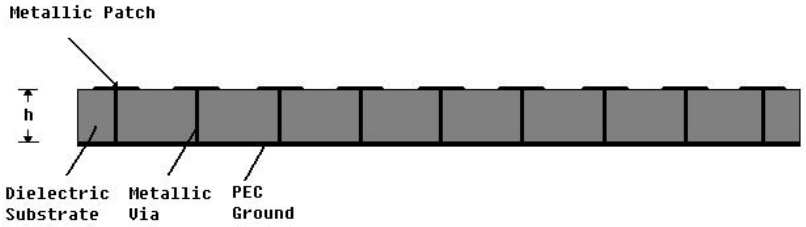

Figure 2.4: Mushroom Structure on a dielectric slab (side view), reproduced from [9]

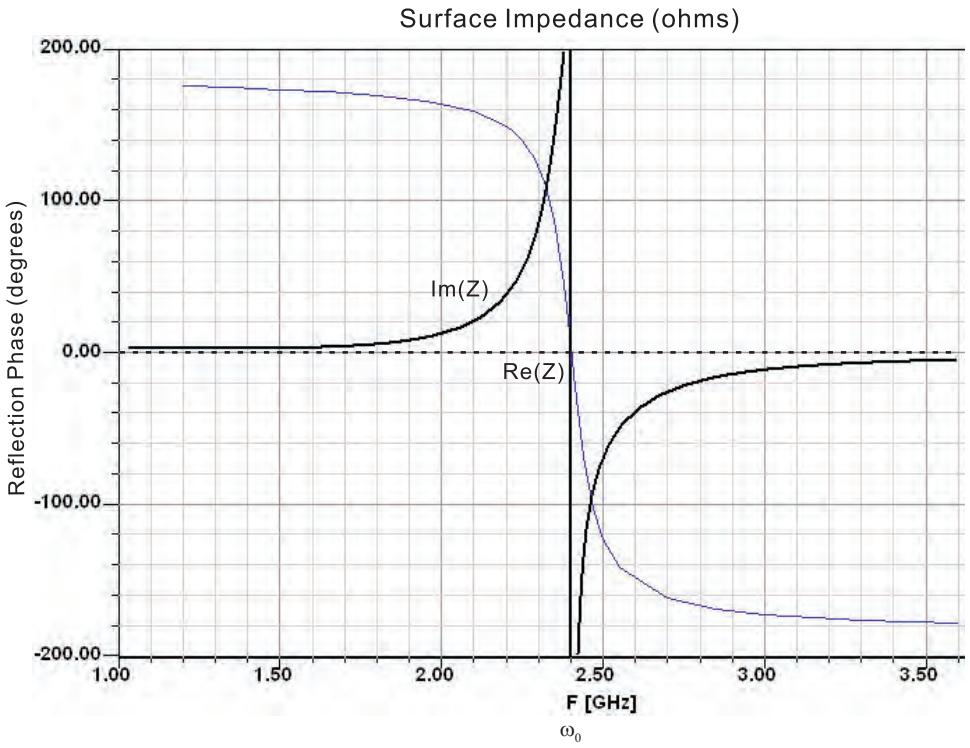

Figure 2.5: Reflection phase chart of a typical EBG structure (Blue: Reflection phase; Black: Surface Impedance)

gap between patches and height of substrate, as shown in Fig 2.3 and 2.4. ε_r is the relative permittivity of the dielectric substrate. ω_0 is the bandgap centre frequency.

The LRCC model also gives a formula for the effective surface impedance of the surface.

$$Z = \frac{j\omega L}{1 - \omega^2 LC} \tag{2.4}$$

From this formula, it is interesting to notice that at ω_0, the bandgap frequency, the surface impedance Z is infinity, much larger than the impedance of free space, $Z \gg \eta_0 = 377\Omega$. This reveals the high impedance feature of the EBG structure, at the bandgap frequency. That is why it is also called a high impedance surface (HIS). The surface impedance plot versus the frequency is shown as the black curve in Fig 2.5.

As specified in [12] by Sievenpiper, below ω_0, the surface is inductive and supports transverse magnetic (TM) surface waves. Above ω_0 it is capacitive and supports transverse electric (TE) surface waves. Between the TM and TE bands lies the bandgap, where

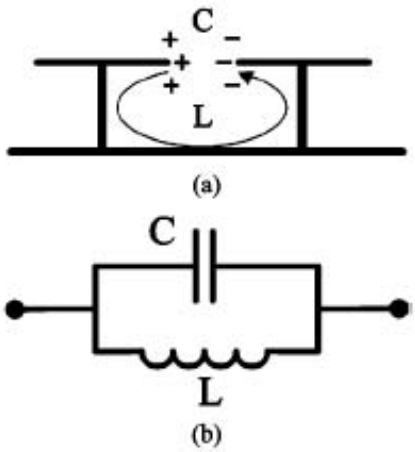

Figure 2.6: LRCC model of mushroom EBG structure (a) origin of the equivalent circuit elements (b) a parallel local resonant LC circuit [11]

surface waves are not supported. The fractional bandwidth B of the bandgap is [13],

$$B = h\frac{2\pi}{\lambda_0} \tag{2.5}$$

where h is the thickness of the surface, and λ_0 is the wavelength at ω_0 [13]. This prohibited surface wave feature is very important, which leads to the applications of isolation improvement etc. [10][20].

Note that this LRCC model is only valid when the E field of the incident wave is parallel to the patch surfaces and orthogonal to the edges of the square patches, as illustrated in Fig 2.7 where an E vector is applied along the y direction.

The typical unit cell model representation of the mushroom structure is also shown in Fig 2.7. To duplicate the unit along the surface in two directions, Perfect Electric Conductor (PEC) and Perfect Magnetic Conductor (PMC) boundaries are imposed as sidewalls. The metallic via is embedded inside the dielectric.The unit cell is terminated at the bottom with a PEC ground plane. On the top lies a PML surface layer, which is behind the source of the incident wave. Normally, a unit cell approach is simulated numerically, which essentially assumes an infinite structure along the x and y directions. Generally for the analysis of high impedance features of the mushroom EBG structure, the dispersion diagram like the one shown in Fig 2.2 is not absolutely necessary. The reflection phase

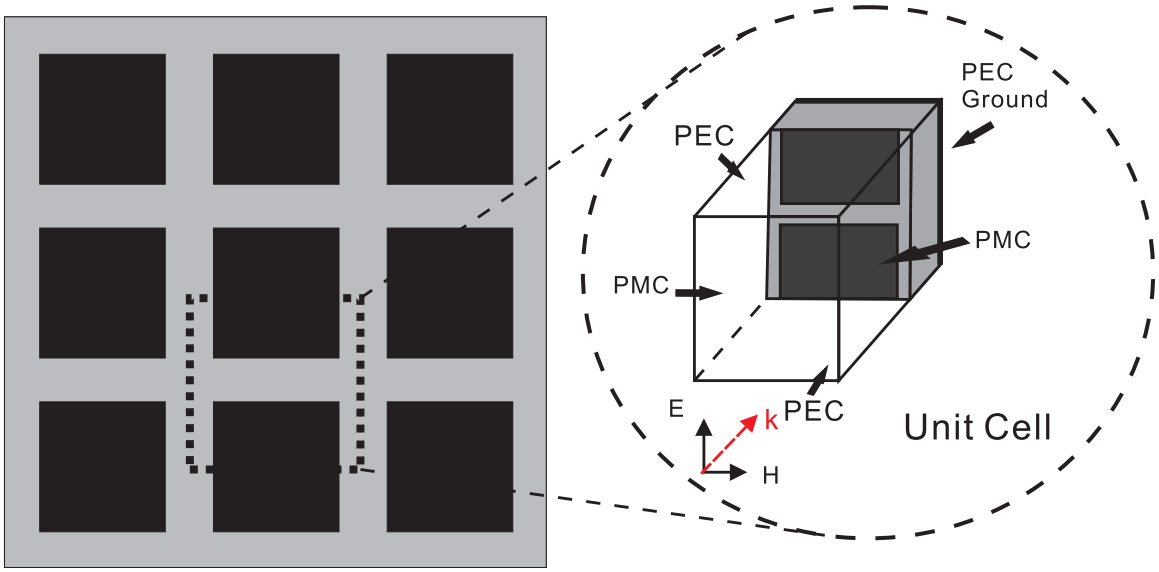

Figure 2.7: Unit cell of the mushroom EBG structure, reproduced from [14]

chart is more than enough to tell the working frequency, bandwidth etc.

Besides the standing wave features, it is found in [12] that the beam steering ability of the mushroom EBG controlled by embedded varactor diodes could be achieved, which possess similar forward and backward capability as a leaky wave antenna. By changing the illumination method (the angle of the E-field of the incident plain wave relative to the patches), a simple mushroom structure without diodes can achieve similar leaky wave characteristics [14].

When the electric field is at an angle to the patch gaps in the y-direction, the capacitances located in the x-direction will not have the same influence as those in the y-direction[14]. Therefore the equivalent circuit can be altered, which yields an unbalanced leaky wave model. [14]

The dispersion equation for the leaky wave model [14] is shown as,

$$\frac{1}{Z_1}\sin^2\left(\frac{\varphi_1}{2}\right)+\frac{1}{Z_2}\sin^2\left(\frac{\varphi_2}{2}\right)=0 \tag{2.6}$$

Z_1 is considered as the impedance due to the inductor L in parallel with capacitor C_1, Z_2 is impedance due to the inductor in parallel with capacitor C_2. φ_1, φ_2 are the phase shifts in y and x directions, accordingly.

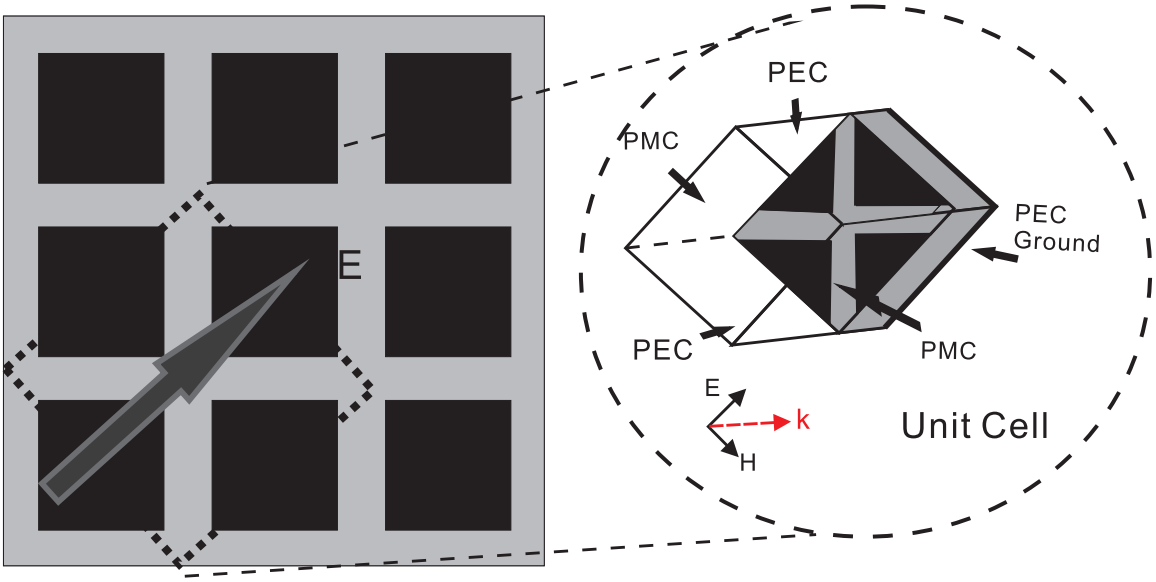

Figure 2.8: Unit cell of the mushroom HIS, excited with TE wave at 45°

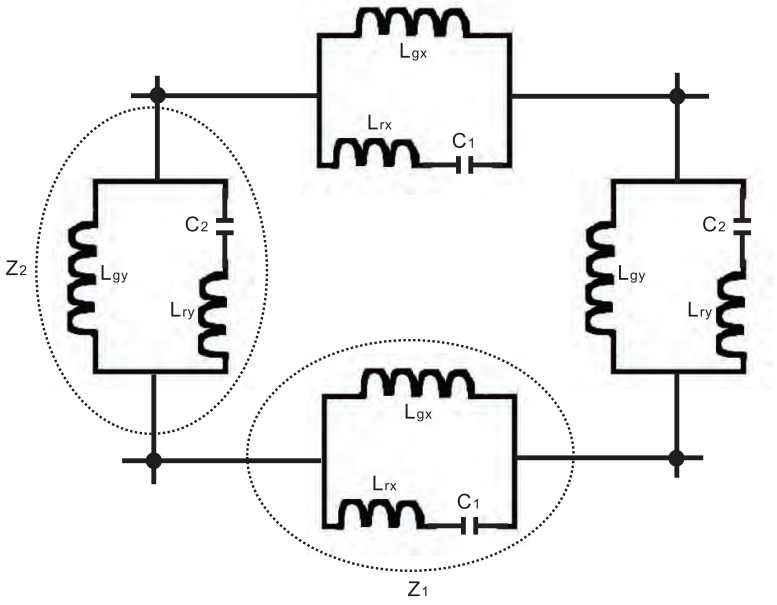

Figure 2.9: A leaky wave circuit model, reproduced from[14]

$$Z_1 = j\omega L_{gx}\frac{1-\omega^2 C_1 L_{rx}}{1-\omega^2 C_1(L_{rx}+L_{gx})} \approx \frac{j\omega L_{gx}}{1-\omega^2 C_1 L_{gx}} \tag{2.7}$$

$$Z_2 = j\omega L_{gy}\frac{1-\omega^2 C_2 L_{ry}}{1-\omega^2 C_2(L_{ry}+L_{gy})} \approx \frac{j\omega L_{gy}}{1-\omega^2 C_2 L_{gy}} \tag{2.8}$$

Such approximations only exist when L_{rx} and L_{ry} are infinitesimal. The total phase shift is a function of individual phase shifts φ_1 and φ_2,

$$\beta = \sqrt{\varphi_1^2 + \varphi_2^2} \tag{2.9}$$

From this it can be inferred that for $C_1 < C_2$, a forward wave propagation condition exists. For $C_1 = C_2$, a standing wave can be observed. For $C_1 > C_2$, a condition of backward wave radiation is satisfied.

The LRCC and the leaky wave models are deemed to have good insight of the mushroom EBG structure [11]. Still, they do not account for the radius of the via. And they do not deal with truncated structures where a unit cell approach is not valid. Yet there are many other types of planar EBG structures, such as the Uniplanar Compact Photonic-Bandgap (UC-PBG) structure shown in Fig 2.10(a), the Gangbuster Surface shown in Fig 2.10(b) and so on. Not every EBG structure can be explained by simple equivalent circuit. The best verification procedure is to do a full-wave numerical simulation, manufacture a sample and experimentally measure it.

2.3 Existing antenna applications of EBG structures

Various EBG structures have been reported in applications to enhance the antenna performance. They have been applied to many positions along with the antenna radiating elements: on the top of antenna (as a superstrate), surrounding the antenna (to form a Fabry Perot cavity), at the bottom of the antenna (as a ground plane or reflector), as well as in antenna array to improve the isolation. In a number of applications reported in literature (mostly reflectors, substrate materials, resonator antennas, passive waveguide components, mixers and subsystems, etc.), the EBG shows great potential to resolve

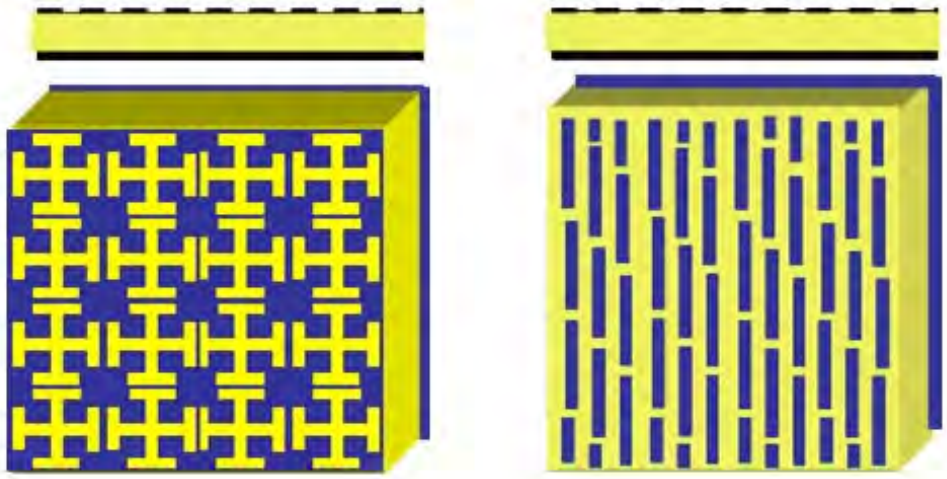

Figure 2.10: (a)UC-PBG structure without via (b) Gangbuster Surface, reproduced from[18]

limitations in conventional antennas.

Traditionally, the PEC ground plane can be used as a reflector in planar small antennas. With sufficient size relative to the radiating elements, the ground plane blocks the backward radiation and improves the antenna gain by 3dB when the reflected wave is in-phase. When a PEC reflector is placed one quarter-wave length apart from the antenna, the reflected wave is constructive and in-phase, as shown in Fig 2.11. But when the distance is much less than a quarter-wave length, the PEC cancels the electric current close to it so the reflected wave will be destructive. This destructive effect results in downgraded radiation efficiency and deteriorated gain of the antenna.

To reduce the distance between the reflector and the antenna, in other words to miniaturize the overall structure, an EBG reflector can be utilized. The typical configuration is shown in Fig 2.12. The EBG reflector has no phase shift within its bandgap frequencies and provides in-phase reflection of the wave, therefore the antenna radiating element can be placed very close to the reflector and still performs well in terms of radiation efficiency.

Dan Sievenpiper *et al.* have done pioneering work in utilizing the EBG as a reflector, as well as a surface wave suppressing structure. If a monopole antenna is placed vertically against a finite-sized PEC ground plane, because of the existence of the surface

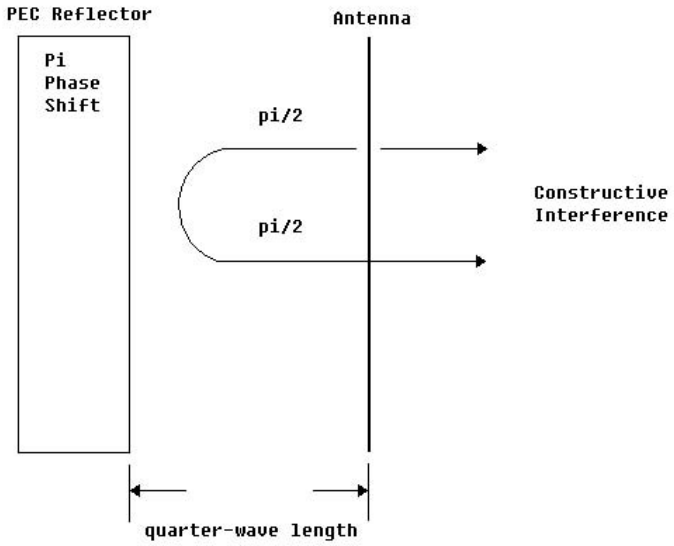

Figure 2.11: A quarter-wave length apart PEC reflector, reproduced from[9]

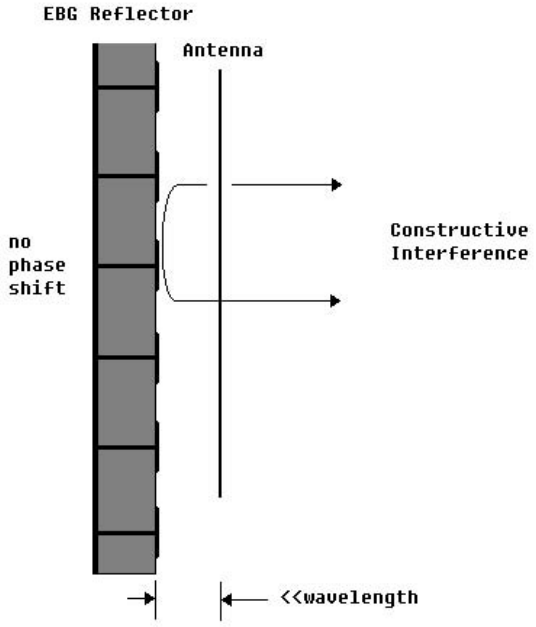

Figure 2.12: EBG reflector antenna with a mushroom structure, reproduced from[9]

wave along the PEC conducting plane and the edge effects of the ground, the antenna radiation pattern will be distorted, as shown in Fig 2.14(a). The backward radiation is noticeably large too.

By replacing the PEC reflector with an EBG reflector with appropriate bandgap frequencies, the radiation pattern of the antenna will be smoother, shown in Fig 2.14(b). The surface wave is suppressed and the backward radiation significantly reduced. But along with the advantages, the gain at the horizontal direction is reduced, due to the reverse direction of the image currents.

The cases of horizontal monopoles are shown in Fig 2.15. With the PEC ground, the image current is in the opposite direction to the monopole source, which results in a cancelling effect and hence poor radiation. With the EBG reflector, the image current is in the same direction as the source, which means physically the reflection is in-phase. The overall performance is enhanced, with much less backward radiation, as shown in Fig 2.16.

Fusco *et al.* utilized the tunable leaky wave feature of the mushroom EBG to create a reflector [15]. The equivalent circuit model also enabled them to design the EBG as ultra thin absorbers as well as polarization preservation reflectors.

Fan Yang *et al.* demonstrated that EBG structure can be used to reduce the mutual coupling in a patch antenna array, when placed between the antenna elements, as shown in Fig 2.17 [10]. About 8dB of measured isolation improvement is seen in their paper at the bandgap frequency around 5.8GHz. FDTD method is used to analyse the EBG structure. It is believed that E-plane coupling affects the isolation more than H-plane. The E-plane and H-plane coupling configuration are shown in Fig 2.18. The mutual coupling levels with different substrate configurations are shown in Fig 2.19. This EBG design shows its advantage on thick and high permittivity dielectric substrates. It has to be emphasized that the isolation improvement is achieved only when the array is linearly polarized. In later chapters, designs that achieved isolation improvement on a circular polarized antenna array will be demonstrated.

Akimasa Hirata further expands the idea to block the surface wave in a two-by-two

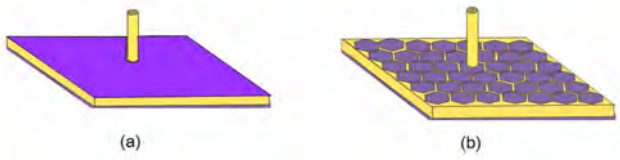

Figure 2.13: Vertical monopole on top of (a) a PEC reflector (b) a EBG reflector [9]

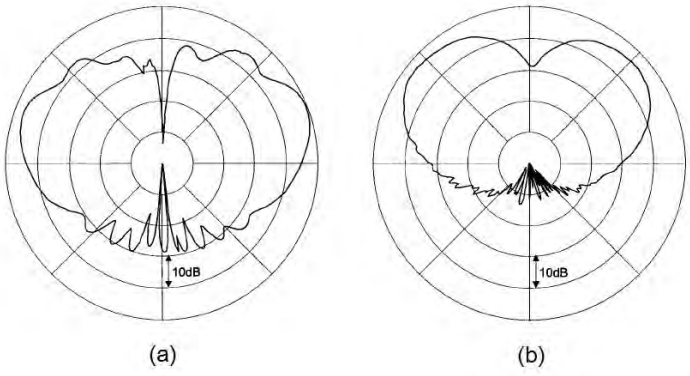

Figure 2.14: Radiation pattern of a vertical monopole (a) over a PEC reflector (b) over a EBG reflector [9]

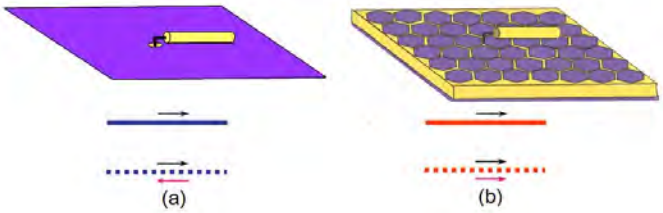

Figure 2.15: Horizontal monopole on top of (a) a PEC reflector, yielding a destructive image current (b) a EBG reflector, yielding a constructive image current [9]

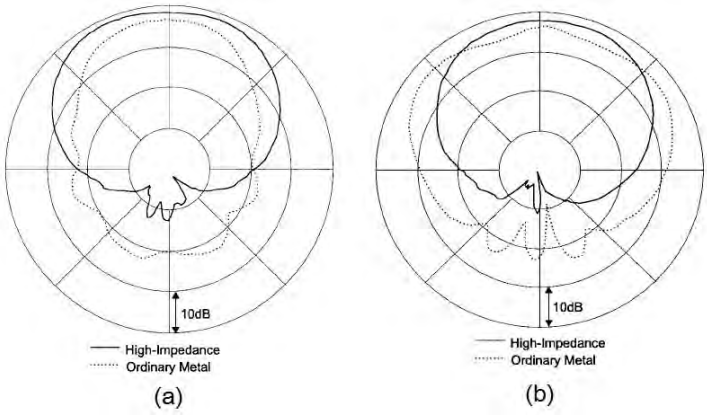

Figure 2.16: Radiation Pattern of horizontal monopole over PEC and EBG reflector (a)H-plane (b)E-plane [9]

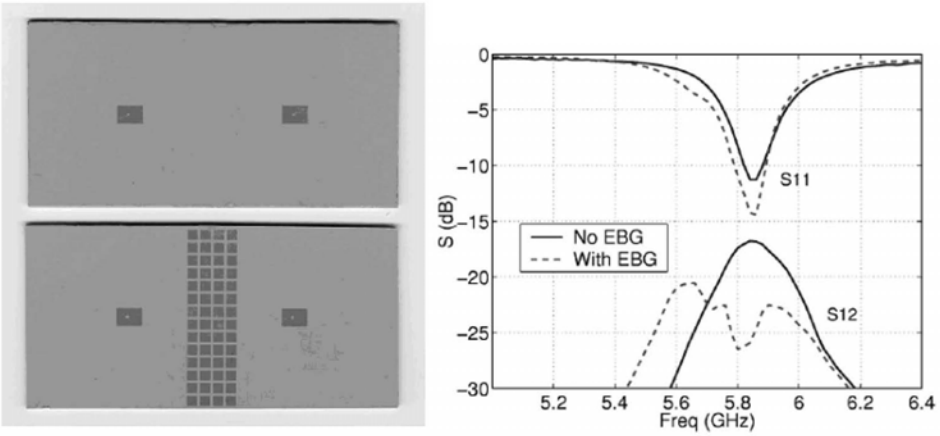

Figure 2.17: Microstrip patch antenna with and without mushroom EBG structure, [10]

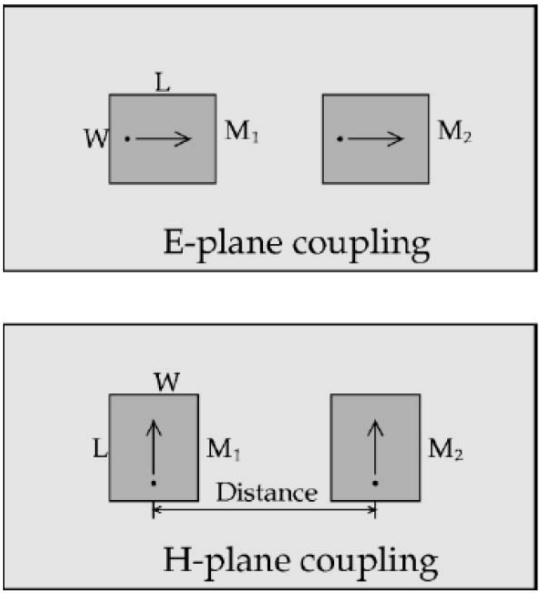

Figure 2.18: E-plane and H-plane coupled antennas, [10]

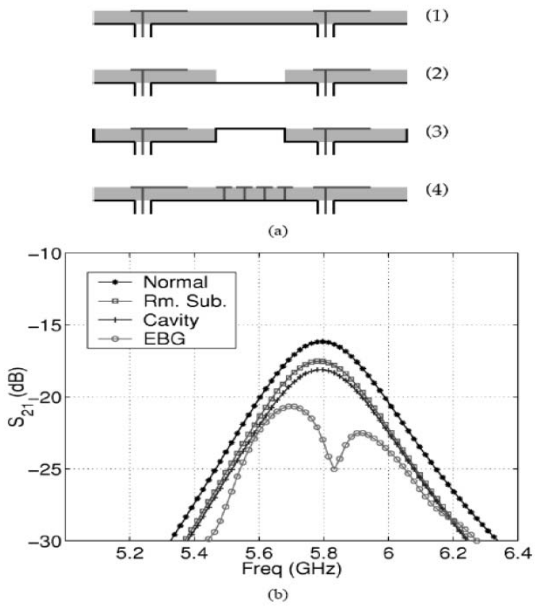

Figure 2.19: E-plane coupling with different substrate configurations, [10]

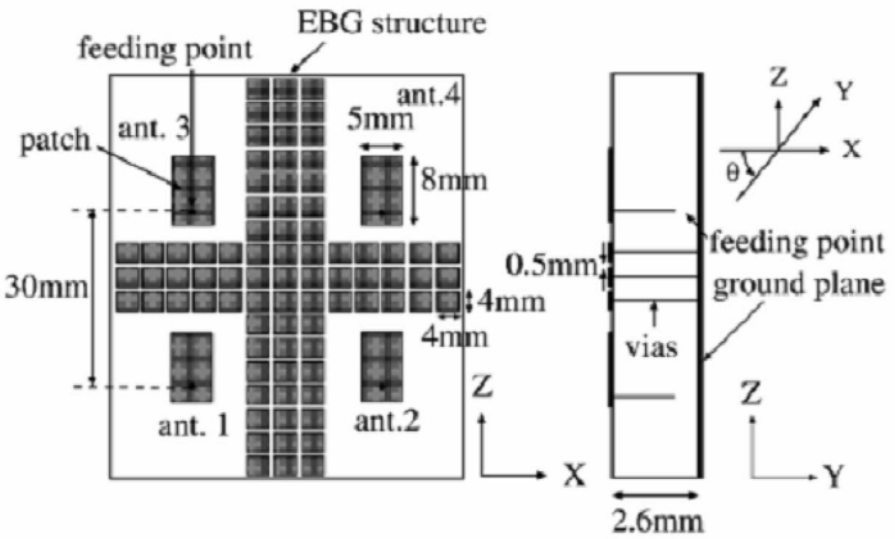

Figure 2.20: Patch antenna array with EBG structure to block surface wave / reduce mutual coupling, [20]

linear polarized patch array, as shown in Fig 2.20 [20]. More than 8dB isolation improvement is claimed from simulation using their in-house numerical code. Hirata's paper is more focused on the system performance than the antenna property, discussing a so called MUSIC nulling method. Still this paper extends the idea of utilizing EBG structure to block surface wave and improve isolation.

Boutayeb *et al.* published a paper on a cylindrical EBG (CEBG) antenna [21]. The antenna uses a monopole antenna as a source. With the layered metal cylinders, it becomes highly directive and the beam and directivity can be controlled by modifying the surrounding CEBG structures. It is unique in having a reconfigurable directive antenna at low frequency with relatively small overall volume.

The theoretical recursive method is used to analyze the CEBG structure as a Fabry-Perot cavity. The calculated transmission coefficient of the structure without defect (as shown in Fig 2.21 (a)) is quite similar to results from their FDTD simulation, which shows that without the defect, the layered CEBG has maximum transmission at around 2.3GHz, and the bandgap covers the lower frequencies. When such a structure is with defect at the bandgap frequencies, the wave will be reflected by the surrounded CEBG structure which boost the outgoing radiation at the defect region. Hence it forms a highly directive antenna. The four-layered CEBG with defect is shown in Fig 2.21 (b), with its radiation patterns at 1.77GHz shown in Fig 2.22.

Bao *et al.* reported a fractal EBG enhanced circular patch antenna [22]. It further develops Sievenpiper's embedded patch idea. As shown in Fig 2.23, the embedded patch with surrounded mushroom EBG takes advantage of surface wave suppression, and thus has better radiation pattern at broadside and significantly lower backward radiation. Bao's fractal EBG structure is shown in Fig 2.24. It seems that these fractal elements are complete planar structures without vias. From our experience, the planar periodic structure without via can be classified into Frequency Selective Surface (FSS) category. Typical FSS only behave like High Impedance Surface (HIS) in very narrow range of incident angles around the normal direction. The compact fractal elements are reported to have wide bandgap between 1.27GHz and 2.05GHz on a FR4 substrate. A low axial ratio is achieved over a reasonably wide bandwidth.

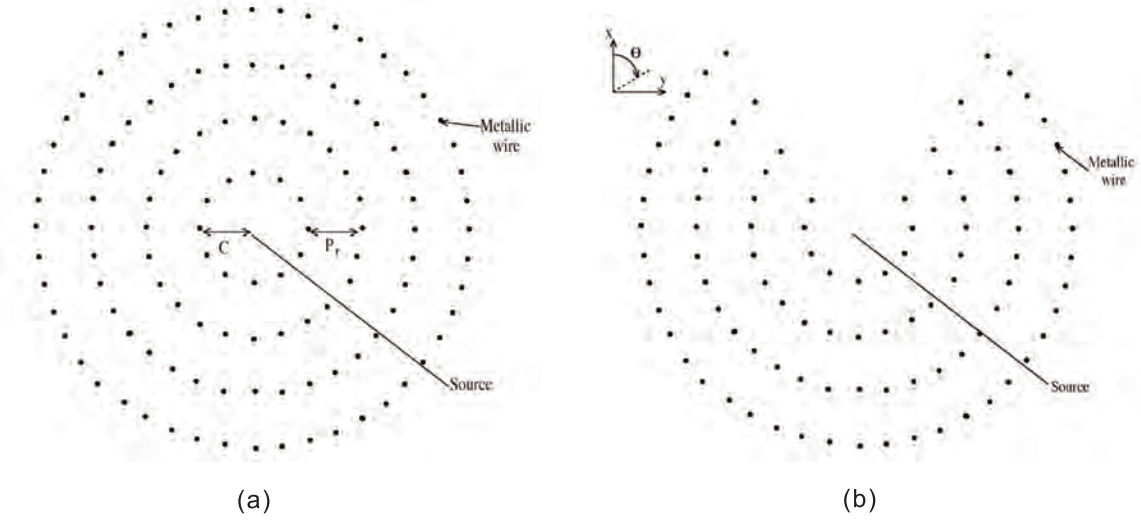

Figure 2.21: (a) CEBG structure composed of multilayer cylinders (b) Four-layered CEBG structure with defect [21]

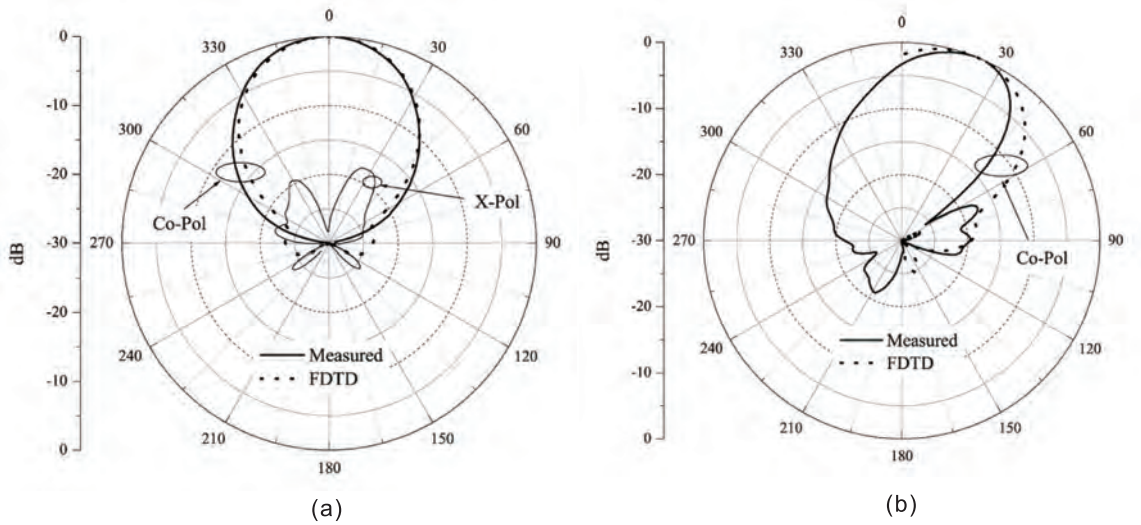

Figure 2.22: Radiation Pattern of defected four-layered CEBG structure (a) H-plane, 1.77GHz (b) E-plane, 1.77GHz [21]

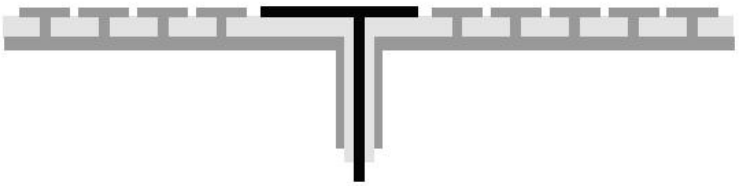

Figure 2.23: Probe-fed embedded patch antenna with surrounding mushroom elements [22]

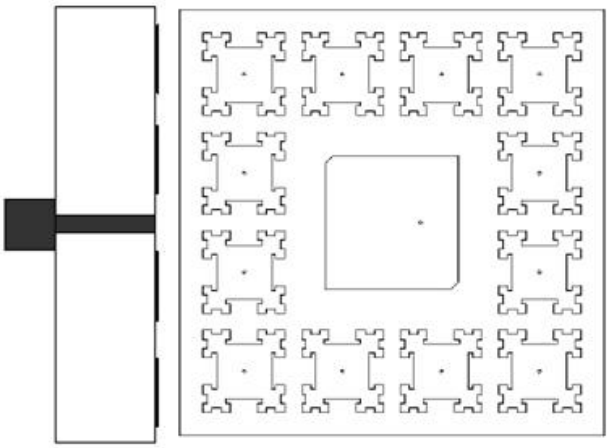

Figure 2.24: Probe-fed circular patch with surrounding fractal planar elements [22]

Li Yang *et al.* have a similar idea presented in [23]. A fork shaped EBG element and an F shaped EBG element have been invented to get an increased bandwidth with a reduced element size. The structures are shown in Fig 2.25 and 2.26. These structures contain vias, theoretically they are better than complete planar ones in terms of angular dependence of bandgap characteristics. Basically, the technique to create compact EBG structure is to increase the interaction between elements which increases the capacitance C in the aforementioned formula to bring down the resonant frequency ω_0. These designs have some impact on the design of spiral EBG structure which will be presented in a later chapter.

A loop antenna above an EBG surface has been published by Kim *et al.* [24]. It is interesting to notice that they claim that the EBG reflection phase for this antenna is selected at 90 degree rather than 0 degree. The total structure is shown in Fig 2.27. More than 14% bandwidth around 2.3GHz is achieved for the manufactured sample [24].

Finally, it's very interesting to note that Qu *et al.* have investigated a two-layered EBG

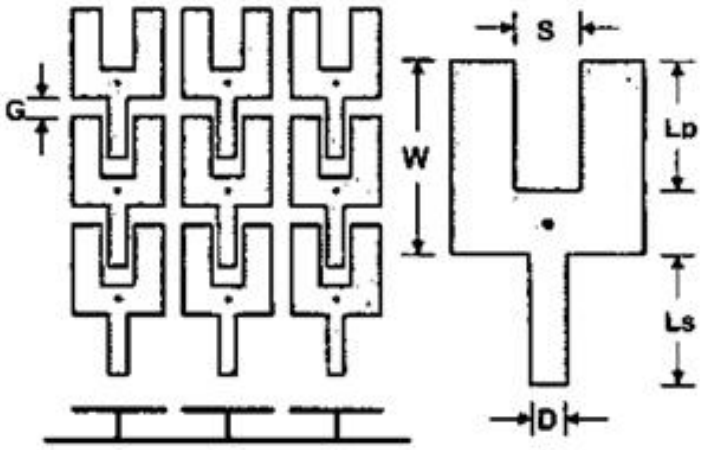

Figure 2.25: Folk shaped EBG with vias [23]

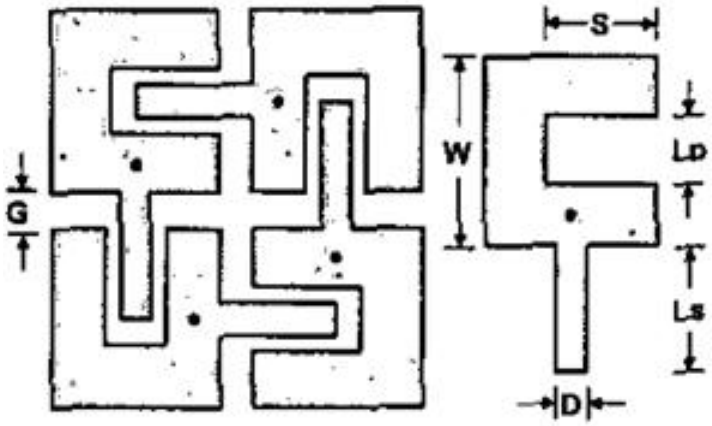

Figure 2.26: F shaped EBG with vias [23]

structure with patch antenna [26], which is quite similar to the structure proposed by the author of this thesis [4] [7]. Their structure is shown in Fig 2.28, while the author's approach will be explained in detail in later chapter. Their structure employs the identical dielectric substrate for both layer, with claim to have achieved 25% bandwidth of the antenna and similar gain improvement. The structure proposed in this thesis uses different dielectric materials for different layers, aiming at dual or multiple resonance of the antenna. Still, it was very useful investigating the gain improvement reported in their work.

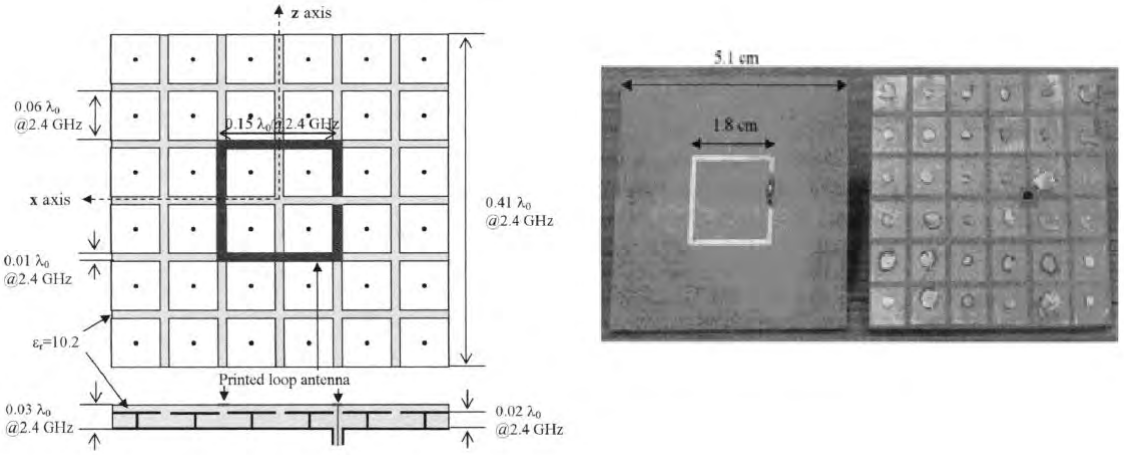

Figure 2.27: Loop antenna above mushroom structure [24]

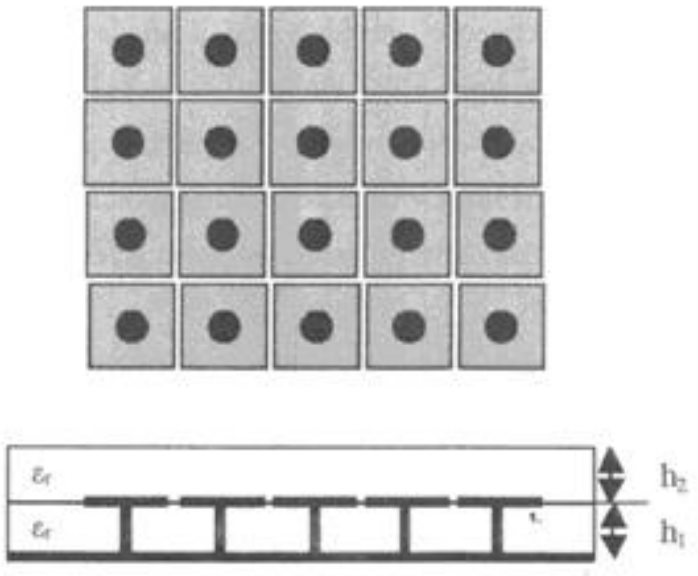

Figure 2.28: Qu's two layered EBG structure [26]

2.4 A brief introduction to the conventional FDTD method

As aforementioned, much of the existing numerical analysis of the EBG structures rely heavily on commercial software based on the unit cell approach. In order to facilitate a full-wave simulation, where the complexity in physical structures normally translates to memory intensive computations, efficient algorithms are sought after.

The finite-difference time-domain (FDTD) method is one of the traditional full-wave techniques used to solve complex EM problem. It was first proposed by Yee in 1966 [30] [31]. The mathematical simplicity of the FDTD method in terms of algorithm formulation has proved to be its greatest advantage. Basically, it uses finite differences to approximate the spatial and temporal derivatives in the Maxwell's equations. The method does not involve any integral functions, differential functions (as approximated by the central difference between cells(grids)), therefore become stepwise arithmetic calculations. In addition, since the FDTD grids are employed with a controllable cell size and the total number of cells, FDTD proves to be versatile (however only up to a limit) when used in complicated geometries. The main computational issues associated are the radiation boundary conditions or absorbing boundary conditions (ABC) for open structures, numerical dispersion, and stability conditions. The major drawbacks include its massive computational memory consumption, as well as long computational time.

To understand the theory and the constraints of FDTD, its one dimensional case is presented and examined here. For a one-dimensional case, a plane wave that propagates in the x direction within a non-lossy homogeneous material satisfies the following Maxwell equations.

$$\frac{\partial E_z}{\partial t} = \frac{1}{\varepsilon} \cdot \frac{\partial H_y}{\partial x} \tag{2.10}$$

$$\frac{\partial H_y}{\partial t} = \frac{1}{\mu} \cdot \frac{\partial E_z}{\partial x} \tag{2.11}$$

These equations can then be written by replacing the derivatives with finite differences between adjacent cells.

$$\frac{E_z^{q+1}[m] - E_z^{q}[m]}{\Delta t} = \frac{1}{\varepsilon} \cdot \frac{H_y^{q+\frac{1}{2}}[m+\frac{1}{2}] - H_y^{q+\frac{1}{2}}[m-\frac{1}{2}]}{\Delta x} \tag{2.12}$$

$$\frac{H_y^{q+\frac{1}{2}}[m+\frac{1}{2}] - H_y^{q-\frac{1}{2}}[m+\frac{1}{2}]}{\Delta t} = \frac{1}{\mu} \cdot \frac{E_z^q[m+1] - E_z^q[m]}{\Delta x} \tag{2.13}$$

where the index m corresponds to the spatial step and the index q corresponds to the temporal step, as shown in Fig 2.29. Basically, along the propagation direction, the spatial domain is discretized with equal sized grids, which is defined as the cells mentioned before. Solving these equations for $E_z^{q+1}[m]$ and $H_y^{q+\frac{1}{2}}[m+\frac{1}{2}]$ respectively, we have the

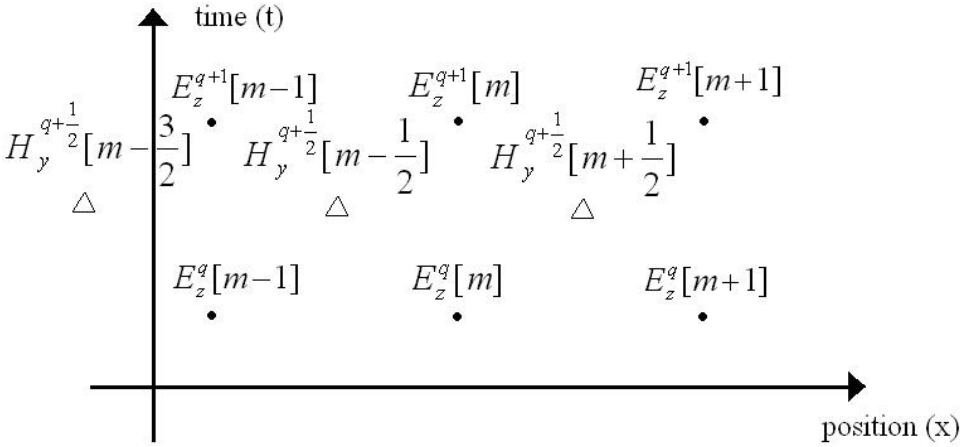

Figure 2.29: One-dimensional FDTD nodes arrangement, reproduced from [30]

update equations for the 1D FDTD.

$$E_z^{q+1}[m] = E_z^q[m] + \frac{\Delta t}{\varepsilon \Delta x}(H_y^{q+\frac{1}{2}}[m+\frac{1}{2}] - H_y^{q+\frac{1}{2}}[m-\frac{1}{2}]) \tag{2.14}$$

$$H_y^{q+\frac{1}{2}}[m+\frac{1}{2}] = H_y^{q-\frac{1}{2}}[m+\frac{1}{2}] + \frac{\Delta t}{\mu \Delta x}(E_z^q[m+1] - E_z^q[m]) \tag{2.15}$$

The field values of the current time step are updated with the electric and magnetic fields of the past time step. The ratio of $\frac{c\Delta t}{\Delta x}$ is often called the Courant number, labelled as S_c which represents the ratio of how far energy can propagate in a single temporal step to the spatial step. The coefficients in the update equations can then be written in terms of S_c.

$$\frac{1}{\varepsilon}\frac{\Delta t}{\Delta x} = \frac{1}{\varepsilon_r \varepsilon_0}\frac{\sqrt{\varepsilon_0 \mu_0}}{\sqrt{\varepsilon_0 \mu_0}}\frac{\Delta t}{\Delta x} = \frac{\sqrt{\varepsilon_0 \mu_0}}{\varepsilon_r \varepsilon_0}\frac{c\Delta t}{\Delta x} = \frac{\eta_0}{\varepsilon_r}\frac{c\Delta t}{\Delta x} = \frac{\eta_0}{\varepsilon_r} S_c \tag{2.16}$$

$$\frac{1}{\mu}\frac{\Delta t}{\Delta x} = \frac{1}{\mu_r \mu_0}\frac{\sqrt{\varepsilon_0 \mu_0}}{\sqrt{\varepsilon_0 \mu_0}}\frac{\Delta t}{\Delta x} = \frac{\sqrt{\varepsilon_0 \mu_0}}{\mu_r \mu_0}\frac{c\Delta t}{\Delta x} = \frac{1}{\eta_0 \mu_r}\frac{c\Delta t}{\Delta x} = \frac{1}{\mu_r \eta_0} S_c \tag{2.17}$$

where $\eta_0 = \sqrt{\frac{\mu_0}{\varepsilon_0}}$ is the characteristic impedance of free space.

For the lossy material case, Maxwell's equations can be modified.

$$\varepsilon \frac{\partial E_z}{\partial t} + \sigma E_z = \frac{\partial H_y}{\partial x} \tag{2.18}$$

$$\frac{\partial H_y}{\partial t} = \frac{1}{\mu} \frac{\partial E_z}{\partial x} \tag{2.19}$$

The conductivity σ can then be introduced into the FDTD update equations based on these Maxwell's equations. For 2D and 3D cases, the approaches are similar, with more field components from Maxwell equations. Fig 2.30 illustrates a 3D unit cell in the FDTD lattice. Now this is not the concept of Unit-cell approach introduced in the aforementioned EBG analysis. Here the unit cell is the single most basic computational block in FDTD, with one E and one H representing each and every cell in the computational domain. In fact, in Yee's FDTD configuration of unit cell, the electric and magnetic fields are spaced apart by half a grid in every direction, as shown in Fig 2.30, just like the $\frac{1}{2}$ cell distance in the 1D case which was shown in Fig 2.29.

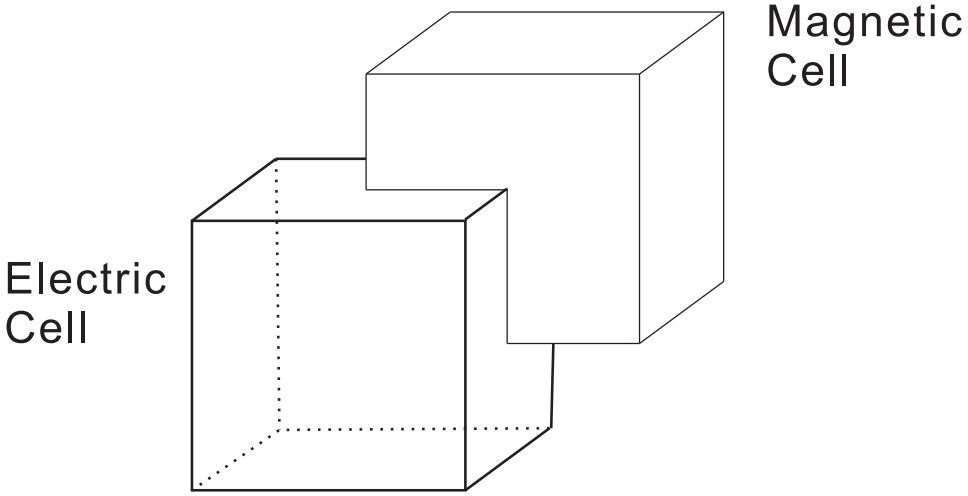

Figure 2.30: Standard Yee FDTD unit cell [30]

At the port, a Gaussian pulse is normally chosen as the excitation signal to yield the time-domain characteristic of the structure. The Gaussian pulse contains energy spread over a wide frequency range, therefore the time-domain solving process yields a wide-band solution, for example a return loss performance from 0GHz to 20GHz etc.. This

is one of the advantages of FDTD, compared to narrow band methods like the Finite Element Method (FEM).

$$E_z = e^{-\frac{(t-t_0)^2}{T^2}} \tag{2.20}$$

The FDTD method is arguably one of the simplest full-wave EM techniques [30]. However, the FDTD is computationally intensive. It suffers from serious limitations due to the lack of computer resources when modelling large electromagnetic problems [2]. Empirically, the FDTD requires at least 10 grids per wavelength in order to get a reasonable accuracy (in some cases, the requirement can be as large as 30 grids per wavelength, depending on the smallest detail that has to be included) . From the one-dimensional case, this requires that spatial step "Δx" to be at least equivalent or less than $\frac{1}{10}\lambda$. As for the stability requirement, the temporal step "Δt" can not be too large, in order to circumvent meaningless unstable results. A logical insight is that the energy should not propagate more than one spatial cell within each single temporal step. To ensure the stability of the time-stepping algorithm, a time increment is chosen to satisfy $c\Delta t \leq \frac{1}{\sqrt{\frac{1}{\Delta x^2}+\frac{1}{\Delta y^2}+\frac{1}{\Delta z^2}}}$, where c is the velocity of light. In terms of the Courant number "S_c", the stability requirement can be translated as $S_c \leqq 1$ for 1D case ($S_c \leqq \frac{1}{\sqrt{2}}$ for 2D case, and $S_c \leqq \frac{1}{\sqrt{3}}$ for 3D case).

To summarize, the traditional FDTD algorithm generally requires fine meshes in the spatial domain and reasonably short steps in the time domain. Therefore, the FDTD is quite memory intensive when comes to real computation. There are many approaches to improve the efficiency of Yee's algorithm, some of which include various hybrid FDTD techniques. Also, in addition to the orthogonal grid system, other meshing techniques are developed to tackle curved structures etc.

The finite difference mesh has to be truncated at the end of the computational domain. The field components tangential to the truncation planes cannot be evaluated from the equations (2.14) and (2.15), since the values of the field components outside the mesh are required and not available. The tangential E field components on the truncation planes must be specified to make sure there is no radiation reflection. The numerical configuration to specify this is known as an Absorbing Boundary Condition (ABC). There are many ways of configuring an ABC. One of the most widely used is the Perfectly Matched

Layer (PML), invented by Berenger [55]. The PML technique theoretically allows the electromagnetic waves to be absorbed with a reflection as short as needed. Using the PML technique allows better accuracy and less computational constraints. The detail of the PML method will be introduced in Chapter 4, along with its novel configuration in the Haar MRTD scheme.

Another disadvantage of the classic Yee's FDTD is numerical dispersion, which introduces significant errors when dealing with electrically large problems [34][35]. In short, the numerical dispersion is caused by a non-constant phase velocity in FDTD, whereas in real free space the phase velocity is a constant. For example, the original Yee's algorithm will accumulate 1.12 degrees of phase error per wavelength (free space, 20 cells per wavelength, $S_c = 0.5$) [32]. Several methods exist that can be used to tackle this dispersion problem, typically with higher-order approximations to the spatial or temporal derivatives[30]. However some complications arise with the use of higher-order central differences, which are associated with increased spatial stencils, typically at the material interfaces [30] [32].

2.5 A brief introduction to Moment Methods

The Moment Methods (MoM) is the first widely used numerical EM algorithm, introduced by Roger F. Harrington [42]. The general principle of MoM is to reduce functional equations to matrix equations which can be solved using matrix inversion. In general, the MoM solves the Maxwell integral equations (electric field integral equation (EFIE) and magnetic field integral equation (MFIE)) in frequency domain. However, the time-domain MoM is also available now.

The MoM first defines a mesh throughout the structure. For each cell, it computes the surface current by calculating interactions between cells.

$$I(x, y, z) = \sum_{n=1}^{N} b_n \cdot I_n(x_n, y_n, z_n) \tag{2.21}$$

The unknown coefficients b_1, b_2, b_N are to be determined. This equation shows that the current at each segment is a linear combination of contribution from other segments.

In is the basis function. The basis functions for MoM can be full domain functions such as sine, cosine, polynomials, etc. Common choices are pulse functions and triangle functions [53].

Then the MoM carries out the calculation between voltage and current by introducing the impedance matrix.

$$\begin{bmatrix} V_1 \\ V_2 \\ \vdots \\ V_N \end{bmatrix} = \begin{bmatrix} Z_{11} & \cdots & Z_{1N} \\ \vdots & \ddots & \vdots \\ Z_{N1} & \cdots & Z_{NN} \end{bmatrix} \begin{bmatrix} I_1 \\ I_2 \\ \vdots \\ I_N \end{bmatrix} \tag{2.22}$$

Every element of impedance Z matrix is a function of basis and weighting function. Two common procedures for dealing with the weighting functions are Galerkin's method and point matching method [53]. To obtain the current distribution, in the meanwhile get the field distribution, MoM uses matrix inversion, where $[I] = [Z]^{-1}[V]$.

The main disadvantages of MoM are its expensive computational cost and slow convergence. In fact, the request for powerful computer is very common in computational electromagnetics. But for MoM particularly, to solve an N order full matrix by matrix inversion requires N^3 scale number of operations. When N increases, the total number of operations increases more rapidly.

2.6 Conclusions

The EBG structures are newly emerged complex EM structures. They suppress the electromagnetic wave from propagation at certain frequency bands (the bandgap). Such stop bands are basically determined by the periodicity of the structure. By modifying the EBG to adapt to various applications, they possess great potential to resolve limitations in conventional antennas. The basic theory and typical applications are reviewed.

As the interest is mounting, the need to analyze the EBGs is also increasing. Analytical solutions only exist when the periodic structures are simplified to equivalent circuits, like the LRCC model for the mushroom structure reviewed in this chapter. Numerical

solutions are typically done with commercial software, utilizing the unit cell approach of periodicity. To construct and solve a finite-sized and electrically large structure, which suits the case of hybrid EBG antennas, efficient numerical algorithm is sought after. The FDTD method is briefly introduced in this chapter, which serves as a reference algorithm for developing and benchmarking the proposed Haar MRTD technique. An brief introduction of Moment Methods is also included.

Chapter 3

Wavelets and The Multi-Resolution Time-Domain Technique

Since first published in 1996, the Multi-Resolution Time-Domain (MRTD) technique has developed rapidly. It has advantages over conventional FDTD method in being less numerically dispersive [2] and less memory intensive [34]. Therefore, the MRTD technique is particularly of interest for analyzing the aforementioned electrically large and finite-sized structures.

To understand the MRTD, we have to understand the underlying mathematics regarding wavelet functions. These have been applied as basis functions for the efficient solution of EM integral equations and partial-differential equations (PDEs) in the form of Maxwell's equations. Every function in the function space defined by the Maxwell's equations (therefore the solutions) can be represented as a linear combination of basis functions. In addition, the wavelets when used as basis functions are indeed orthogonal bases. The orthogonality provides specific computational advantages over conventional FDTD method.

We will firstly take a look at wavelets, then the wavelet transform, and finally various MRTD schemes existing in literature.

3.1 Wavelets

3.1.1 Wavelet functions

The term wavelet is translated from the french word *ondelette*, meaning small wave. As aforementioned, the mathematical development dates back to 1910. A Hungarian mathematician Alfréd Haar published the very first paper [1] on the stair-cased approximation of a function, using piecewise constants later named Haar wavelets.

A wavelet is a small wave in the sense of being of short duration with finite energy; it must have amplitude which quickly decays to zero in both the positive and negative directions [38]. This is the precise meaning of being local. Most data used in the EM modeling are localized in time or frequency, i.e. have a certain correlation structure in spatial domain and spectral domain. Computational modeling seeks building blocks to approximate these data, which possess both the time and frequency localization. Therefore, being naturally local, the wavelet has the potential to be used as basis functions in EM modelling.

In mathematical terms, a wavelet ψ is a function with zero average in the time domain: $\int_{-\infty}^{\infty} \psi(t)\, dt = 0$ [38]. Basically that means a wavelet must have zero DC component and must be a bandpass function. It must also satisfy the condition that the integral of $\psi^2(t)$ is unity, that $\int_{-\infty}^{\infty} \psi^2(t)\, dt = 1$ [38].

There are many wavelet functions that meet these definitions, such as
the Morlet wavelet: $\psi(t) = e^{j\omega_0 t} e^{-t^2/2}$, shown in Fig 3.1;
the Haar wavelet: $\psi(t) = \begin{cases} 1 & \text{if } 0 \le t < 0.5; \\ -1 & \text{if } 0.5 \le t < 1; \\ 0 & \text{otherwise.} \end{cases}$ shown in Fig 3.2;
as well as Daubechies, Bessel, Coifman, Lemarie and Meyer wavelets etc.
Shannon wavelet, the most popular one in Meyer family, as $\psi(t) = \frac{\sin \frac{\pi t}{2}}{\frac{\pi t}{2}} \cos \frac{3\pi t}{2}$ is shown in Fig 3.3 . New wavelets are being discovered/invented on a regular basis.

These wavelet functions can be used as mother wavelets to generate daughter wavelets

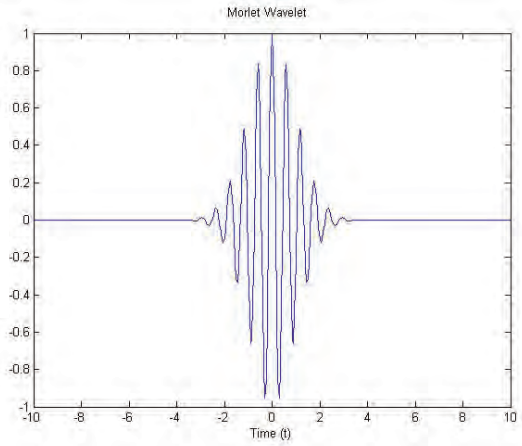

Figure 3.1: The Morlet wavelet, $\psi(t) = e^{j\omega_0 t} e^{-t^2/2}$, plotted real part

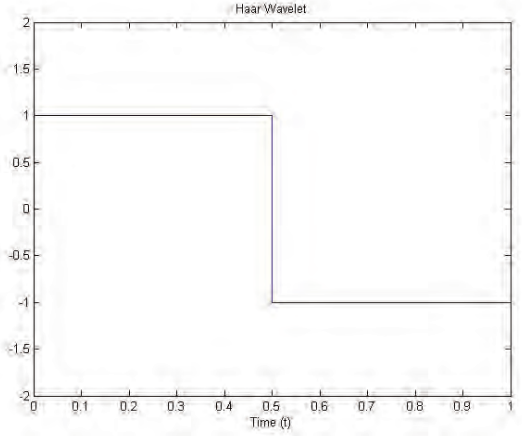

Figure 3.2: The Haar wavelet

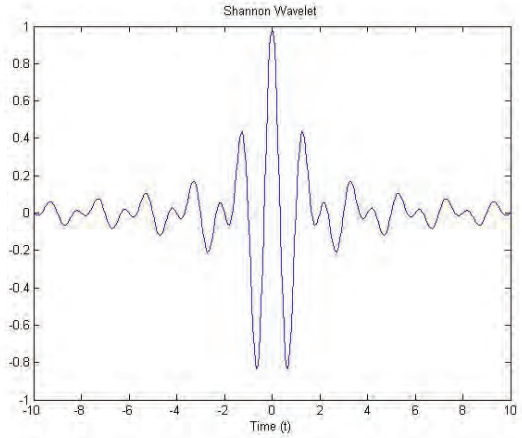

Figure 3.3: The Shannon wavelet, $\psi(t) = \frac{\sin \frac{\pi t}{2}}{\frac{\pi t}{2}} \cos \frac{3\pi t}{2}$

that form a set of basis functions. The generation process is based on translation and dilation. Translation basically is shifting the function along time: $\psi(t) \rightarrow \psi(t+k)$, while dilation is in fact scaling: $\psi(t) \rightarrow \psi(mt)$, where k is the translation factor and m is the scaling factor.

For example, the Harr wavelet can be dilated and translated into the following series.

$$\{\psi_{p,q}(t) = \frac{1}{\sqrt{2^p}}\psi(\frac{t-2^p q}{2^p})\}_{(p,q)\in Z^2} \tag{3.1}$$

where p is the scaling factor and q the translation factor, corresponding to m and k in previous general case. Normalized (i.e. the $\frac{1}{\sqrt{2^p}}$ variation in the absolute amplitude ignored) level 3 Haar wavelets are shown in Fig 3.4 as an example of a daughter wavelet series. From the level 1 Haar wavelet shown in Fig 3.2 to the level 3 ones, the sense of scaling (i.e. to condense from $[0,1]$ to $[0,\frac{1}{4}]$ along the time axis) and shifting (i.e. to move from $[0,\frac{1}{4}]$ to $[\frac{1}{4},\frac{1}{2}]$ along the time axis) can be seen. This series can be considered as orthogonal basis functions of linear space $L^2\mathcal{R}$. By orthogonality, the basis functions satisfy the following inner product equation:

$$\int_{-\infty}^{\infty}\psi_i(t)\psi_j(t)dt = \begin{cases} n & i=j; \\ 0 & i\neq j. \end{cases} \tag{3.2}$$

where n is a normalization factor. n equals the square of the norm (see Appendix A), in this particular Haar series case $n = \frac{1}{2^p}$. From equation 3.2, each of the wavelets can be seen as a vector perpendicular to each other, i.e. the inner product is 0. The only non-zero inner product yields when $i = j$.

The orthogonality of the daughter wavelet series provides a useful feature to sparsify a matrix. The method is to multiply a $N \times N$ wavelet matrix and its transpose on both sides of the original matrix $[Z]$ [38].

$$[Z'] = [W][Z][W]^t \tag{3.3}$$

where $[W]$ is the $N \times N$ wavelet matrix. W is constructed in such a way that wavelet basis vectors form its rows. Since $[W]$ is designed to be an orthogonal matrix, its transpose

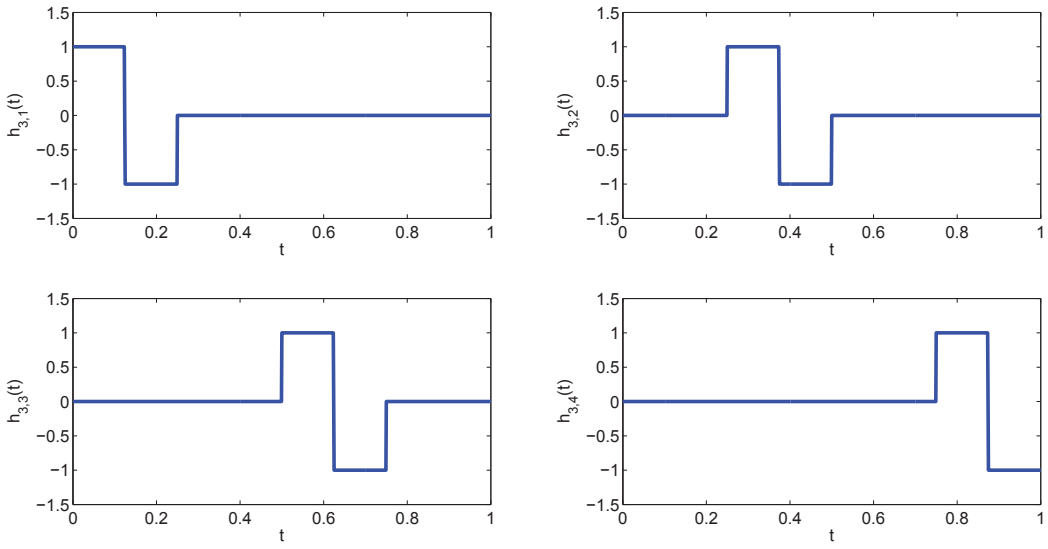

Figure 3.4: Level 3 Haar wavelets

matrix is in fact its inverse matrix: $[W]^t = [W]^{-1}$. By multiplying the $[W]$ and $[W]^t$ on both sides, it creates a lot of zeros since all the orthogonal vectors have a mutual inner product of 0. Also, many of the elements in $[Z']$ are infinitesimal, which can be neglected if smaller than a predetermined threshold. After this procedure, the derived matrix $[Z']$ is sparse.

The beauty of such a procedure is that it reduces the computational effort significantly. A computer derives a transpose $[W]^t$ from the original matrix $[W]$ (which only involves mapping and copying elements) much faster than calculating its inverse $[W]^{-1}$. By constructing the $[W]$ deliberately with wavelet bases, the extra effort of multiplying $[W]$ and $[W]^t$ pays off when the resulting sparse matrix $[Z']$ is passed on and solved using some sparse solver. This procedure is particularly recommended in literature [38], for improving the computational efficiency in solving electrically large problems in Method of Moments (MoM). Because MoM usually suffers from generating dense matrix and therefore slow in convergence.

In EM modeling, the compactly supported (i.e. strictly localized in space) wavelets may be used as basis functions, such as the Haar wavelet series shown above. These wavelets, by Fourier analysis, can be either strictly local in space (e.g. Daubechies and

Coifman wavelets) or strictly local in spectrum (e.g. Meyer wavelets), but cannot be local in both. They are not smooth and consequently not continuously differentiable.

However, this property of vanishing outside a finite interval does bring some advantage over the traditional sines and cosines bases that are used in the Fourier analysis. The sines and cosines extend infinitely along the domain. Therefore they are non-local, more suitable for analyzing signals spreads infinitely. The compactly supported wavelets, on the other hand, are much more suited to approximate data with sharp discontinuities. This partially leads to the superiority of wavelet transform over the Fourier transform [36].

3.1.2 The Wavelet transform

A family of time-frequency atoms is obtained by scaling ψ by s and translating it by u [36]:

$$\psi_{u,s}(t) = \frac{1}{\sqrt{s}}\psi(\frac{t-u}{s}) \tag{3.4}$$

where ψ is the chosen mother wavelet, s and u are continuously varying scaling and translation parameters, respectively. The mother wavelet ψ can be any type of wavelet function.

Then the Continuous Wavelet Transform (CWT) of $f \in L^2\mathcal{R}$ at time u and scale s is defined as [36]:

$$CWT(u,s) = Wf(u,s) = \langle f, \psi_{u,s}\rangle = \int_{-\infty}^{+\infty} f(t)\frac{1}{\sqrt{s}}\psi(\frac{t-u}{s})\,dt \tag{3.5}$$

The CWT is in fact the inner product of the signal $f(t)$ and the daughter wavelet series $\psi_{u,s}$. The wavelet transform overcomes the shortcomings of the Fourier transform, in that it outperforms when dealing with spiky signals. Just like the windowed Fourier transform, a fully scalable modulated window is used. The window is shifted along the signal being sampled, with a spectrum generated from every position the window sweeps. This procedure is then repeated with different window sizes (different resolution). The end result is a two-dimensional surface or a contour plot known as a scalogram, which maps the

original one-dimensional signal to the wavelet domain (or spectrum), across scale s and translation u defined by the CWT in equation 3.5. The transform coefficient $CWT(a,b)$ displays the matchness between the signal $f(t)$ and the wavelet bases.

Practically, the discrete wavelet transform (DWT) is more suitable for computational implementation. The original signal $f(t)$ is sampled first, which yields a discrete version: $f(n)$. The DWT of the $f(n)$ series is given here:

$$DWT(u,s) = Wf(u,s) = \frac{1}{\sqrt{s}} \sum_{n=u}^{sL+u-1} f(n)\psi(\frac{t-u}{s}) \tag{3.6}$$

where $\psi(n)$ is the discrete mother wavelet, again it can be of any type. L is the window width of the original ψ. Both the scaling parameter s and translation parameter u are functions of a hidden integer parameter m, $s = s_0^m$ and $u = na_0^m$. The result is a geometric scaling of $1, \frac{1}{s}, \frac{1}{s^2}, ...$ and translation by $0, n, 2n, ...$

To demonstrate its ability in analyzing signals, the discrete wavelet transform has been programmed using different underlying wavelet functions. The DWT is capable of discovering small details in signal variations in the time domain as well as in the frequency domain by transforming the signal into wavelet domain. In the following case, a wiggle monopole antenna was simulated in a commercial software, the CST Microwave Studio. A Gaussian pulse was applied to the port. Some of the energy was reflected back and received at the port as the reflected (output) signal. Both signals were then extracted from the CST model and imported into the MatLab based wavelet transform program.

The original signal together with the resulting spectrum are shown in the following figures. A Morlet wavelet based DWT is performed on the Gaussian pulse shown in Fig. 3.5, which yields spectrum Fig. 3.6. A Haar wavelet based DWT is performed on the output signal shown in Fig. 3.7, which results a spectrum of Fig. 3.8. Since the DWT is not directly related to the MRTD modeling work we are about to demonstrate, the details are exempt here. The significance of this DWT demonstration is that it reveals the property of the original signal, with respect of the particular underlying wavelet basis. Also it does not need the signal to be very long in duration, which is required if analyzed by the Fourier transform. More of the theory and analysis of the CWT and DWT can be

found in Mallat's book [36].

Wavelets is a topic of considerable interest in applied mathematics, more generally than Multi-Resolution Analysis (MRA). It is used to decompose data, functions, and operators into different frequency components. Then after the decomposition, each component can be studied at a resolution level matches its scale. Different scales of different components yield different resolutions. Loosely speaking, the wavelet transform performs the optimal sampling. The MRA outperforms the Fourier analysis in that both the time domain and frequency domain information is preserved. More detail of the MRA can be found in Mallat's [37] and Meyer's works [49]. The MRTD technique is based on the MRA analysis. More of the wavelets' properties will be discussed along their usage in the MRTD technique in next section.

3.2 Multi-Resolution Time-Domain (MRTD) technique

The initial development of MRTD was done by Krumpholz and Katehi [2]. They applied a so-called cubic spline Battle-Lemarie scaling and wavelet functions in the spatial domain to expand the electric and magnetic field components in the Maxwell equations (E and H), while keeping the use of rectangular-pulse functions in the time domain. This expansion procedure is somewhat similar to the Method of Moments (MoM), while the form of the update functions are generally comparable to the FDTD. The use of different levels of wavelet basis in addition to the scaling functions in MRTD allows a multi-resolution analysis to be applied to the spatial domain, with a high resolution (corresponding to a higher level of wavelet basis functions in the expansion of the field components) at regions where the field varies rapidly (i.e. material interfaces) and a low but adequate resolution (lower level of wavelet basis or even scaling functions alone) in homogeneous regions.

To introduce the typical MRTD approach, we start from the wavelet expansion of a one-dimensional signal f. It can be interpreted as a field component in 1D case [52].

$$f = \sum_{m=-\infty}^{\infty} \langle f, \phi_m \rangle \widetilde{\phi_m} + \sum_{n=0}^{\infty} \sum_{m=-\infty}^{\infty} \langle f, \psi_{n,m} \rangle \widetilde{\psi_{n,m}} \tag{3.7}$$

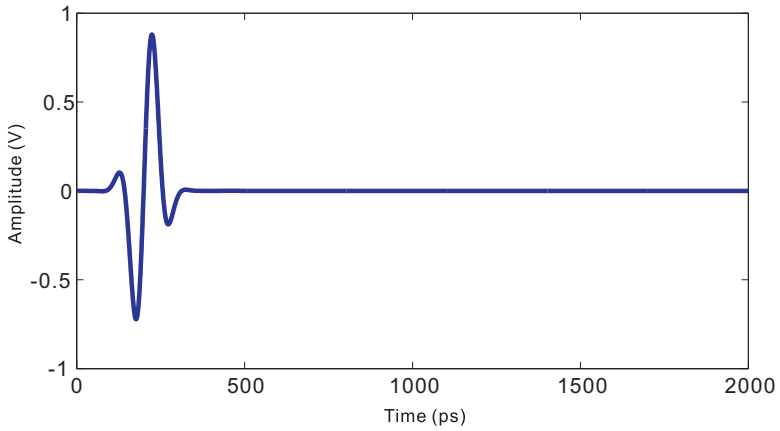

Figure 3.5: The original time-domain input signal

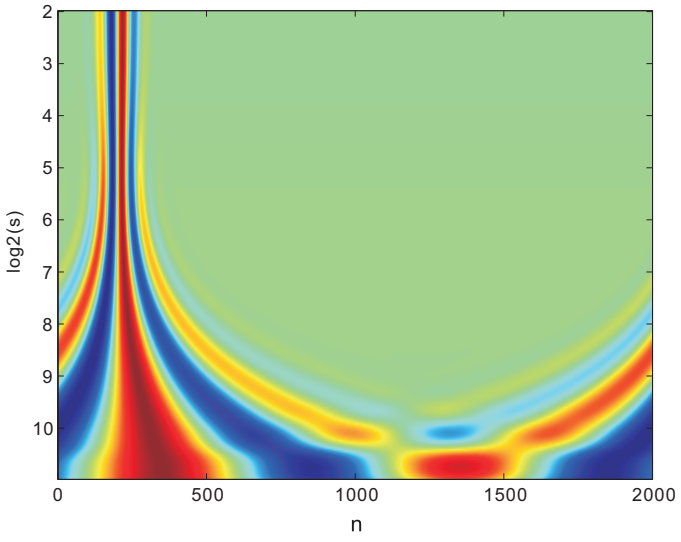

Figure 3.6: The wavelet spectrum of the input signal, after DWT with Morlet wavelet

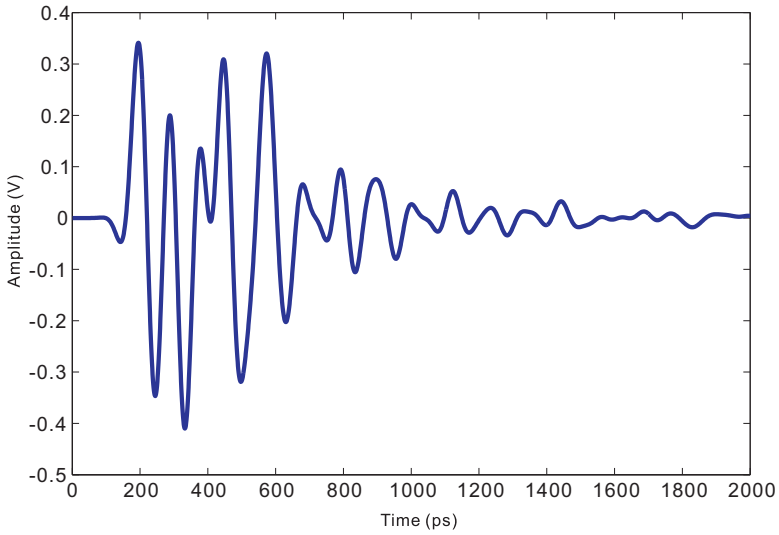

Figure 3.7: The original time-domain output signal

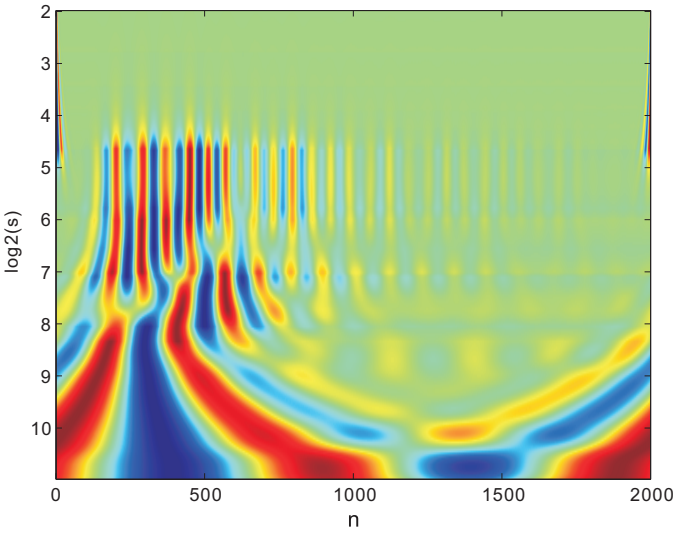

Figure 3.8: The wavelet spectrum of the output signal, after DWT with Haar wavelet

where ϕ_m is the scaling function and $\widetilde{\phi_m}$ represents its dual function (the dual function is explained in Appendix A) ; $\psi_{n,m}$ is the wavelet basis function, $\widetilde{\psi_{n,m}}$ is its dual. The index m represents shifts of the associated scaling or wavelet function. The index n corresponds to the scale of the wavelet basis function, with shifts performed in increments of $\frac{1}{2^n}$ ($n = 0$ for the scaling functions). The $\langle f, \phi_m \rangle$ denotes the conventional inner product between functions f and ϕ_m , that $\langle f, \phi_m \rangle = \int_{-\infty}^{\infty} f(x)\phi_m(x)dx$.

The scaling and wavelet basis functions in the expansion formula are designed to satisfy the following equations.

$$\langle \psi_{n,m}, \widetilde{\psi_{n',m'}} \rangle = \delta_{nn'}\delta_{mm'} \tag{3.8}$$

$$\langle \phi_m, \widetilde{\phi_{m'}} \rangle = \delta_{mm'} \tag{3.9}$$

$$\langle \psi_{n,m}, \widetilde{\phi_{m'}} \rangle = \langle \phi_m, \widetilde{\psi_{n',m'}} \rangle = 0 \tag{3.10}$$

where δ is the Kronecker delta function. If $\phi_m = \widetilde{\phi_{m'}}$ and $\psi_{n,m} = \widetilde{\psi_{n',m'}}$ then the expansion is called an orthonormal expansion, and otherwise it is called a biorthogonal expansion.

The Yee FDTD scheme can be derived using expansions of field components with rectangular pulse basis functions in both the time and space domains [43]. The similarity will be demonstrated in next chapter along with the Haar based MRTD. The use of different levels of wavelet basis in addition to the scaling functions in MRTD allows a multiresolution analysis to be applied to the spatial domain, with higher resolution at rapidly varying zones (with more wavelet basis functions in the expansion) and lower resolution at smooth areas (with scaling functions employed alone), maintaining the benefit of far less dispersion error. Some dispersion comparison between the MRTD and FDTD will be included in a later section, while the rigorous examination can be found in literature [2] [45].

Based on the MoM procedure, any complete set of orthonormal basis functions can be used for the expansion of field components. The different selection of wavelet functions leads to different variations of MRTD. Krumpholz and Katehi's work [2] used cubic spline Battle-Lemarie scaling and wavelet functions in the spatial domain, while keeping

rectangular-pulse basis functions for time domain (the so-called W-MRTD). Other types of wavelet functions being employed as the scaling functions and the wavelet basis functions have lead to many variations of MRTD. Variations based on Haar [34], Daubechies [47], Cohen-Daubechies-Feauveau (CDF) [45] and many other types of wavelet functions have appeared in literature.

Some other wavelet based approaches emerged after the introduction of MRTD. One major topic is wavelet Galerkin scheme, variously termed the Wavelet-Galerkin Time-Domain (WGTD) [47] [48] scheme or Interpolating Collocation Time-Domain (ICTD) method [50]. The wavelet Galerkin scheme employs level 2 Daubechies scaling function to do direct expansion of E and H field components. The approach is quite similar to MoM, but it can also have iteration equations, thus can be combined with the classic FDTD. It is claimed that the wavelet Galerkin scheme is superior to MRTD in terms of algorithm simplicity. But the disadvantage is reported to be slow convergence, requiring more time steps to reach steady-state. Another approach using Daubechies wavelets is introduced by Werthen and Wolff [51].

Due to this limitation of the wavelet Galerkin scheme, and the purpose of this research (to establish a fast and efficient algorithm for periodic structure / EBGs), the wavelet based MRTD approach is chosen instead of the wavelet Galerkin scheme.

As for the detailed review of MRTD, the basic theory from literature of Battle-Lemarie and Cohen-Daubechies-Feauveau (CDF) based MRTD are summarized here. The Haar MRTD is explained in the next chapter.

3.2.1 Battle-Lemarie wavelets based MRTD

If any E or H component is expanded in equation 3.7, instead of one variable, there will be two sets of variables representing the physical value of the field component at every single point throughout the discretized spatial domain. One set (we can have one variable in the set, or dozens of variables) is associated with the scaling function series, the other is related to the wavelet basis. Basically it means, corresponding to every E component in the Maxwell's equations, after the expansion there will be E^{ϕ_m} and $E^{\psi_{n,m}}$. The number

of variables in these two sets, actually indicates the resolution of the expansion. The more sub-components expanded, the greater resolution of the physics.

The following was summarized from Katehi's paper [2]. In [2], the expansion approach where the field components are represented by Battle-Lemarie scaling functions in the spatial domain and pulse functions in the time domain, was called S-MRTD. The approach with both Battle-Lemarie scaling functions and Battle-Lemarie wavelet functions in the spatial domain (still pulse function in the time domain) was denoted as W-MRTD.

As a starting point, the S-MRTD scheme which employs scaling functions alone is derived for a homogenous medium. Then by adding in the wavelet basis functions to the expansion, the W-MRTD scheme can be derived.

The emphasis here is no longer on the field expansion part of the algorithm, but rather the update functions where all the separated sub-components are rolled in. The update procedure basically spreads out these sub-components in the same way as it does for the field components in FDTD. Replacing each and every field component, one set of the expanded sub-component will "propagate" in the loop of the update functions for the S-MRTD and two sets for the W-MRTD case.

Similar to the FDTD, we start from the Maxwell's equations. The Maxwell vector equations can be written in the form of three scalar cartesian equations. For example, the equation $\nabla \times H = \varepsilon \frac{\partial E}{\partial t}$ is equivalent to the following three equations.

$$\nabla \times H = \varepsilon \frac{\partial E}{\partial t} \Longleftrightarrow \begin{cases} \frac{\partial H_z}{\partial y} - \frac{\partial H_y}{\partial z} = \varepsilon \frac{\partial E_x}{\partial t}; \\ \frac{\partial H_x}{\partial z} - \frac{\partial H_z}{\partial x} = \varepsilon \frac{\partial E_y}{\partial t}; \\ \frac{\partial H_y}{\partial x} - \frac{\partial H_x}{\partial y} = \varepsilon \frac{\partial E_z}{\partial t}. \end{cases} \tag{3.11}$$

In the same way, the equation $\nabla \times E = -\mu \frac{\partial H}{\partial t}$ can be split up. All the electric and magnetic field components can then be expanded using the scaling function, shown as following.

$$\begin{cases} E_x(\vec{r},t) = \sum_{k,l,m,n=-\infty}^{+\infty} E^{\phi x}_{k,l+\frac{1}{2},m,n} h_k(t)\phi_{l+\frac{1}{2}}(x)\phi_m(y)\phi_n(z); \\ E_y(\vec{r},t) = \sum_{k,l,m,n=-\infty}^{+\infty} E^{\phi y}_{k,l,m+\frac{1}{2},n} h_k(t)\phi_l(x)\phi_{m+\frac{1}{2}}(y)\phi_n(z); \\ E_z(\vec{r},t) = \sum_{k,l,m,n=-\infty}^{+\infty} E^{\phi z}_{k,l,m,n+\frac{1}{2}} h_k(t)\phi_l(x)\phi_m(y)\phi_{n+\frac{1}{2}}(z). \end{cases} \tag{3.12}$$

$$\begin{cases} H_x(\vec{r},t) = \sum_{k,l,m,n=-\infty}^{+\infty} H^{\phi x}_{k+\frac{1}{2},l,m+\frac{1}{2},n+\frac{1}{2}} h_{k+\frac{1}{2}}(t)\phi_l(x)\phi_{m+\frac{1}{2}}(y)\phi_{n+\frac{1}{2}}(z); \\ H_y(\vec{r},t) = \sum_{k,l,m,n=-\infty}^{+\infty} H^{\phi y}_{k+\frac{1}{2},l+\frac{1}{2},m,n+\frac{1}{2}} h_{k+\frac{1}{2}}(t)\phi_{l+\frac{1}{2}}(x)\phi_m(y)\phi_{n+\frac{1}{2}}(z); \\ H_z(\vec{r},t) = \sum_{k,l,m,n=-\infty}^{+\infty} H^{\phi z}_{k+\frac{1}{2},l+\frac{1}{2},m+\frac{1}{2},n} h_{k+\frac{1}{2}}(t)\phi_{l+\frac{1}{2}}(x)\phi_{m+\frac{1}{2}}(y)\phi_n(z). \end{cases} \tag{3.13}$$

where $E^{\phi a}_{k,l,m,n}$ and $H^{\phi a}_{k,l,m,n}$ with $a = x, y, z$ are the coefficients for the field expansions in terms of scaling functions. The indexes l, m, n and k are the discrete space and time indices related to the space and time coordinates via $x = l\delta x, y = m\delta y, z = n\delta z, t = k\delta t$, where $\delta x, \delta y, \delta z, \delta t$ represent the spatial and time steps. The function $h_m(x)$is defined as a shift of the rectangular pulse function $h(x)$.

$$h_m(x) = h(\frac{x}{\delta x} - m) \tag{3.14}$$

$$h(x) = \begin{cases} 1 & \text{for } |x| < \frac{1}{2}; \\ \frac{1}{2} & \text{for } |x| = \frac{1}{2}; \\ 0 & \text{for } |x| > \frac{1}{2}. \end{cases} \tag{3.15}$$

The function $\phi_m(x)$ is defined as a shift of the cubic spline Battle-Lemarie scaling function $\phi(x)$. $\phi_m(x) = \phi(\frac{x}{\delta x} - m)$, while $\phi(x)$ is shown in Fig. 3.9. The Fig. 3.10 shows $\widetilde{\phi(k)}$, the Fourier counterpart of $\phi(x)$ in the spectral domain.

$\widetilde{\psi(k)}$ has a closed form expression in the spectral domain with low-pass spectral characteristics [2].

$$\widetilde{\psi(k)} = (\frac{sin(\frac{k}{2})}{\frac{k}{2}})^4 \frac{1}{\sqrt{1 - \frac{4}{3}sin^2(\frac{k}{2}) + \frac{2}{5}sin^4(\frac{k}{2}) - \frac{4}{315}sin^2(\frac{k}{2})}} \tag{3.16}$$

These expansions can then be inserted back to the six scalar Maxwell equations. The scalar equations can be sampled using the rectangular pulse functions as test functions in

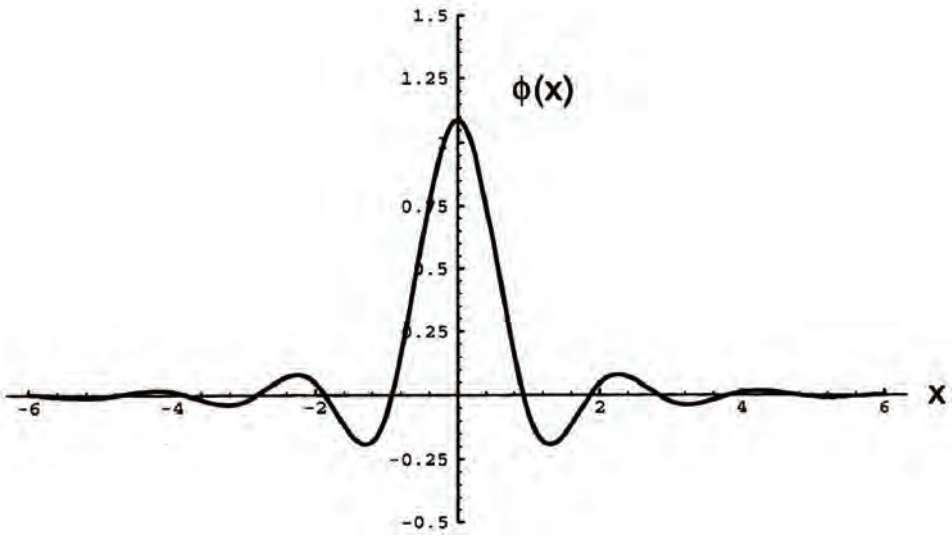

Figure 3.9: Cubic spline Battle-Lemarie scaling functions in spatial domain [2]

time domain and Battle-Lemarie scaling functions as test functions in the spatial domain. As an example of the results, the equation $\frac{\partial H_z}{\partial y} - \frac{\partial H_y}{\partial z} = \varepsilon \frac{\partial E_x}{\partial t}$ can be expanded to:

$$\frac{\varepsilon}{\Delta t}(E^{\phi x}_{k+1,l+\frac{1}{2},m,n} - E^{\phi x}_{k,l+\frac{1}{2},m,n}) = \frac{1}{\Delta y}\sum_{i=-9}^{+8} a(i) H^{\phi z}_{k+\frac{1}{2},l+\frac{1}{2},m+i+\frac{1}{2},n} - \frac{1}{\Delta z}\sum_{i=-9}^{+8} a(i) H^{\phi y}_{k+\frac{1}{2},l+\frac{1}{2},m,n+i+\frac{1}{2}} \tag{3.17}$$

The coefficients $a(i)$ come from the approximation:

$$\int_{-\infty}^{+\infty} \phi_m(x) \frac{\partial \phi_{m'+\frac{1}{2}}(x)}{\partial x} dx \approx \sum_{i=-9}^{+8} a(i)\delta_{m+i,m'} \tag{3.18}$$

For the Battle-Lemarie function, it doesn't have compact support but exponential decay support, as shown in Fig.3.9. So $a(i)$ is an infinite exponential decay series of coefficients. For $i > 8$, the coefficients are not zero but negligible. Note $a(i)$ satisfies $a(-1-i) = -a(i)$ for $i < 0$.

All six scalar functions can be expanded in this way, generating six update functions. The unit cell of the S-MRTD scheme is shown in Fig. 3.11.

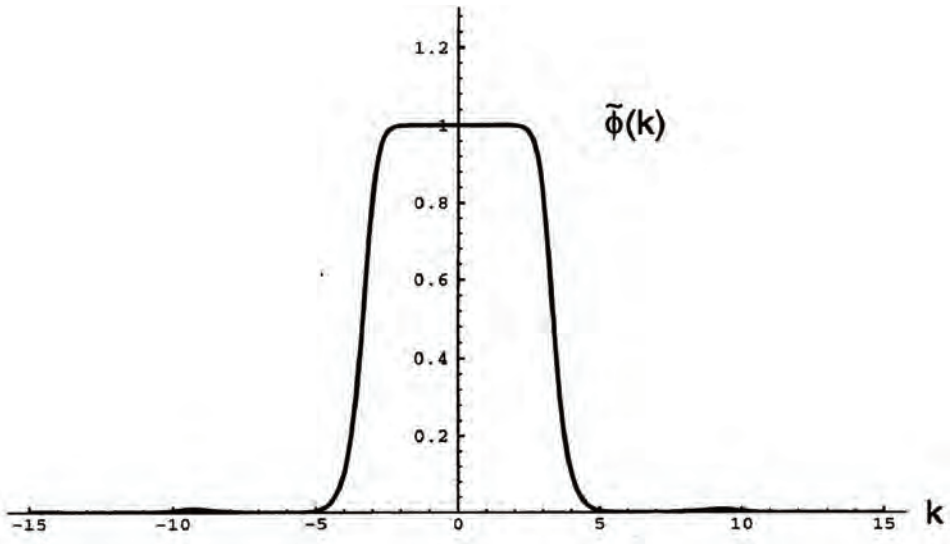

Figure 3.10: Cubic spline Battle-Lemarie scaling functions in spectral domain [2]

The stability condition for a uniform discretized 3D S-MRTD scheme is

$$\Delta t \leq 0.368112 \frac{\Delta}{c} \Longleftrightarrow S_c \leq 0.368112 \tag{3.19}$$

where c is the speed of light, and $\Delta = \Delta x = \Delta y = \Delta z$.

The W-MRTD procedure is similar to S-MRTD. It uses a two-fold expansion with scaling functions and wavelet basis functions, instead of scaling functions alone, to expand the field components. For simplicity of demonstration, the wavelet expansion is limited to a one-dimensional case ($\phi_m(y)$ and $\psi_{m+\frac{1}{2}}(y)$, as demonstrated) and in a single-resolution level here. For example, the E field component in x-direction can be expanded as [2]:

$$E_x(\vec{r},t) = \sum_{k,l,m,n=-\infty}^{+\infty} (E^{\phi x}_{k,l+\frac{1}{2},m,n}\phi_m(y) + E^{\psi x}_{k,l+\frac{1}{2},m+\frac{1}{2},n}\psi_{m+\frac{1}{2}}(y))h_k(t)\phi_{l+\frac{1}{2}}(x)\phi_n(z) \tag{3.20}$$

The parameters are defined as the same as in the S-MRTD scheme. The wavelet basis $\psi_{m+\frac{1}{2}}(y)$ is a shift of the cubic spline Battle-Lemarie wavelet function $\psi(y)$, $\psi_{m+\frac{1}{2}}(y) = \psi(\frac{x}{\Delta x} - m)$. $\psi_{m+\frac{1}{2}}(y)$ is shown in Fig. 3.12, while its Fourier counterpart $\widetilde{\psi}(k)$ is shown Fig. 3.13. $\psi_{m+\frac{1}{2}}(y)$ is symmetric with the respect to $y = \frac{1}{2}$. $\widetilde{\psi}(k)$ has a closed form

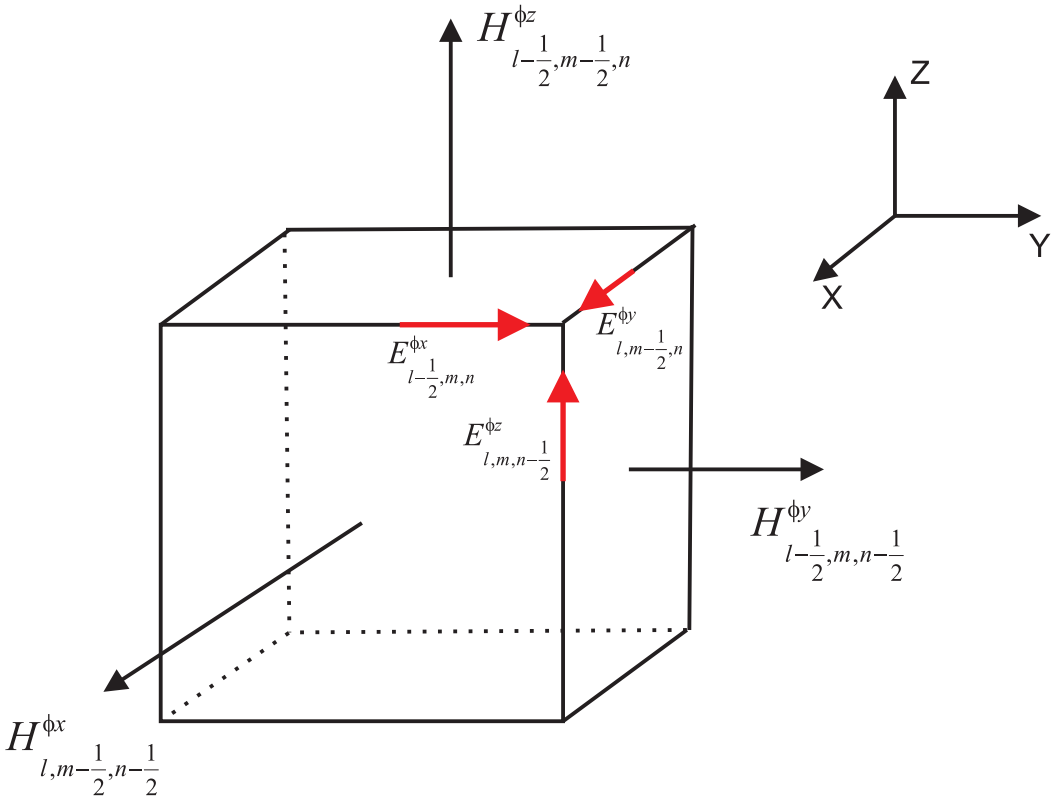

Figure 3.11: Unit cell of S-MRTD scheme [2]

expression:

$$\begin{aligned}\widetilde{\psi}(k) &= e^{j\frac{k}{2}}\frac{\widetilde{\phi}(k+2\pi)}{\widetilde{\phi}(\frac{k}{2}+\pi)}\widetilde{\phi}(\frac{k}{2}) \\ &= \frac{e^{j\frac{k}{2}}(\frac{2}{k}\sin(\frac{k}{2})\tan(\frac{k}{2}))^4}{\sqrt{1-\frac{4}{3}\sin^2(\frac{k}{2})+\frac{2}{5}\sin^4(\frac{k}{2})-\frac{4}{315}\sin^6(\frac{k}{2})}}\sqrt{\frac{1-\frac{4}{3}\cos^2(\frac{k}{2})+\frac{2}{5}\cos^4(\frac{k}{2})-\frac{4}{315}\cos^6(\frac{k}{2})}{1-\frac{4}{3}\sin^2(\frac{k}{2})+\frac{2}{5}\sin^4(\frac{k}{2})-\frac{4}{315}\sin^6(\frac{k}{2})}} \\ &= \frac{e^{j\frac{k}{2}}(\frac{2}{k}\sin(\frac{k}{2})\tan(\frac{k}{2}))^4\sqrt{1-\frac{4}{3}\cos^2(\frac{k}{2})+\frac{2}{5}\cos^4(\frac{k}{2})-\frac{4}{315}\cos^6(\frac{k}{2})}}{1-\frac{4}{3}\sin^2(\frac{k}{2})+\frac{2}{5}\sin^4(\frac{k}{2})-\frac{4}{315}\sin^6(\frac{k}{2})}\end{aligned} \tag{3.21}$$

Taking the expansions into the differential scalar equations generates the update equations.

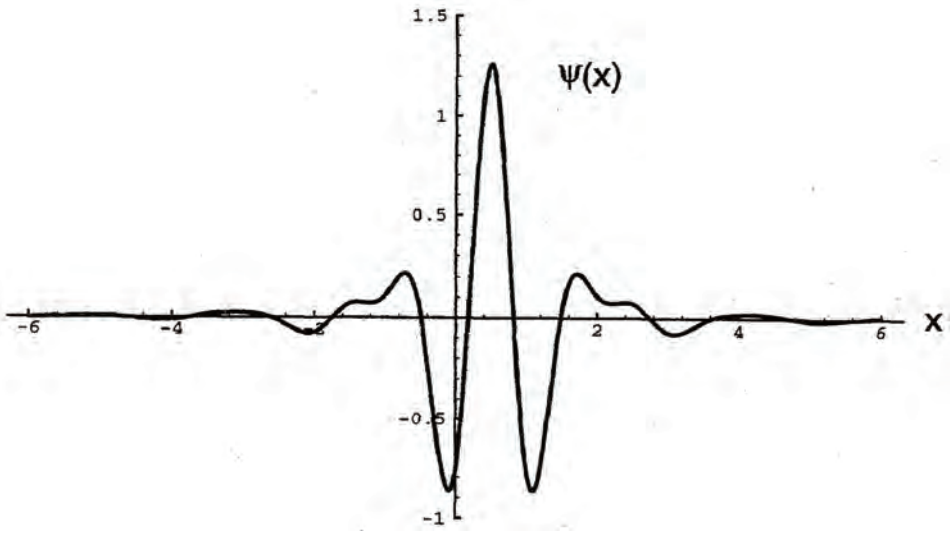

Figure 3.12: Cubic spline Battle-Lemarie scaling functions in spatial domain [2]

$$\frac{\varepsilon}{\Delta t}(E^{\phi x}_{k+1,l+\frac{1}{2},m,n} - E^{\phi x}_{k,l+\frac{1}{2},m,n}) = \frac{1}{\Delta y}\sum_{i=-9}^{+8} a(i)H^{\phi z}_{k+\frac{1}{2},l+\frac{1}{2},m+i+\frac{1}{2},n} \tag{3.22}$$
$$+\frac{1}{\Delta y}\sum_{i=-9}^{+8} c(i)H^{\psi z}_{k+\frac{1}{2},l+\frac{1}{2},m+i,n} - \frac{1}{\Delta z}\sum_{i=-9}^{+8} c(i)H^{\phi y}_{k+\frac{1}{2},l+\frac{1}{2},m,n+i+\frac{1}{2}}$$

$$\frac{\varepsilon}{\Delta t}(E^{\psi x}_{k+1,l+\frac{1}{2},m,n} - E^{\phi x}_{k,l+\frac{1}{2},m+\frac{1}{2},n}) = \frac{1}{\Delta y}\sum_{i=-9}^{+8} C(i)H^{\phi z}_{k+\frac{1}{2},l+\frac{1}{2},m+i+\frac{1}{2},n} \tag{3.23}$$
$$+\frac{1}{\Delta y}\sum_{i=-9}^{+8} b(i)H^{\psi z}_{k+\frac{1}{2},l+\frac{1}{2},m+i+1,n} - \frac{1}{\Delta z}\sum_{i=-9}^{+8} c(i)H^{\psi y}_{k+\frac{1}{2},l+\frac{1}{2},m+\frac{1}{2},n+i+\frac{1}{2}}$$

The stability condition for a uniform discretized W-MRTD ($\Delta = \Delta x = \Delta y = \Delta z$) scheme is

$$\Delta t \leq 0.253064\frac{\Delta}{c} \Longleftrightarrow S_c \leq 0.253064 \tag{3.24}$$

Due to the discretization in space and time, the MRTD (include both the S-MRTD and W-MRTD) exhibits FDTD-like deviations from the desired linear dispersion behavior, although much less intensive.

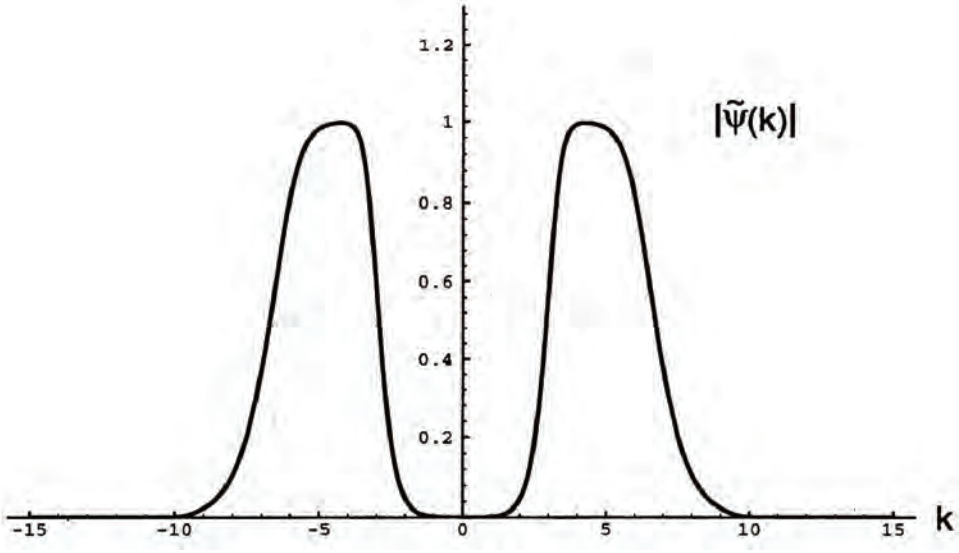

Figure 3.13: Cubic spline Battle-Lemarie scaling functions in spectral domain [2]

The Battle-Lemarie wavelet functions are smooth and therefore have good dispersion properties. However, as mentioned earlier, the Battle-Lemarie wavelet family has infinite support. Therefore, compact support can only be achieved by truncating the associated scaling and wavelet functions [52]. Having finite temporal and spatial support makes plane wave easily implemented and material inhomogeneity easily handled. Even the truncated Battle-Lemarie functions do not have finite support in the spatial domain, which results in a MRTD scheme with update functions involving a large amount of adjacent field coefficients [34].

3.2.2 Cohen-Daubechies-Feauveau (CDF) wavelet based MRTD

The later emerged Cohen-Daubechies-Feauveau (CDF) wavelet MRTD scheme was proposed as a balanced scheme between smoothness of the functions and reduced spatial (compact) support. In another word, the aim is to find a balanced wavelet function that minimize the numerical dispersion for a given discretiztion rate while maintaining the minimal support to prevent infinite number of coefficients in the update equations. This

aim would also be of our interest, with the suitability of applications to EBG / metamaterials in mind. The CDF MRTD procedure is explained as follows. The majority of the procedure explained here comes from Dogaru and Carin's paper [45].

The generalized wavelet expansion for a 1-D case has been demonstrated before. The procedure for a biorthogonal expansion is quite similar to the orthogonal one. The full wavelet expansion of E_z for a one dimensional wave propagating in x-direction is:

$$E_z(x,t) = \sum_{k,m=-\infty}^{\infty} [E_{k,m}^{\phi} \widetilde{\phi}_m(x) + \sum_{l=0}^{\infty} E_{k,m}^{\psi^L} \widetilde{\psi}_m^l(x)] h_k(t) \tag{3.25}$$

where $\widetilde{\phi}_m$ is denoted as the dual scaling function shifted by m units.$\widetilde{\psi}_m^l$ is denoted as the lth level dual wavelet basis function displaced by $\frac{m}{2^l}$ units. $h_k(t)$ is rectangular pulse function for time discretization. The dual scaling and wavelet basis functions for CDF(2,2) are shown in Fig. 3.14.

If the scaling function is considered alone for the expansion (CDF S-MRTD), the equation will be:

$$E_z(x,t) = \sum_{k,m=-\infty}^{\infty} E_{k,m}^{\phi} \widetilde{\phi}_m(x) h_k(t) \tag{3.26}$$

The update equation for 1D CDF S-MRTD are

$$H_{k,m}^{\phi} = H_{k-1,m}^{\phi} + \frac{\Delta t}{\mu \Delta x} \sum_{i=1}^{n_a} a(i)(E_{k,m+i}^{\phi} - E_{k,m-i+1}^{\phi}) \tag{3.27}$$

$$E_{k+1,m}^{\phi} = E_{k,m}^{\phi} + \frac{\Delta t}{\varepsilon \Delta x} \sum_{i=1}^{n_a} a(i)(H_{k,m+i-1}^{\phi} - H_{k,m-i}^{\phi}) \tag{3.28}$$

where $a(i)$ can be derived from the equation $\int \frac{\partial \widetilde{\phi}_{m+i}(x)}{\partial x}$. The number is called the "stencil size" and equals half the number of the nonzero coefficients in the MRTD scheme.

The stability criteria for 1D CDF S-MRTD is

$$S_c = \frac{c\Delta t}{\Delta x} \leq \frac{1}{\sum_{i=1}^{n_a} |a(i)|} \tag{3.29}$$

For CDF(2,2), this criteria is equivalent to $S_c \leq 0.75$. The dispersion relationship can be written as following equation: $\frac{1}{S_c} \sin \frac{\pi S_c}{n_l} = \sum_{i=1}^{n_a} a(i) \sin[\frac{\pi u}{n_l}(2i-1)]$. u is the ratio

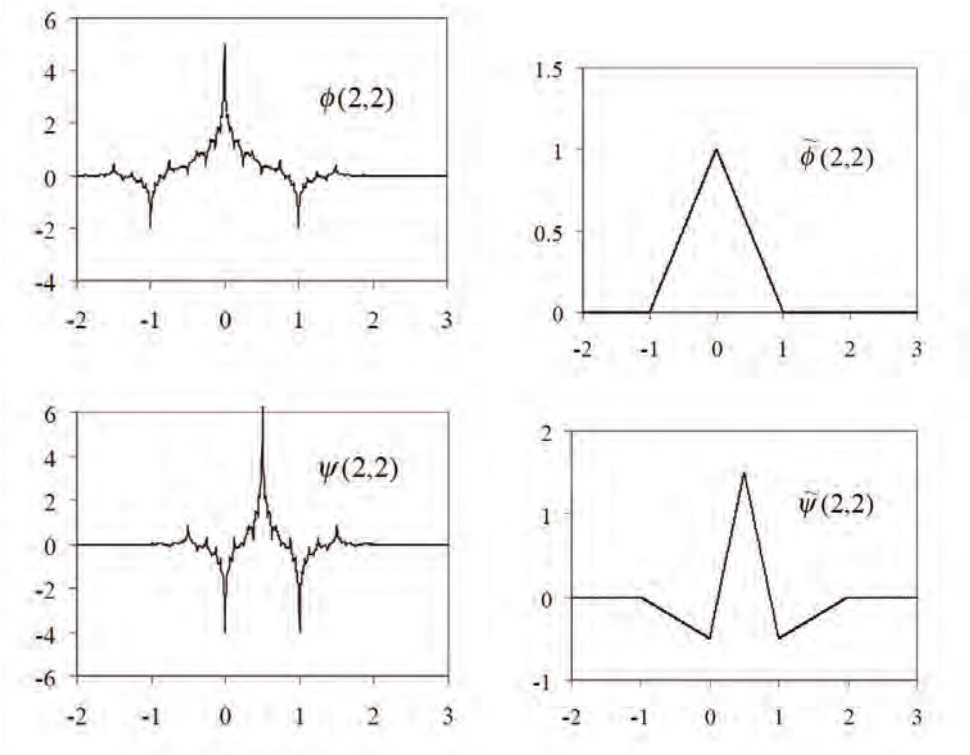

Figure 3.14: The scaling and wavelet functions of the CDF (2,2) biorthogonal wavelets, and their duals [45]

between the theoretical and numerical wavelength, n_l is the number of sampling points per wavelength.

The biorthogonal wavelet basis can be added into the algorithm to form the 1D CDF W-MRTD. The 1D symmetric case would have update equations as follows:

$$\begin{cases} H^{\phi}_{k,m} = H^{\phi}_{k-1,m} + \frac{\Delta t}{\mu \Delta x}\left(\sum_{i=1}^{n_a} a(i)(E^{\phi}_{k,m+i} - E^{\phi}_{k,m-i+1}) + \sum_{i=1}^{n_c} c(i)(E^{\psi}_{k,m+i} - E^{\psi}_{k,m-i})\right); \\ H^{\psi}_{k,m} = H^{\psi}_{k-1,m} + \frac{\Delta t}{\mu \Delta x}\left(\sum_{i=1}^{n_d} d(i)(E^{\phi}_{k,m+i} - E^{\phi}_{k,m-i}) + \sum_{i=1}^{n_b} b(i)(E^{\psi}_{k,m+i-1} - E^{\psi}_{k,m-i})\right); \\ E^{\phi}_{k+1,m} = E^{\phi}_{k,m} + \frac{\Delta t}{\varepsilon \Delta x}\left(\sum_{i=1}^{n_a} a(i)(H^{\phi}_{k,m+i-1} - H^{\phi}_{k,m-i}) + \sum_{i=1}^{n_c} c(i)(H^{\psi}_{k,m+i} - H^{\psi}_{k,m-i})\right); \\ E^{\psi}_{k+1,m} = E^{\psi}_{k,m} + \frac{\Delta t}{\varepsilon \Delta x}\left(\sum_{i=1}^{n_d} d(i)(H^{\phi}_{k,m+i} - H^{\phi}_{k,m-i}) + \sum_{i=1}^{n_b} b(i)(H^{\psi}_{k,m+i} - H^{\psi}_{k,m-i+1})\right). \end{cases} \tag{3.30}$$

The stability criteria becomes more complicated, shown in the following equation.

$$S_c = \frac{c\Delta t}{\Delta x} \leq \frac{\sqrt{2}}{\sqrt{A}} \tag{3.31}$$

where

$$A = (\sum_{i=1}^{n_a} |a(i)|)^2 + (\sum_{i=1}^{n_b} |b(i)|)^2 + 2\sum_{i=1}^{n_c} |c(i)| \sum_{i=1}^{n_d} |d(i)| \tag{3.32}$$
$$+(\sum_{i=1}^{n} |a(i)+b(i)|)\sqrt{(\sum_{i=1}^{n} |a(i)-b(i)|)^2 + 4\sum_{i=1}^{n_c} |c(i)| \sum_{i=1}^{n_d} |d(i)|}$$

The dispersion relationship for a 1D CDF W-MRTD can be written as the following equation:

$$1 - (S_a^2 + S_b^2 + S_{c'} S_d) + (S_a S_b - S_{c'} S_d)^2 = 0 \tag{3.33}$$

where

$$S_a = S_c \frac{\sum_{i=1}^{n_a} a(i) \sin[\frac{\pi u}{n_l}(2i-1)]}{\sin \frac{\pi S_c}{n_l}} \tag{3.34}$$

$$S_b = S_c \frac{\sum_{i=1}^{n_b} b(i) \sin[\frac{\pi u}{n_l}(2i-1)]}{\sin \frac{\pi S_c}{n_l}} \tag{3.35}$$

$$S_c' = S_c \frac{\sum_{i=1}^{n_c} c(i) \sin[\frac{\pi u}{n_l}(2i-1)]}{\sin \frac{\pi S_c}{n_l}} \tag{3.36}$$

$$S_d = S_c \frac{\sum_{i=1}^{n_d} d(i) \sin[\frac{\pi u}{n_l}(2i-1)]}{\sin \frac{\pi S_c}{n_l}} \tag{3.37}$$

More information regarding MRTD dispersion and the comparison to FDTD can be found in [45]. It will not be wise to go into further details into the CDF wavelet based MRTD scheme. As shown above in the one-dimensional case, the complexity of the algorithm has been explored by other researchers and demonstrated in literature. Since our goal clearly states that we are looking for a computational efficient and implementable

algorithm to solve the EBG hybrid structure, the CDF MRTD falls short on the simplicity side. Therefore it only has sense to be included in the study of the various MRTD techniques as a background, not any further in our specific research.

3.3 Conclusions

In this chapter, the wavelet functions and the wavelet transform that based upon them are introduced. A wavelet is a small wave that is localized in time and frequency. Based on dilation and translation, a chosen mother wavelet can generate a series of daughter wavelets. Then the CWT of a signal $f(t)$ is in fact the inner product of $f(t)$ and the daughter wavelet series. DWT is the CWT in discrete form, which is more suitable for computational purposes. Due to the orthogonality of the wavelet basis, the wavelet transform outperforms the Fourier transform, in that it handles better when dealing with signals with sharp discontinuities or short duration.

The MRTD techniques have been reviewed. The main advantages of the MRTD include: adaptable resolution, less memory intensive and far less numerical dispersion. Almost all of these nice features are related to wavelet expansion of the field components, be it the way the expansion is done or the basis that the expansion relies upon. The basics and common features of the Battle-Lemarie MRTD and CDF MRTD are explained.

The Battle-Lemarie wavelets are smooth, with finite support in the spectral domain thus good dispersion properties. The CDF functions are not smooth, but their duals have compact support, which provides limited adjacent field coefficients. They both suffer from a common problem, that the update equations involve the summation of the product of coefficients (e.g. $a(i)$) and field components (e.g. E^{ϕ}). The summation computation makes the update functions messy thus difficult to implement, even though the coefficient series can somehow be limited to a range (e.g. the $i = -9$ to 8 in the Battle-Lemarie case). Although CDF's dual is compactly supported, the CDF itself is not, the summation term is therefore still required. The problem becomes dramatic when higher-level wavelet functions are introduced to achieve higher resolution. This in fact puts the

burden to the human programming side, which is a drawback comparing to the coding-easy FDTD algorithm.

Bearing in mind of the MRTD's advantages and our goal to numerically solve the hybrid EBG structure, the research was later determined to focus on the Haar wavelet based MRTD, thanks to its algorithmic simplicity. The details are shown in next chapter.

Chapter 4

Haar Wavelet Based Multi-Resolution Time-Domain (MRTD) Technique

The Haar wavelet and scaling functions are one of the simplest family of their kind. Unlike the Battle-Lemarie and CDF wavelets, Haar wavelets have compact temporal/spatial support, which significantly simplifies the MRTD implementation. The ease of implementation, as well as the preservation of the desirable features derived from orthogonality make Haar based MRTD the ideal candidate in solving the hybrid EBG structure.

Based on a thorough study on existing Haar MRTD literature, one-dimensional, two-dimensional and three dimensional level-one Haar based MRTD simulators have been constructed. An explicit form of Perfectly Matched Layer (PML) configuration is proposed, proved and presented. The source expansion scheme is proposed thereafter. These latter two pieces of work contribute to the existing literature, as their explicit mathematical and computational forms are original. More importantly, as general mathematical solutions, their extensions suit every single level of Haar wavelet function. This paves the way to boost the resolution even higher, which indicates the algorithm's future potential.

In a later chapter, the targeted application of the MRTD in solving the EBG hybrid antenna will be reported. However, this chapter does include several useful EM scenarios, especially the eletrically large Luneburg Lens antenna, which showcases the MRTD's capability to handle complicated geometry. Also, in order to verify the results, some FDTD simulations were performed. A comparison between the results as well as the resources requirement will be provided in this chapter.

4.1 One-dimensional level-one Haar MRTD and its applications

As introduced in the previous chapter, the level-one Haar wavelet is the mother wavelet. Other levels of Haar functions are derived from level-one Haar. Therefore, to study the general form of Haar MRTD, we start from the level-one case. Before going into details of the algorithm, we clarify the basic mathematics.

The Haar scaling function is in fact a rectangular pulse function, defined as

$$\phi(x) = \begin{cases} 1 & \text{if } 0 < x < 1; \\ 0 & \text{otherwise.} \end{cases} \tag{4.1}$$

The level-one Haar wavelet is defined as

$$\psi(x) = \begin{cases} 1 & \text{if } 0 \leq x < 0.5; \\ -1 & \text{if } 0.5 \leq x < 1; \\ 0 & \text{otherwise.} \end{cases} \tag{4.2}$$

A spatial distribution of the level-one Haar wavelet is shown in Fig.4.1. The scaling function is shown in Fig. 4.2. It is clear that the scaling function and the Haar wavelet are orthogonal to each other, since

$$\langle \phi(x), \psi(x) \rangle = \int_{-\infty}^{\infty} \phi(x)\psi(x)dx = 0 \tag{4.3}$$

Keep in mind, that all the nice dispersion features of the Haar MRTD come from this orthogonal nature. We note that there is nothing outside the $[0, 1]$ interval, i.e. the presence

of compact support. There is no need for the Haar to use a coefficient series (e.g. the a(i) in Battle-Lemarie and CDF cases) to approximate the function outside that bracket. This brings in the simplicity to the MRTD algorithm, which is a common feature of all levels of Haar based MRTD.

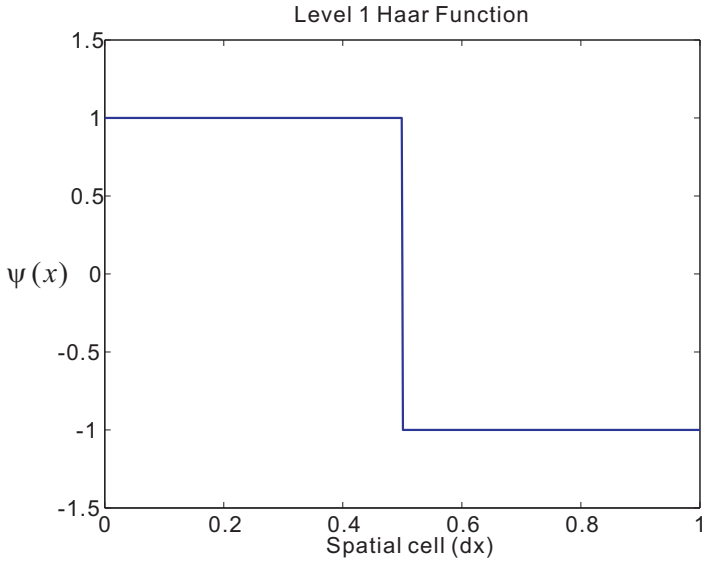

Figure 4.1: Level-one Haar wavelet function ψ^0.

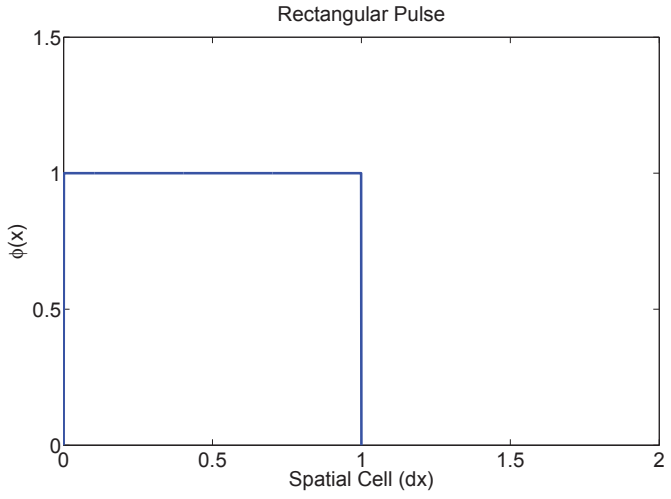

Figure 4.2: Level-one Haar scaling function ϕ^0.

Other levels of Haar wavelet basis can be derived from the following formula by using the level-one $\psi^0(x)$ as the mother wavelet. Note that in equation (4.4), ψ^{n-1} denotes

level n Haar wavelets [40]. Fig 4.3 demonstrates a level-two Haar wavelet as an example demonstrating how higher order wavelets evolve from ψ^0.

$$\psi_m^{n-1}(x) = 2^{\frac{n-1}{2}}\psi_m^0(2^{n-1}x - m) \tag{4.4}$$

Corresponding to higher level wavelet functions, higher level of scaling functions are defined as

$$\phi_m^n(x) = 2^{\frac{n}{2}}\phi(2^n x - m) \tag{4.5}$$

where n denotes the scale (i.e. the level), and m is the shift. We write ϕ^n for ϕ_0^n and ψ^n for ψ_0^n. It is easy to prove that at higher levels, the Haar scaling and wavelet functions are still orthogonal to each other.

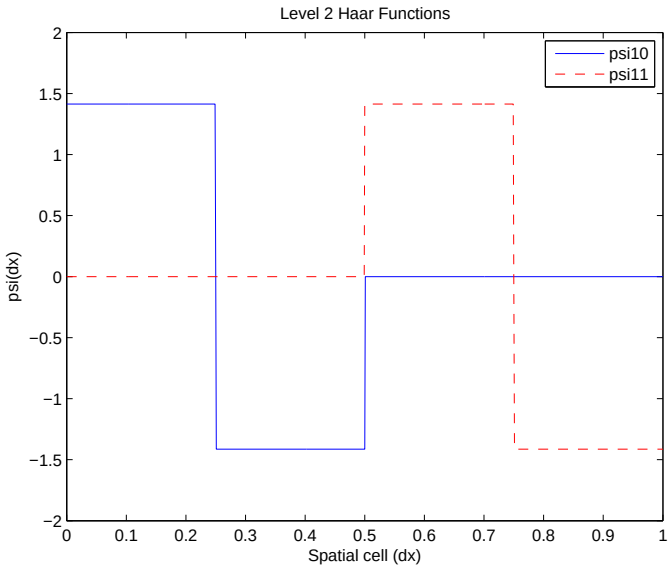

Figure 4.3: Level-two Haar wavelet functions ψ^{10}, ψ^{11}.

4.1.1 The formulation of 1D level-one Haar MRTD

For simplicity, a one-dimensional Haar MRTD scenario is introduced here first to illustrate how update equations can be derived. For a 1D case, a plane wave that propagates in the x-direction within a lossless homogeneous material satisfies the following Maxwell

equations:

$$\frac{\partial E_z}{\partial t} = \frac{1}{\varepsilon} \cdot \frac{\partial H_y}{\partial x} \tag{4.6}$$

$$\frac{\partial H_y}{\partial t} = \frac{1}{\mu} \cdot \frac{\partial E_z}{\partial x} \tag{4.7}$$

In the FDTD, these equations are written by replacing the derivatives with a central difference approximation. However, in the MRTD, the electric and magnetic field components E and H need to be expanded first, using the aforementioned level-one scaling function and the wavelet basis, before the updating equations can be developed. Conventionally, the level-one Haar expansion can be written as follows [34].

$$E_z(x,t) = \sum_{k,m=-\infty}^{\infty} [E_{k,m}^{\phi^0} h_k(t)\phi_m^0(x) + E_{k,m}^{\psi^0} h_k(t)\psi_m^0(x)] \tag{4.8}$$

$$H_y(x,t) = \sum_{k,m=-\infty}^{\infty} [H_{k,m}^{\phi^0} h_{k+\frac{1}{2}}(t)\phi_{m+\frac{1}{4}}^0(x) + H_{k,m}^{\psi^0} h_{k+\frac{1}{2}}(t)\psi_{m+\frac{1}{4}}^0(x)] \tag{4.9}$$

where k and m are the index numbers of temporal and spatial steps, respectively; $h_k(t) = h(\frac{t}{\Delta t} - k)$ is defined as a shift of the rectangular pulse function $h(t)$ at a given time with a step of Δt; $\phi_m^0(t) = \phi^0(\frac{x}{\Delta x} - m)$ represents the scaling function at a spatial interval of Δx, also a rectangular pulse in the Haar MRTD; and $\psi_m^0(t) = \psi^0(\frac{x}{\Delta x} - m)$ represents the level-one wavelet basis function.

Let the E and H in the Maxwell equations (4.6) and (4.7) be replaced by their expanded versions, one can obtain the update equations of the level-one Haar MRTD, as in [34]:

$$\begin{cases} E_{k+1,m}^{\phi^0} = E_{k,m}^{\phi^0} + \frac{\Delta t}{\varepsilon \Delta x}(H_{k,m}^{\phi^0} - H_{k,m}^{\psi^0} - H_{k,m-1}^{\phi^0} + H_{k,m-1}^{\psi^0}) \\ E_{k+1,m}^{\psi^0} = E_{k,m}^{\psi^0} + \frac{\Delta t}{\varepsilon \Delta x}(H_{k,m}^{\phi^0} + 3H_{k,m}^{\psi^0} - H_{k,m-1}^{\phi^0} + H_{k,m-1}^{\psi^0}) \\ H_{k,m}^{\phi^0} = H_{k-1,m}^{\phi^0} + \frac{\Delta t}{\mu \Delta x}(E_{k,m+1}^{\phi^0} + E_{k,m+1}^{\psi^0} - E_{k,m}^{\phi^0} - E_{k,m}^{\psi^0}) \\ H_{k,m}^{\psi^0} = H_{k-1,m}^{\psi^0} + \frac{\Delta t}{\mu \Delta x}(-E_{k,m+1}^{\phi^0} - E_{k,m+1}^{\psi^0} + E_{k,m}^{\phi^0} - 3E_{k,m}^{\psi^0}) \end{cases} \tag{4.10}$$

The gridding configuration of E and H is critical, since inappropriate gridding degrades the numerical dispersion superiority inherent in MRTD [41]. According to the equivalence of level-one Haar MRTD and the FDTD with half of the cell size (thus twice the resolution when using the same cell size, as described in [34]), the spatial offset between

E and H can be considered as $\frac{1}{4}$ of the MRTD cell size. Therefore, $H_{k,m}^{\psi,\phi}$ components at time step "k" and spatial step "m" are actually a quarter cell away from $E_{k,m}^{\psi,\phi}$, as indicated by the parts $\phi_{m+\frac{1}{4}}^{0}(x), \psi_{m+\frac{1}{4}}^{0}(x)$ in the H expansion equation.

Let's prove the equivalence here. A FDTD scheme with half the cell size ($\frac{\Delta x}{2}$) has the following update functions.

$$\begin{cases} E_{k+1,2m}^{Y} = E_{k,2m}^{Y} + \frac{2\Delta t}{\varepsilon \Delta x}(H_{k,2m}^{Y} - H_{k,2m-1}^{Y}) \\ E_{k+1,2m+1}^{Y} = E_{k,2m+1}^{Y} + \frac{2\Delta t}{\varepsilon \Delta x}(H_{k,2m+1}^{Y} - H_{k,2m}^{Y}) \\ H_{k,2m}^{Y} = H_{k-1,2m}^{Y} + \frac{2\Delta t}{\mu \Delta x}(E_{k,2m+1}^{Y} - E_{k,2m}^{Y}) \\ H_{k,2m+1}^{Y} = H_{k-1,2m+1}^{Y} + \frac{2\Delta t}{\mu \Delta x}(E_{k,2m+2}^{Y} - E_{k,2m+1}^{Y}) \end{cases} \tag{4.11}$$

From reference [34], equation 4.11 is somewhat cumbersome. The indices can be simplified. Once the indices are properly labeled, the update functions become easier to understand.

$$\begin{cases} E_{k+1,p}^{Y} = E_{k,p}^{Y} + \frac{2\Delta t}{\varepsilon \Delta x}(H_{k,p}^{Y} - H_{k,p-1}^{Y}) \\ H_{k,p}^{Y} = H_{k-1,p}^{Y} + \frac{2\Delta t}{\mu \Delta x}(E_{k,p+1}^{Y} - E_{k,p}^{Y}) \end{cases} \tag{4.12}$$

where p is the spatial step in the FDTD, $p = 2m$ since the FDTD would have twice the number of cells. The Y label denotes the Yee-FDTD scheme. Since the cell size is only $\frac{\Delta x}{2}$, the coefficient 2 in both equations are justified. The equivalence between equations 4.10 and 4.12 becomes more evident when we note that

$$\begin{cases} E_{k,m}^{\phi^0} = \frac{1}{\sqrt{2}}(E_{k,p}^{Y} + E_{k,p+1}^{Y}) \\ E_{k,m}^{\psi^0} = \frac{1}{\sqrt{2}}(E_{k,p}^{Y} - E_{k,p+1}^{Y}) \\ H_{k,m}^{\phi^0} = \frac{1}{\sqrt{2}}(H_{k,p}^{Y} + H_{k,p+1}^{Y}) \\ H_{k,m}^{\psi^0} = \frac{1}{\sqrt{2}}(H_{k,p}^{Y} - H_{k,p+1}^{Y}) \end{cases} \tag{4.13}$$

If equation 4.13 is taken back into the first equation of 4.10, we have

$$\begin{aligned} E_{k+1,m}^{\phi^0} &= E_{k,m}^{\phi^0} + \frac{\Delta t}{\varepsilon \Delta x}(H_{k,m}^{\phi^0} - H_{k,m}^{\psi^0} - H_{k,m-1}^{\phi^0} + H_{k,m-1}^{\psi^0}) \\ &= E_{k,m}^{\phi^0} + \frac{\Delta t}{\varepsilon \Delta x}(\sqrt{2}H_{k,p+1}^{Y} - \sqrt{2}H_{k,p-1}^{Y}) \\ E_{k+1,m}^{\phi^0} - E_{k,m}^{\phi^0} &= \frac{\Delta t}{\varepsilon \Delta x}(\sqrt{2}H_{k,p+1}^{Y} - \sqrt{2}H_{k,p-1}^{Y}) \end{aligned} \tag{4.14}$$

Following the same procedure, taking equation 4.13 into the second equation of 4.10 yields:

$$E^{\psi^0}_{k+1,m} - E^{\psi^0}_{k,m} = \frac{\Delta t}{\varepsilon \Delta x}(2\sqrt{2}H^Y_{k,p} - \sqrt{2}H^Y_{k,p+1} - \sqrt{2}H^Y_{k,p-1}) \tag{4.15}$$

Notice that in both equations, the "1" in indices associated with "m" and "p" mean different increment in physical distance due to different cell size. Now, add these two equations together, we have

$$\begin{aligned} E^{\phi^0}_{k+1,m} - E^{\phi^0}_{k,m} + E^{\psi^0}_{k+1,m} - E^{\psi^0}_{k,m} &= \frac{\Delta t}{\varepsilon \Delta x}(2\sqrt{2}H^Y_{k,p} - \sqrt{2}H^Y_{k,p+1} - \sqrt{2}H^Y_{k,p-1} \\ +\sqrt{2}H^Y_{k,p+1} - \sqrt{2}H^Y_{k,p-1}) &= \frac{\Delta t}{\varepsilon \Delta x}(2\sqrt{2}H^Y_{k,p} - 2\sqrt{2}H^Y_{k,p-1}) \end{aligned} \tag{4.16}$$

Substitute $E^{\phi^0}_{k,m}$ and $E^{\psi^0}_{k,m}$ with the first two equations in 4.13, the equivalence is clearly demonstrated, as we derived the $\frac{\Delta x}{2}$ FDTD update function out of it:

$$\begin{aligned} E^{\phi^0}_{k+1,m} - E^{\phi^0}_{k,m} + E^{\psi^0}_{k+1,m} - E^{\psi^0}_{k,m} &= \frac{\Delta t}{\varepsilon \Delta x}(2\sqrt{2}H^Y_{k,p} - 2\sqrt{2}H^Y_{k,p-1}) \\ \frac{1}{\sqrt{2}}(E^Y_{k+1,p} + E^Y_{k+1,p+1}) - \frac{1}{\sqrt{2}}(E^Y_{k,p} + E^Y_{k,p+1}) + \frac{1}{\sqrt{2}}(E^Y_{k+1,p} - E^Y_{k+1,p+1}) - & \\ \frac{1}{\sqrt{2}}(E^Y_{k,p} - E^Y_{k,p+1}) &= \frac{\Delta t}{\varepsilon \Delta x}(2\sqrt{2}H^Y_{k,p} - 2\sqrt{2}H^Y_{k,p-1}) \\ \sqrt{2}E^Y_{k+1,p} - \sqrt{2}E^Y_{k,p} &= \frac{\Delta t}{\varepsilon \Delta x}(2\sqrt{2}H^Y_{k,p} - 2\sqrt{2}H^Y_{k,p-1}) \\ E^Y_{k+1,p} - E^Y_{k,p} &= \frac{\Delta t}{\varepsilon \Delta x}(2H^Y_{k,p} - 2H^Y_{k,p-1}) \\ E^Y_{k+1,p} &= E^Y_{k,p} + \frac{\Delta t}{\varepsilon \Delta x}(2H^Y_{k,p} - 2H^Y_{k,p-1}) \end{aligned} \tag{4.17}$$

Furthermore, another equation can be combined with equation 4.13,

$$E_{k,m} = \frac{1}{\sqrt{2}}(E^{\phi^0}_{k,m}\phi^0_m + E^{\psi^0}_{k,m}\psi^0_m) \tag{4.18}$$

where $E_{k,m}$ represents the overall E field value in the 1D MRTD cell, reconstructed from the $E^{\phi^0}_{k,m}$ and $E^{\psi^0}_{k,m}$. All these field components are illustrated in Fig.4.4. At corresponding positions between the MRTD and FDTD scenarios, the field components can have such values, which reveals their relations. Normalized value is being used in the figure.

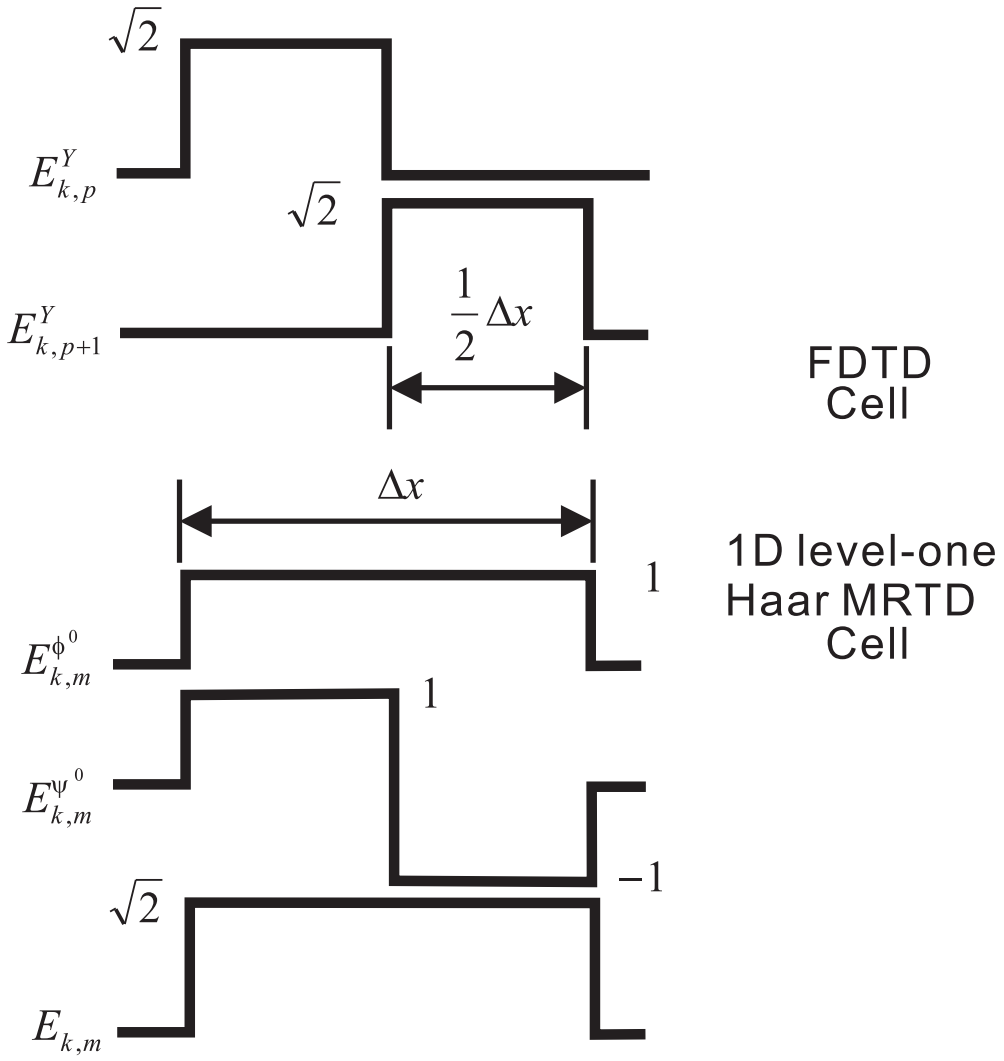

Figure 4.4: The equivalence between level-one Haar MRTD and FDTD

In fact, the above explains the 1D case of source expansion, without explicitly mentioning where the $E^Y_{k,p}$ and $E^Y_{k,p+1}$ come from. In the source cell, a sub-cell expansion scheme is effectively running to generate the $E^Y_{k,p}$ and $E^Y_{k,p+1}$. In some way, this sub-cell expansion mimics a FDTD procedure. The sub-cell FDTD divide the 1D MRTD source cell into 2 FDTD cells with half the cell size. This FDTD-like sequence only runs within the source cell and nowhere else. The expansion will use the H field values from nearby MRTD cells, to update the E field within the source cell. The H field components in nearby MRTD cells are in forms of H^{ϕ^0} and H^{ψ^0}. The overall H field value has to be

reconstructed in the nearby cells.

After the source cell update is completed, the $E^Y_{k,p}$ and $E^Y_{k,p+1}$ are generated within the source cell, then E^{ϕ^0} and E^{ψ^0}. E^{ϕ^0} and E^{ψ^0} are to be used in the MRTD procedures that update nearby cells in the scenario. A more comprehensive explanation is provided in later session specifically for source expansion.

The FDTD equivalence is undoubtably important here, which leads to a fundamental algorithmic understanding of the MRTD from the FDTD perspective: More than one components of E (as well as H) propagate within and across every single MRTD cell. For 1D level-one Haar MRTD, it's two. For 2D, it's four. For 3D, it's $2^3 = 8$. But bear in mind, as seen above, the MRTD with a Δx cell uses the same amount of computational memory as a FDTD with $\frac{\Delta x}{2}$. The MRTD employs two variables E^{ϕ^0} and E^{ψ^0} for every cell, or every distance of Δx. The FDTD needs $E^Y_{k,p}$ and $E^Y_{k,p+1}$ to cover the same distance of Δx, basically also two variables.

Furthermore, it can be mathematically proven that an one-dimensional MRTD with level n Haar basis is equivalent to a FDTD with $\frac{1}{2^n}$ of the MRTD cell size. The detailed proof procedure is omitted here but included in Appendix B, in order to maintain the conciseness of this thesis. Based upon the $\frac{1}{2^n}$ equivalence, the level-n Haar MRTD PML cell offset of E and H is thus $\frac{1}{2^{n+1}}\Delta x$. This also implies that with the same cell size, the level n Haar MRTD has a resolution of 2^n greater than the traditional FDTD. As a consequence, the temporal step Δt for the MRTD is correspondingly smaller to satisfy the Courant stability condition, which leads to 2^n times longer time steps in one simulation. In another word, the tradeoff for achieving vastly high spatial resolutions in the MRTD appear to be the repeated updating loops and a prolonged computational time. In reality, thanks to the development of multi-core CPUs, simulation time of Matlab based level-one code is now within the range of $1.2 \sim 1.5$ times the FDTD one, while yielding a result twice the resolution.

4.1.2 The application of 1D level-one Haar MRTD

The 1D MRTD is applied to analyze a three-layer composite structure made of Duroid. It is corrugated with air gaps in between. The configuration is shown in Fig 4.5. Unlike shown in the drawing, since the code is one-dimensional, the three layers are effectively infinite in the y-z directions (not bounded between $[-1, 1]$ as shown in Fig 4.5). Also, one dimension can only deal with one propagation direction, which makes the incident wave essentially a plane wave propagating perpendicular to the duroid layers.

As shown in Fig.4.5, a gaussian pulse centered at 5GHz is launched at point 100. The voltage is displayed at every point along the x-direction. As the time proceeds, the wave will propagate along x-direction towards both ends. In this basic 1D setup, every cell is 5mm long. So $\Delta x = 5mm$, $\Delta t = \frac{\Delta x}{2c}$ is applied in order to satisfy the MRTD Courant stability criteria. Three layers of duroid, each of length of 60 cells, stands at point 400, 520 and 640. The air gaps in between are also of length of 60 cells. A 20-cell layer of Perfect Matching Layer (PML) is placed at both end of the domain. The details of the PML will be revealed in a later section in this chapter. For the time being, the PML can be considered to absorb all of the incoming wave. Nothing reflects from the end of the domain. The source is designed to be a soft source, which will pass on the reflections. Details about hard and soft sources are included in the source expansion section later.

Such a model can be used to examine the mechanism of multiple reflections within a layered structure. The simulated scenario itself doesn't have a bandgap, but rather behaves as a simplified trial prototype for the EBG applications. As the waves hit and pass through the structure, some will be reflected back. The reflected wave from the multi-layer structure can be collected and analyzed. It is interesting to compare the results to the ones from a FDTD model with an identical scenario.

First, the general analysis method is detailed here. Then different scenarios of numerical experiments will be introduced. The signal at the point 160 (observation point) was collected and recorded. The excitation and the reflection can then be separated, given the distance and delay between the structure and the observing point. The separated signal is demonstrated in Fig. 4.6.

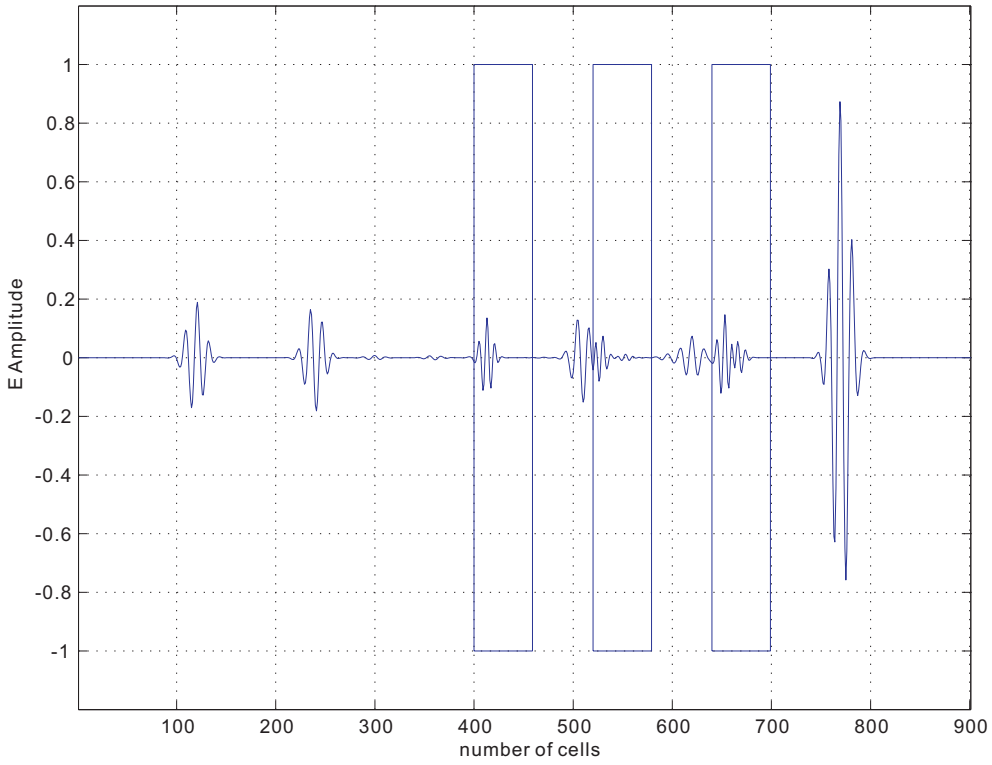

Figure 4.5: A wave propagated through three duroid layers in 1D Haar level-one MRTD.

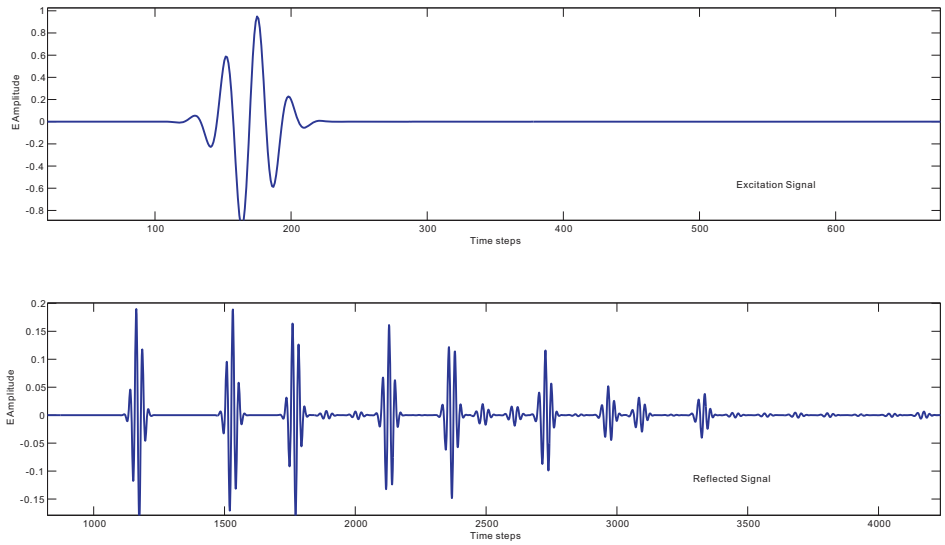

Figure 4.6: Separated excitation and reflected signal at observing point 160

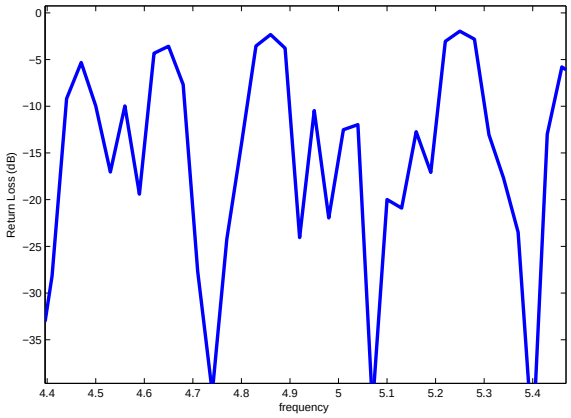

Figure 4.7: Return loss derived from the separated signals at observing point 160

With the time steps labeled on the x-axis, the excitation pulse is seen to pass the observing point at about 120 time steps after the initiation, partially due to the delay at the source as well as the distance to the source. The amplitude of the excitation is limited to the range of $[-1, 1]$ as specified by a unit source. In the reflection figure, the reflected signal arrives after 1100 time steps. Due to the multi-layer structure, multiple reflections bounce forth and back and several blocks of waves are seen after the first hit.

Of course, one can go on to compute a return loss from these excitations and reflections, such as the one shown in Fig. 4.7. However a 1D setup of this sort doesn't make too much sense in reality. Hence there is no necessity to carry out further Fourier Transform steps to derive the S_{11} in this scenario. On the other hand, the MRTD result of the reflected signal can be compared with those from FDTD simulation with an identical cell size Δx. The cell size can be varied, specifically from 5mm to 15mm ($\frac{\lambda}{12}$ and $\frac{\lambda}{4}$) in this scenario. The physical structure will be the same, hence sixty 5mm cells for each duroid layer translates to twenty cells in the 15mm scheme. Correspondingly, the observing point will be moved to point 120, to keep a equal distance to the source point 100. As aforementioned, the FDTD would expect some stability issues at low resolution, bearing in mind the gaussian pulse does have frequency components higher than the 5GHz center frequency, which makes the stability even worse. The permittivity of the center

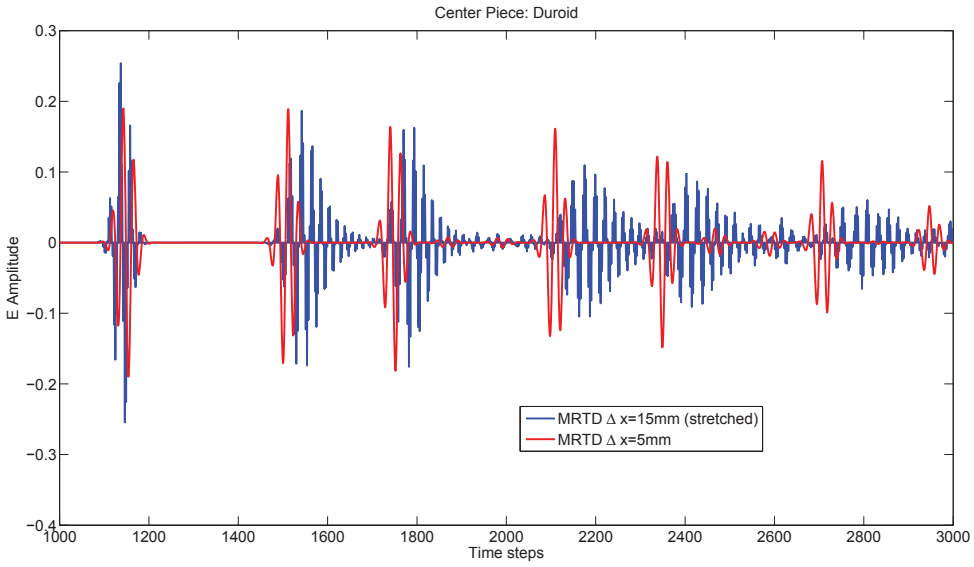

Figure 4.8: Reflected signal at observing point in two MRTD simulations; Red:$\Delta x = 5mm$, Blue:$\Delta x = 15mm$.

piece of this tri-layer structure can be modified to further observe the handling of material irregularity. Three situations are simulated, $\varepsilon_r = 2.2, 11.7, 50$ to approximate Duroid, silicon and high permittivity dielectric. The larger the contrast between the material and the air gaps enclosing it, the finer mesh is required, since the transition to and from the guided wavelength (which is much smaller) to the free-space wavelength happens on the thin edge between the air and the material. Our goal is to demonstrate the superiority of the MRTD code, as well as to discuss the difference between the two algorithms.

Fig. 4.8 shows the reflected signal observed in two MRTD simulations, one with $\Delta x = 5mm$, the other $\Delta x = 15mm$. One can see clearly in the case of $\Delta x = 15mm$, it has more spikes at every block of waves and it is almost impossible to differentiate separate reflections as they interfere. At such a low resolution, even the level-one MRTD generates erroneous results, and multiple reflections in some way amplifies the error. Nevertheless, the reflected signal has the trend of decaying along the time-axis, which generally means the algorithm is stable though not accurate. On the other hand, the 5mm cell size case yields much better results. At this resolution, the result is considered to be adequately reliable and can be used as a reference for FDTD comparison. Note that since the Δt is

fixed at a ratio of $\frac{\Delta x}{2c}$, when the cell size changes, the temporal step size also changes with it. Thus in order to display the result in a meaningful way, the reflected signal from the $\Delta x = 15mm$ case has to be stretched to suit the time scale of the 5mm case.

Fig. 4.9 shows two corresponding FDTD simulations. The 15mm one is noticeably erroneous, as the first block of reflected wave has an maximum amplitude close to 1. This kind of reflection would suggest a complete metallic structure, which clearly is not the case of this tri-layer Duroid panels. At $\frac{1}{4}$ wavelength per-cell, the error in FDTD is obviously unacceptable. The 5mm FDTD simulation on the other hand suits the computational purpose. In order to further compare the MRTD and FDTD with reasonable accuracy, the 5mm cell size is chosen. Also, knowing the mathematical equivalence between MRTD and FDTD with half cell size, it is tempting to add a $\Delta x = 2.5mm$ FDTD case to the comparison. Such a set-up is applied to the further scenarios where the center piece is replaced by silicon and a high permittivity material.

Figs. 4.10, 4.11 and 4.12 are results from the simulations, with center piece made of Duroid, silicon and high permittivity material correspondingly. As shown, in all three scenarios, the 5mm cell-size MRTD yields exactly the same reflection as 2.5mm cell-size FDTD does. It once again proves the mathematical equivalence of the two numerical algorithms, experimentally this time. It is therefore fair to state that a 1D MRTD with a Δx cell size has twice the resolution than a 1D Yee FDTD with Δx cell size. Comparing these two, the 5mm FDTD simulation theoretically yields a less accurate reflection signal. It is confirmed by the simulations, seen as deviations of the red curve from the green and blue ones. However, the deviations vary in different scenarios. The 5mm FDTD simulation performs better in the Duroid and high permittivity dielectric scenarios, but poorly in the silicon case. The explanation lies within the number of reflections happening during the wave propagation. As a whole, the multi-layer structure tends to have multiple internal reflections, given the inhomogeneity of the material/air distribution along the wave propagation direction. In the Duroid case, the center layer tends to let the energy pass through, while in the high permittivity dielectric case the major portion is reflected. Either way, the majority of the wave leaves the structure after a relatively small number of reflections. On the other hand, the silicon case clearly demonstrates some resonance. Due

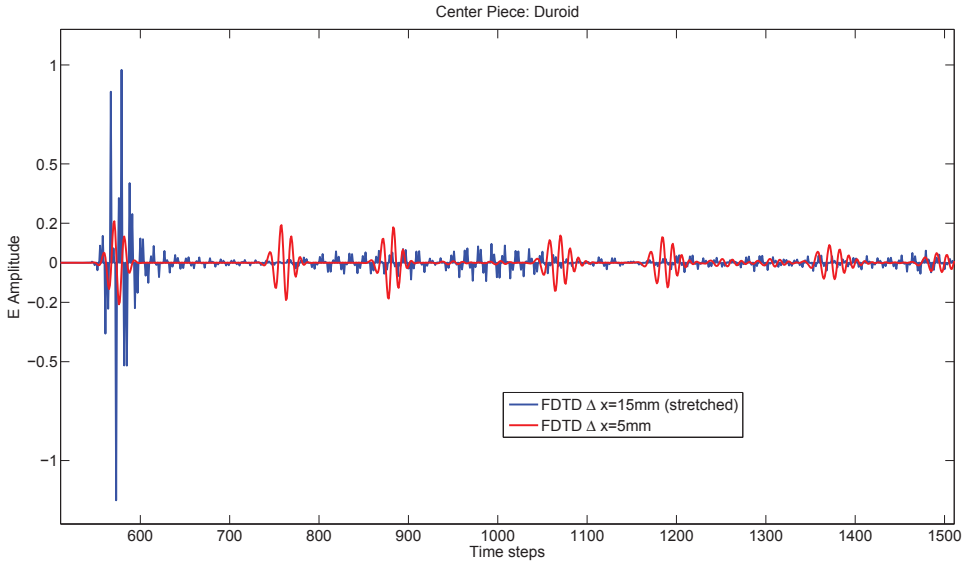

Figure 4.9: Reflected signal at observing point in two FDTD simulations; Red:$\Delta x = 5mm$, Blue:$\Delta x = 15mm$.

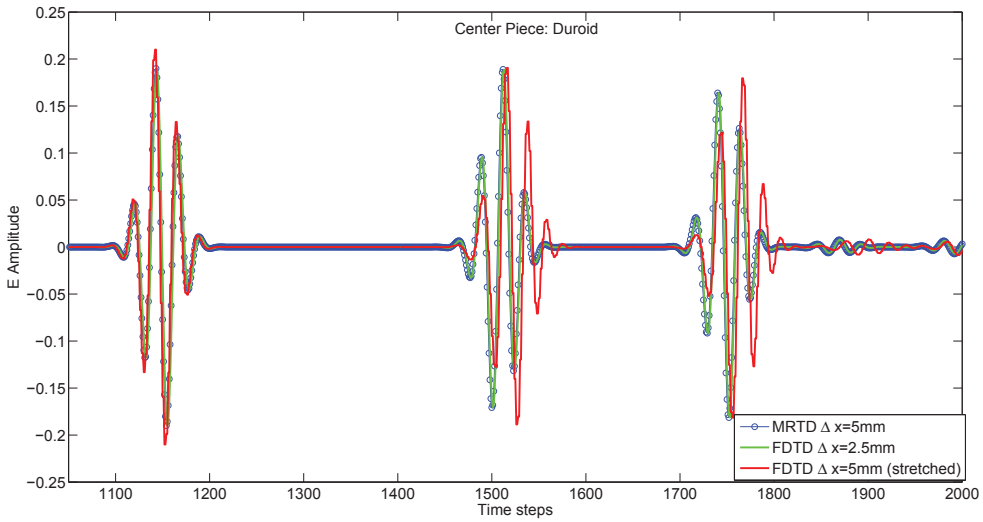

Figure 4.10: Reflected signal at observing point, center piece duroid; Blue: MRTD $\Delta x = 5mm$, Green: FDTD $\Delta x = 2.5mm$, Red: FDTD $\Delta x = 5mm$.

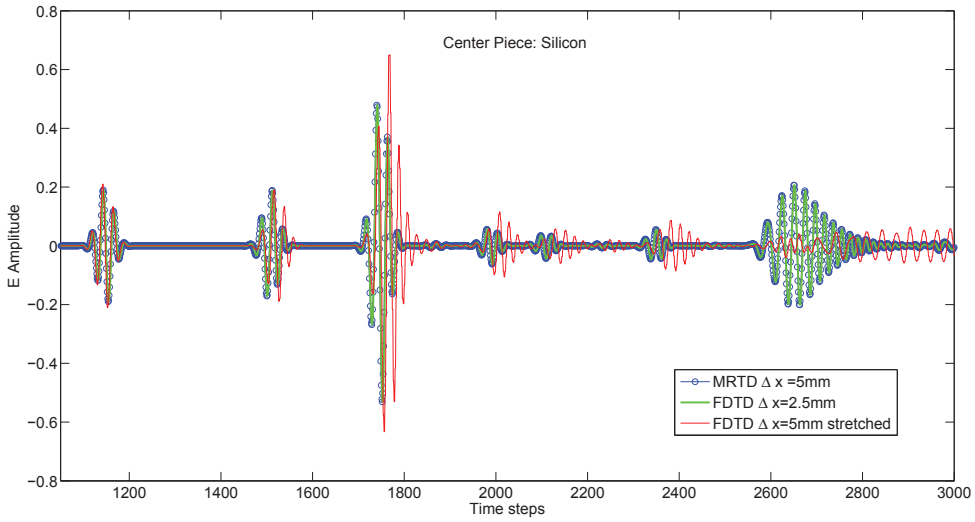

Figure 4.11: Reflected signal at observing point, center piece silicon; Blue: MRTD $\Delta x = 5mm$, Green: FDTD $\Delta x = 2.5mm$, Red: FDTD $\Delta x = 5mm$.

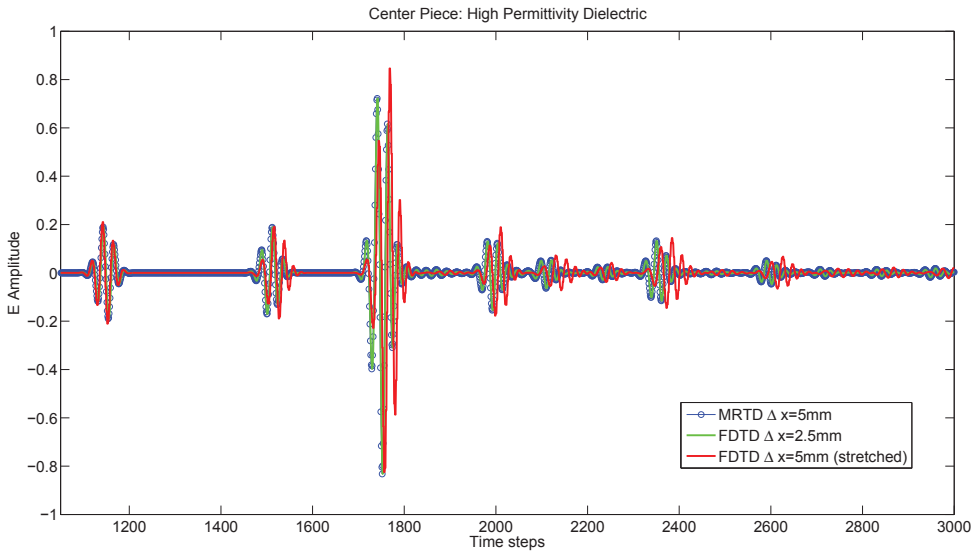

Figure 4.12: Reflected signal at observing point, center piece high permittivity dielectric($\varepsilon = 50$); Blue: MRTD $\Delta x = 5mm$, Green: FDTD $\Delta x = 2.5mm$, Red: FDTD $\Delta x = 5mm$.

to noticeable (but not huge) permittivity contrast between the silicon and surrounding air gaps, a good portion of the energy is kept inside the structure until dozens of reflections have occurred. Because of such an extensive propagation route, the error from the under-resolved 5mm FDTD simulation is accumulated, eventually more evidently pronounced in the reflection result. Apart from the spurious spikes around 1800 time steps, Fig. 4.11 clearly shows the red signal did not account for the block of reflection happened around 2500 to 2800 time steps. Instead, it starts to resonate with an everlasting wave inside the structure. To the end of the 9000 simulated time steps, the reflected wave coming out of the structure never depreciates again.

4.2 Two-dimensional level-one Haar MRTD and its applications

4.2.1 The formulation of 2D level-one Haar MRTD

In analogy to the 1D MRTD, a two-dimensional MRTD is developed by expanding the 2D Maxwell equations using Haar wavelet basis. Again we start from the 3D Maxwell equations in a lossless medium, repeating the equation 3.11 as well as adding in the other curl equation.

$$\nabla \times H = \varepsilon \frac{\partial E}{\partial t} \Longleftrightarrow \begin{cases} \frac{\partial H_z}{\partial y} - \frac{\partial H_y}{\partial z} = \varepsilon \frac{\partial E_x}{\partial t}; \\ \frac{\partial H_x}{\partial z} - \frac{\partial H_z}{\partial x} = \varepsilon \frac{\partial E_y}{\partial t}; \\ \frac{\partial H_y}{\partial x} - \frac{\partial H_x}{\partial y} = \varepsilon \frac{\partial E_z}{\partial t}. \end{cases} \tag{4.19}$$

$$\nabla \times E = -\mu \frac{\partial H}{\partial t} \Longleftrightarrow \begin{cases} \frac{\partial E_y}{\partial z} - \frac{\partial E_z}{\partial y} = \mu \frac{\partial H_x}{\partial t}; \\ \frac{\partial E_z}{\partial x} - \frac{\partial E_x}{\partial z} = \mu \frac{\partial H_y}{\partial t}; \\ \frac{\partial E_x}{\partial y} - \frac{\partial E_y}{\partial x} = \mu \frac{\partial H_z}{\partial t}. \end{cases} \tag{4.20}$$

In a 2D TM wave problem, there are only three equations, since $\frac{\partial}{\partial z} = 0$ and $H_z = 0$.

The remaining three are

$$\begin{cases} \frac{\partial H_y}{\partial x} - \frac{\partial H_x}{\partial y} = \varepsilon \frac{\partial E_z}{\partial t} \\ \frac{\partial E_z}{\partial y} = -\mu \frac{\partial H_x}{\partial t} \\ \frac{\partial E_z}{\partial x} = \mu \frac{\partial H_y}{\partial t} \end{cases} \tag{4.21}$$

After discretization of the Maxwell equations using Haar level-one wavelet function and rectangular pulse scaling functions, the update equations for Haar level-one 2D TM MRTD are shown as following:

$$\begin{cases} H_{y_{k,m,n}}^{\phi\phi} = H_{y_{k-1,m,n}}^{\phi\phi} + \frac{\Delta t}{\mu \Delta x}(-E_{z_{k,m,n}}^{\phi\phi} + E_{z_{k,m+1,n}}^{\phi\phi} - E_{z_{k,m,n}}^{\psi\phi} + E_{z_{k,m+1,n}}^{\psi\phi}) \\ H_{y_{k,m,n}}^{\phi\psi} = H_{y_{k-1,m,n}}^{\phi\psi} + \frac{\Delta t}{\mu \Delta x}(-E_{z_{k,m,n}}^{\phi\psi} + E_{z_{k,m+1,n}}^{\phi\psi} - E_{z_{k,m,n}}^{\psi\psi} + E_{z_{k,m+1,n}}^{\psi\psi}) \\ H_{y_{k,m,n}}^{\psi\phi} = H_{y_{k-1,m,n}}^{\psi\phi} + \frac{\Delta t}{\mu \Delta x}(E_{z_{k,m,n}}^{\phi\phi} - E_{z_{k,m+1,n}}^{\phi\phi} - 3E_{z_{k,m,n}}^{\psi\phi} - E_{z_{k,m+1,n}}^{\psi\phi}) \\ H_{y_{k,m,n}}^{\psi\psi} = H_{y_{k-1,m,n}}^{\psi\psi} + \frac{\Delta t}{\mu \Delta x}(E_{z_{k,m,n}}^{\phi\psi} - E_{z_{k,m+1,n}}^{\phi\psi} - 3E_{z_{k,m,n}}^{\psi\psi} - E_{z_{k,m+1,n}}^{\psi\psi}) \end{cases} \tag{4.22}$$

$$\begin{cases} H_{x_{k,m,n}}^{\phi\phi} = H_{x_{k-1,m,n}}^{\phi\phi} + \frac{\Delta t}{\mu \Delta x}(-E_{z_{k,m,n}}^{\phi\phi} + E_{z_{k,m,n+1}}^{\phi\phi} - E_{z_{k,m,n}}^{\phi\psi} + E_{z_{k,m,n+1}}^{\phi\psi}) \\ H_{x_{k,m,n}}^{\psi\phi} = H_{x_{k-1,m,n}}^{\psi\phi} + \frac{\Delta t}{\mu \Delta x}(-E_{z_{k,m,n}}^{\psi\phi} + E_{z_{k,m,n+1}}^{\psi\phi} - E_{z_{k,m,n}}^{\psi\psi} + E_{z_{k,m,n+1}}^{\psi\psi}) \\ H_{x_{k,m,n}}^{\phi\psi} = H_{x_{k-1,m,n}}^{\phi\psi} + \frac{\Delta t}{\mu \Delta x}(E_{z_{k,m,n}}^{\phi\phi} - E_{z_{k,m,n+1}}^{\phi\phi} - 3E_{z_{k,m,n}}^{\phi\psi} - E_{z_{k,m,n+1}}^{\phi\psi}) \\ H_{x_{k,m,n}}^{\psi\psi} = H_{x_{k-1,m,n}}^{\psi\psi} + \frac{\Delta t}{\mu \Delta x}(E_{z_{k,m,n}}^{\psi\phi} - E_{z_{k,m,n+1}}^{\psi\phi} - 3E_{z_{k,m,n}}^{\psi\psi} - E_{z_{k,m,n+1}}^{\psi\psi}) \end{cases} \tag{4.23}$$

$$\begin{cases} E_{zy_{k+1,m,n}}^{\phi\phi} = E_{zy_{k,m,n}}^{\phi\phi} + \frac{\Delta t}{\varepsilon \Delta x}(-H_{x_{k,m,n-1}}^{\phi\phi} + H_{x_{k,m,n}}^{\phi\phi} + H_{x_{k,m,n-1}}^{\phi\psi} - H_{x_{k,m,n}}^{\phi\psi}) \\ E_{zy_{k+1,m,n}}^{\phi\psi} = E_{zy_{k,m,n}}^{\phi\psi} + \frac{\Delta t}{\varepsilon \Delta x}(-H_{x_{k,m,n-1}}^{\phi\phi} + H_{x_{k,m,n}}^{\phi\phi} + H_{x_{k,m,n-1}}^{\phi\psi} + 3H_{x_{k,m,n}}^{\phi\psi}) \\ E_{zy_{k+1,m,n}}^{\psi\phi} = E_{zy_{k,m,n}}^{\psi\phi} + \frac{\Delta t}{\varepsilon \Delta x}(-H_{x_{k,m,n-1}}^{\psi\phi} + H_{x_{k,m,n}}^{\psi\phi} + H_{x_{k,m,n-1}}^{\psi\psi} - H_{x_{k,m,n}}^{\psi\psi}) \\ E_{zy_{k+1,m,n}}^{\psi\psi} = E_{zy_{k,m,n}}^{\psi\psi} + \frac{\Delta t}{\varepsilon \Delta x}(-H_{x_{k,m,n-1}}^{\psi\phi} + H_{x_{k,m,n}}^{\psi\phi} + H_{x_{k,m,n-1}}^{\psi\psi} + 3H_{x_{k,m,n}}^{\psi\psi}) \end{cases} \tag{4.24}$$

$$\begin{cases} E_{zx_{k+1,m,n}}^{\phi\phi} = E_{zx_{k,m,n}}^{\phi\phi} + \frac{\Delta t}{\varepsilon \Delta x}(-H_{y_{k,m-1,n}}^{\phi\phi} + H_{y_{k,m,n}}^{\phi\phi} + H_{y_{k,m-1,n}}^{\psi\phi} - H_{y_{k,m,n}}^{\psi\phi}) \\ E_{zx_{k+1,m,n}}^{\phi\psi} = E_{zx_{k,m,n}}^{\phi\psi} + \frac{\Delta t}{\varepsilon \Delta x}(-H_{y_{k,m-1,n}}^{\phi\psi} + H_{y_{k,m,n}}^{\phi\psi} + H_{y_{k,m-1,n}}^{\psi\psi} - H_{y_{k,m,n}}^{\psi\psi}) \\ E_{zx_{k+1,m,n}}^{\psi\phi} = E_{zx_{k,m,n}}^{\psi\phi} + \frac{\Delta t}{\varepsilon \Delta x}(-H_{y_{k,m-1,n}}^{\phi\phi} + H_{y_{k,m,n}}^{\phi\phi} + H_{y_{k,m-1,n}}^{\psi\phi} + 3H_{y_{k,m,n}}^{\psi\phi}) \\ E_{zx_{k+1,m,n}}^{\psi\psi} = E_{zx_{k,m,n}}^{\psi\psi} + \frac{\Delta t}{\varepsilon \Delta x}(-H_{y_{k,m-1,n}}^{\phi\psi} + H_{y_{k,m,n}}^{\phi\psi} + H_{y_{k,m-1,n}}^{\psi\psi} + 3H_{y_{k,m,n}}^{\psi\psi}) \end{cases} \tag{4.25}$$

$$\begin{cases} {E_z}^{\phi\phi}_{k+1,m,n} = {E_{zx}}^{\phi\phi}_{k+1,m,n} + {E_{zy}}^{\phi\phi}_{k+1,m,n} \\ {E_z}^{\psi\phi}_{k+1,m,n} = {E_{zx}}^{\psi\phi}_{k+1,m,n} + {E_{zy}}^{\psi\phi}_{k+1,m,n} \\ {E_z}^{\phi\psi}_{k+1,m,n} = {E_{zx}}^{\phi\psi}_{k+1,m,n} + {E_{zy}}^{\phi\psi}_{k+1,m,n} \\ {E_z}^{\psi\psi}_{k+1,m,n} = {E_{zx}}^{\psi\psi}_{k+1,m,n} + {E_{zy}}^{\psi\psi}_{k+1,m,n} \end{cases} \tag{4.26}$$

$$E_{zk+1,m,n} = {E_z}^{\phi\phi}_{k+1,m,n} + {E_z}^{\phi\psi}_{k+1,m,n} + {E_z}^{\psi\phi}_{k+1,m,n} + {E_z}^{\psi\psi}_{k+1,m,n} \tag{4.27}$$

where k, m are the index numbers of time and spatial steps, respectively. As seen in the above equations, each of the split field component (e.g. E_{zx}) is decomposed into four wavelet components, denoted with superscripts (i.e. ${E_{zx}}^{\phi\phi}$, ${E_{zx}}^{\phi\psi}$, ${E_{zx}}^{\psi\phi}$, ${E_{zx}}^{\psi\psi}$). Basically the superscripts represent the corresponding sampling functions. For example, ${E_{zx}}^{\phi\psi}$ means to sample E_{zx} with ϕ (rectangular pulse) in x-direction and ψ (Haar level-one wavelet)in y-direction. So in every cell, instead of one component E_z that is propagating, there are 8 components (${E_{zx}}^{\phi\phi}$, ${E_{zx}}^{\phi\psi}$, ${E_{zx}}^{\psi\phi}$, ${E_{zx}}^{\psi\psi}$, ${E_{zy}}^{\phi\phi}$, ${E_{zy}}^{\phi\psi}$, ${E_{zy}}^{\psi\phi}$, ${E_{zy}}^{\psi\psi}$) propagating. Or as in the combined representation, 4 components (${E_z}^{\phi\phi}$, ${E_z}^{\phi\psi}$, ${E_z}^{\psi\phi}$, ${E_z}^{\psi\psi}$) as in equation 4.26 are propagating throughout the cell.

It may be difficult to visualize the situation and Fig. 4.13 is included to facilitate the understanding of the decomposition. As shown, using a pulse point source, the energy propagation is mostly done by the ${E_z}^{\phi\phi}$ component. ${E_z}^{\phi\psi}$ and ${E_z}^{\psi\phi}$ transfers less energy, whereas ${E_z}^{\psi\psi}$ hardly transfers any. One would notice this by observing the scale range of the intensity of the E-field in Fig. 4.13. For example, the scale of ${E_z}^{\psi\psi}$ are set to be in the range of $[-0.03, 0.03]$, even then the field distribution of the component is still hard to see.

No matter how insignificant the ${E_z}^{\psi\psi}$ looks like, it nevertheless carries the same weight as other components, to satisfy the resolution and stability requirement of the MRTD. From equations 4.22, 4.23, 4.25 and 4.24, the interconnections between these components can be seen.

As mentioned in Chapter 2, the 2D FDTD has a maximum stability criterion of $S_c \leqq \frac{1}{\sqrt{2}}$ when the cell size along x and y directions are identical ($\Delta x = \Delta y$), in order to generate meaningful results. The 2D level-one MRTD has a similar criterion for the Courant

number S_c, however due to the twice resolution equivalence linearly, S_c is bounded by $\frac{1}{2\sqrt{2}}$ when $\Delta x = \Delta y$. It turns out that the optimum ratio for the Courant number is also the the maximum ratio, so that numerical error is minimized. That sets S_c in the 2D MRTD code to be exactly $\frac{1}{2\sqrt{2}}$.

In a 2D TE polarization case, E_x, E_y and H_z are non-zero, the electric field is transverse to the z-direction. The fields may vary in the x and y directions, but not in the z-direction. The Maxwell equations can be reduced to the following set,

$$\begin{cases} \frac{\partial E_y}{\partial x} - \frac{\partial E_x}{\partial y} = -\mu \frac{\partial H_z}{\partial t} \\ \frac{\partial H_z}{\partial y} = \varepsilon \frac{\partial E_x}{\partial t} \\ \frac{\partial H_z}{\partial x} = -\varepsilon \frac{\partial E_y}{\partial t} \end{cases} \tag{4.28}$$

Similar to the TM case detailed before, the TE update equations can be constructed. The equations are omitted here, as it is fairly easy to derive, following the TM case as an example.

4.2.2 The application of a 2D level-one Haar MRTD: Luneburg Lens

In order to test the accuracy and stability of the implemented 2D code, a well-known Luneburg lens structure has been applied for verification purpose, since it can be compared to numerical and experimental results in the published literature.

R. K. Luneburg proposed the lens in 1944 [58]. The structure appeared in antenna literature as early as in the 1960s. In antenna applications, their ability to form multiple beams that may point in arbitrary directions, and their broadband behavior are utilized [57]. However, after all the years, even though the lens weight problem can be eluded by increasing the targeted frequency range, the complex nature of the multilayered structure still imposes manufacturing problems.

Before the computer era, the Luneburg lens was mainly analysed and designed using Geometrical Optical (GO) principles [57]. At microwave frequencies, the geometrical optical principles do not work, since the theory is based on the assumption that the lens

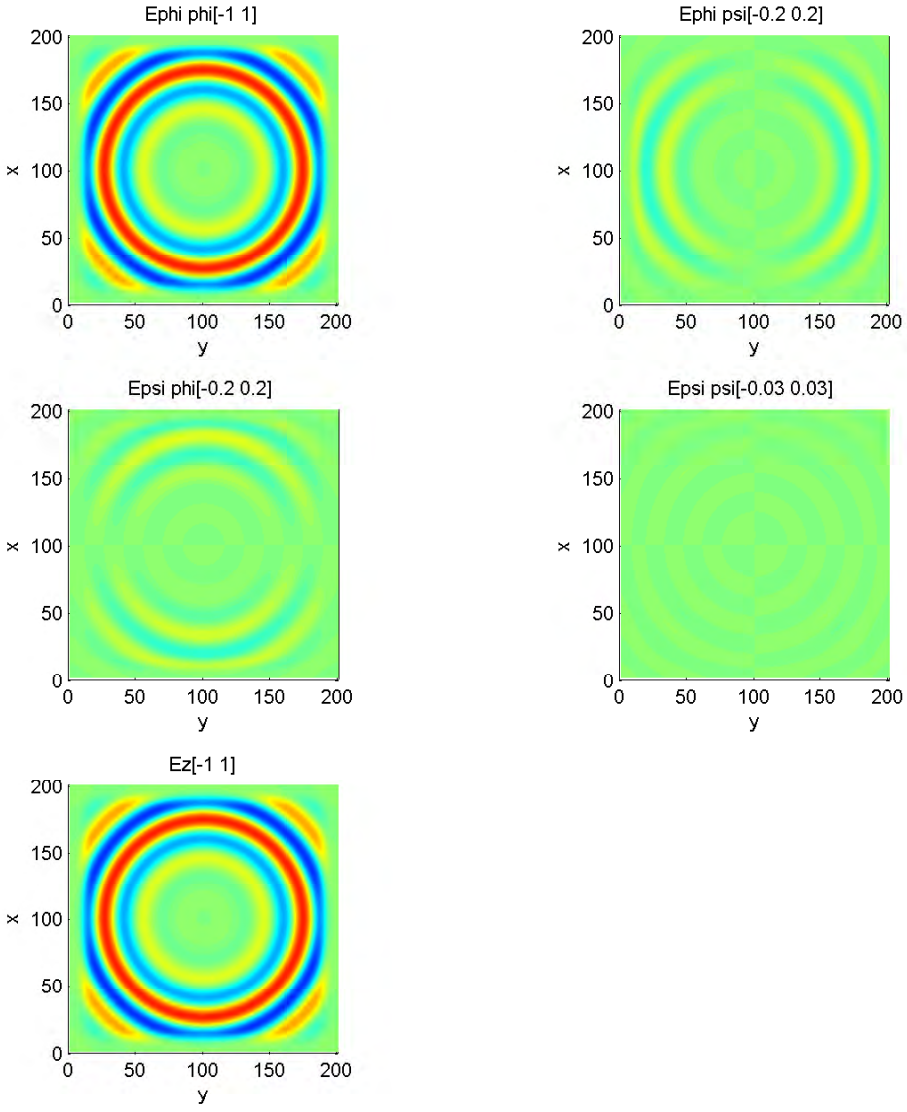

Figure 4.13: The E components in 2D TM Haar level-one MRTD ($E_z{}^{\phi\phi}$, $E_z{}^{\phi\psi}$, $E_z{}^{\psi\phi}$, $E_z{}^{\psi\psi}$, and E_z)

structure dimensions are much larger than the operating wavelength. As more sophisticated computational equipments become available, the structure has been analysed using various techniques, such as Ray-tracing (basically the computational version of GO) and spectral domain approach based on Green's functions [56].

More recently, many commercial simulators have emerged. One of the drawbacks in using these to simulate the Luneburg lens is the vast contrast and the huge electrical size of the lens (in the range of 10λ or more) and the resulting fine mesh required in order to analyse the multi-shell structure. This translates into huge numbers of simulation cells and hence a huge amount of memory as well as excessively long computation time. This is quite similar to the situation associated with hybrid EBG antennas. Therefore, this showcases the memory saving feature and the computational capability of the Haar MRTD algorithm.

Instead of the classical spherical structure, which has to be handled in a 3D full-wave simulator, a cylindrical luneburg lens can be implemented in the 2D MRTD codes. The concept of this simulation is that the Luneburg lens could convert a continuous point source at its focal point into a plain wave at the far-field region, by gradually varying the permittivity of concentric dielectric layers (shells). The 12-shell structure parameters are shown in the following table. There is existing literature [56][60] available for this particular structure with these specific dimensions, which can be used in comparison thus serving the purpose of verification.

The operating frequency is 10GHz and a hard sine source is being used. The outer shell of the lens has a radius of 15.9cm which is about 10λ. Therefore the lens has a diameter that is not significantly larger than the wavelength, which invalidates the use of GO. From the literature, the main purpose of those small imaginary parts in the material permittivity table is to introduce material loss to stabilize the numerical simulation. It is therefore not included in our model, since the Haar MRTD does not impose any particular stability problem in modelling such a structure.

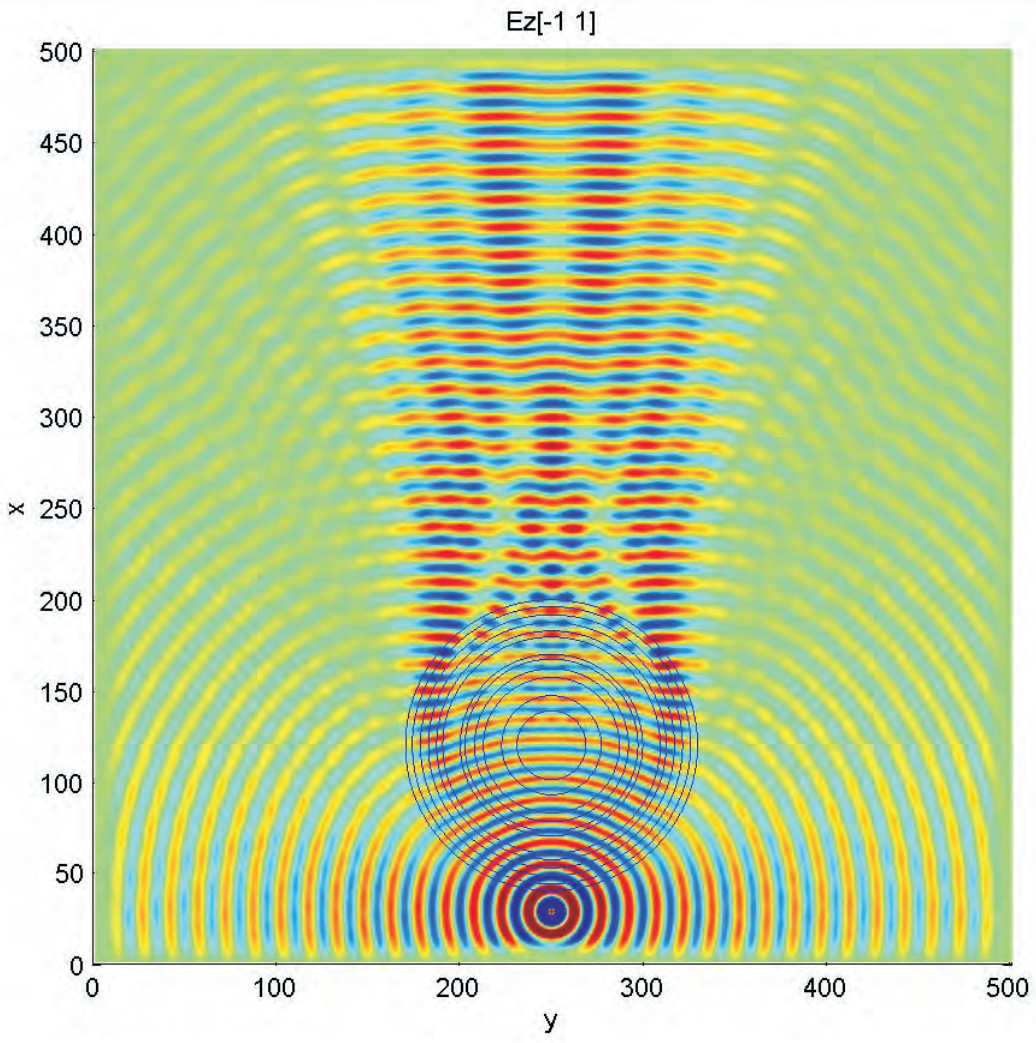

Figure 4.14: The Luneburg Lens and the source

Shell	Radius (cm)	Permittivity ε	MRTD simulated ε
1	3.755	1.93+0.0003j	1.93
2	5.52	1.74+0.0003j	1.74
3	7.41	1.71+0.0003j	1.71
4	8.38	1.65+0.0003j	1.65
5	9.415	1.63+0.0003j	1.63
6	9.94	1.56+0.0003j	1.56
7	11.84	1.54+0.0003j	1.54
8	12.5	1.50+0.0003j	1.50
9	13.4	1.4+0.0003j	1.4
10	14.27	1.28+0.0003j	1.28
11	15.15	1.2+0.0003j	1.2
12	15.9	1.1+0.0003j	1.1

Table 4.1: Luneburg lens geometry and permittivity [56]

On the other hand, since the cylindrical structure requires curved interfaces between layers, the stair-case mapping technique is employed. The layers are illustrated as concentric circles in Fig. 4.14, which only showcase the ideal mapping outcome. In reality the curvatures are far from smooth. We define the coordinates of the lens circle center to be $(center_x, center_y)$ first, then define the distance between the center and every point of each layer. According to the permittivity-radius table, using the following procedure the proper material coefficients can be assigned.

$$
\begin{aligned}
&for\ i = 1 : cellnum \\
&\quad for\ j = 1 : cellnum \\
&\qquad dist = ((i - center_x)/r)^2 + ((j - center_y)/r)^2; \\
&\qquad if\ \ dist <= 1.0 \\
&\qquad \varepsilon(i, j) = \varepsilon; \\
&\qquad end \\
&\quad end \\
&end
\end{aligned}
\tag{4.29}
$$

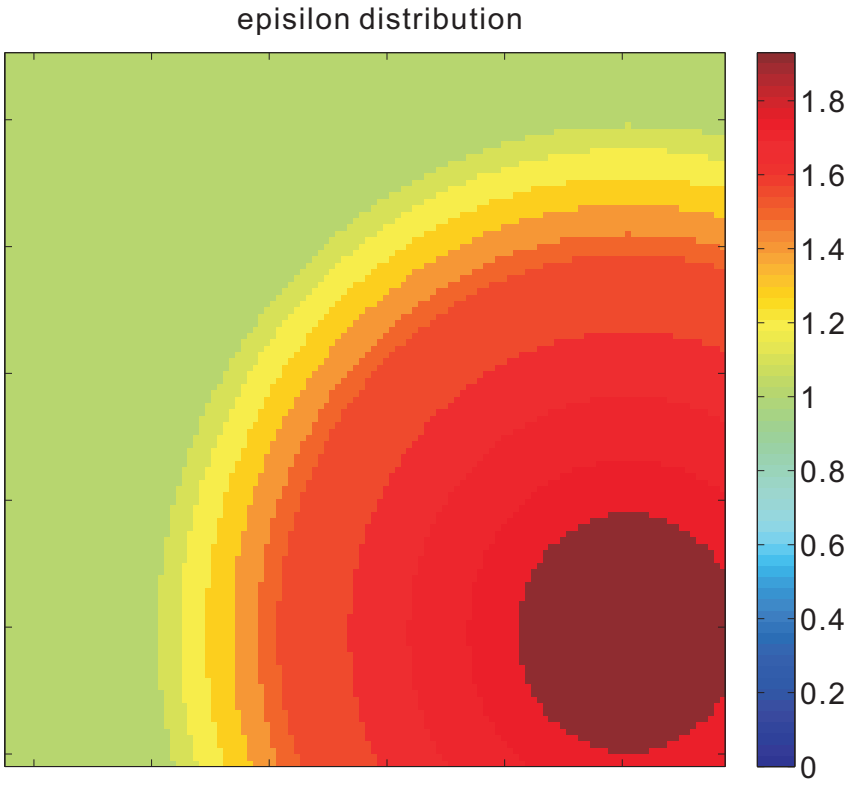

Figure 4.15: The ε_r distribution after staircase mapping

As the concentric annuli material distribution mandates, the permittivity is assigned according to the outmost layer's (layer 12's) r and ε first. Then, the same assignment procedure is used for the next outmost layer (layer 11 in this case) with corresponding r and ε. Repeat this step until the core circle is assigned properly. Upon completion, the staircase mapping generates rough edges consisting small square blocks to approximate the overall envelops of circles, as seen in Fig. 4.15.

In order to study the far field pattern, a straightforward method was chosen that simply simulates a rather large area of field and observe the E-field intensity at a far-field distance. The range is calculated as to be larger than $\frac{2D^2}{\lambda}$. One may argue the use of near-far field transformation in this instance. However, combining the near-far field transformation into the 2D MRTD code is not readily available even mathematically. Existing FDTD procedure of such transformation is of no use from the MRTD perspective, since to yield

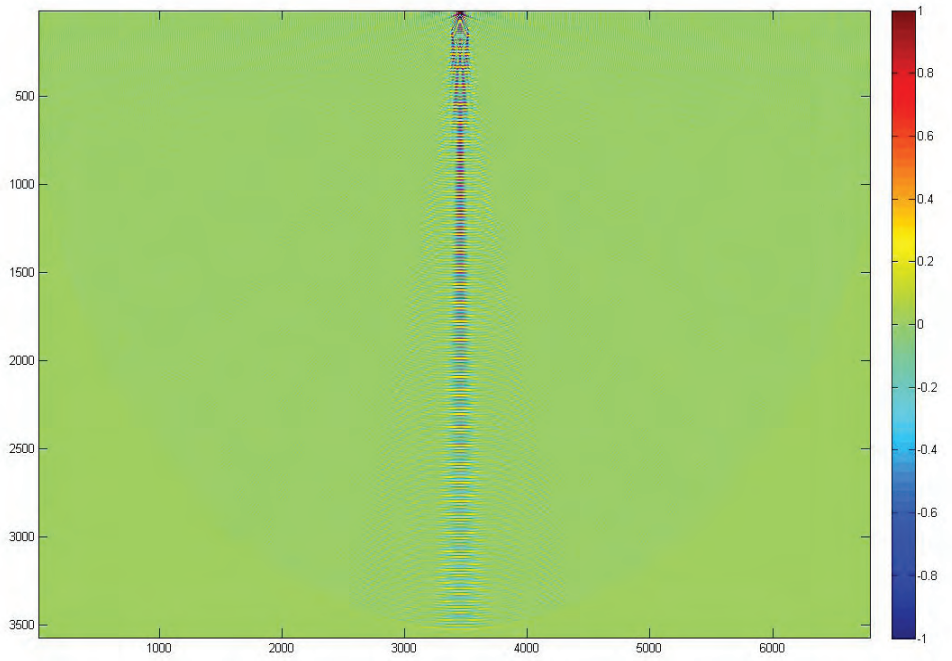

Figure 4.16: The far-field simulation scenario of Luneburg Lens

sufficient resolution requires detail at the sub-components level, which in turn messes up the procedure. The MRTD near-far field transformation remains a good potential future topic. On the other hand, since only $\frac{1}{2}$ number of cells is required by MRTD linearly comparing to FDTD, overall 2D simulation only costs a quarter of the number of cells compared to a corresponding FDTD simulation. Such memory saving features make this simulation possible with just 12GB memory, as this amounts to 6900×6900 spatial cells and temporal step iterates from 1 to 10000. The whole simulated scenario is shown in Fig. 4.16. In the picture, the lens is placed at [120,3450] (note: the Matlab displays matrix in transverse format), a 10GHz sine point source is again placed at the lens' focal point.

Fig. 4.17 shows the far-field pattern results from the MRTD simulation. The E field is collected every 0.05 degrees within the $[-90, 90]$ degrees range, from the perspective of the far-field of the lens. Fig. 4.18 shows the far-field patterns of an identical Luneburg lens from the literature for comparison purpose, where the solid black trace represents the results from a Ray-tracing technique, the dashed red curve indicates their measurements.

Comparing these two figures, the MRTD clearly yields reasonably accurate beamwidth and side lobe angles in the radiation pattern. For example, the first side lobes peak at about ± 9 degrees in both figures. Interestingly, the amplitude of the side lobes are higher in simulation than in reality. Also there are some obvious amplitude fluctuations in the second and third side lobes in the MRTD results.

To sum up, the MRTD simulation yields radiation patterns that reasonably resemble those from the literature. There are some deviations as mentioned above. The deviations are attributed to two reasons, one being the staircase mapping, and second the E field collection procedure. The staircase mapping approximates the annuli with square grids, which creates discrepancies between simulated and measured structures found in the literature. Therefore when multiple reflections happen between these curved layers, the approximation error accumulates. On the other hand, the far-field collection procedure takes the absolute value of E field at a distance far away from the structure. Again this semi-circle curve is approximated using similar procedures as the staircase mapping. This explains why there are some fluctuations in the amplitude. Sometimes nearby cells which are not of exact distance from the center of the lens are chosen, simply because of rounding error in the procedure.

4.2.3 Stability comparison between 2D level-one Haar MRTD and FDTD

During the course of analyzing the Luneburg structure, the stability of the two-dimensional MRTD and FDTD is compared based on a simplified two-layer dielectric structure. As shown in Fig. 4.19, a two-layer cylindrical structure is configured. In both simulations, Perfect Matching Layers (PML) are placed at the outer boundary of the domain. The reflections from these absorbing layers can be ignored.

Slightly different from the case of practical Luneburg lens where the dielectric constant increases layer by layer towards the core, the two layered structure only consists of a thin Duroid $\varepsilon = 2.2$ shell and a dielectric core whose $\varepsilon = 1.2$. The outer shell has a radius of 15.9cm where the radius of the inner cylinder is 15.15cm. The left part of Fig. 4.20 shows an unstable condition in FDTD with a $2mm \times 2mm$ cell size. A 10GHz sinusoidal

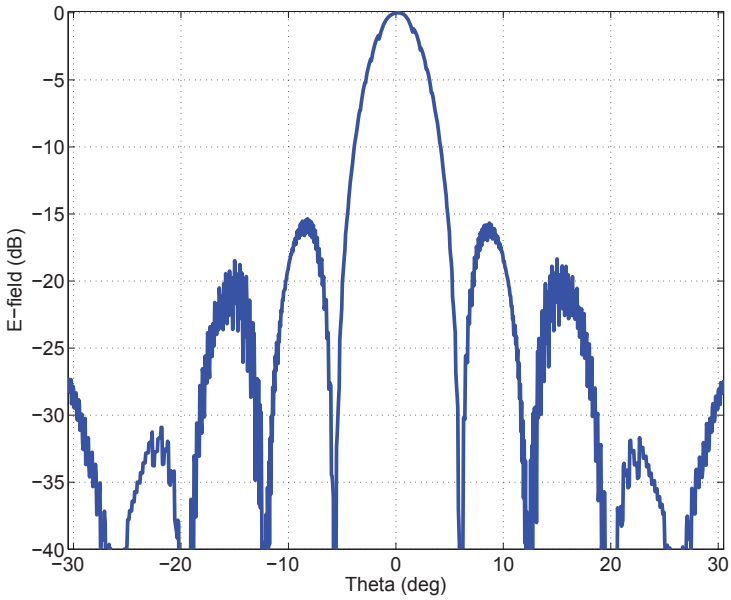

Figure 4.17: The far-field pattern of Luneburg Lens

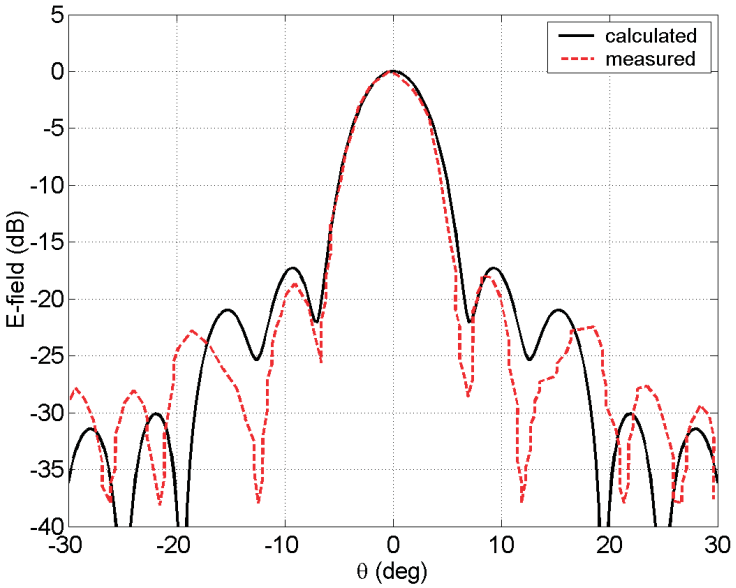

Figure 4.18: The far-field pattern of Luneburg Lens from literature for comparison purpose. Solid Black: Ray-tracing technique from [56]; Dashed Red: Measured data from [56]

point source is located at the focal point of the structure, 18.2cm away from the center of the cylinder. At 10GHz, the 2mm cell size is about $\frac{\lambda}{15}$, which should be sufficient for both FDTD and MRTD. After several time steps, even before the wave reaches the upper corner of the computational domain, the instability starts to appear at one side of the curved structure close to the source, as shown in the figure. A MRTD simulation with identical cell size is shown in the right part of Fig. 4.20, demonstrating a numerically stable scenario. The courant number S_c is chosen to be $\frac{1}{\sqrt{2}}$ for the 2D FDTD and $\frac{1}{2\sqrt{2}}$ for the 2D level-one MRTD.

With an identical spatial resolution, it is concluded the MRTD provides improved numerical stability and accuracy over the FDTD, through its orthogonal wavelet expanded field components.

4.3 Three-dimensional level-one Haar MRTD

Similar to the 2D cases, we start from the Maxwell equations to derive the 3D level-one Haar MRTD update equations, which would include a procedure converting the equations (4.19) and (4.20) to the 3D update equations. The procedure itself is omitted here. First of all, the field components are split. In order to present these in a clear yet concise way, the matrix form is chosen.

Now within any single cell at any time, (hence the temporal steps k, and spatial indices l, m, n are not labeled in the equations below),

$$\overrightarrow{E_{XY}} = [E_{xy}^{\phi\phi\phi}, E_{xy}^{\phi\phi\psi}, E_{xy}^{\phi\psi\phi}, E_{xy}^{\phi\psi\psi}, E_{xy}^{\psi\phi\phi}, E_{xy}^{\psi\phi\psi}, E_{xy}^{\psi\psi\phi}, E_{xy}^{\psi\psi\psi}] \tag{4.30}$$

$$\overrightarrow{E_{XZ}} = [E_{xz}^{\phi\phi\phi}, E_{xz}^{\phi\phi\psi}, E_{xz}^{\phi\psi\phi}, E_{xz}^{\phi\psi\psi}, E_{xz}^{\psi\phi\phi}, E_{xz}^{\psi\phi\psi}, E_{xz}^{\psi\psi\phi}, E_{xz}^{\psi\psi\psi}] \tag{4.31}$$

$$\overrightarrow{E_X} = [E_X^{\phi\phi\phi}, E_X^{\phi\phi\psi}, E_X^{\phi\psi\phi}, E_X^{\phi\psi\psi}, E_X^{\psi\phi\phi}, E_X^{\psi\phi\psi}, E_X^{\psi\psi\phi}, E_X^{\psi\psi\psi}]. \tag{4.32}$$

We do the same vectorization for $\overrightarrow{E_{YZ}}, \overrightarrow{E_{YX}}, \overrightarrow{E_Y}, \overrightarrow{E_{ZX}}, \overrightarrow{E_{ZY}}, \overrightarrow{E_Z}, \overrightarrow{H_{XY}}, \overrightarrow{H_{XZ}}, \overrightarrow{H_X}, \overrightarrow{H_{YZ}}$, $\overrightarrow{H_{YX}}, \overrightarrow{H_Y}, \overrightarrow{H_{ZX}}, \overrightarrow{H_{ZY}}, \overrightarrow{H_Z}$, with the same sampling sequence. In another word, the expansion sequence would always be $\phi\phi\phi, \phi\phi\psi, \phi\psi\phi, \phi\psi\psi, \psi\phi\phi, \psi\phi\psi, \psi\psi\phi, \psi\psi\psi$, as it's aligned in the same way to facilitate the explanation.

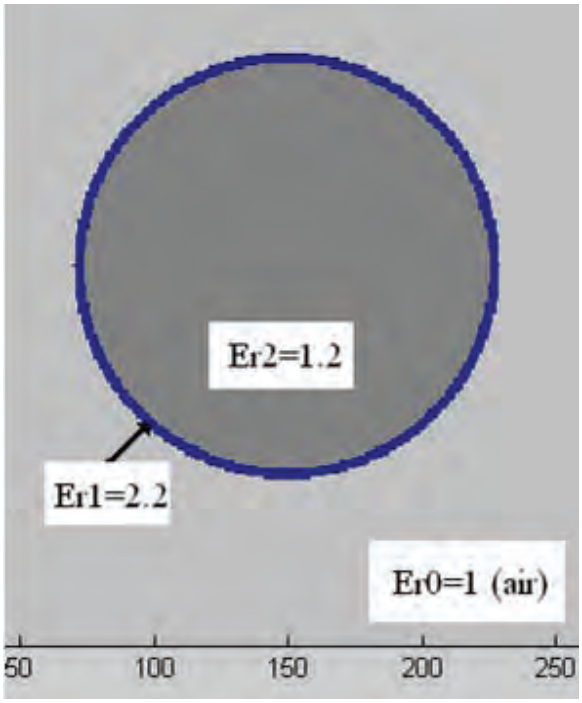

Figure 4.19: The two-layer stair-cased cylindrical structure

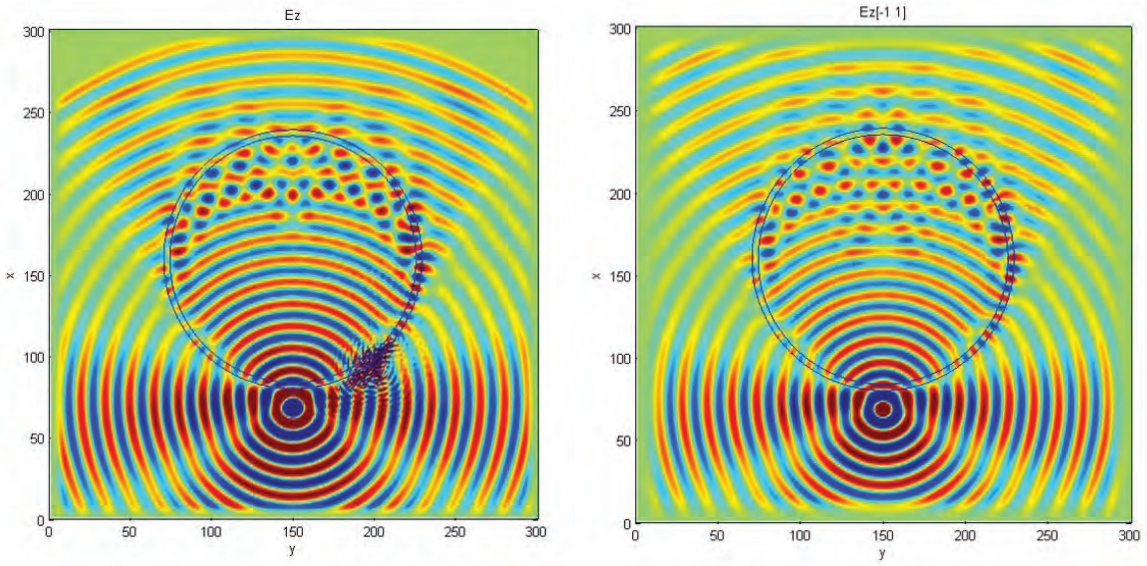

Figure 4.20: Left: A unstable simulation in FDTD ($2mm \times 2mm$ cell size)
Right: A stable simulation in MRTD ($2mm \times 2mm$ cell size)

The relations between these vectors are derived from their corresponding single variables. For example, the $\overrightarrow{E_X}$ is derived components by components from such procedure,

$$\begin{cases} E_X^{\phi\phi\phi} = E_{xz}^{\phi\phi\phi} + E_{xy}^{\phi\phi\phi} \\ E_X^{\phi\phi\psi} = E_{xz}^{\phi\phi\psi} + E_{xy}^{\phi\phi\psi} \\ ... \\ E_X^{\psi\psi\psi} = E_{xz}^{\psi\psi\psi} + E_{xy}^{\psi\psi\psi} \end{cases} \tag{4.33}$$

therefore

$$\overrightarrow{E_X} = \overrightarrow{E_{XY}} + \overrightarrow{E_{XZ}} \tag{4.34}$$

However, notice that $\overrightarrow{E_X}$ is used differently from the value of the E_X. In fact, E_X is the sum of all the elements; $E_X = E_X^{\phi\phi\phi} + E_X^{\phi\phi\psi} + E_X^{\phi\psi\phi} + E_X^{\phi\psi\psi} + E_X^{\psi\phi\phi} + E_X^{\psi\phi\psi} + E_X^{\psi\psi\phi} + E_X^{\psi\psi\psi}$. Whereas $\overrightarrow{E_X}$ represents a vector that contains every single of them. $\overrightarrow{E_X} = [E_X^{\phi\phi\phi}, E_X^{\phi\phi\psi}, E_X^{\phi\psi\phi}, E_X^{\phi\psi\psi}, E_X^{\psi\phi\phi}, E_X^{\psi\phi\psi}, E_X^{\psi\psi\phi}, E_X^{\psi\psi\psi}]$

Similar to the above, we can have,

$$\overrightarrow{E_Y} = \overrightarrow{E_{YZ}} + \overrightarrow{E_{YX}} \tag{4.35}$$

$$E_Y = E_Y^{\phi\phi\phi} + E_Y^{\phi\phi\psi} + E_Y^{\phi\psi\phi} + E_Y^{\phi\psi\psi} + E_Y^{\psi\phi\phi} + E_Y^{\psi\phi\psi} + E_Y^{\psi\psi\phi} + E_Y^{\psi\psi\psi} \tag{4.36}$$

$$\overrightarrow{E_Z} = \overrightarrow{E_{ZX}} + \overrightarrow{E_{ZY}} \tag{4.37}$$

$$E_Z = E_Z^{\phi\phi\phi} + E_Z^{\phi\phi\psi} + E_Z^{\phi\psi\phi} + E_Z^{\phi\psi\psi} + E_Z^{\psi\phi\phi} + E_Z^{\psi\phi\psi} + E_Z^{\psi\psi\phi} + E_Z^{\psi\psi\psi} \tag{4.38}$$

Then the same arrangements are done for H components: $\overrightarrow{H_X}, \overrightarrow{H_Y}, \overrightarrow{H_Z}$.

Inevitably we have to get down to the component level in order to present the update functions. In an update loop, E components are updated first. Then the source expansion procedure is applied to update the E field within the source point. Lastly the H components are updated. We briefly includes parts of the 3D update functions here, while the

complete set is covered in Appendix C.

$$\begin{cases}
{E_{xy}}^{\phi\phi\phi}_{k+1,l,m,n} = A^{E_{xy}}_{l,m,n}{E_{xy}}^{\phi\phi\phi}_{k,l,m,n} + B^{E_{xy}}_{l,m,n}({H_Z}^{\phi\phi\phi}_{k,l,m,n} - {H_Z}^{\phi\psi\phi}_{k,l,m,n} - {H_Z}^{\phi\phi\phi}_{k,l,m-1,n} + {H_Z}^{\phi\psi\phi}_{k,l,m-1,n}) \\
{E_{xy}}^{\phi\phi\psi}_{k+1,l,m,n} = A^{E_{xy}}_{l,m,n}{E_{xy}}^{\phi\phi\psi}_{k,l,m,n} + B^{E_{xy}}_{l,m,n}({H_Z}^{\phi\phi\psi}_{k,l,m,n} - {H_Z}^{\phi\psi\psi}_{k,l,m,n} - {H_Z}^{\phi\phi\psi}_{k,l,m-1,n} + {H_Z}^{\phi\psi\psi}_{k,l,m-1,n}) \\
{E_{xy}}^{\phi\psi\phi}_{k+1,l,m,n} = A^{E_{xy}}_{l,m,n}{E_{xy}}^{\phi\psi\phi}_{k,l,m,n} + B^{E_{xy}}_{l,m,n}({H_Z}^{\phi\phi\phi}_{k,l,m,n} + 3{H_Z}^{\phi\psi\phi}_{k,l,m,n} - {H_Z}^{\phi\phi\phi}_{k,l,m-1,n} + {H_Z}^{\phi\psi\phi}_{k,l,m-1,n}) \\
{E_{xy}}^{\phi\psi\psi}_{k+1,l,m,n} = A^{E_{xy}}_{l,m,n}{E_{xy}}^{\phi\psi\psi}_{k,l,m,n} + B^{E_{xy}}_{l,m,n}({H_Z}^{\phi\phi\psi}_{k,l,m,n} + 3{H_Z}^{\phi\psi\psi}_{k,l,m,n} - {H_Z}^{\phi\phi\psi}_{k,l,m-1,n} + {H_Z}^{\phi\psi\psi}_{k,l,m-1,n}) \\
{E_{xy}}^{\psi\phi\phi}_{k+1,l,m,n} = A^{E_{xy}}_{l,m,n}{E_{xy}}^{\psi\phi\phi}_{k,l,m,n} + B^{E_{xy}}_{l,m,n}({H_Z}^{\psi\phi\phi}_{k,l,m,n} - {H_Z}^{\psi\psi\phi}_{k,l,m,n} - {H_Z}^{\psi\phi\phi}_{k,l,m-1,n} + {H_Z}^{\psi\psi\phi}_{k,l,m-1,n}) \\
{E_{xy}}^{\psi\phi\psi}_{k+1,l,m,n} = A^{E_{xy}}_{l,m,n}{E_{xy}}^{\psi\phi\psi}_{k,l,m,n} + B^{E_{xy}}_{l,m,n}({H_Z}^{\psi\phi\psi}_{k,l,m,n} - {H_Z}^{\psi\psi\psi}_{k,l,m,n} - {H_Z}^{\psi\phi\psi}_{k,l,m-1,n} + {H_Z}^{\psi\psi\psi}_{k,l,m-1,n}) \\
{E_{xy}}^{\psi\psi\phi}_{k+1,l,m,n} = A^{E_{xy}}_{l,m,n}{E_{xy}}^{\psi\psi\phi}_{k,l,m,n} + B^{E_{xy}}_{l,m,n}({H_Z}^{\psi\phi\phi}_{k,l,m,n} + 3{H_Z}^{\psi\psi\phi}_{k,l,m,n} - {H_Z}^{\psi\phi\phi}_{k,l,m-1,n} + {H_Z}^{\psi\psi\phi}_{k,l,m-1,n}) \\
{E_{xy}}^{\psi\psi\psi}_{k+1,l,m,n} = A^{E_{xy}}_{l,m,n}{E_{xy}}^{\psi\psi\psi}_{k,l,m,n} + B^{E_{xy}}_{l,m,n}({H_Z}^{\psi\phi\psi}_{k,l,m,n} + 3{H_Z}^{\psi\psi\psi}_{k,l,m,n} - {H_Z}^{\psi\phi\psi}_{k,l,m-1,n} + {H_Z}^{\psi\psi\psi}_{k,l,m-1,n})
\end{cases} \tag{4.39}$$

In this equation, $A^{E_{xy}}_{l,m,n}$ and $B^{E_{xy}}_{l,m,n}$ are $l \times m \times n$ coefficient matrices. Normally, A is an array filled with 1, while every element of B on the other hand equals $\frac{\eta_0}{\varepsilon_r}S_c$, where η_0 is the free space impedance. By assigning different ε_r, different material permittivity can be achieved. S_c here is the Courant number for MRTD. Like the Courant number of FDTD introduced in Chapter 2, S_c is defined to be $\frac{c\Delta t}{\Delta x}$. However, due to the effective double resolution, S_c is set to be $\frac{1}{2\sqrt{3}}$, which is different from 3D Yee FDTD's $\frac{1}{\sqrt{3}}$. By assigning different A and B values, the PML boundary can be imposed at the outer computation domain. Also, since different B matrices can be associated with different components of E, materials with anisotropic permittivity can be implemented in this 3D code. For example, $B^{E_{xy}}_{l,m,n}$ can be very different from $B^{E_{xz}}_{l,m,n}$ in equation 4.40.

$$\begin{cases}
{E_{xz}}^{\phi\phi\phi}_{k+1,l,m,n} = A^{E_{xz}}_{l,m,n}{E_{xz}}^{\phi\phi\phi}_{k,l,m,n} + B^{E_{xz}}_{l,m,n}(-{H_Y}^{\phi\phi\phi}_{k,l,m,n} + {H_Y}^{\phi\phi\psi}_{k,l,m,n} + {H_Y}^{\phi\phi\phi}_{k,l,m,n-1} - {H_Y}^{\phi\phi\psi}_{k,l,m,n-1}) \\
{E_{xz}}^{\phi\phi\psi}_{k+1,l,m,n} = A^{E_{xz}}_{l,m,n}{E_{xz}}^{\phi\phi\psi}_{k,l,m,n} + B^{E_{xz}}_{l,m,n}(-{H_Y}^{\phi\phi\phi}_{k,l,m,n} - 3{H_Y}^{\phi\phi\psi}_{k,l,m,n} + {H_Y}^{\phi\phi\phi}_{k,l,m,n-1} - {H_Y}^{\phi\phi\psi}_{k,l,m,n-1}) \\
{E_{xz}}^{\phi\psi\phi}_{k+1,l,m,n} = A^{E_{xz}}_{l,m,n}{E_{xz}}^{\phi\psi\phi}_{k,l,m,n} + B^{E_{xz}}_{l,m,n}(-{H_Y}^{\phi\psi\phi}_{k,l,m,n} + {H_Y}^{\phi\psi\psi}_{k,l,m,n} + {H_Y}^{\phi\psi\phi}_{k,l,m,n-1} - {H_Y}^{\phi\psi\psi}_{k,l,m,n-1}) \\
{E_{xz}}^{\phi\psi\psi}_{k+1,l,m,n} = A^{E_{xz}}_{l,m,n}{E_{xz}}^{\phi\psi\psi}_{k,l,m,n} + B^{E_{xz}}_{l,m,n}(-{H_Y}^{\phi\psi\phi}_{k,l,m,n} - 3{H_Y}^{\phi\psi\psi}_{k,l,m,n} + {H_Y}^{\phi\psi\phi}_{k,l,m,n-1} - {H_Y}^{\phi\psi\psi}_{k,l,m,n-1}) \\
{E_{xz}}^{\psi\phi\phi}_{k+1,l,m,n} = A^{E_{xz}}_{l,m,n}{E_{xz}}^{\psi\phi\phi}_{k,l,m,n} + B^{E_{xz}}_{l,m,n}(-{H_Y}^{\psi\phi\phi}_{k,l,m,n} + {H_Y}^{\psi\phi\psi}_{k,l,m,n} + {H_Y}^{\psi\phi\phi}_{k,l,m,n-1} - {H_Y}^{\psi\phi\psi}_{k,l,m,n-1}) \\
{E_{xz}}^{\psi\phi\psi}_{k+1,l,m,n} = A^{E_{xz}}_{l,m,n}{E_{xz}}^{\psi\phi\psi}_{k,l,m,n} + B^{E_{xz}}_{l,m,n}(-{H_Y}^{\psi\phi\phi}_{k,l,m,n} - 3{H_Y}^{\psi\phi\psi}_{k,l,m,n} + {H_Y}^{\psi\phi\phi}_{k,l,m,n-1} - {H_Y}^{\psi\phi\psi}_{k,l,m,n-1}) \\
{E_{xz}}^{\psi\psi\phi}_{k+1,l,m,n} = A^{E_{xz}}_{l,m,n}{E_{xz}}^{\psi\psi\phi}_{k,l,m,n} + B^{E_{xz}}_{l,m,n}(-{H_Y}^{\psi\psi\phi}_{k,l,m,n} + {H_Y}^{\psi\psi\psi}_{k,l,m,n} + {H_Y}^{\psi\psi\phi}_{k,l,m,n-1} - {H_Y}^{\psi\psi\psi}_{k,l,m,n-1}) \\
{E_{xz}}^{\psi\psi\psi}_{k+1,l,m,n} = A^{E_{xz}}_{l,m,n}{E_{xz}}^{\psi\psi\psi}_{k,l,m,n} + B^{E_{xz}}_{l,m,n}(-{H_Y}^{\psi\psi\phi}_{k,l,m,n} - 3{H_Y}^{\psi\psi\psi}_{k,l,m,n} + {H_Y}^{\psi\psi\phi}_{k,l,m,n-1} - {H_Y}^{\psi\psi\psi}_{k,l,m,n-1})
\end{cases} \tag{4.40}$$

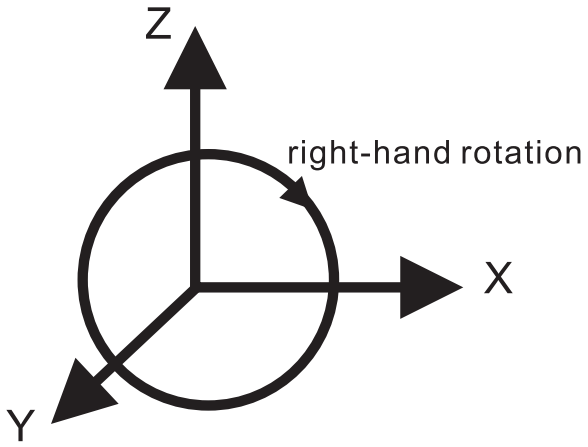

Figure 4.21: The right-hand rotation

The update functions for ${E_{xz}}^{\phi\phi\phi}$ to ${E_{xz}}^{\psi\psi\psi}$ are listed above. One can go on to figure out the update functions for other E components, namely $E_{yz}, E_{yx}, E_{zx}, E_{zy}$ series, to arrive at the complete set listed in Appendix C. Comparing equations 4.39 and 4.40, the coefficients in front of the H_Z and H_Y are quite different. In fact, these coefficients are all different for every E and H update functions, as seen in Appendix C. None of the previous literature showed the complete set, as the equations are very complicated as well as all different.

The rules for determining the proper coefficients lies within the sampling/expansion procedure of the E or H components. Parts of equations 4.39 and 4.40 are used here as examples.

$$E_{xy}{}^{\phi\phi\phi}_{k+1,l,m,n} = A^{E_{xy}}_{l,m,n} E_{xy}{}^{\phi\phi\phi}_{k,l,m,n} + B^{E_{xy}}_{l,m,n} (H_Z{}^{\phi\phi\phi}_{k,l,m,n} - H_Z{}^{\phi\psi\phi}_{k,l,m,n} - H_Z{}^{\phi\phi\phi}_{k,l,m-1,n} + H_Z{}^{\phi\psi\phi}_{k,l,m-1,n}) \tag{4.41}$$

1. To update each and every E component (for example $E_{xy}{}^{\phi\phi\phi}_{k+1,l,m,n}$), only two corresponding H components are needed, one with the exact same sampling sequence (i.e. $H_Z{}^{\phi\phi\phi}_{k,l,m,n}$), one with its dual (i.e. $H_Z{}^{\phi\psi\phi}_{k,l,m,n}$, since E_{xy} emphasizes (or project itself) on y-direction).

$$E_{xz}{}^{\phi\phi\psi}_{k+1,l,m,n} = A^{E_{xz}}_{l,m,n} E_{xz}{}^{\phi\phi\psi}_{k,l,m,n} + B^{E_{xz}}_{l,m,n}(-H_Y{}^{\phi\phi\phi}_{k,l,m,n} - 3H_Y{}^{\phi\phi\psi}_{k,l,m,n} + H_Y{}^{\phi\phi\phi}_{k,l,m,n-1} - H_Y{}^{\phi\phi\psi}_{k,l,m,n-1}) \tag{4.42}$$

2. As long as the desired E component is in right-hand rotation, the coefficients for H^{ϕ} are $+1$ and -1. For example, in equation 4.41, to derive $E_{xy}{}^{\phi\phi\phi}_{k+1,l,m,n}$, $+1H_Z{}^{\phi\phi\phi}_{k,l,m,n}$ and $-1H_Z{}^{\phi\phi\phi}_{k,l,m-1,n}$ are required in the update function. This applies to x-y direction, y-z direction, z-x direction cases, includes E_{xy}, E_{yz}, E_{zx} totaling 24 components. Otherwise if the sequence is in left-hand rotation (x-z, y-x, z-y), the coefficients for H^{ϕ} are -1 and $+1$ correspondingly. In equation 4.42, to derive $E_{xz}{}^{\phi\phi\psi}_{k+1,l,m,n}$, $-1H_Y{}^{\phi\phi\phi}_{k,l,m,n}$ and $+1H_Y{}^{\phi\phi\phi}_{k,l,m,n-1}$ are used.

3. If the projection of the E component vector also marks its wavelet expansion (for example, $E_{xz}{}^{\phi\phi\psi}_{k+1,l,m,n}$, where ψ appears at z-direction), coefficient 3 ($+3$ for right-hand rotation or -3 for left-hand rotation) appears before the corresponding H component (in equation 4.42, $H_Y{}^{\phi\phi\psi}_{k,l,m,n}$).

The E_X, E_Y, E_Z will be reconstructed from their components, using procedures like the one shown in equation 4.36. After updating the E field, the source expansion scheme modifies the E field at the source cell(s). This part will be explained in detail in later source expansion section.

Once the source expansion is finished, the H field will be updated. The update equations follow similar format and rules as the ones for E components. Coefficient arrays C and D are used instead of A and B. Usually C is filled with 1, while $D = \frac{S_c}{\mu_r \eta_0}$. Again, S_c here is set to be $\frac{1}{2\sqrt{3}}$. The complete set of equations is included in Appendix C.

To illustrate the final product of all these equations, a figure of a point source implemented in the 3D code is included above, Fig. 4.22. The 3D level-one Haar MRTD was later applied to solve the hybrid EBG structure, which will be detailed in Chapter 6.

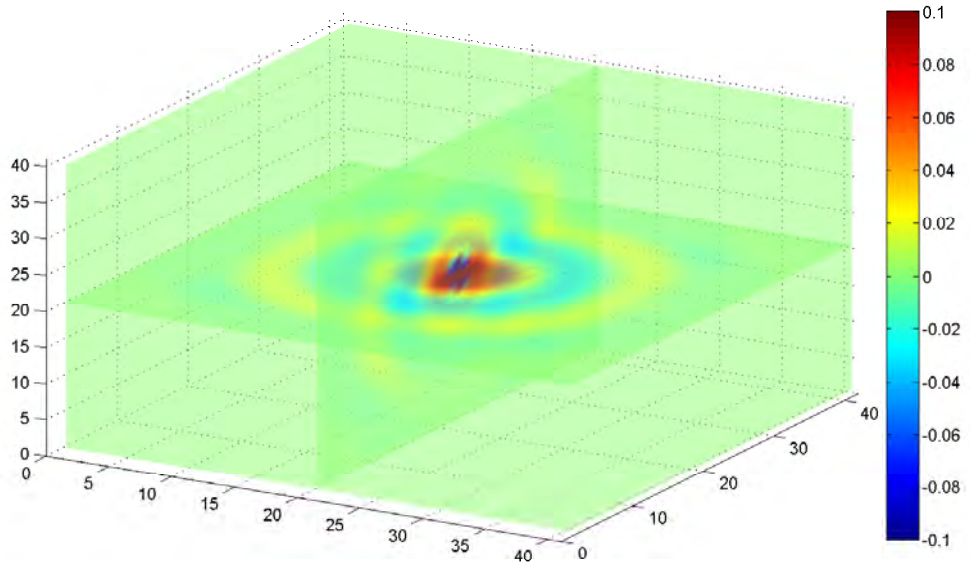

Figure 4.22: A point source in Haar level-one 3D MRTD code

4.4 Arbitrary level Haar MRTD

A 1D simple case is used to illustrate an arbitrary level of Haar MRTD. If n levels of wavelets are used for expansions at a point m, the MRTD equations can be summarized in a matrix vector form, using approach similar to the aforementioned level one's:

$$[E^n_{k+1,m}] = [E^n_{k,m}] + \frac{\Delta t}{\varepsilon \Delta x}[G^n_E][H^n_{k,m-1,m}] \tag{4.43}$$

$$[H^n_{k,m}] = [H^n_{k-1,m}] + \frac{\Delta t}{\mu \Delta x}[G^n_H][E^n_{k,m,m+1}] \tag{4.44}$$

where

$$[E^n_{k,m}] = [E^{\phi^{0,0}}_{k,m}, E^{\psi^{0,0}}_{k,m}, E^{\psi^{1,0}}_{k,m}, \ldots E^{\psi^{n-1,0}}_{k,m}, \ldots E^{\psi^{n-1,2^{n-1}-1}}_{k,m}] \tag{4.45}$$

$$[H^n_{k,m}] = [H^{\phi^{0,0}}_{k,m}, H^{\psi^{0,0}}_{k,m}, H^{\psi^{1,0}}_{k,m}, \ldots H^{\psi^{n-1,0}}_{k,m}, \ldots H^{\psi^{n-1,2^{n-1}-1}}_{k,m}] \tag{4.46}$$

$$[E^n_{k,m,m+1}] = [E^{\phi^{0,0}}_{k,m}, E^{\phi^{0,1}}_{k,m}, E^{\psi^{0,0}}_{k,m}, E^{\psi^{0,1}}_{k,m}, \ldots E^{\psi^{n-1,0}}_{k,m}, \ldots E^{\psi^{n-1,2^n}}_{k,m}] \tag{4.47}$$

$$[H^n_{k,m-1,m}] = [H^{\phi^{0,-1}}_{k,m}, H^{\phi^{0,0}}_{k,m}, H^{\psi^{0,-1}}_{k,m}, H^{\psi^{0,0}}_{k,m}, \ldots H^{\psi^{n-1,-2^{n-1}}}_{k,m}, \ldots H^{\psi^{n-1,2^{n-1}-1}}_{k,m}] \tag{4.48}$$

The coefficient matrices $[G_E^n]$ and $[G_H^n]$ are of the size of $2^n \times 2^{n+1}$. The elements can be expressed from following integral [34].

$$\int \frac{\partial \phi, \psi_m^{n,i}(x)}{\partial x} \phi, \psi_m^{p,j}(x \pm 2^{-n-1}) dx \tag{4.49}$$

where $\phi_m^{n,i}(x)$ and $\psi_m^{n,i}(x)$ are related to the original scaling and wavelet functions ϕ_m^0 and ψ_m^0,

$$\phi_m^{n,i}(x) = 2^{\frac{n}{2}} \phi_m^0(2^n x - i) \tag{4.50}$$

$$\psi_m^{n,i}(x) = 2^{\frac{n}{2}} \psi_m^0(2^n x - i) \tag{4.51}$$

As shown in [34], $[G_E^n]$ and $[G_H^n]$ are not easy to derive. The step from the level-1, level-2 Haar MRTD requires the following G coefficient matrices [34].

$$[G_E^2] = \begin{bmatrix} -1 & 1 & 1 & -1 & 0 & \sqrt{2} & 0 & -\sqrt{2} \\ -1 & 1 & 1 & 3 & 0 & \sqrt{2} & -2\sqrt{2} & \sqrt{2} \\ -\sqrt{2} & \sqrt{2} & \sqrt{2} & \sqrt{2} & 0 & 2 & 6 & 0 \\ 0 & 0 & 0 & -2\sqrt{2} & 0 & 0 & 2 & 6 \end{bmatrix} \tag{4.52}$$

$$[G_H^2] = \begin{bmatrix} -1 & 1 & -1 & 1 & -\sqrt{2} & 0 & \sqrt{2} & 0 \\ 1 & -1 & -3 & -1 & -\sqrt{2} & 2\sqrt{2} & -\sqrt{2} & 0 \\ 0 & 0 & 2\sqrt{2} & 0 & -6 & -2 & 0 & 0 \\ \sqrt{2} & -\sqrt{2} & -\sqrt{2} & -\sqrt{2} & 0 & -6 & -2 & 0 \end{bmatrix} \tag{4.53}$$

As seen above, the coefficients for 1D level-2 are already very complicated, let alone the level-n case. Also, as seen in the level-one cases, 2 expansion components in 1D translates to 8 components in 3D to split every E component. For level 2, 4 E components are required for 1D alone, 16 for 2D, 64 for 3D. In total, the level-2 3D code will have $64 \times 12 = 768$ separate equations just to update all the field components. Even using matrix form of update functions will not help. It requires a step of figuring out the G coefficient arrays. There will be 12 G arrays needed, 6 G_E^2 and 6 G_H^2, each of them is 64×64 in size.

Nonetheless the 3D capability is necessary for analyzing the hybrid EBG structure,

based on typical structures. A level-n code would be great, but practically not achievable by a one-man team. After the 2D level-one MRTD was materialized, it is decided that a 3D level-one code would be adequate for the specific multi-layer EBG antenna. Therefore the level-n approach was not developed. However, it is worth a glance since this may turn out to be a useful future development of the MRTD code. After all, the level-n follows the very same principle and expansion procedure, it's only a matter of time and effort to figure out hundreds of coefficients, if deemed necessary.

4.5 A novel MRTD Perfectly Matched Layer (PML) formulation

In general, the MRTD Perfectly Matched Layer (PML) formulation remains uncharted territory, since the update equations and absorbing boundary conditions are highly dependent on the choice of wavelet basis functions. Many existing MRTD algorithms utilize the FDTD PML by converting the MRTD to FDTD at outer boundaries of the computational domain and they are often computationally intensive [39].

In this section, we present an intrinsic level-one Haar MRTD PML formulation; while the PML for any level of Haar basis can be extended based upon the level-one case with proper shifting in spatial domain indices. The proposed intrinsic PML formulation is anticipated to further increase numerical efficiency in the MRTD algorithm, since no conversion (grid matching) procedure is required. The level-one Haar MRTD PML is implemented and numerically validated in comparison with the conventional Berenger's PML used in the FDTD method.

4.5.1 The intrinsic PML for Haar wavelet based MRTD

In this section, an intrinsic PML formulation is discussed. It is important that the proper gridding is applied as the intrinsic Haar MRTD PML can be considered as a modified conventional PML in accordance with the offset gridding. In analogy to the FDTD Berenger's PML, the update function within a level-one Haar MRTD PML region can be written as

a set of equations below:

$$E^{\phi^0}_{k+1,m} = AE^{\phi^0}_{k,m} + B(H^{\phi^0}_{k,m} - H^{\psi^0}_{k,m} - H^{\phi^0}_{k,m-1} + H^{\psi^0}_{k,m-1}) \tag{4.54}$$

$$E^{\psi^0}_{k+1,m} = AE^{\psi^0}_{k,m} + B(H^{\phi^0}_{k,m} + 3H^{\psi^0}_{k,m} - H^{\phi^0}_{k,m-1} + H^{\psi^0}_{k,m-1}) \tag{4.55}$$

$$H^{\phi^0}_{k,m} = CH^{\phi^0}_{k-1,m} + D(E^{\phi^0}_{k,m+1} + E^{\psi^0}_{k,m+1} - E^{\phi^0}_{k,m} - E^{\psi^0}_{k,m}) \tag{4.56}$$

$$H^{\psi^0}_{k,m} = CH^{\psi^0}_{k-1,m} + D(-E^{\phi^0}_{k,m+1} - E^{\psi^0}_{k,m+1} + E^{\phi^0}_{k,m} - 3E^{\psi^0}_{k,m}) \tag{4.57}$$

where A, B, C and D are four decaying factors. For the PML region on the left of the computational domain, A and B satisfy the formulas (4.58) and (4.59). For the right side, A and B satisfy a shifted set (4.60) and (4.61):

$$A_i = e^{\frac{3\Delta t \cdot c_0 \cdot log(R)}{2\Delta x \cdot l} \cdot (\frac{i-\frac{3}{4}}{l})^2} \tag{4.58}$$

$$B_i = \frac{-2(A_i - 1) \cdot l}{3\varepsilon_0 \cdot c_0 \cdot log(R)} \cdot (\frac{l}{i - \frac{3}{4}})^2 \tag{4.59}$$

$$A_j = e^{\frac{3\Delta t \cdot c_0 \cdot log(R)}{2\Delta x \cdot l} \cdot (\frac{j-\frac{1}{4}}{l})^2} \tag{4.60}$$

$$B_j = \frac{-2(A_j - 1) \cdot l}{3\varepsilon_0 \cdot c_0 \cdot log(R)} \cdot (\frac{l}{j - \frac{1}{4}})^2 \tag{4.61}$$

where *i, j* are integer indices of the PML cell ($1 \leq i, j \leq l$), increasing towards the PEC wall shown in Fig.4.23; *l* is the total number of PML layers; *R* is the pre-defined overall reflection coefficient of the PML (e.g.$1e^{-}5$). For the entire PML region, no matter which side of the computational domain is, C and D satisfy the equations (4.62) and (4.63), where *p* is also an integer index ($1 \leq p \leq l$), increasing towards the PEC wall (as in Fig.4.23).

$$C_p = e^{\frac{3\Delta t \cdot c_0 \cdot log(R)}{2\Delta x \cdot l} \cdot (\frac{p}{l})^2} \tag{4.62}$$

$$D_p = \frac{-2(C_p - 1) \cdot l}{3\mu_0 \cdot c_0 \cdot log(R)} \cdot (\frac{l}{p})^2 \tag{4.63}$$

One can consider the $\frac{i-\frac{3}{4}}{l}$ part similar to the concept of phase shift. Since the PML is

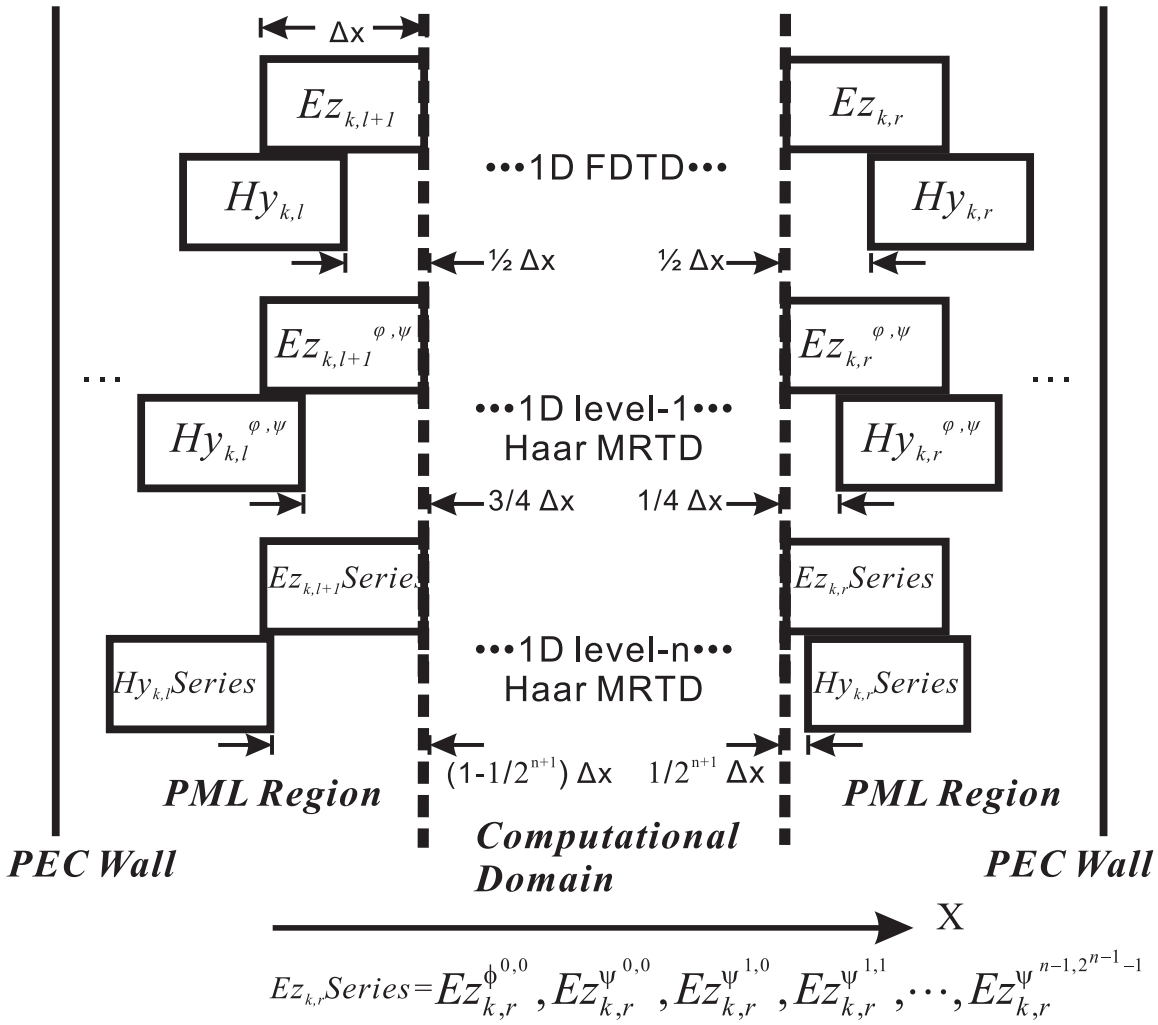

Figure 4.23: PML configuration for 1D FDTD, 1D level one Haar MRTD and 1D level n Haar MRTD.

applied to E first, to the left of the domain, the E is attenuated ahead of the H by $\frac{3}{4}$ of a cell. To the right of the computational domain, the E is attenuated ahead of the H by $\frac{1}{4}$ of a cell. Therefore the A coefficient of the PML to the right has a phase shift of $\frac{i-\frac{1}{4}}{l}$.

This set of equations can be further extended to 1D level-n case, where the corresponding shifts have to be applied to the indices. For a level-n Haar PML, there will be a set of 2^n E update equations and 2^n H update equations in similar formulation as in (4.54)-(4.57). The $i-\frac{3}{4}$ parts in A and B will be replaced by $i-1+\frac{1}{2^{n+1}}$ while the $j-\frac{1}{4}$ parts will be substituted by $j-\frac{1}{2^{n+1}}$ in equations (4.58)-(4.61). The C and D for H components remain unchanged. Fig.4.23 shows a comparison of proper PML settings (shifting of first pair of PML cells) between FDTD, level-one Haar MRTD and level-n Haar MRTD. Note that the PML region is always applied to the E components first. The indexing issue is explained in following 2D PML session.

4.5.2 The Two-dimensional PML for Haar wavelet based MRTD

First of all, the 2D level-one update functions are parameterized, similar to what has been done in the 1D PML configuration. Again a TM scenario is presented.

$$\begin{cases} H_{y_{k,m,n}}^{\phi\phi} = C_{m,n}^{H_y} H_{y_{k-1,m,n}}^{\phi\phi} + D_{m,n}^{H_y}(-E_{z_{k,m,n}}^{\phi\phi} + E_{z_{k,m+1,n}}^{\phi\phi} - E_{z_{k,m,n}}^{\psi\phi} + E_{z_{k,m+1,n}}^{\psi\phi}) \\ H_{y_{k,m,n}}^{\phi\psi} = C_{m,n}^{H_y} H_{y_{k-1,m,n}}^{\phi\psi} + D_{m,n}^{H_y}(-E_{z_{k,m,n}}^{\phi\psi} + E_{z_{k,m+1,n}}^{\phi\psi} - E_{z_{k,m,n}}^{\psi\psi} + E_{z_{k,m+1,n}}^{\psi\psi}) \\ H_{y_{k,m,n}}^{\psi\phi} = C_{m,n}^{H_y} H_{y_{k-1,m,n}}^{\psi\phi} + D_{m,n}^{H_y}(E_{z_{k,m,n}}^{\phi\phi} - E_{z_{k,m+1,n}}^{\phi\phi} - 3E_{z_{k,m,n}}^{\psi\phi} - E_{z_{k,m+1,n}}^{\psi\phi}) \\ H_{y_{k,m,n}}^{\psi\psi} = C_{m,n}^{H_y} H_{y_{k-1,m,n}}^{\psi\psi} + D_{m,n}^{H_y}(E_{z_{k,m,n}}^{\phi\psi} - E_{z_{k,m+1,n}}^{\phi\psi} - 3E_{z_{k,m,n}}^{\psi\psi} - E_{z_{k,m+1,n}}^{\psi\psi}) \end{cases} \tag{4.64}$$

$$\begin{cases} H_{x_{k,m,n}}^{\phi\phi} = C_{m,n}^{H_x} H_{x_{k-1,m,n}}^{\phi\phi} + D_{m,n}^{H_x}(-E_{z_{k,m,n}}^{\phi\phi} + E_{z_{k,m,n+1}}^{\phi\phi} - E_{z_{k,m,n}}^{\phi\psi} + E_{z_{k,m,n+1}}^{\phi\psi}) \\ H_{x_{k,m,n}}^{\psi\phi} = C_{m,n}^{H_x} H_{x_{k-1,m,n}}^{\psi\phi} + D_{m,n}^{H_x}(-E_{z_{k,m,n}}^{\psi\phi} + E_{z_{k,m,n+1}}^{\psi\phi} - E_{z_{k,m,n}}^{\psi\psi} + E_{z_{k,m,n+1}}^{\psi\psi}) \\ H_{x_{k,m,n}}^{\phi\psi} = C_{m,n}^{H_x} H_{x_{k-1,m,n}}^{\phi\psi} + D_{m,n}^{H_x}(E_{z_{k,m,n}}^{\phi\phi} - E_{z_{k,m,n+1}}^{\phi\phi} - 3E_{z_{k,m,n}}^{\phi\psi} - E_{z_{k,m,n+1}}^{\phi\psi}) \\ H_{x_{k,m,n}}^{\psi\psi} = C_{m,n}^{H_x} H_{x_{k-1,m,n}}^{\psi\psi} + D_{m,n}^{H_x}(E_{z_{k,m,n}}^{\psi\phi} - E_{z_{k,m,n+1}}^{\psi\phi} - 3E_{z_{k,m,n}}^{\psi\psi} - E_{z_{k,m,n+1}}^{\psi\psi}) \end{cases} \tag{4.65}$$

$$\begin{cases} {E_{zy}}^{\phi\phi}_{k+1,m,n} = A^{E_{zy}}_{m,n}{E_{zy}}^{\phi\phi}_{k,m,n} + B^{E_{zy}}_{m,n}(-{H_x}^{\phi\phi}_{k,m,n-1} + {H_x}^{\phi\phi}_{k,m,n} + {H_x}^{\phi\psi}_{k,m,n-1} - {H_x}^{\phi\psi}_{k,m,n}) \\ {E_{zy}}^{\phi\psi}_{k+1,m,n} = A^{E_{zy}}_{m,n}{E_{zy}}^{\phi\psi}_{k,m,n} + B^{E_{zy}}_{m,n}(-{H_x}^{\phi\phi}_{k,m,n-1} + {H_x}^{\phi\phi}_{k,m,n} + {H_x}^{\phi\psi}_{k,m,n-1} + 3{H_x}^{\phi\psi}_{k,m,n}) \\ {E_{zy}}^{\psi\phi}_{k+1,m,n} = A^{E_{zy}}_{m,n}{E_{zy}}^{\psi\phi}_{k,m,n} + B^{E_{zy}}_{m,n}(-{H_x}^{\psi\phi}_{k,m,n-1} + {H_x}^{\psi\phi}_{k,m,n} + {H_x}^{\psi\psi}_{k,m,n-1} - {H_x}^{\psi\psi}_{k,m,n}) \\ {E_{zy}}^{\psi\psi}_{k+1,m,n} = A^{E_{zy}}_{m,n}{E_{zy}}^{\psi\psi}_{k,m,n} + B^{E_{zy}}_{m,n}(-{H_x}^{\psi\phi}_{k,m,n-1} + {H_x}^{\psi\phi}_{k,m,n} + {H_x}^{\psi\psi}_{k,m,n-1} + 3{H_x}^{\psi\psi}_{k,m,n}) \end{cases} \tag{4.66}$$

$$\begin{cases} {E_{zx}}^{\phi\phi}_{k+1,m,n} = A^{E_{zx}}_{m,n}{E_{zx}}^{\phi\phi}_{k,m,n} + B^{E_{zx}}_{m,n}(-{H_y}^{\phi\phi}_{k,m-1,n} + {H_y}^{\phi\phi}_{k,m,n} + {H_y}^{\psi\phi}_{k,m-1,n} - {H_y}^{\psi\phi}_{k,m,n}) \\ {E_{zx}}^{\phi\psi}_{k+1,m,n} = A^{E_{zx}}_{m,n}{E_{zx}}^{\phi\psi}_{k,m,n} + B^{E_{zx}}_{m,n}(-{H_y}^{\phi\psi}_{k,m-1,n} + {H_y}^{\phi\psi}_{k,m,n} + {H_y}^{\psi\psi}_{k,m-1,n} - {H_y}^{\psi\psi}_{k,m,n}) \\ {E_{zx}}^{\psi\phi}_{k+1,m,n} = A^{E_{zx}}_{m,n}{E_{zx}}^{\psi\phi}_{k,m,n} + B^{E_{zx}}_{m,n}(-{H_y}^{\phi\phi}_{k,m-1,n} + {H_y}^{\phi\phi}_{k,m,n} + {H_y}^{\psi\phi}_{k,m-1,n} + 3{H_y}^{\psi\phi}_{k,m,n}) \\ {E_{zx}}^{\psi\psi}_{k+1,m,n} = A^{E_{zx}}_{m,n}{E_{zx}}^{\psi\psi}_{k,m,n} + B^{E_{zx}}_{m,n}(-{H_y}^{\phi\psi}_{k,m-1,n} + {H_y}^{\phi\psi}_{k,m,n} + {H_y}^{\psi\psi}_{k,m-1,n} + 3{H_y}^{\psi\psi}_{k,m,n}) \end{cases} \tag{4.67}$$

where $C^{H_x}_{m,n}, C^{H_y}_{m,n}, D^{H_x}_{m,n}, D^{H_y}_{m,n}, A^{E_{zy}}_{m,n}, A^{E_{zx}}_{m,n}, B^{E_{zy}}_{m,n}, B^{E_{zx}}_{m,n}$ are all matrices of $m \times n$ size. Then these A, B, C, D coefficient matrices can be defined, similar to the ones used in the 1D PML configuration, only in two-dimensional forms. In 2D, the labeling became much more complicated. But the essence stays the same, proper shifting in the corresponding coefficient matrices, especially A and B for E components. As previously mentioned, the end of each PML region is terminated by PEC. By not updating the E field in the last cell after the PML, effectively a PEC boundary is placed. Therefore, the PML E-field coefficients configuration starts from the second cell in each direction.

For the left of the domain, the PML region starts from (if seen from the perspective of decaying order, ends at) the first cell for H coefficients and second cell for E coefficients. It seems odd that the PML region does not cover identical indexed cell for E and H coefficients. Here comes the unfinished explanation of the 1D PML configuration figure Fig. 4.23, to aid the digestion.

From the center of that figure, the PML region is always applied to the E components first, or in another word E coefficients first. For right part of the domin, it does not create any particular indexing problem, as H grids are naturally a quarter cell trailing the corresponding E grids. But to implement PML to the left of the computational domain,

one has to ignore the first encountered H cell. In Fig. 4.23, to the left of the computational domain, the first encountered H cell with the index $l+1$ overlaps with the computational domain thus ignored. As explained before, the end of the PML domain is terminated by PEC, the decaying factors are applied to E coefficients indexed 2 to $l+1$, l being the total number of PML layers (e.g. $l = 20$, in previous 1D 3-layer structure example). $Ez_{k,l+1}$ (in 2D case, $E_{zxk,l+1,j}$, where j is arbitrary) is the first attenuated, by the PML, while $Ez_{k,2}$ being the last. Therefore A and B coefficients can be assigned accordingly to cell $l+1$ to 2. The first H attenuation happens within cell l and ends in the first cell, cell 1. Through this, the indexing issue is cleared.

For the left of the 2D domain, the following PML coefficients configuration are abided by. Different indexing to the 1D PML equations are used here. i, j represents the real element in matrix here, the i th row j th column.

for $(2 \leq i \leq l+1)$,

$$\begin{cases} A_{i,j}^{E_{zx}} = e^{\frac{3\Delta t \cdot c_0 \cdot log(R)}{2\Delta x \cdot l} \cdot (\frac{l+2-i-\frac{3}{4}}{l})^2} \\ B_{i,j}^{E_{zx}} = \frac{-2(A_{i,j}^{E_{zx}}-1) \cdot l}{3\varepsilon_0 \cdot c_0 \cdot log(R)} \cdot (\frac{l}{l+2-i-\frac{3}{4}})^2 \end{cases} \tag{4.68}$$

for $(1 \leq i \leq l)$,

$$\begin{cases} C_{i,j}^{H_y} = e^{\frac{3\Delta t \cdot c_0 \cdot log(R)}{2\Delta x \cdot l} \cdot (\frac{l+1-i}{l})^2} \\ D_{i,j}^{H_y} = \frac{-2(C_{i,j}^{H_y}) \cdot l}{3\mu_0 \cdot c_0 \cdot log(R)} \cdot (\frac{l}{l+1-i})^2 \end{cases} \tag{4.69}$$

As explained before, to the right of the computational domain, the indexing is valid without any issue. So both E and H are attenuated in parallel indexed grids. Leave the grid m for the PEC wall, the PML covers from $m-l$ to $m-1$.

for $(m-l \leq i \leq m-1)$,

$$\begin{cases} A_{i,j}^{E_{zx}} = e^{\frac{3\Delta t \cdot c_0 \cdot log(R)}{2\Delta x \cdot l} \cdot (\frac{i-m+l+1-\frac{1}{4}}{l})^2} \\ B_{i,j}^{E_{zx}} = \frac{-2(A_{i,j}^{E_{zx}}-1) \cdot l}{3\varepsilon_0 \cdot c_0 \cdot log(R)} \cdot (\frac{l}{i-m+l+1-\frac{1}{4}})^2 \\ C_{i,j}^{H_y} = e^{\frac{3\Delta t \cdot c_0 \cdot log(R)}{2\Delta x \cdot l} \cdot (\frac{i-m+l+1}{l})^2} \\ D_{i,j}^{H_y} = \frac{-2(C_{i,j}^{H_y}) \cdot l}{3\mu_0 \cdot c_0 \cdot log(R)} \cdot (\frac{l}{i-m+l+1})^2 \end{cases} \tag{4.70}$$

Note that in the equations above, indices are labeled as $l+2-i-\frac{3}{4}$ or $i-m+l+1-\frac{1}{4}$

without being further reduced. This is to keep the proper shifting part of $-\frac{3}{4}$ and $-\frac{1}{4}$ clear, so that one would not be confused by them. Similar to the "left case", the upper side of the domain requires similar shifting in the index.

for $(2 \leq j \leq l+1)$,

$$\begin{cases} A_{i,j}^{E_{zy}} = e^{\frac{3\Delta t \cdot c_0 \cdot log(R)}{2\Delta x \cdot l} \cdot (\frac{l+2-j-\frac{3}{4}}{l})^2} \\ B_{i,j}^{E_{zy}} = \frac{-2(A_{i,j}^{E_{zy}}-1) \cdot l}{3\varepsilon_0 \cdot c_0 \cdot log(R)} \cdot (\frac{l}{l+2-j-\frac{3}{4}})^2 \end{cases} \tag{4.71}$$

for $(1 \leq j \leq l)$,

$$\begin{cases} C_{i,j}^{H_x} = e^{\frac{3\Delta t \cdot c_0 \cdot log(R)}{2\Delta x \cdot l} \cdot (\frac{l+1-j}{l})^2} \\ D_{i,j}^{H_x} = \frac{-2(C_{i,j}^{H_x}) \cdot l}{3\mu_0 \cdot c_0 \cdot log(R)} \cdot (\frac{l}{l+1-j})^2 \end{cases} \tag{4.72}$$

Similar to the "right case", configuring the PML to the bottom of the domain poses no particular indexing issue.

for $(n-l \leq j \leq n-1)$,

$$\begin{cases} A_{i,j}^{E_{zy}} = e^{\frac{3\Delta t \cdot c_0 \cdot log(R)}{2\Delta x \cdot l} \cdot (\frac{j-n+l+1-\frac{1}{4}}{l})^2} \\ B_{i,j}^{E_{zy}} = \frac{-2(A_{i,j}^{E_{zy}}-1) \cdot l}{3\varepsilon_0 \cdot c_0 \cdot log(R)} \cdot (\frac{l}{j-n+l+1-\frac{1}{4}})^2 \\ C_{i,j}^{H_x} = e^{\frac{3\Delta t \cdot c_0 \cdot log(R)}{2\Delta x \cdot l} \cdot (\frac{j-n+l+1}{l})^2} \\ D_{i,j}^{H_x} = \frac{-2(C_{i,j}^{H_x}) \cdot l}{3\mu_0 \cdot c_0 \cdot log(R)} \cdot (\frac{l}{j-n+l+1})^2 \end{cases} \tag{4.73}$$

One can follow the procedure similar to what was described in the 1D PML configuration, to extend this 2D PML to accommodate level-n Haar wavelets, by adjusting to appropriate index shift.

Similar coefficient configurations are also implemented in the 3D MRTD PML. To maintain the conciseness, the full list of 3D PML equations is not included here. However, the PML is incorporated into the 3D code as it is vital to the final 3D EBG simulation.

4.5.3 Verification and comparison

The proposed intrinsic MRTD PML is verified by simulations on wave attenuation in the region consisting of twenty PML layers, as shown in Fig.4.24. The computation domain is square shaped, each side terminated by 20 layers of PML. A point source emitting Gaussian pulse centred at 10GHz is placed in the middle of the computational domain. The wave is seen to propagate without interruption in free space until it hits the PML cells. Penetrating through the 20 layers of PML, the wave will be attenuated by the decaying A, B, C, D factors, as aforementioned in the PML configuration. Since the R (the overall reflection coefficient of the PML) is specified to be $1e^{-5}$ or -50dB, the PML is non-reflective, seen as the smooth circular propagation patterns of the wave in Fig.4.24. The observation of the E field value is taken before the first PML layer and at the end of the 20th PML layers, both as functions of time (e.g.$E_{incident}(t)$, $E_{attenuated}(t)$). These two series of E field values are shown in Fig.4.25, where the incident wave has a clear shape of a Gaussian pulse and the attenuated one was barely seen on the graph. By applying Fast Fourier Transform (FFT) to both incident and attenuated signals, their frequency spectra can be obtained and the attenuation of the PML as a function versus frequency can be derived by division using the two resulting FFT series.

A similar setup is provided in the FDTD for comparison. The resulting attenuations are shown in Fig. 4.26. In both cases, through the PML, the incident wave was decayed by more than 50dB. The MRTD PML provides even greater attenuation, about 2.5dB larger than the FDTD PML, which indicates that the intrinsic PML performs very well in the two-dimensional MRTD configuration.

4.6 A new source expansion scheme

As aforementioned, within a single MRTD cell, the field is first split into several wavelet components in order to utilize the update functions based on orthogonal expansion. This inevitably brings in the source implementation problem. In traditional EM numerical techniques such as the FDTD, the source can be applied to the E or H field directly associated with some cells. However, in Haar MRTD, the E and H are not directly inherited

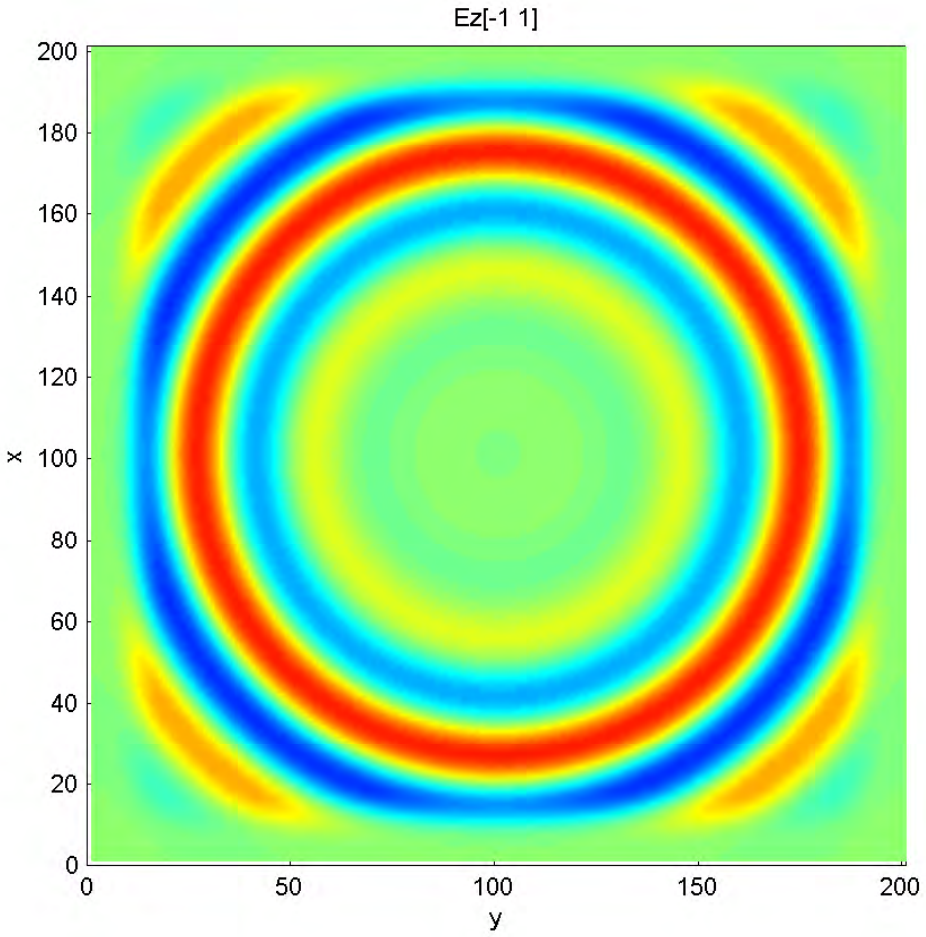

Figure 4.24: Numerical attenuation experiment, with a central Gaussian pulse source and 20 outmost MRTD PML layers.

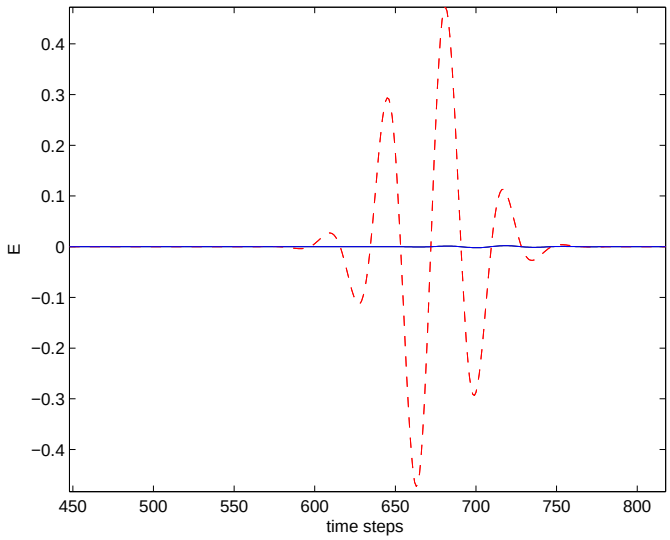

Figure 4.25: The observed E field values before the first PML layer and at the end of the 20th PML layers, as functions of time (dash red: $E_{incident}(t)$ before the first PML layer; solid blue: $E_{attenuated}(t)$ after the 20th PML layer).

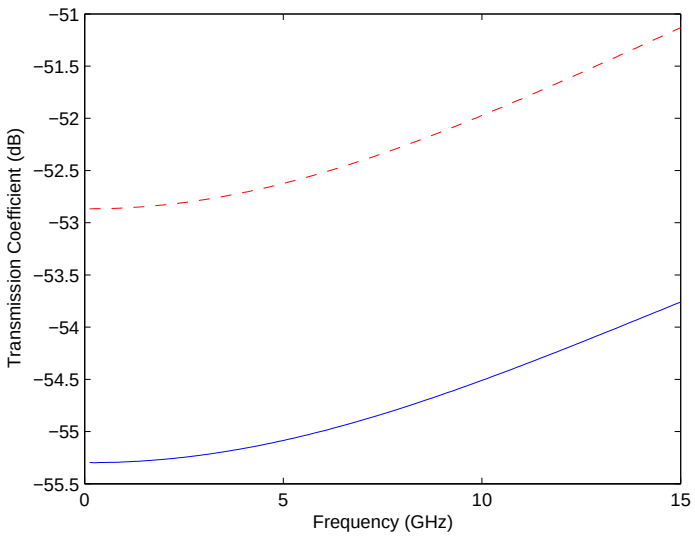

Figure 4.26: Attenuations (transmission coefficients) through 20 PML layers (dash red: FDTD; solid blue: level 1 Haar MRTD).

during iterations. Therefore, a proper source expansion scheme is compulsory in order to excite any structure in MRTD.

In general, different geometrical arrangements of source cells would generate different shapes of sources. For example, field applied to a single cell forms a point source, while fields applied to a line of cells yield a line source. Also, different patterns of excitations would generate different types of sources such as a continuous sine wave source or a gaussian pulse source.

To briefly illustrate the proposed source expansion scheme, we consider the simplest case first, a basic point source with a continuous sine wave excitation. The 2D and 3D formulation of this expansion scheme will be described. Other types of excitation can follow a similar approach. A plane wave excitation will be discussed at latter stage as an example.

4.6.1 2D point source expansion schemes for Haar level-one MRTD

We start with a 2D point source with a continuous sine excitation, $excitation(k) = sin(2\pi ft)$ where f indicates the operating frequency. As aforementioned, the E field propagates in the forms of 4 separate orthogonal components: E_{phi_phi} ($E_z{}^{\phi\phi}$), E_{phi_psi} ($E_z{}^{\phi\psi}$), E_{psi_phi} ($E_z{}^{\psi\phi}$), E_{psi_psi} ($E_z{}^{\psi\psi}$). Since the overall input excitation is applied to the E, which is the sum of these four components, the initial splitting is to generate the components in the source cell. Then the update sequence would take care of the field propagation, which we won't need to worry at this stage.

To expand the E into four orthogonal components within the source cell, the cell is divided into four subcells first. As shown in Fig. 4.27, the E field in each subcell is dubbed as $E1$, $E2$, $E3$, $E4$. Basically, the combinations of these subcell E field values represent the orthogonal wavelet components. The combinations are shown in the following equations:

$$E_{z}{}^{\phi\phi}_{k,SourceposX,SourceposY} = \frac{1}{4}(E1_k + E2_k + E3_k + E4_k) \tag{4.74}$$

$$E_{z}{}^{\psi\phi}_{k,SourceposX,SourceposY} = \frac{1}{4}(E1_k - E2_k + E3_k - E4_k) \tag{4.75}$$

$$E_{z_{k,SourceposX,SourceposY}}^{\phi\psi} = \frac{1}{4}(E1_k + E2_k - E3_k - E4_k) \tag{4.76}$$

$$E_{z_{k,SourceposX,SourceposY}}^{\psi\psi} = \frac{1}{4}(E1_k - E2_k - E3_k + E4_k) \tag{4.77}$$

where $(SourceposX, SourceposY)$ denotes the source's coordinates; k is the temporal step. Again, note that the axis shown in Fig. 4.27 marks real spatial directions. They do not represent the way in which the Matlab handles the x-y matrix.

The above combinations actually represent the decomposition or "sampling" procedure. Basically at any time step, the source cell is being sampled by a set of functions. For example, E_{phi_psi} is derived by sampling the E field value with the rectangular pulse function in x-direction and the level-one Haar function in y-direction. As shown in Fig. 4.27, whenever the parts of sampling functions in both x and y directions are positive (or both negative), that part is sampled as a positive part. For example, for E_{phi_psi}, the lower parts of the source cell are sampled by both positive parts of the wavelets and the scaling functions, which results a positive E1 and E2 marked in white. On the other hand, the E3 and E4 parts are sampled by the negative part of the wavelet in the y direction, but positive part of the scaling function in the x-direction. E3 and E4 end up as negative sampled parts in E_{phi_psi}, marked in grey in the figure.

Then the procedure of assigning the E1 to E4 is applied. Effectively, a 4-cell subcell scheme is required. One can use a subcell FDTD (such as the FDTD-like procedure described in previous 1D MRTD session) within the source cell to update these virtual E field values. However, it would be lengthy and painful since a subcell FDTD would require field values from nearby cells besides the source cell. A pseudo procedure is used here to bypass the subcell FDTD in order to retrieve E1, E2, E3 and E4. The procedure construct E2 to E4 from updated wavelet E components, while assigning excitation signal to E1.

At the first time step, the excitation signal is assigned to E1, while everything else still zero.

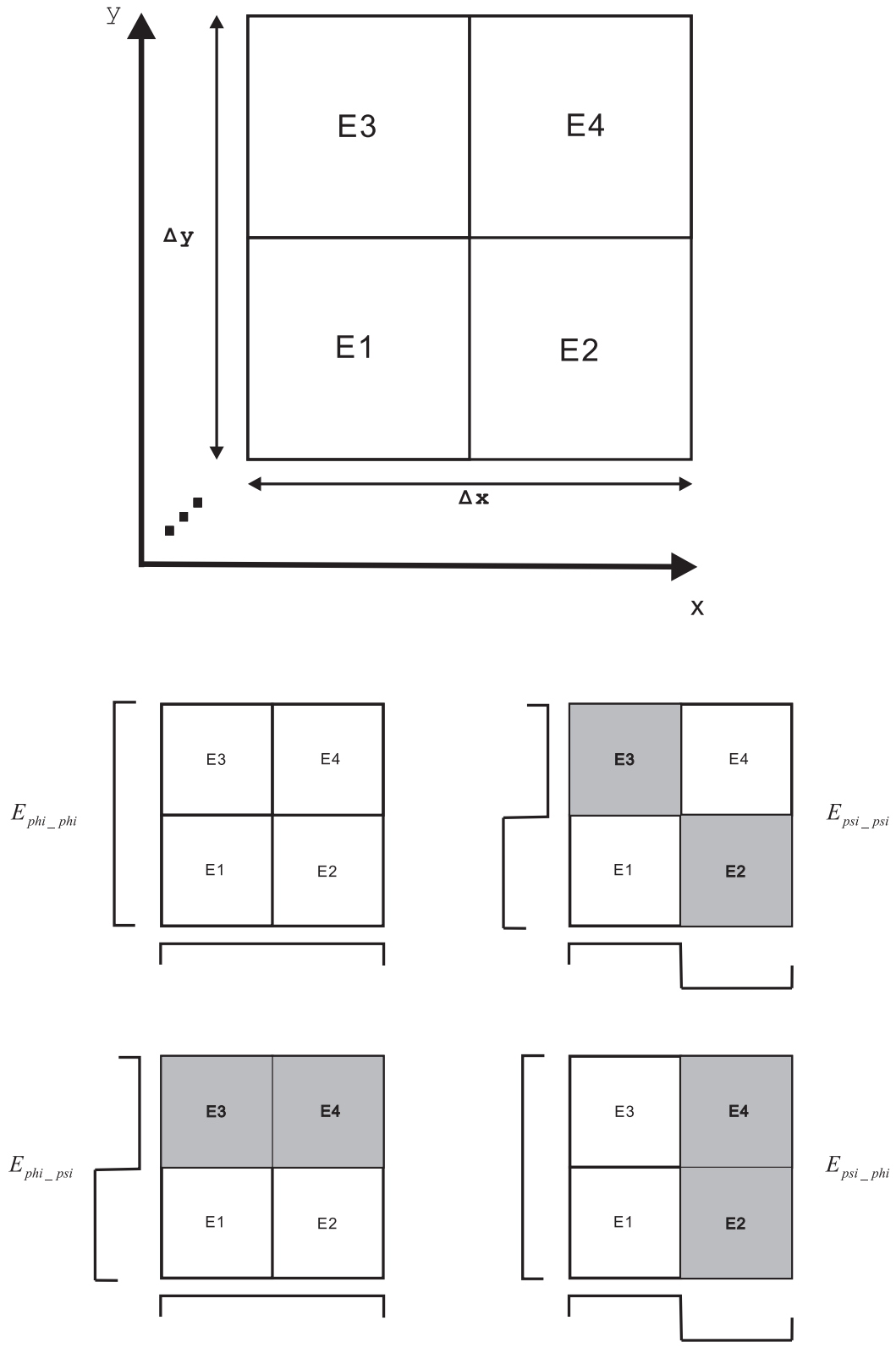

Figure 4.27: Source expansion in two-dimensional level-one Haar MRTD

$$\begin{cases} E1_k = excitation(k); \\ E2_k = 0; \\ E3_k = 0; \\ E4_k = 0; \end{cases} \tag{4.78}$$

At other time steps, E1 is updated with the excitation signal. E2 to E4 are constructed from $E^{\phi\phi}_{z_{k,SourceposX,SourceposY}}$, $E^{\phi\psi}_{z_{k,SourceposX,SourceposY}}$, $E^{\psi\phi}_{z_{k,SourceposX,SourceposY}}$ and $E^{\psi\psi}_{z_{k,SourceposX,SourceposY}}$. These wavelet expanded E components were previously obtained using the 2D MRTD update equations 4.24, 4.25 and 4.26, within the updating loop. The construction follows equation 4.79.

$$\begin{cases} E1_k = excitation(k); \\ E2_k = E^{\phi\phi}_{z_{k,SourceposX,SourceposY}} + E^{\phi\psi}_{z_{k,SourceposX,SourceposY}} \\ \quad -E^{\psi\phi}_{z_{k,SourceposX,SourceposY}} - E^{\psi\psi}_{z_{k,SourceposX,SourceposY}}; \\ E3_k = E^{\phi\phi}_{z_{k,SourceposX,SourceposY}} - E^{\phi\psi}_{z_{k,SourceposX,SourceposY}} \\ \quad +E^{\psi\phi}_{z_{k,SourceposX,SourceposY}} - E^{\psi\psi}_{z_{k,SourceposX,SourceposY}}; \\ E4_k = E^{\phi\phi}_{z_{k,SourceposX,SourceposY}} - E^{\phi\psi}_{z_{k,SourceposX,SourceposY}} \\ \quad -E^{\psi\phi}_{z_{k,SourceposX,SourceposY}} + E^{\psi\psi}_{z_{k,SourceposX,SourceposY}}; \end{cases} \tag{4.79}$$

Then equations 4.74 to 4.77 are used to renew the wavelet components of E. After these, the H components are updated with equations 4.22 and 4.23. So in fact, the source expansion is embedded between the E and H update functions. It uses existing E components within the source cell to construct virtual values E2, E3 and E4, thus bypassing a subcell FDTD procedure. More explanations are offered in following 3D source expansion scheme.

4.6.2 3D point source expansion schemes for Haar level-one MRTD

Again to assist the understanding from a sampling point of view, Fig. 4.28 is included here. As previously described, the source cell is considered being sampled in three directions, hence divided into 8 cubes. The E field value within each cube is labeled according

to Fig. 4.28, from E1 to E8. Then each wavelet expanded E component within the source cell can be expressed using E1 to E8. For example, $E_Z{}^{\psi\psi\phi}_{k,sX,sY,sZ}$ is derived by sampling the source cell at time k, using level-one Haar wavelet (ψ) at x and y direction, as well as rectangular pulse scaling function (ϕ) at z direction. (sX, sY, sZ) here denotes the three-dimensional coordinates of the source cell. From this sampling sequence, it is easily established that $E_Z{}^{\psi\psi\phi}_{k,sX,sY,sZ} = 0.125*(E1_k - E2_k - E3_k + E4_k + E5_k - E6_k - E7_k + E8_k)$;, by mapping out which cube corresponds to which part of the wavelet and scaling functions.

Then the pseudo procedure again is applied. At the first time step, the excitation signal is assigned to E1, while everything else still zero.

$$\begin{cases} E1_k = source(k); \\ E2_k = E3_k = E4_k = E5_k = E6_k = E7_k = E8_k = 0; \end{cases} \tag{4.80}$$

At other time steps, equation 4.81 are used to construct E2 to E8.

$$\begin{cases} E1_k = source(k); \\ E2_k = E_Z{}^{\phi\phi\phi}_{k,sX,sY,sZ} + E_Z{}^{\phi\phi\psi}_{k,sX,sY,sZ} + E_Z{}^{\phi\psi\phi}_{k,sX,sY,sZ} + E_Z{}^{\phi\psi\psi}_{k,sX,sY,sZ} \\ \quad - E_Z{}^{\psi\phi\phi}_{k,sX,sY,sZ} - E_Z{}^{\psi\phi\psi}_{k,sX,sY,sZ} - E_Z{}^{\psi\psi\phi}_{k,sX,sY,sZ} - E_Z{}^{\psi\psi\psi}_{k,sX,sY,sZ}; \\ E3_k = E_Z{}^{\phi\phi\phi}_{k,sX,sY,sZ} + E_Z{}^{\phi\phi\psi}_{k,sX,sY,sZ} - E_Z{}^{\phi\psi\phi}_{k,sX,sY,sZ} - E_Z{}^{\phi\psi\psi}_{k,sX,sY,sZ} \\ \quad + E_Z{}^{\psi\phi\phi}_{k,sX,sY,sZ} + E_Z{}^{\psi\phi\psi}_{k,sX,sY,sZ} - E_Z{}^{\psi\psi\phi}_{k,sX,sY,sZ} - E_Z{}^{\psi\psi\psi}_{k,sX,sY,sZ}; \\ E4_k = E_Z{}^{\phi\phi\phi}_{k,sX,sY,sZ} + E_Z{}^{\phi\phi\psi}_{k,sX,sY,sZ} - E_Z{}^{\phi\psi\phi}_{k,sX,sY,sZ} - E_Z{}^{\phi\psi\psi}_{k,sX,sY,sZ} \\ \quad - E_Z{}^{\psi\phi\phi}_{k,sX,sY,sZ} - E_Z{}^{\psi\phi\psi}_{k,sX,sY,sZ} + E_Z{}^{\psi\psi\phi}_{k,sX,sY,sZ} + E_Z{}^{\psi\psi\psi}_{k,sX,sY,sZ}; \\ E5_k = E_Z{}^{\phi\phi\phi}_{k,sX,sY,sZ} - E_Z{}^{\phi\phi\psi}_{k,sX,sY,sZ} + E_Z{}^{\phi\psi\phi}_{k,sX,sY,sZ} - E_Z{}^{\phi\psi\psi}_{k,sX,sY,sZ} \\ \quad + E_Z{}^{\psi\phi\phi}_{k,sX,sY,sZ} - E_Z{}^{\psi\phi\psi}_{k,sX,sY,sZ} + E_Z{}^{\psi\psi\phi}_{k,sX,sY,sZ} - E_Z{}^{\psi\psi\psi}_{k,sX,sY,sZ}; \\ E6_k = E_Z{}^{\phi\phi\phi}_{k,sX,sY,sZ} - E_Z{}^{\phi\phi\psi}_{k,sX,sY,sZ} + E_Z{}^{\phi\psi\phi}_{k,sX,sY,sZ} - E_Z{}^{\phi\psi\psi}_{k,sX,sY,sZ} \\ \quad + E_Z{}^{\psi\phi\phi}_{k,sX,sY,sZ} - E_Z{}^{\psi\phi\psi}_{k,sX,sY,sZ} - E_Z{}^{\psi\psi\phi}_{k,sX,sY,sZ} + E_Z{}^{\psi\psi\psi}_{k,sX,sY,sZ}; \\ E7_k = E_Z{}^{\phi\phi\phi}_{k,sX,sY,sZ} - E_Z{}^{\phi\phi\psi}_{k,sX,sY,sZ} - E_Z{}^{\phi\psi\phi}_{k,sX,sY,sZ} + E_Z{}^{\phi\psi\psi}_{k,sX,sY,sZ} \\ \quad + E_Z{}^{\psi\phi\phi}_{k,sX,sY,sZ} - E_Z{}^{\psi\phi\psi}_{k,sX,sY,sZ} - E_Z{}^{\psi\psi\phi}_{k,sX,sY,sZ} + E_Z{}^{\psi\psi\psi}_{k,sX,sY,sZ}; \\ E8_k = E_Z{}^{\phi\phi\phi}_{k,sX,sY,sZ} - E_Z{}^{\phi\phi\psi}_{k,sX,sY,sZ} - E_Z{}^{\phi\psi\phi}_{k,sX,sY,sZ} + E_Z{}^{\phi\psi\psi}_{k,sX,sY,sZ} \\ \quad - E_Z{}^{\psi\phi\phi}_{k,sX,sY,sZ} + E_Z{}^{\psi\phi\psi}_{k,sX,sY,sZ} + E_Z{}^{\psi\psi\phi}_{k,sX,sY,sZ} - E_Z{}^{\psi\psi\psi}_{k,sX,sY,sZ}; \end{cases} \tag{4.81}$$

Then the wavelet expanded field components within the source cell is modified using following equation.

$$\begin{cases} E_Z{}^{\phi\phi\phi}_{k,sX,sY,sZ} = 0.125 * (E1_k + E2_k + E3_k + E4_k + E5_k + E6_k + E7_k + E8_k); \\ E_Z{}^{\phi\phi\psi}_{k,sX,sY,sZ} = 0.125 * (E1_k + E2_k + E3_k + E4_k - E5_k - E6_k - E7_k - E8_k); \\ E_Z{}^{\phi\psi\phi}_{k,sX,sY,sZ} = 0.125 * (E1_k + E2_k - E3_k - E4_k + E5_k + E6_k - E7_k - E8_k); \\ E_Z{}^{\phi\psi\psi}_{k,sX,sY,sZ} = 0.125 * (E1_k + E2_k - E3_k - E4_k - E5_k - E6_k + E7_k + E8_k); \\ E_Z{}^{\psi\phi\phi}_{k,sX,sY,sZ} = 0.125 * (E1_k - E2_k + E3_k - E4_k + E5_k - E6_k + E7_k - E8_k); \\ E_Z{}^{\psi\phi\psi}_{k,sX,sY,sZ} = 0.125 * (E1_k - E2_k + E3_k - E4_k - E5_k + E6_k - E7_k + E8_k); \\ E_Z{}^{\psi\psi\phi}_{k,sX,sY,sZ} = 0.125 * (E1_k - E2_k - E3_k + E4_k + E5_k - E6_k - E7_k + E8_k); \\ E_Z{}^{\psi\psi\psi}_{k,sX,sY,sZ} = 0.125 * (E1_k - E2_k - E3_k + E4_k - E5_k + E6_k + E7_k - E8_k); \end{cases} \tag{4.82}$$

Then the aforementioned equation 4.38 takes in hand to combine the overall E_Z. That ends the source expansion part of the 3D procedure.

It might look strange, that equation 4.82 seems to be the exact reverse procedure of what equation 4.81 does. It is not a dummy step. As aforementioned, the source expansion is embedded between the E and H update functions. Therefore, before equation 4.81, the whole domain of wavelet E components were updated. Then, in equation 4.81, E2 to E8 are constructed from the wavelet components of the E field within the source cell, while E1 is renewed from the source. Effectively the source signal only lights up $\frac{1}{8}$ of the source cell in this step. Then equation 4.82 uses these virtual values to convert back to the wavelet expanded form, with new information from the excitation. This inclusion of new information is exactly what the source expansion is for, which is to combine the excitation at the source cell.

4.6.3 Source expansions of other excitations

Basically the point source procedure described above serves as bricks in building any other type of excitation with geometrical shape. For instance, one can align these source cells into a line and apply a continuous wave excitation on every single one of them,

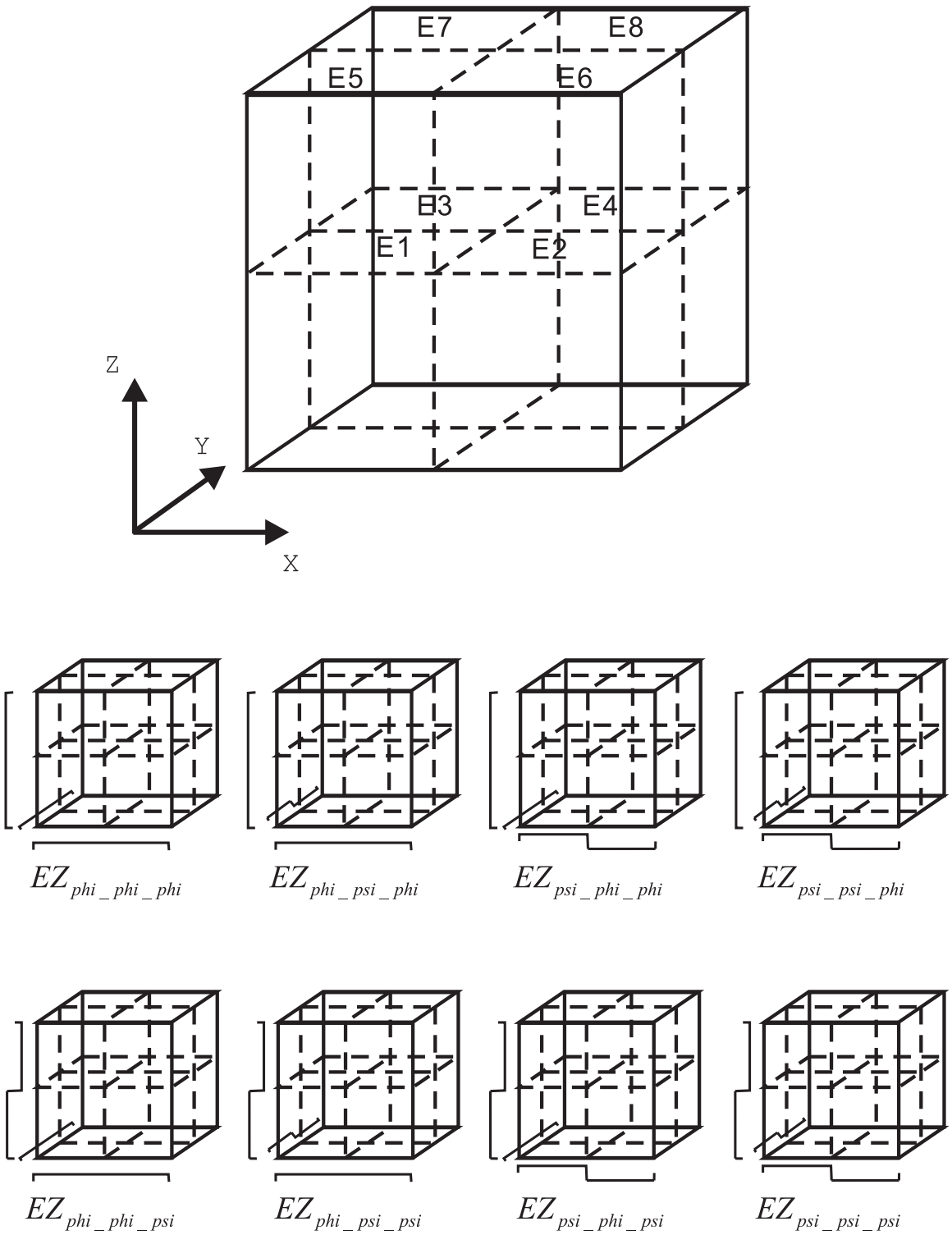

Figure 4.28: Source expansion in three-dimensional level-one Haar MRTD

to form a plane wave excitation. Since the pseudo procedure embraces the wavelet field components passively from the update functions, how these source cells are placed in the domain will not create a difficulty as all the interactions are taken care of by the update functions. A plane wave excitation in a 2D scenario is included in Fig. 4.29. The plane wave is launched along the line $SourceposX = 51$. Again the Matlab displays x-y matrix in rotated manner in the figure.

The source expansion of the illustrated plane wave follows equations 4.78 and 4.79 in their explicit forms mentioned above. However when comes to re-combination, equations 4.74 to 4.77 are replaced by the following equation. Basically, this modified configuration assigns identical source cells to the domain whenever their y coordinate equals $SourceposX$, which in turn aligns the source cells along a line. The symbol : here basically represents all values of y, which corresponds to all cells in the domain with $SourceposX$ as their x coordinates.

$$\begin{cases} E_{z_{k,SourceposX,:}}^{\phi\phi} = \frac{1}{4}(E1_k + E2_k + E3_k + E4_k) \\ E_{z_{k,SourceposX,:}}^{\psi\phi} = \frac{1}{4}(E1_k - E2_k + E3_k - E4_k) \\ E_{z_{k,SourceposX,:}}^{\phi\psi} = \frac{1}{4}(E1_k + E2_k - E3_k - E4_k) \\ E_{z_{k,SourceposX,:}}^{\psi\psi} = \frac{1}{4}(E1_k - E2_k - E3_k + E4_k) \end{cases} \tag{4.83}$$

Other geometry of source can be separately configured, using the single source cell as building blocks. Other type of excitations such as Gaussian pulses can also be easily deployed by replacing the $excitation(k)$.

4.7 Conclusions

Based on a thorough study on existing literature, 1D, 2D and 3D level-one Haar based MRTD simulators have been developed. The core parts of these numerical algorithms are depicted and explained in this chapter. The 1D code was tested using a tri-layer structure, and compared with FDTD results. An electrically large 12-shell Luneburg lens structure was studied using the 2D MRTD code, and further verified with results from reference literature. The MRTD code yields reasonably accurate and steadily stable results. The

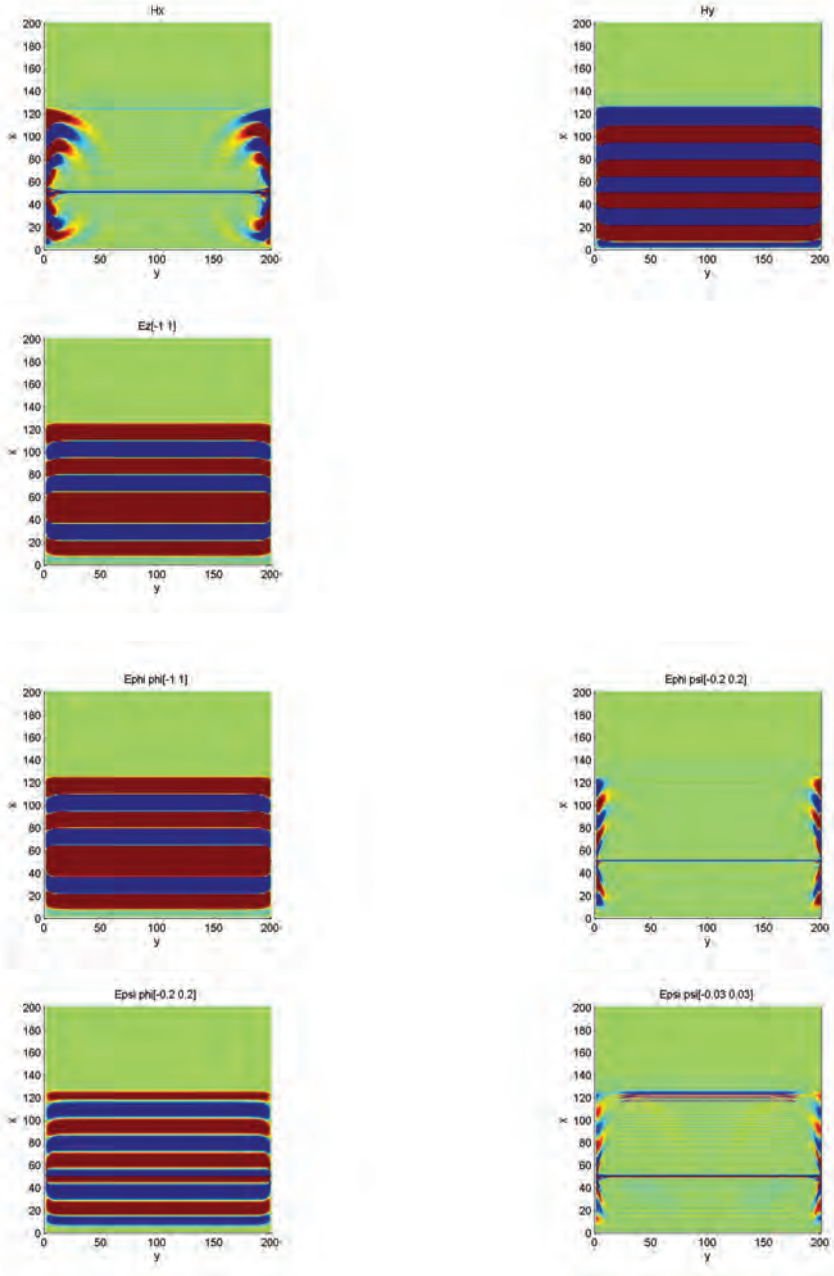

Figure 4.29: A plane wave realized in a two-dimensional level-one Haar MRTD scenario

rules to determine appropriate coefficients in 3D update functions are also included. The complete set of 3D level-one Haar MRTD update functions are reported in Appendix C.

Also in this chapter, a precise formulation of the intrinsic PML boundary condition for the level-one Haar based MRTD is presented, which can be further expanded to any level of the Haar wavelet basis functions. The proposed intrinsic PML formulation introduces even greater numerical efficiency into the MRTD algorithm. The comparison between PMLs in MRTD and FDTD confirms that the MRTD PML has higher attenuation.

A pseudo subcell source expansion scheme is developed. It utilizes the updated E wavelet components to construct several virtual E variables, which also incorporates the excitation impact. Then these virtual values are converted back to the wavelet expanded form, with new information from the excitation. By doing these, the procedure bypasses a FDTD-like difficult subcell scheme. This pseudo source expansion scheme made it easy to assign a simple excitation or even excitations with some shape of geometry.

Chapter 5

Design of Novel EBG Antennas

Recently, Electromagnetic Bandgap (EBG) structures are of growing importance in antenna designs. In this chapter, three different EBG hybrid antennas are being proposed, along with several conventional cases for comparison. At the time, they were designed with the assistance of commercial software, namely Ansoft HFSS 10.1 and CST Microwave Studio. The antennas were later manufactured and measured and the results are included in this chapter.

5.1 A multi-layer EBG antenna for multi-band operation

5.1.1 Introduction

In [27], Mosallaei et al. proposed a single band miniaturized patch antenna that is integrated on a so-called Reactive Impedance Surface (RIS). The RIS, consisting of an array of square mushrooms is used as a "perfect" reflector under a patch antenna. Notably, the dielectric substrates used for the patch antenna and the RIS are quite different in terms of dielectric constant.

In this section, a novel concept of EBG antenna inspired by the RIS configuration is proposed: Dual/multiple band antenna resonances can be achieved by stacking up

various EBG layers with different dielectric materials underneath a single patch radiator. The generalized design procedure is presented. Experimental results demonstrate good agreement with the theoretical prediction and numerical simulation.

5.1.2 Physical configuration and theoretical analysis

The proposed EBG antenna is shown in Fig.5.1. It has a patch radiator on the top, two EBG arrays embedded in the substrates underneath, and the PEC ground at the very bottom. The dielectric materials for each substrate are chosen to achieve multiple resonances with different electrical sizes. From the top layer to the bottom one, the dielectric constants are set to increase, which has led to decreased bandgap frequencies for each EBG array, corresponding to the decreased antenna resonances.

The starting point of this idea is that the EBG structure becomes "transparent" within its pass band, but behaves as a high impedance surface within its stopband. By arranging the dielectric layers and the EBG bandgap frequency in the aforementioned format, we can obtain multiple antenna resonances corresponding to each EBG bandgap frequencies.

Each EBG layer consists of a planar patch array, which forms a HIS within the band gap. The patch together with the metallic ground plane forms a conventional microstrip antenna which has the lowest resonance in the spectrum of interest. Other higher frequency resonances are obtained from the same patch radiator with various EBG layers. The patch with the working EBG surface forms a cavity with PMC ground. Currently, a probe feed is being used for a double layer antenna, with the configuration shown in Fig.5.2.

As aforementioned, the substrates used between each EBG surface are chosen to be different. The overall effective dielectric constant of a double layered substrate can be estimated using the following formulas. First of all, the overall quality factor Q_{eff} can be calculated as:

$$\frac{1}{Q_{eff}} = \frac{1}{Q_1} + \frac{1}{Q_2}, \tag{5.1}$$

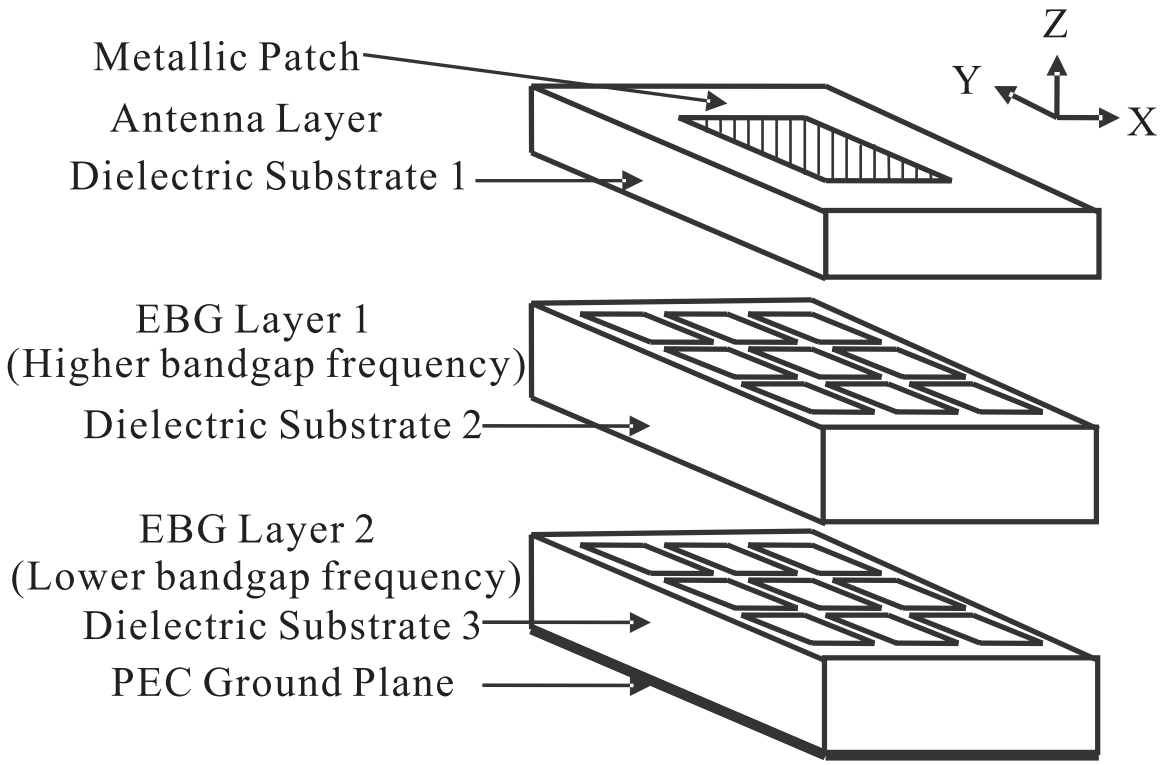

Figure 5.1: Physical configuration of a patch antenna with multi-layer EBG substrates for multiple resonances (2 layers for illustration)

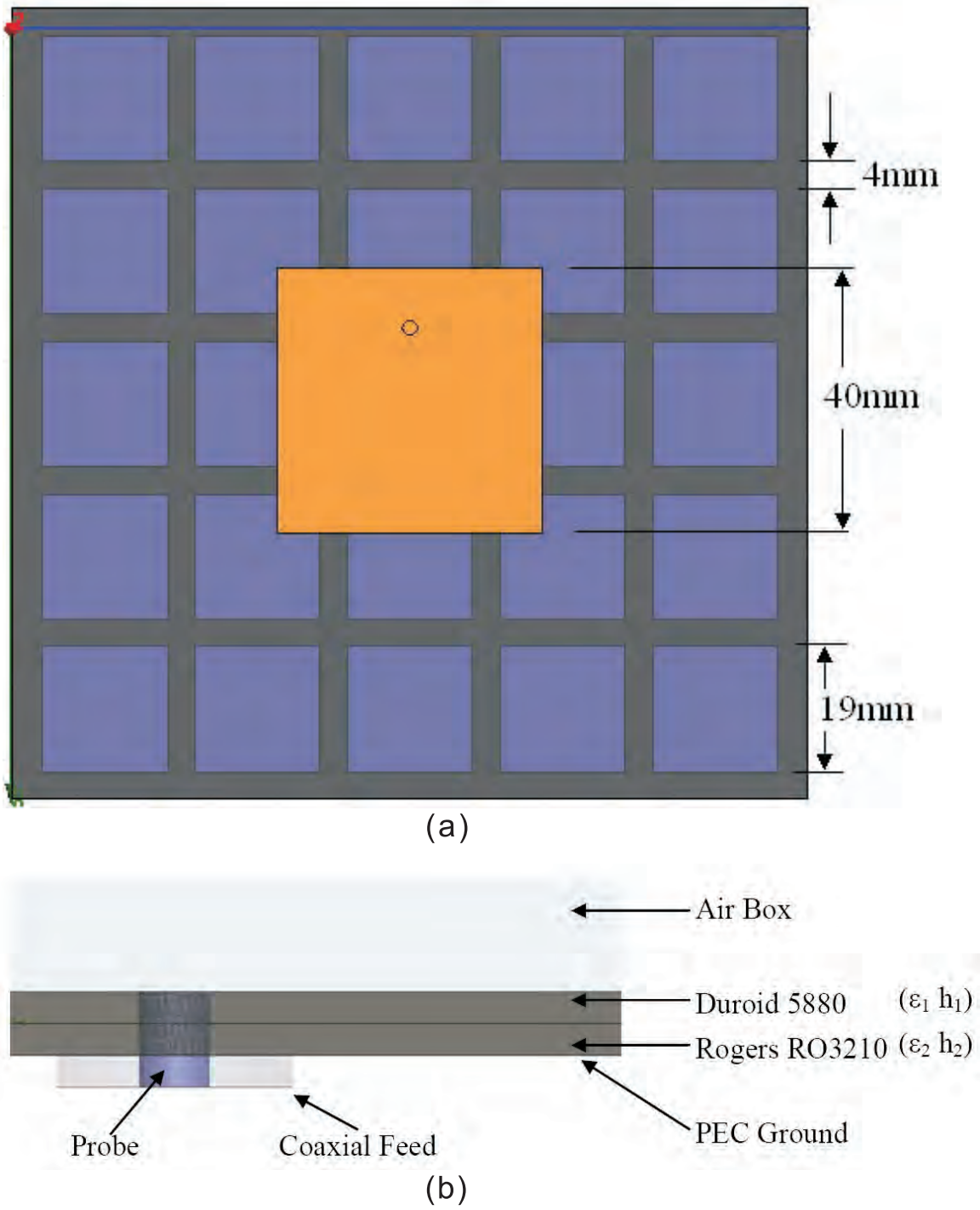

Figure 5.2: A probe fed patch antenna with a single layer of EBG (simulated) (a) top view, top layer transparent, (b) side view.

where Q_1 is the quality factor of the first dielectric substrate and Q_2 is the quality factor of the second dielectric substrate, shown in Fig.5.2(b). For the thin dielectric substrate, Q mainly consists of Q_{rad} . As for the rectangular microstrip patch case [28],

$$Q_{rad} = \frac{2\omega\epsilon_r}{h\frac{G_{rad}}{W}}\frac{L}{4} = \frac{\pi\epsilon_r fWL}{hG_{rad}}, \tag{5.2}$$

where G_{rad} is proportional to $\sqrt{\epsilon_r}$ [28]. So, Q_{rad} is proportional to $\frac{\sqrt{\epsilon_r}}{h}$. Substituting into equation 5.1, we obtain

$$\frac{h_1 + h_2}{\sqrt{\epsilon_{eff}}} = \frac{h_1}{\sqrt{\epsilon_1}} + \frac{h_2}{\sqrt{\epsilon_2}}, \tag{5.3}$$

$$\sqrt{\epsilon_{eff}} = \frac{(h_1 + h_2)\sqrt{\epsilon_1}\sqrt{\epsilon_2}}{h_1\sqrt{\epsilon_2} + h_2\sqrt{\epsilon_1}} \tag{5.4}$$

$$\epsilon_{eff} = \frac{(h_1 + h_2)^2\epsilon_1\epsilon_2}{h_1^2\epsilon_2 + 2h_1h_2\sqrt{\epsilon_1\epsilon_2} + h_2^2\epsilon_1}, \tag{5.5}$$

where h_1, h_2 are the thickness of the two dielectric substrates. ϵ_1, ϵ_2 are the corresponding dielectric constants of them. ϵ_{eff} is the overall effective dielectric constant. Note this ϵ_{eff} is different from the effective dielectric constant of a patch antenna. The proposed ϵ_{eff} is based on the consideration that the two hybrid substrates behave as one homogeneous dielectric slab.

For the proposed structure, the heights of both Duroid ($\epsilon_1 = 2.2$) and RO3210 ($\epsilon_2 = 10.2$) substrates used in the simulations are identical, $1mm$. Using the above formula, we have

$$\epsilon_{eff} = \left(\frac{2\sqrt{\epsilon_1}\sqrt{\epsilon_2}}{\sqrt{\epsilon_1} + \sqrt{\epsilon_2}}\right)^2 \approx 4.1, \tag{5.6}$$

For the manufactured case, 1.575mm thick duroid and 1.27mm thick RO3210 are used. Using the above formula, $\epsilon_{eff} \approx 3.799$.

As a result, the combined lower resonant frequency can be predicted, once the higher resonance is chosen.

$$f_2 \approx \frac{\sqrt{\epsilon_1}}{\sqrt{\epsilon_{eff}}} f_1, \tag{5.7}$$

Since the higher resonances are fixed at 2.4GHz for both the simulated and the manufactured cases, the lower resonances are predicted at 1.758GHz and 1.826GHz. Later measurements show good agreement, although the simulated resonance is 4.4% lower than predicted.

5.1.3 Numerical simulated results

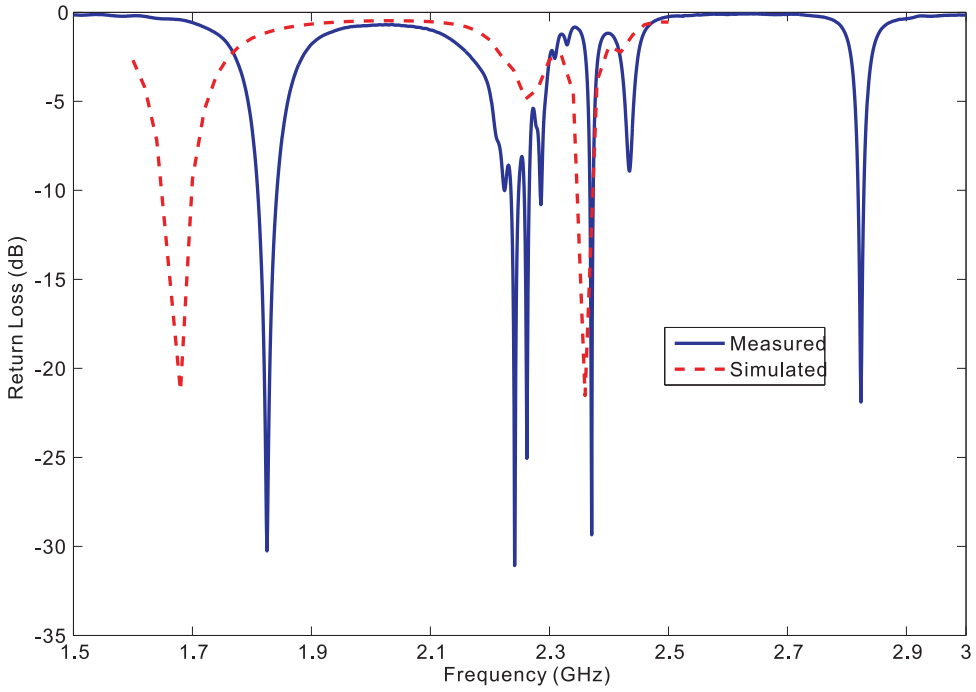

Figure 5.3: Return losses of the EBG antenna. Simulated structure: 1mm thick Duroid and 1mm thick RO3210. Manufactured Structure: 1.575mm thick Duroid and 1.27mm thick RO3210

Simulations are carried out using the Ansoft HFSS. Illustrations of the simulated structure are shown in Fig.5.2 (a) and (b). Initial simulations indicate dual band resonances at 2.36GHz and 1.68GHz, as shown in Fig.5.3. Simulated radiation patterns at

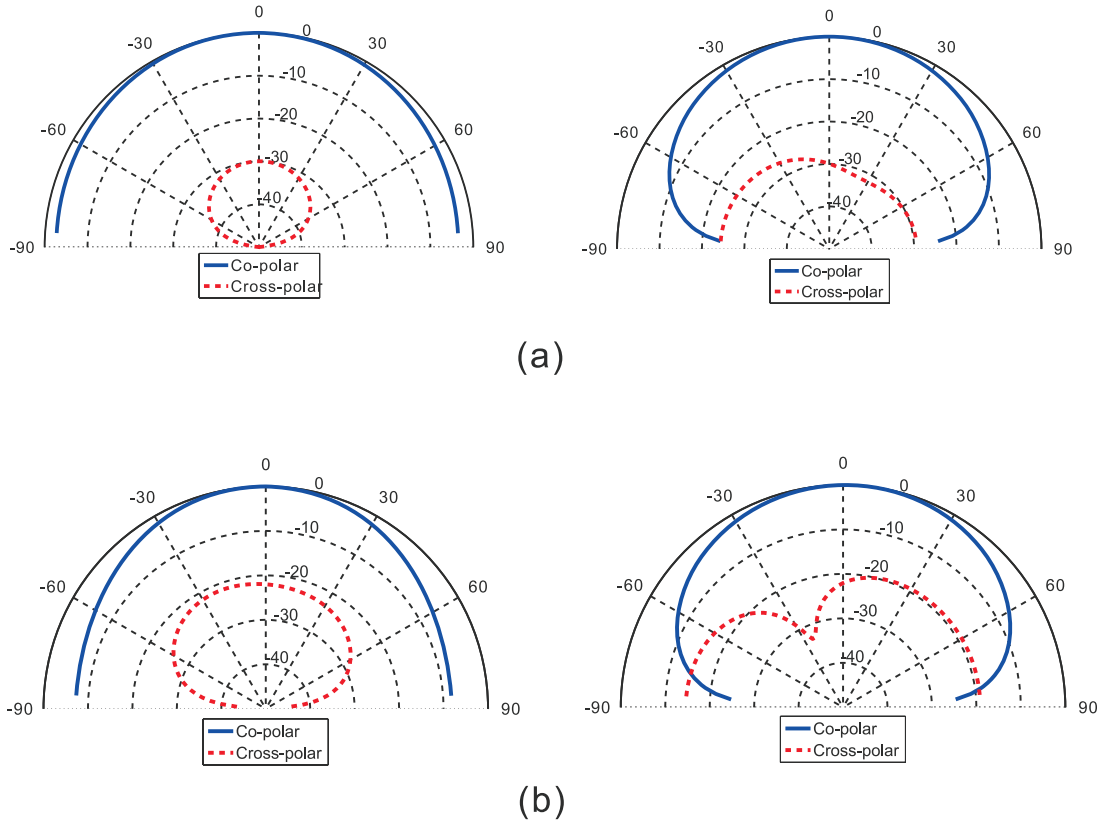

Figure 5.4: Simulated radiation pattern of the dual-band EBG antenna (a) Simulated radiation pattern at 1.68GHz (E-plane and H-plane) (b) Simulated radiation pattern at 2.36GHz (E-plane and H-plane)

both frequencies of the proposed EBG antenna remain the same as a typical microstrip patch, with above 20dB co-polar and cross-polar difference. Fig.5.4(a) shows the simulated radiation pattern at 1.68GHz. Fig.5.4(b) shows the simulated radiation pattern at 2.36GHz.

5.1.4 Measured performances of the EBG antenna

Due to commercial availability of the dielectric substrates, 1.575mm thick Duroid and 1.27mm thick RO3210 (ceramic filled) substrates are used for fabrication. The manufactured antenna is shown in Fig.5.5. The measured return loss is shown in Fig. 5.3.

The measured dual resonances are 2.37GHz and 1.82GHz, which are in close agreement with the theoretical predictions (2.4GHz and 1.826GHz, respectively). Beside the 2.37GHz and 1.82GHz predicted resonances, there are two more peaks below -10dB, around 2.24GHz and 2.82GHz. The broadside radiation at 2.24GHz is very weak. It is believed that this is due to an unwanted surface wave mode. There are always high order modes generated among various EBG layers and the ground, which may store energy inside the substrates or leak it as surface wave, hence weakening the antenna gain. This phenomenon is typical in multilayer stacked structure, but more critical with layered EBGs.

Another peak found at 2.82GHz is believed due to parasitic coupling between the radiating patch and the EBG elements. From the plotted current flow in the simulation, it's also found that the probe feed has strong coupling with the EBG elements. It's interesting to notice that within the 2.82GHz band, the antenna is radiating well at broadside. Fig. 5.6(a) and (b) show the measured radiation patterns at 1.82GHz and 2.37 GHz, respectively.

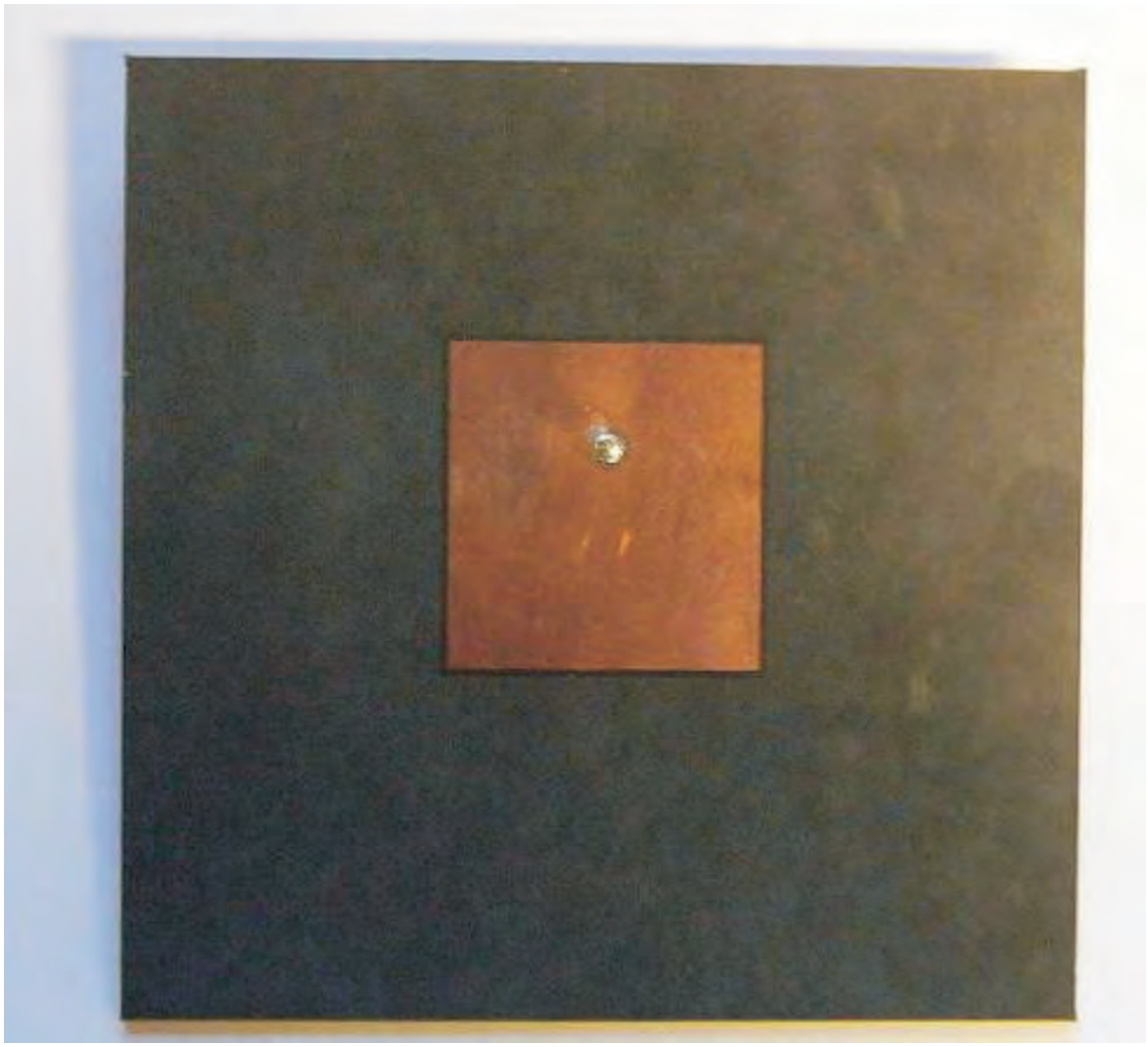

(a)

(b)

Figure 5.5: A probe fed patch antenna with a single layer of EBG (manufactured) (a) top view (b) side view

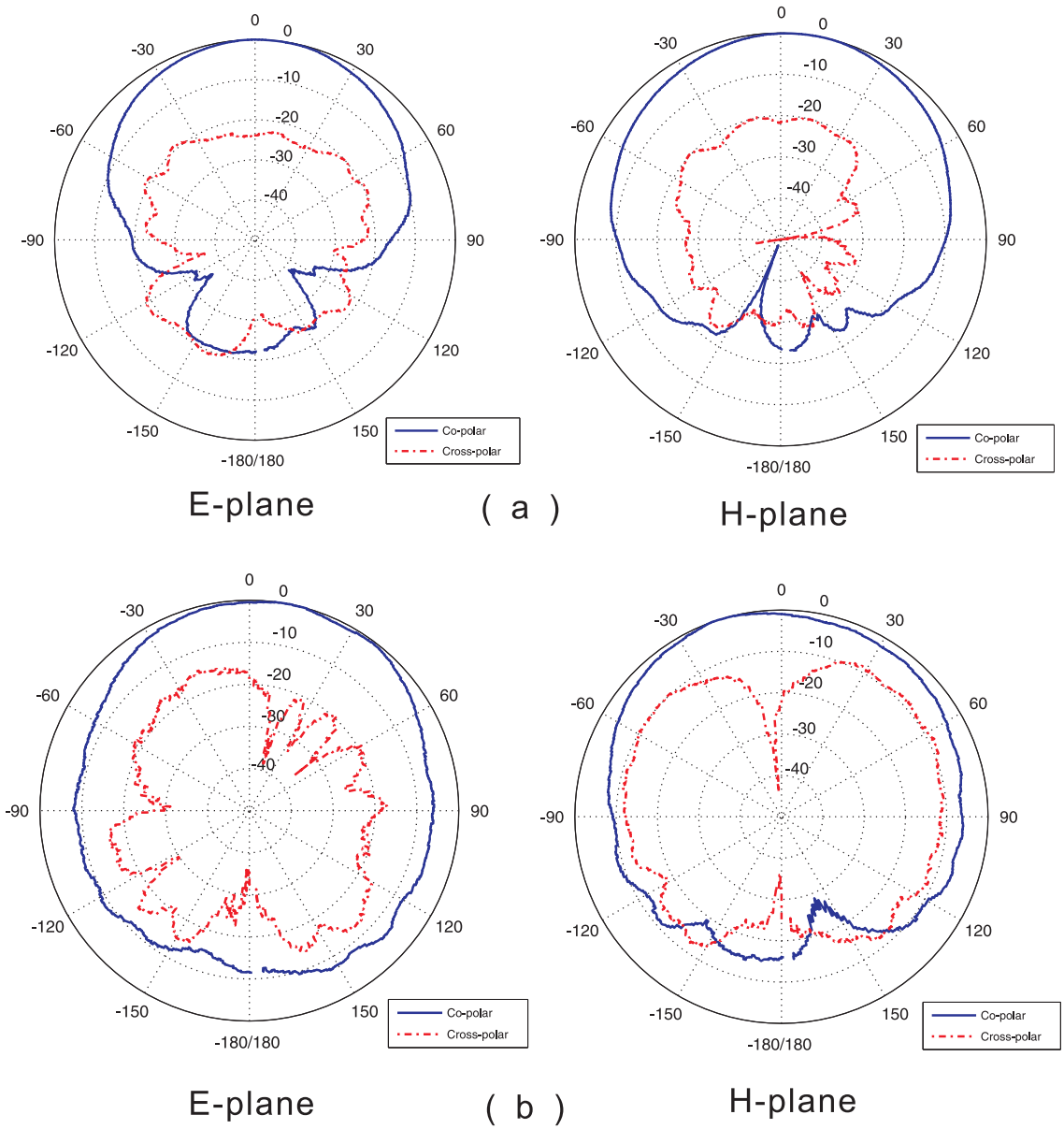

Figure 5.6: Measured radiation pattern of the dual-band EBG antenna (a)Measured radiation pattern at 1.82GHz (E-plane and H-plane) (b)Measured radiation pattern at 2.37GHz (E-plane and H-plane)

5.2 The proposed EBG photonic antennas

5.2.1 Background information

Distribution of multiple wireless services including GSM/UMTS, TETRA and WLAN via installed fibers in buildings has become a commercial reality because of the broadband, low-loss and modulation format independent features that the radio-over-fiber technique offers. Distributing multiple services over fibers also centralizes the management of telecom and network equipments. Das et al [61] and Crisp et al [62] demonstrated the transmissions of IEEE 802.11b and 802.11g data over fiber in the 2.4 GHz band using discrete, conventional and commercially available lasers, photodetectors and microwave antennas.

Photonic antennas find applications in such indoor and in-building scenarios by acting as the interface between the installed fibre infrastructure and the wireless users. The cost of manufacturing a photonic antenna can potentially be reduced further if they are integrated directly with a dual-function Asymmetric Fabry-Perot Modulator (AFPM) device, which performs both the optical-electrical and electrical-optical conversions in a single device.

The AFPM device is designed by colleagues in University College London in a joint EPSRC project and is shown in Fig. 5.7. The unmodulated input light was beamed through fibers vertically onto the AFPM. By modulating the electric field inside the multiple-quantum-well (MQW) cavity, the intensity of the reflected light will also be modulated due to the quantum-confined stark effect (QCSE). Because the light is absorbed and electron-hole pairs are generated within the MQW region as a result, the AFPM device also conveniently doubles as a photon detector. Since the incident light falls upon the AFPM vertically, the electric field of the light is always in the plane of the MQW region and therefore is optically polarization insensitive. The AFPM performs both optical intensity modulation and photon detection in a single device, making it a simple electrical/optical transducer. An illustration of the MQW cavity is shown in Fig. 5.8.

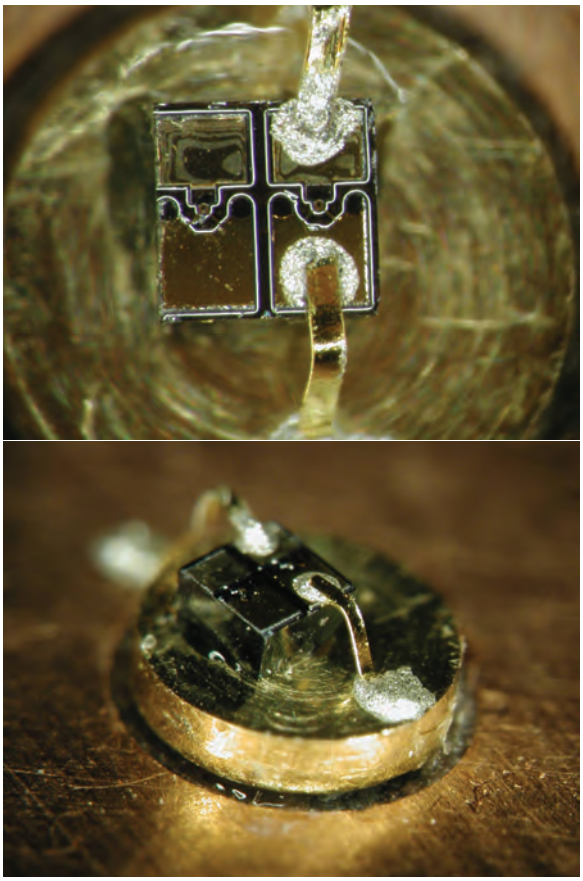

Figure 5.7: The mounted AFPM device, top view and side view

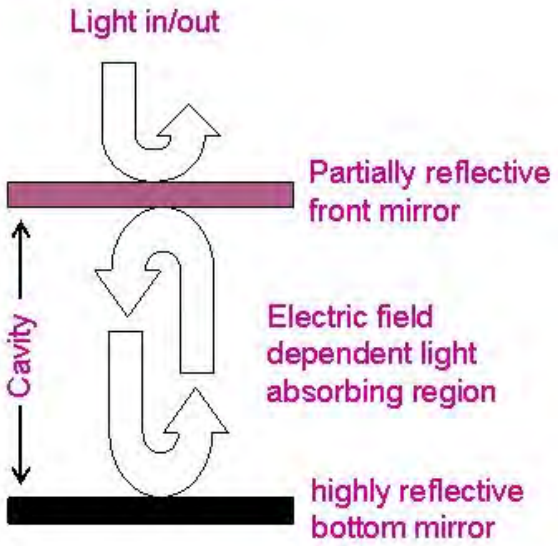

Figure 5.8: A brief illustration of multiple-quantum-well (MQW) cavity

Several critical requirements are imposed for the antenna design, hence the corresponding solutions:

1) A solid ground plane is required for the AFPM device to be mounted upon. It would also make the optical fibre attached to the AFPM more stable in alignment. The AFPM will sit on the ground plane and be connected to the antenna feeding point using a metallic pin. Based on the requirements, a planar patch antenna becomes the chosen type of host. The metallic surface on the back of the planar dielectric substrate serves as a ground plane.

2) The antenna should be designed at 100Ω at 5.2GHz in order to match to the input/output impedance of the AFPM device. A 100Ω antenna enables better return loss from an AFPM perspective, thus providing better system integration performance. The impedance matching is done by adjusting the probe feeding position on the patch.

3) A DC biasing network has to be attached to the antenna to provide a DC voltage to operate the AFPM. There will also be physical connections, which would inevitably bring in radiation disruption. In order to minimize the radiation disruption caused by this irregularity, the DC feed line has to be optimized to be very narrow and end with a radial stub. By properly tuning the width and length of the feed line and the shape of the stub, the impedance of the DC biasing at 5.2GHz can be adjusted to be very high, which in turn reduces the current induced.

4) The antenna should have a -10dB bandwidth of more than 500MHz centered at 5.2GHz. Also to accommodate the aimed 802.11a standard, the antenna is expected to handle a circular polarized electromagnetic field. For the single element antenna, a minimum 3dBi gain is required. For the array antenna, a minimum 10dBi gain at broadside is expected.

These solutions enabled the concept of AFPM integrated photonic antenna. The general integration layout of a photonic antenna is shown in Fig 5.9.

Critical to the integration of the photonic antenna are advanced packaging techniques, supplied by an external collaborator, the Millimetre Wave Technology Group at the Rutherford Appleton Laboratory.

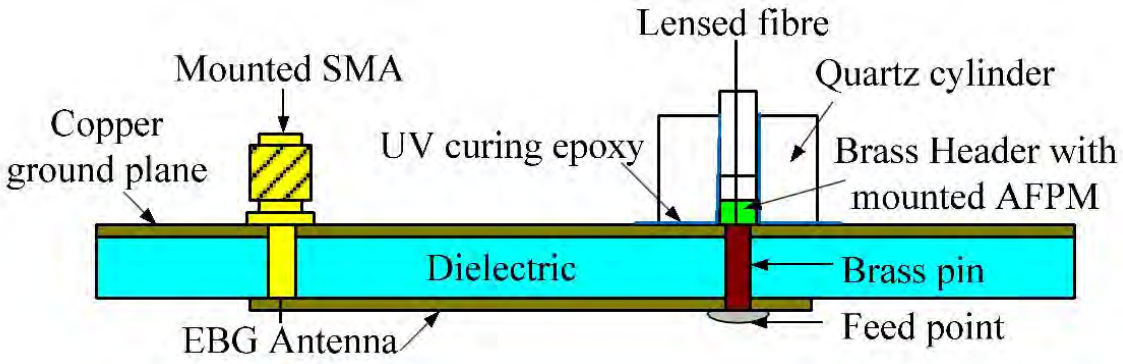

Figure 5.9: The Photonic Antenna with mounted fiber and AFPM device

Overall, the main objective of this study is to develop several compact photonic antennas at 5.2GHz to host the AFPM. A single element patch and a 2×2 patch array are to be designed. Then EBG enhancement will be incorporated, while keeping the radiator part identical. The EBG enhanced single and array antennas will be compared to the conventional items to reveal their achievements.

5.2.2 The EBG single element antennas

There are many antenna applications that utilize the EBG structures' stopband features, which prohibit wave propagation at bandgap frequencies. Sievenpiper published an embedded patch idea [9]. An embedded patch antenna surrounded by a "mushroom" EBG structure can take advantage of surface wave suppression. The antenna had better radiation patterns at broadside and exhibited significantly lower backward radiation. Alternative approaches to the "mushroom" type EBG elements, which further develops this idea by employing EBG elements of other shapes, include fractals without metallic grounding vias [22] and convoluted spirals [64].

In this section, an array of Split Ring Resonators (SRRs) is proposed to encircle a circular polarized patch antenna to tackle the harmful backward radiation as well as to boost the broadside gain. The SRR can be considered as a planar EBG structure, with the bandgap frequencies coincident with the antenna resonance. The performance of both conventional and EBG antennas are simulated and measured for comparison.

A conventional circular polarized rectangular patch antenna, resonating at 5.2GHz, is designed and fabricated. The simulated structure with dimensions is shown in Fig. 5.10. Fig. 5.14 (a) shows the photograph of the fabricated antenna. The patch size is 14.1 mm by 15.9 mm and it is supported by a 3.08mm thick Rogers Duroid 6002 ($\varepsilon_r = 2.94, \tan\sigma = 0.0012$) substrate.

The antenna's input impedance is chosen to be 100Ω in order to match the input/output impedance of the AFPM. This is in contrast to the conventional 50Ω impedance matching. The feed point is at about one third on the diagonal of the square patch, to enable circular polarization. The AFPM is mounted on the rear ground plane and is connected to the patch using a solid metallic via, which is shown in Fig. 5.14 (c). A 0.2mm wide microstrip line ($Z_0 = 200\Omega$) with a terminating radial stub extends from the patch. This line enables the application of a DC bias voltage to the AFPM device also the monitoring of the photocurrent. By fine tuning the length of this line and the shape of the radial stub, the input impedance at 5.2GHz from the patch edge towards the line is set to be very high, which reduces spurious current. The simulated performance of a single conventional antenna is presented in Fig. 5.11. From simulation, the single element conventional antenna has a bandwidth of more than 500MHz, from 5.0GHz to 5.5GHz. The broadside gain is estimated to be more than 5dBi. This is relatively large for a single element patch antenna, mainly due to the large ($75mm \times 100mm$) substrate and ground plane underneath.

The EBG enhanced antenna is identical to the conventional one in terms of ground plane and radiator sizes, except that it incorporates an array of SRR around the patch. The simulated scenario with size details is shown in Fig. 5.12, while the fabricated sample is shown in Fig.5.14 (b). The SRR EBG structure is used to reduce the backward radiation. Four rows of SRRs are placed surrounding the antenna, while a gap is reserved for the DC biasing line. The four radius of the SRR ring is designed to be 1.5mm, 1.9mm, 2.3mm and 2.7mm, which enables a line width of 0.4mm also a gap width of 0.4mm. The thinnest gap between the SRR array is about 0.21mm, which requires an elaborate manufacturing technique. The distance between the radiating patch and the SRRs is also optimized to minimize unwanted coupling. The simulated performance of single EBG antenna is presented in Fig. 5.13. The EBG antenna has a bandwidth of more than 500MHz, covering

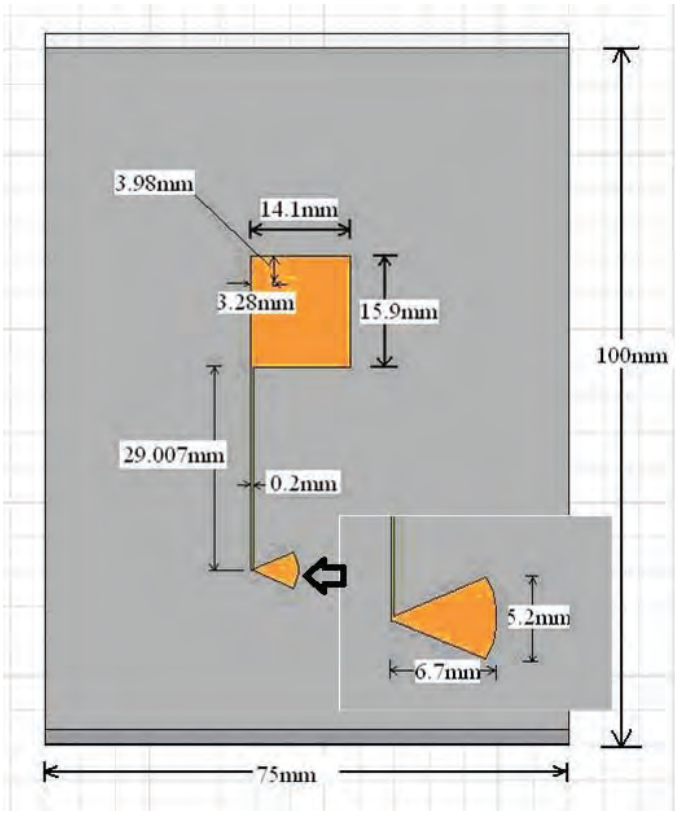

Figure 5.10: Simulated single conventional antenna with size details

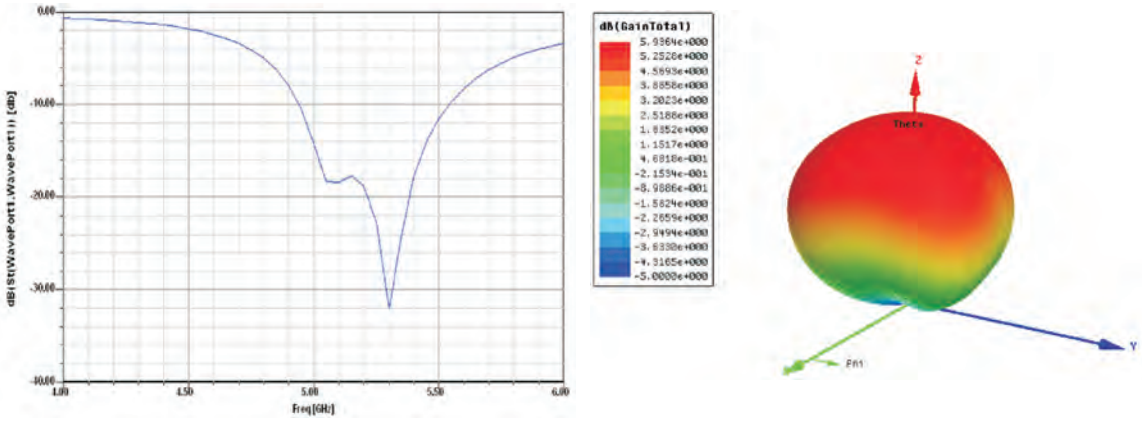

Figure 5.11: Simulated performance of single conventional antenna (a) Return loss (b) 3D gain pattern at 5.2GHz

from 4.95GHz to 5.45GHz. More than 6dBi gain is predicted at broadside at 5.2GHz.

Due to the limit of the equipments, the return losses of the antennas are measured in a 50Ω environment, and are then re-normalized to 100Ω to estimate performance with integrated AFPM devices. Fig. 5.15(a) shows that both antennas have bandwidths of about 1.5 GHz between the -10dB points, 5.0 and 6.5 GHz. Fig. 5.15(b) indicates that the measured radiation pattern of the EBG antenna at broadside is improved by 2 dB, whilst the backward radiation is suppressed by more than 5 dB between the angles of -135° to -90°. The SRR reflect the incident wave in an in-phase manner at the bandgap frequencies. At the other side of the antenna, for angles from $+90^\circ$ to $+135^\circ$, radiation levels remain similar to that of the conventional antenna. Obviously, this is due to the biasing line and stub which is located within the defect of the SRR structure, since the patterns are measured linearly along the vertical axis of the antennas shown in Fig. 5.14.

Finally, the system link loss is measured for both conventional and EBG antennas with optical links. The integrated AFPM are used as modulators of reflected optical radiation, i.e. as receivers at 5.2GHz. The transmitter is a conventional microwave patch antenna, driven at a power of 10dBm, at a distance of 1.5 meter apart from the receiver. The bi-directional measurement set-up is illustrated in Fig. 5.16, although only downlink is used. The conventional and EBG antenna are tested separately and then compared. The measured link losses as functions of frequency are shown in Fig. 5.18. A typical 5dB decrease in link loss (i.e. 5dB higher in S_{21}) between 4.7 and 5.3 GHz was found for the EBG antenna. Only less than 2dB of this enhancement can be attributed to the EBG structure. The remainder comes from the better optical alignment achieved between fibre and AFPM mounted on this antenna. In other words, the amended packaging technique of the AFPM device makes most of improvement in link loss. At this stage, it is difficult to produce two identical AFPM integrated antennas, since the mounting process is very much manual. The 0.1 volts difference in the biasing circuits made almost no difference in the AFPMs' operation.

The SRR structure also provides some higher order harmonic suppression, at 10.4GHz in this case. The EBG antenna exhibits a 5dB higher link loss from 10.4GHz to 11.6GHz

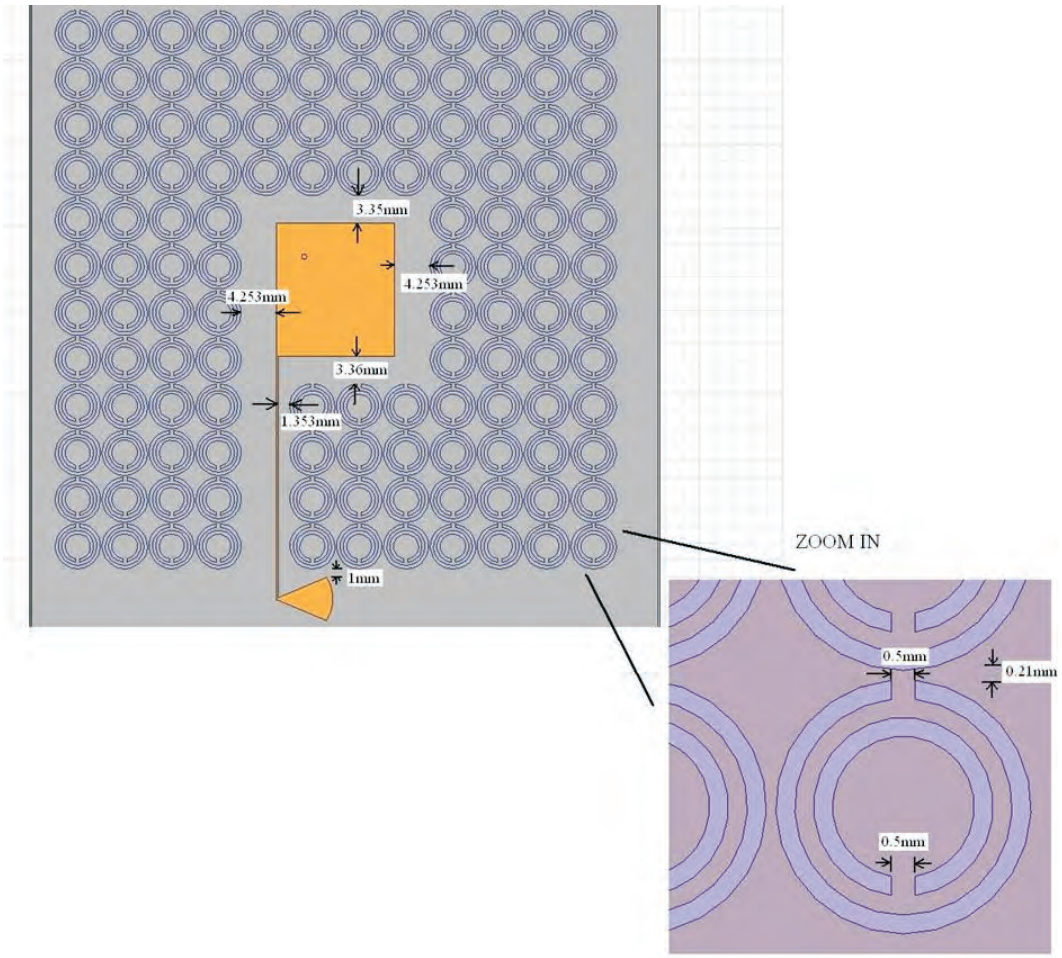

Figure 5.12: Simulated EBG single element antenna with size details

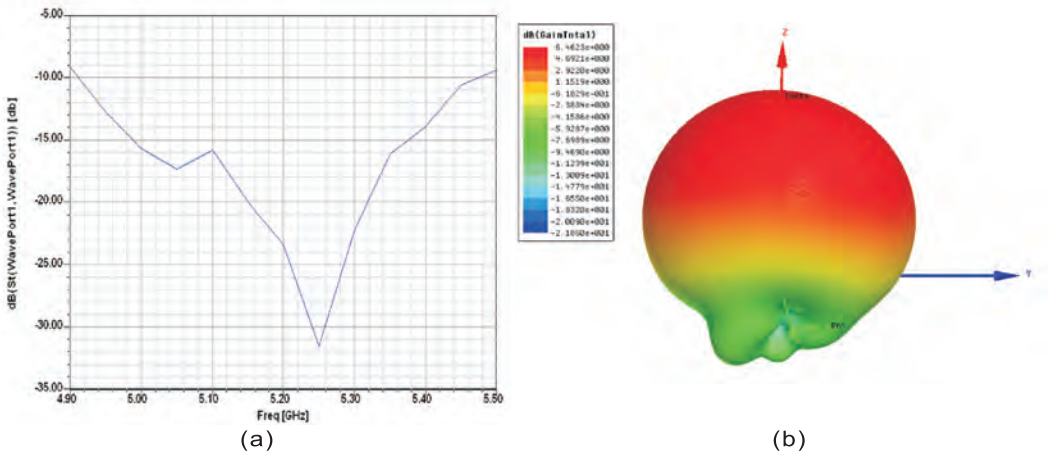

(a) (b)

Figure 5.13: Simulated performance of single EBG antenna (a) Return loss (b) 3D gain pattern at 5.2GHz

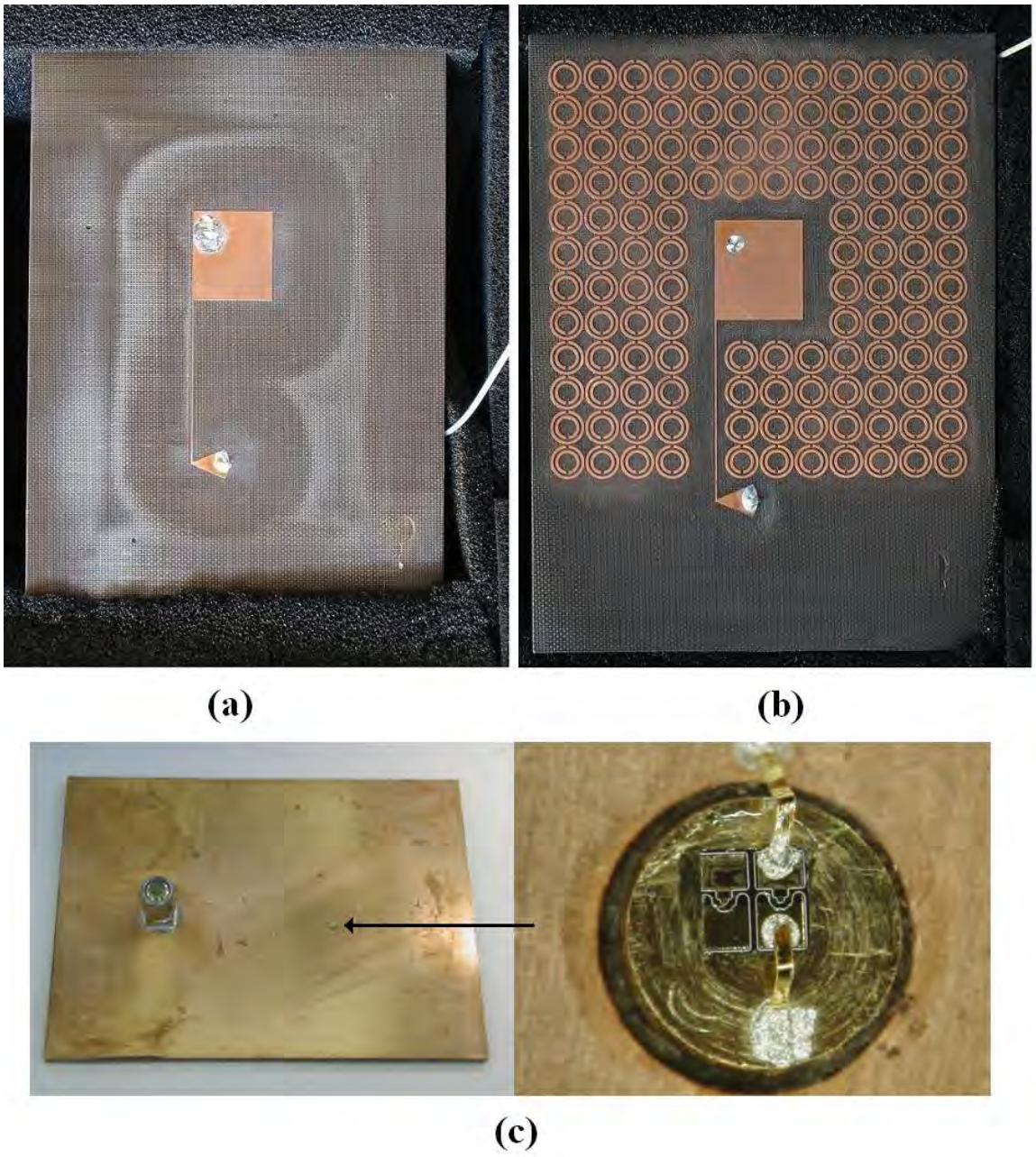

Figure 5.14: Patch antennas: (a) Conventional and (b) EBG. The rear of the antenna has (c) a SMA bias port and an AFPM device mounted on the ground plane.

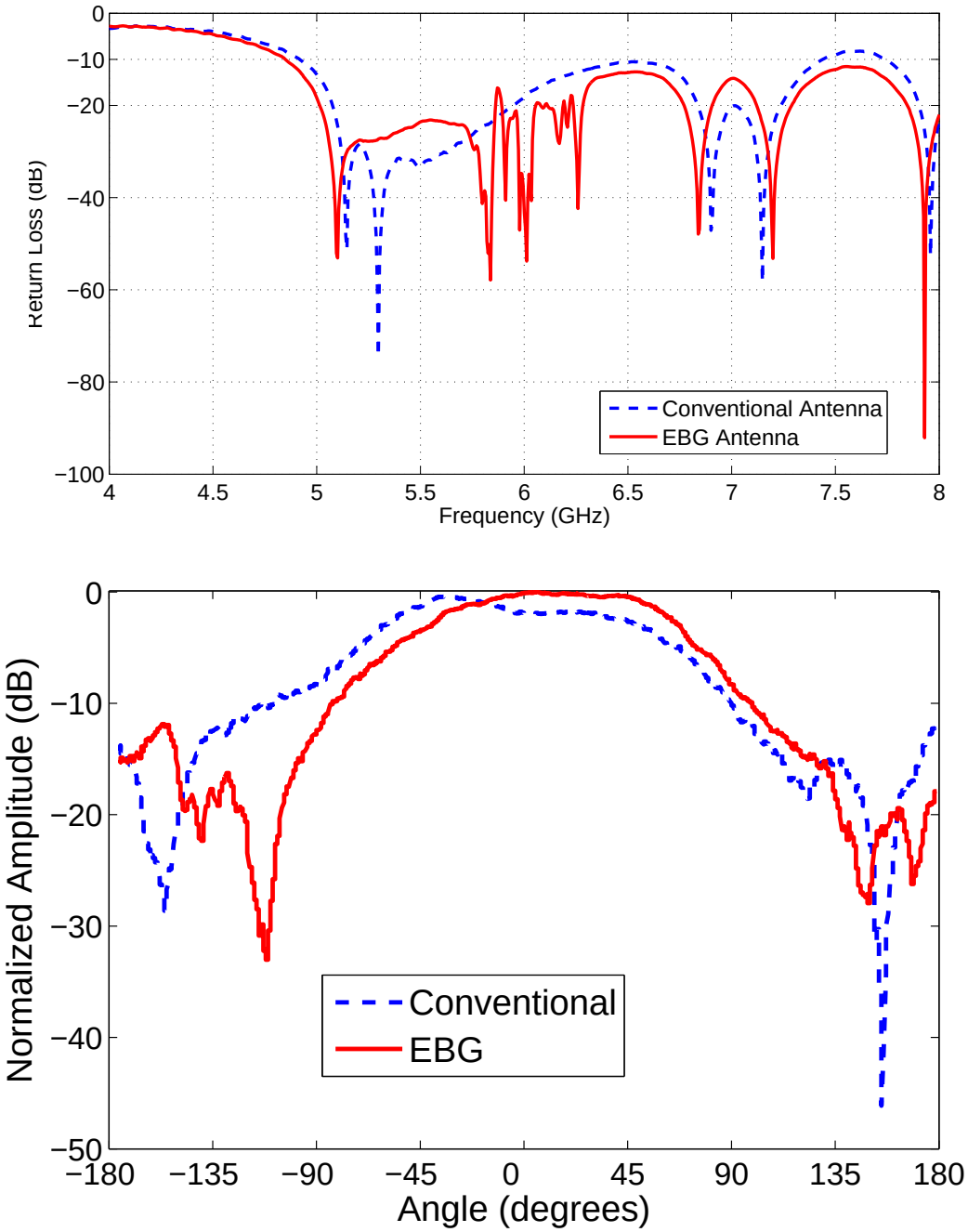

Figure 5.15: Measured performances of the conventional and EBG enhanced patch antennas: (a) Return Loss normalized to 100Ω and (b) Normalized Radiation Pattern. The maximum EBG antenna radiation sets the scale.

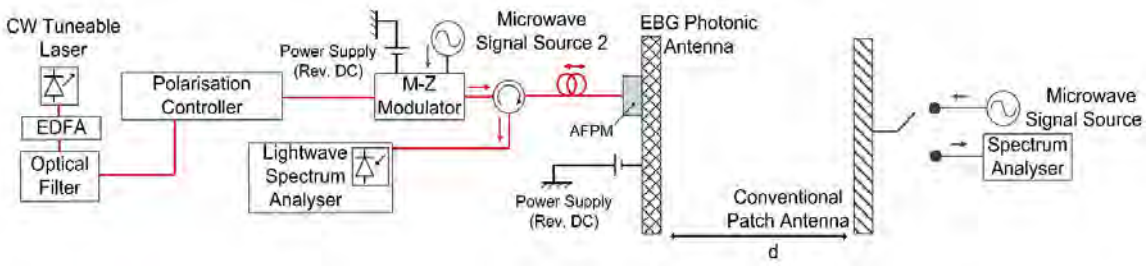

Figure 5.16: The Bi-directional Experiment Setup

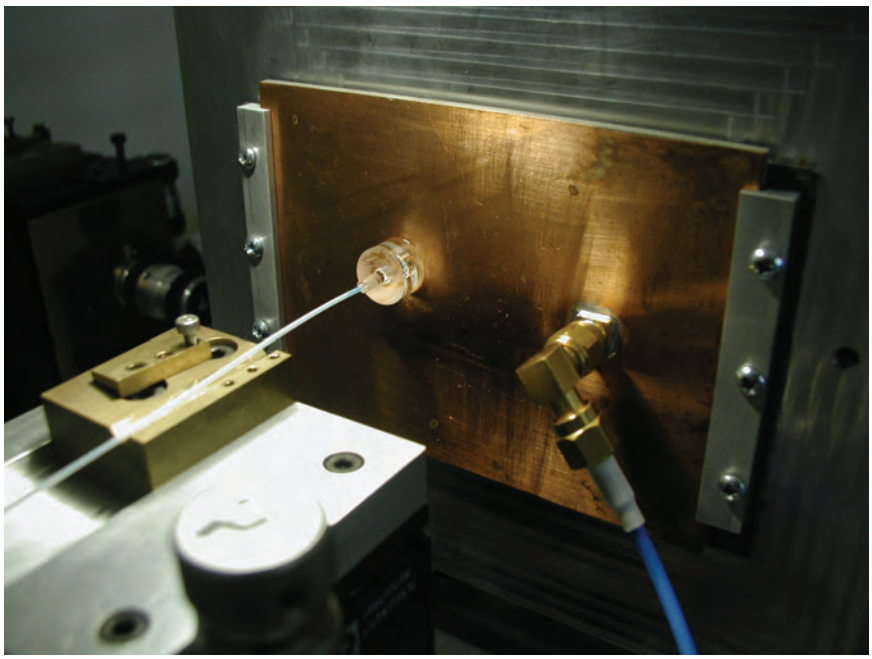

Figure 5.17: AFPM, optical fibre and biasing cable mounted on a single element antenna, with holding frame (back view)

than the conventional patch in Fig. 5.19. This is due to a change in impedance matching conditions at the second harmonic frequency because of the insertion of the EBG structure. The overall aperture of the patch and surrounding SRR's becomes larger when excited at frequencies other than the fundamental bandgap range. This inevitably worsens the impedance matching of the antenna at the harmonic frequency, which is good from a system integration point of view. The lower the level of harmonics, the less the noise received at the AFPM device.

Note that the experimental set-up in higher order harmonic link loss is different from the conditions generating Fig. 5.18, therefore they are not directly comparable in terms

of the link loss numeric values. The harmonic experiment is carried out with pure microwave antennas, both conventional and EBG, without AFPM devices.

5.2.3 The EBG array antenna

Generally, array antennas possess great advantages over single element ones in terms of increased directivity/gain, controllable beam etc., while having inevitably greater design difficulty. A typical n-element planar array antenna is shown in Fig. 5.20. One critical measure of antenna array is to maintain the high isolation between inputs, which is affected mainly by mutual coupling between radiating elements. If the radiators are placed far away, the mutual coupling will decrease but the grating lobes shall emerge. An illustration of grating lobes in radiation pattern is demonstrated in Fig. 5.21. It harms the performance of the array by dispensing radiation towards unwanted direction. Recently, the utilization of EBG structure upon planar array antennas demonstrated its potential advantage over conventional means to solve the dilemma. That is to bring down the mutual coupling level while keeping the radiating elements relatively close.

In [10], Fan Yang *et al.* reported that mushroom EBG structure can be used to reduce the mutual coupling in linear polarized patch antenna array, when placed between the antenna elements. Hirata further expands the idea to block surface wave in a two-by-two linear polarized patch array in [20]. In [65], Yang *et al.* used spiral EBG elements to tackle the mutual coupling between linear polarized array elements. In this section, a circular polarized two-by-two patch array is designed and manufactured with the enhancement of spiral EBG elements. The design procedure of the EBG elements is described, as well as the simulated and measured antenna performance. A mutual coupling comparison is made between the conventional and EBG enhanced antennas. The overall isolation improvement is no less than $5dB$.

A conventional 2×2 array antenna is firstly designed to accommodate four individual AFPM transducers as the input sources. Again, the input impedance of each of the four input ports is designed at 100Ω, to match the characteristic impedance of the AFPM. A DC biasing network (microstrip lines and radial stubs) is attached to each and every

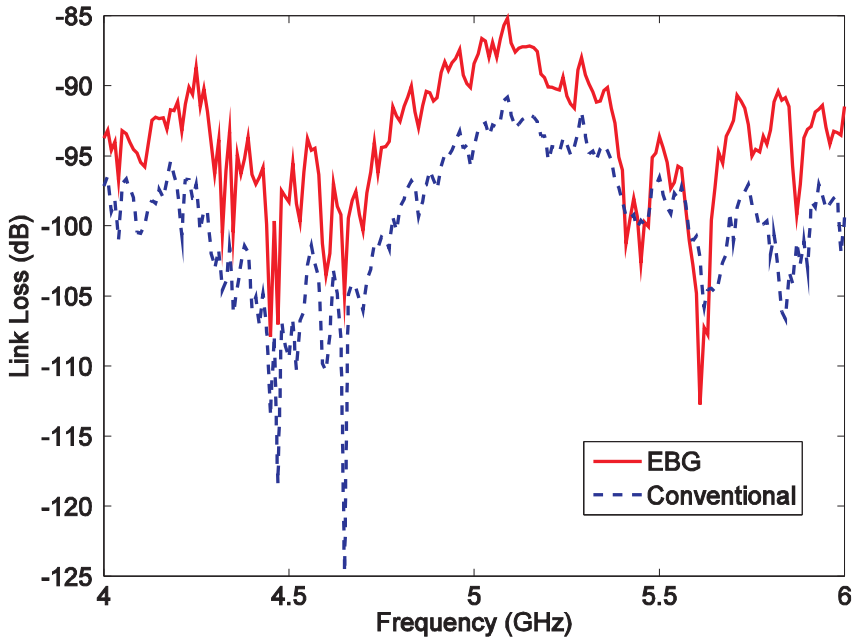

Figure 5.18: Measured system link loss performance with AFPM used as a receiver with 3 dBm of incident optical power at a wavelength of 1550 nm and an applied bias of 3.25 ± 0.05V.

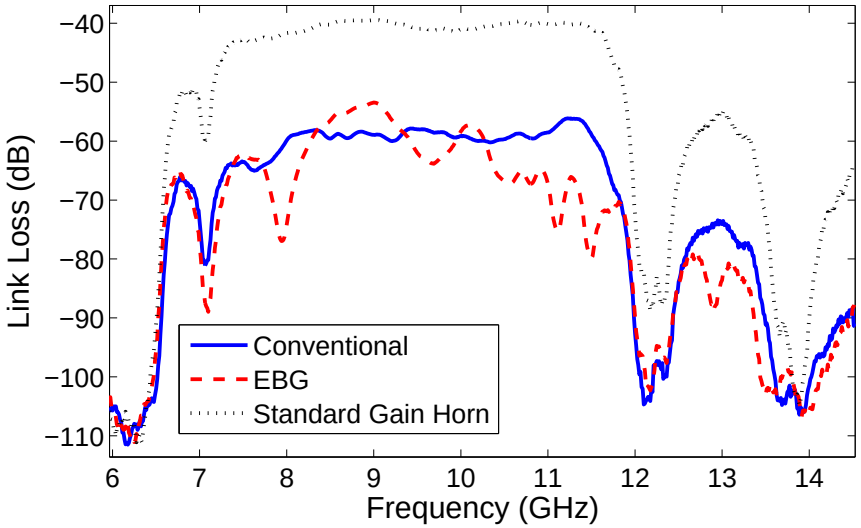

Figure 5.19: Microwave link loss at frequencies above the design range. The transmitter was a feedhorn: the plot compares a standard gain feedhorn with the conventional and EBG enhanced patch antennas.

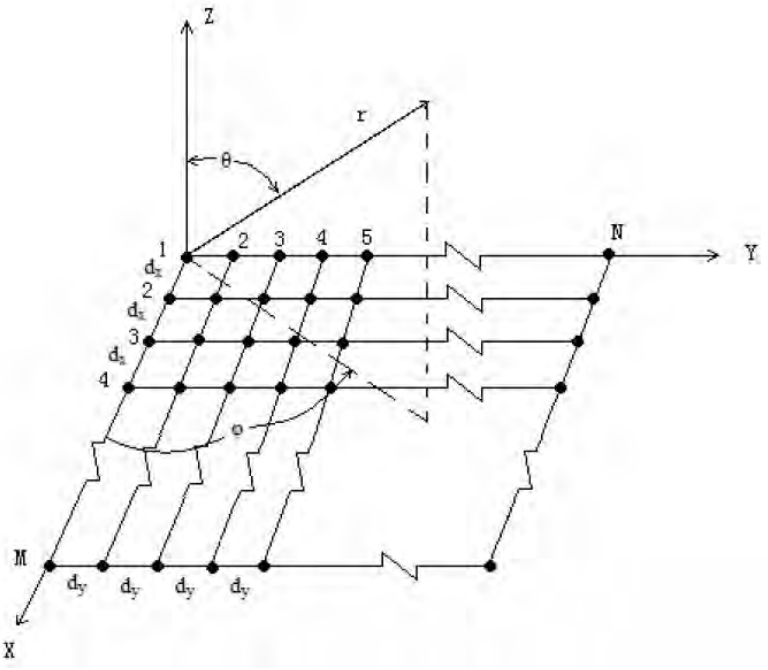

Figure 5.20: A typical n-element planar array antenna

patch radiator to provide DC voltage to operate the AFPM. This biasing network might introduce complicated coupling situation, especially under circular polarized field. This complication is dealt later with introduction of spiral EBG elements.

In order to prevent grating lobes, the spacing between radiating patches is fixed at 30mm, around half wavelength at 5.2GHz in free space. The simulated conventional 2×2 array with size details is shown in Fig. 5.22. The array is manufactured on a 3.08mm thick duroid 6002 substrate board ($\varepsilon_r = 2.94, \tan\sigma = 0.0012$), which can be seen in Fig. 5.23. Comparing to the single element antenna, the array provides larger broadside gain to boost the microwave signal, which is critical for the system integration.

A spiral shaped EBG element (Fig. 5.24) is selected to enhance the performance of the proposed antenna array, due to the compactness of the spiral structure over others such as the mushroom structure. A 55% size reduction is reported in [64]. A size comparison between various spiral EBG elements is listed in Fig. 5.25. In Fig. 5.25, spiral EBGs with same periodicity as the mushrooms lead to about 60% reduction in bandgap center frequency. That translates to "When designed to operate at the same bandgap center

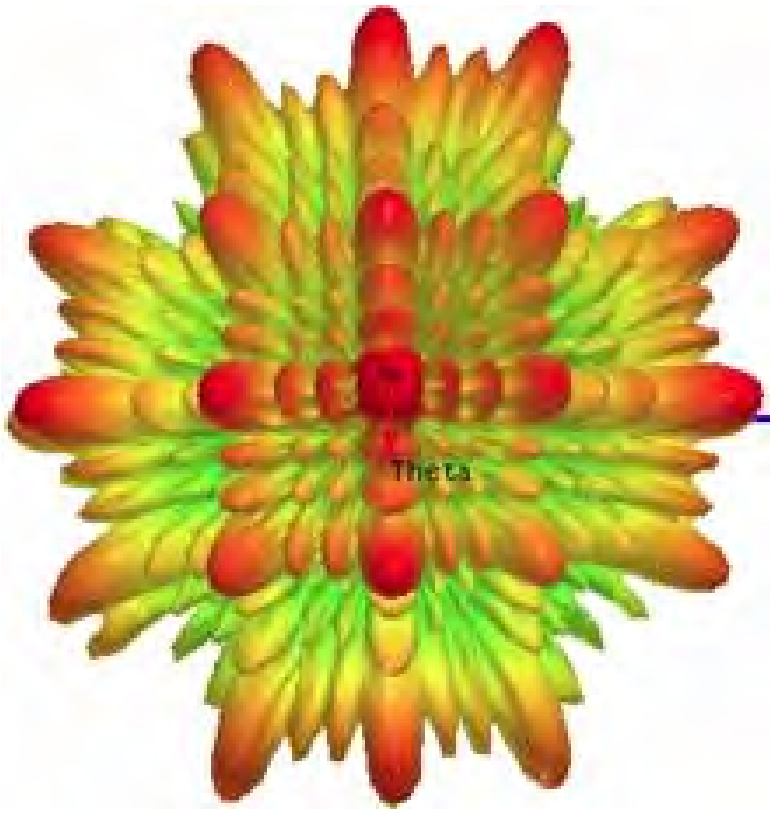

Figure 5.21: Grating lobes in radiation pattern, due to large distance between radiating elements

frequency, the spiral EBGs can have much smaller periodicity or element size". Spiral EBG elements tackles the circular polarized field by the curved arms. As a side effect, the bandgap bandwidth of the spiral EBG is significantly narrowed when comparing with traditional mushroom structure.

A unit-cell based parametric study on the width of the spiral arm, the gap between arms and the center block size is carried out to create the spiral with bandgap around 5.2GHz. Since the unit-cell approach has been introduced in previous chapter, the detail is omitted here. Fine tuning of the spiral shape is achieved by simulating a scenario with 2 rows of spiral EBGs placed between 2 patch radiators. As shown in Fig. 5.24, the best cell size "a" is determined to be 3.75mm, the gap between arms "g" to be 0.35mm, the arm width "s" to be 0.3mm and the center width "2w" to be 1.05mm. This spiral has a relative EBG bandgap bandwidth of 3.1% at 5.24GHz, which basically means a stopband of 16MHz. It's a tradeoff that spirals offer compact size but smaller bandgap. However,

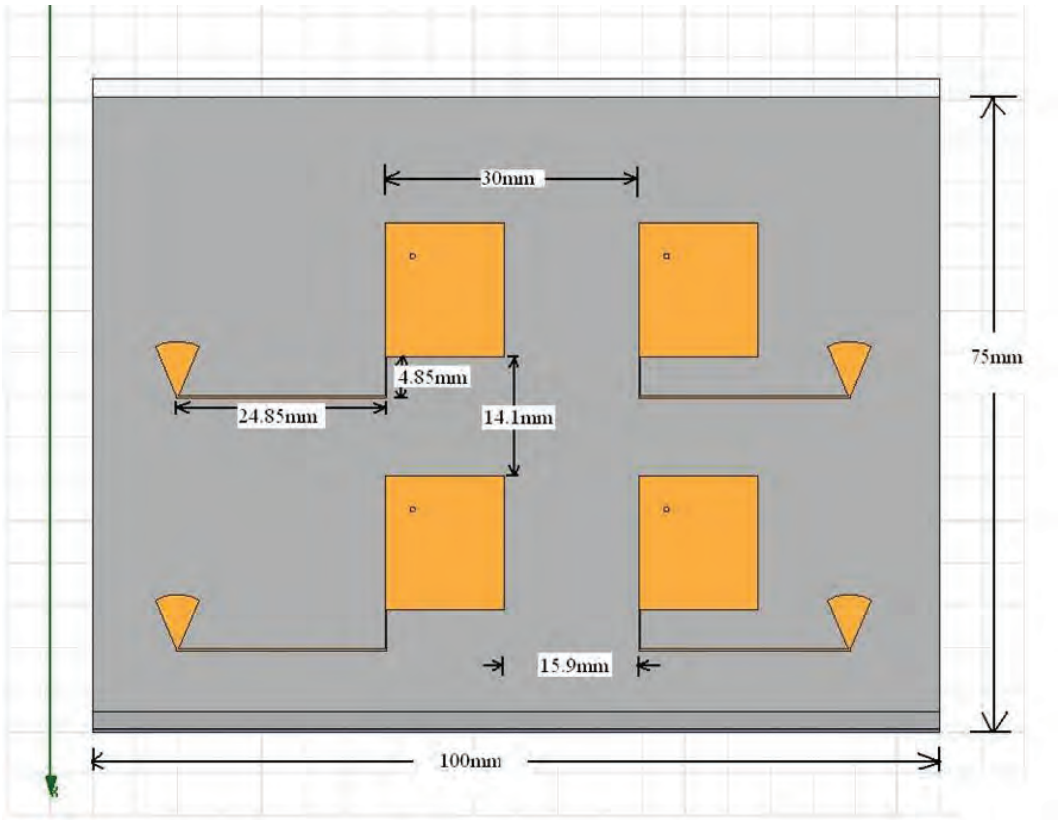

Figure 5.22: The simulated conventional 2×2 array with size details

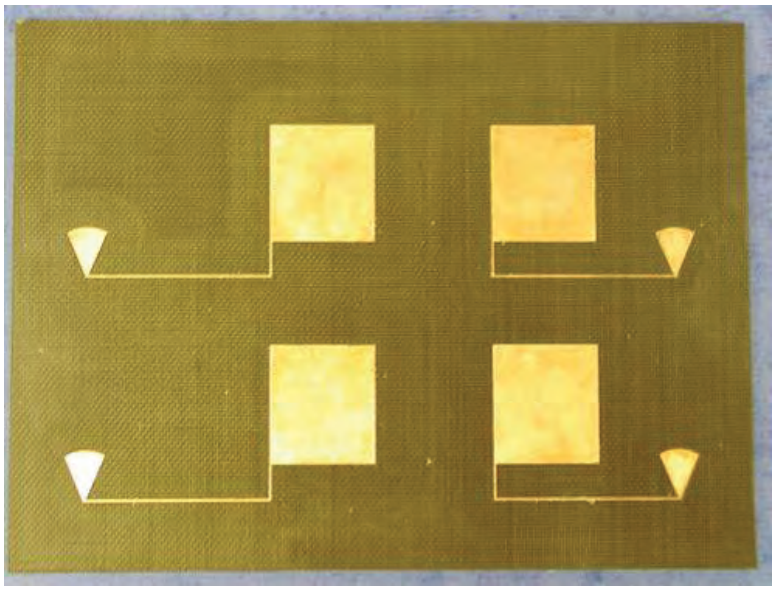

Figure 5.23: The manufactured conventional 2×2 array

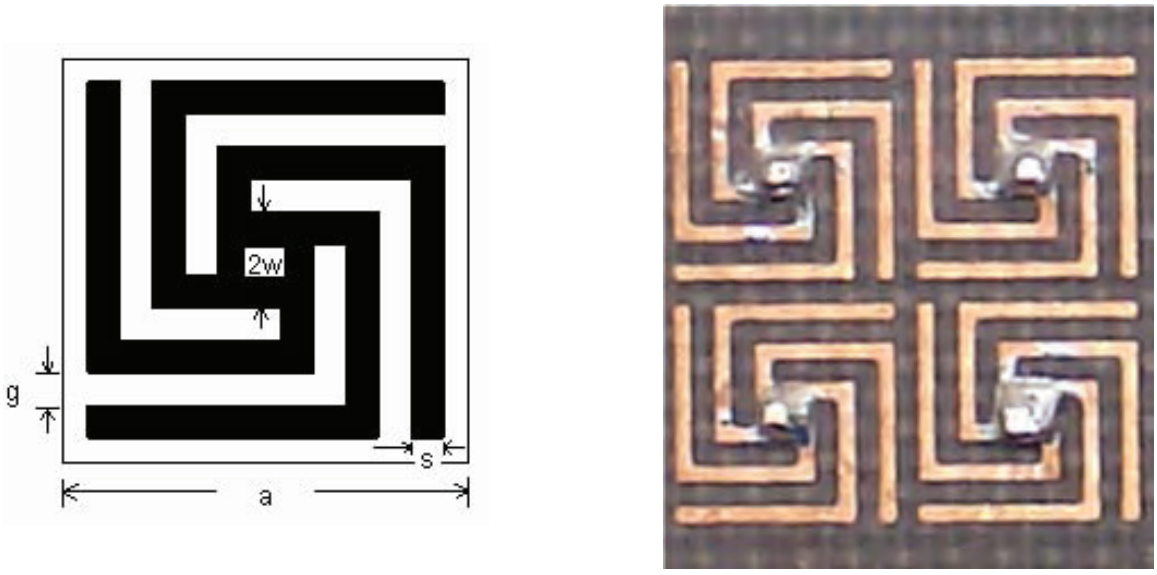

(a) (b)

Figure 5.24: The spiral shaped EBG element (a) size details (b) manufactured ones (Note the metallic vias soldered in the center)

the compactness is the aimed feature here, in order to fit more EBG elements into the already tight spacing budget between patches.

Two rows of these spiral EBGs with vias soldered to the ground are placed in the gaps between those radiating patches. The simulated structure is shown in Fig. 5.26. The DC biasing network is re-routed to give more space, although the total length of the line only varies a little from the single patch design. The spacing and shape of the radiating patches remain unchanged, as well as other aspects of the antenna. For a fair comparison, the ground plane size also stays the same at $75mm \times 100mm$. The manufactured EBG array is shown in Fig. 5.27. This array is only for microwave test purpose, so instead of AFPM device, a SMA port is fitted at the back of the patch. Another batch of AFPM mounted EBG array is demonstrated in Fig. 5.32 and 5.33.

Both of the conventional and the EBG array are simulated first. The measured radiation pattern of the conventional array confirms simulation results of 14dBi broadside gain at 5.2GHz when all ports are fed in a simultaneous manner, with sidelobe level 20dB lower than the major lobe, as shown in Fig. 5.28. The simulated gain pattern of the EBG antenna at 5.2GHz is almost identical to the conventional one. Therefore for the EBG

Design	1	2	3	4	5	6	7
							
l / p	0.91	0.92	1.12	1.0	1.0	1.06	1.0
Center Freq. Band f_c *(GHz)*	4.06	3.65	2.90	2.91	2.35	1.81	1.6
Reduction in f_c	-	10.0%	28.6%	28.3%	42.2%	55.4%	60.6%
Bandgap width(MHz)	445	350	225	110	100	95	50
Bandgap as %age of f_c	11.0%	9.6%	7.8%	3.8%	4.3%	5.2%	3.1%

Figure 5.25: Size comparison between various spiral EBG elements [64]

array, the gain pattern is no longer a concern, as the radiator elements are placed close enough to prevent any grating lobes.

Simulated mutual coupling levels of the conventional and EBG array is shown in Fig. 5.29. The measured mutual coupling levels are shown in Fig. 5.30 and 5.31. Generally, the distance between element one and four in the diagonal is larger than others, hence the coupling is minimal. At 5.24GHz, the measured mutual couplings of the EBG array are $S_{12} = -26dB$, $S_{13} = -28dB$, $S_{14} = -35dB$. The respective values of the conventional array at 5.24GHz are $S_{12} = -21dB$, $S_{13} = -23dB$, $S_{14} - 28dB$. Comparing to the conventional array, the isolations at 5.24GHz at all ports are improved by at least 5dB. As aforementioned, the spiral EBG element has a very narrow bandgap at this frequency. The noticeable sudden rise in S_{12} levels at above 5.3GHz in Fig. 5.31 can be explained by that the spiral no longer behaves like a bandgap structure beyond the stopband, thus starts to attract crossover space wave which increases mutual coupling.

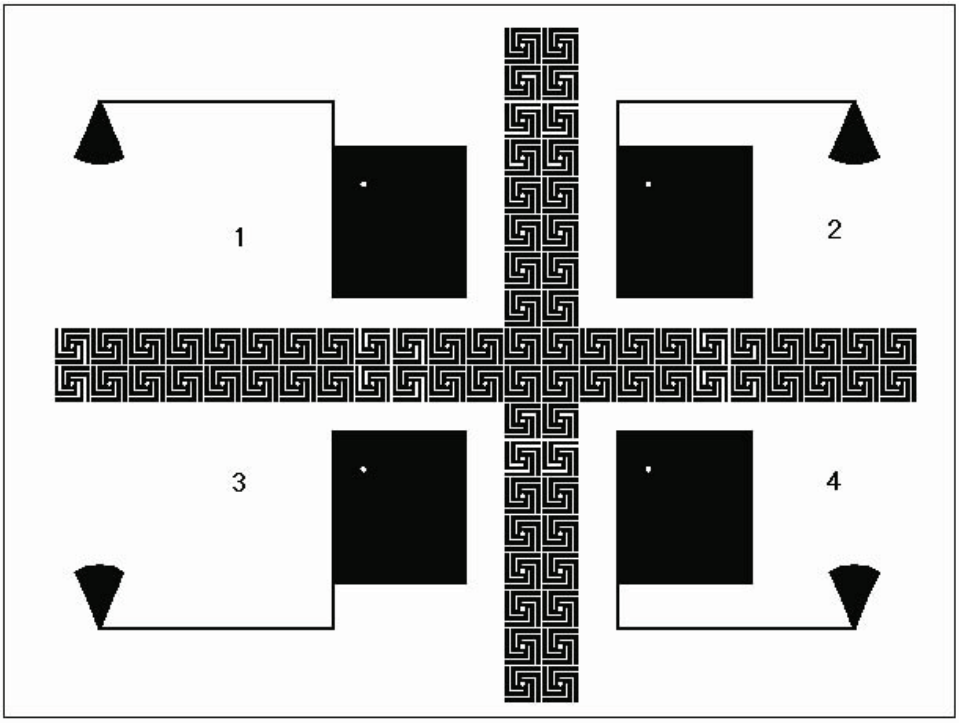

Figure 5.26: Simulated 22 array with spiral EBG elements

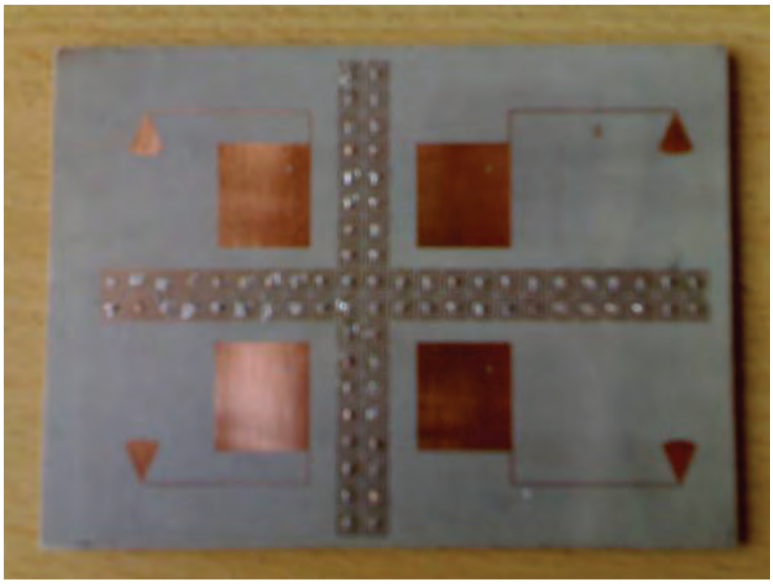

Figure 5.27: The manufactured pure microwave EBG 2×2 array

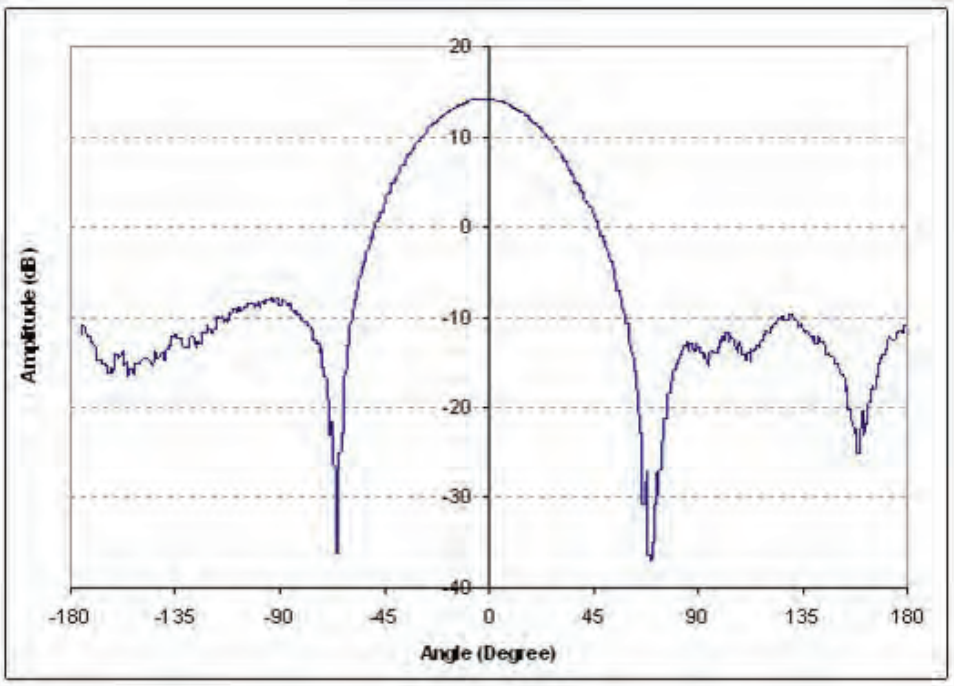

Figure 5.28: Measured radiation pattern of the 2×2 conventional array

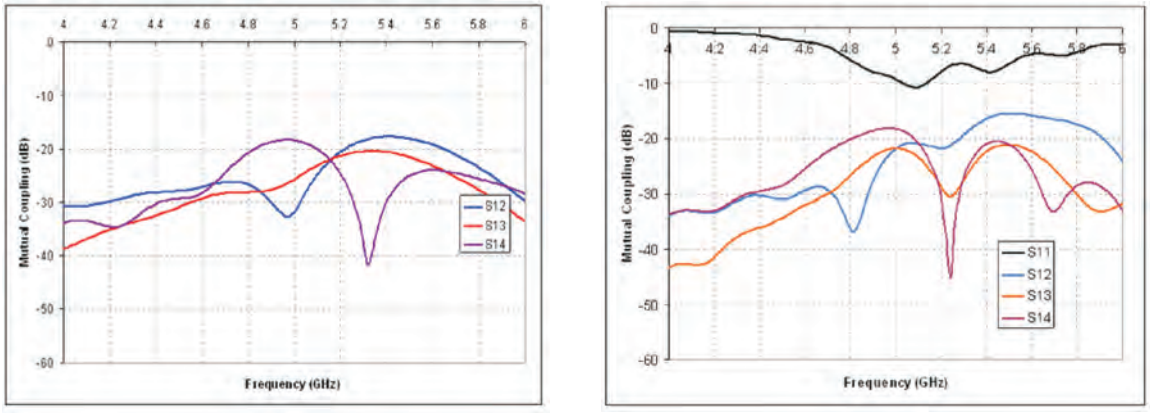

(a) (b)

Figure 5.29: Simulated mutual coupling of the 2×2 array antenna (a) conventional (b) EBG

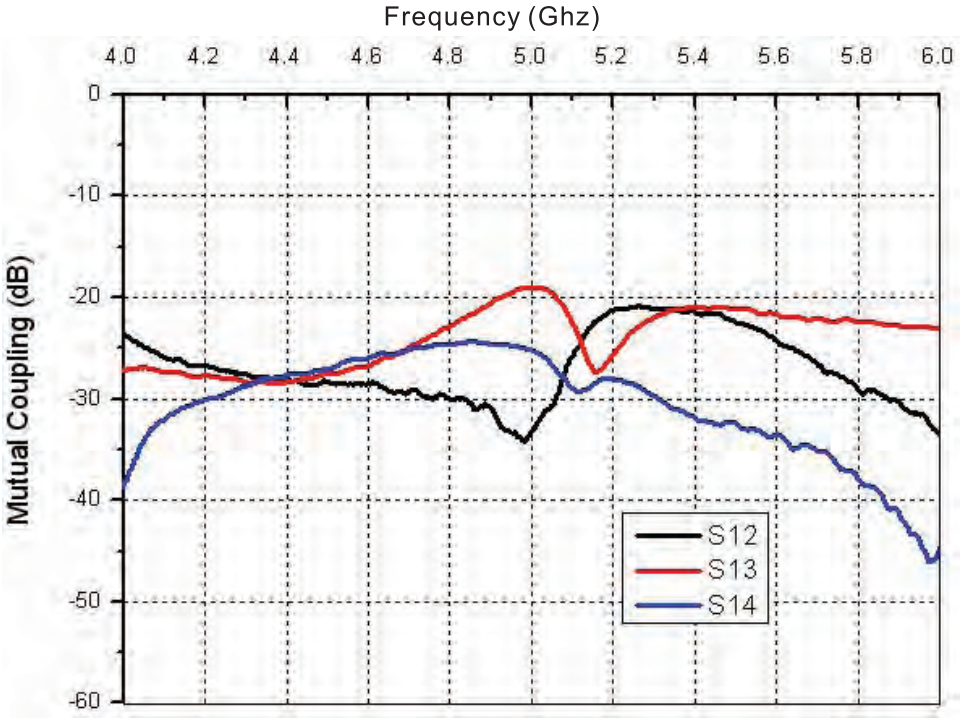

Figure 5.30: Measured mutual coupling of 2×2 conventional array

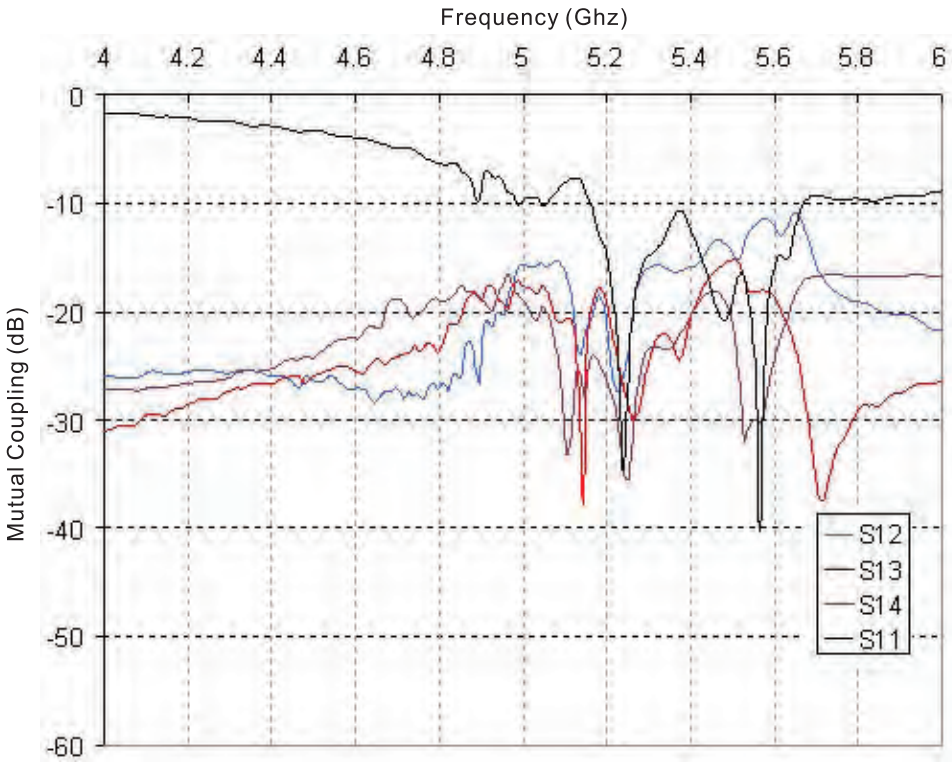

Figure 5.31: Measured mutual coupling of 2×2 array with spiral EBG element

5.3 Conclusions

This chapter demonstrates three hybrid EBG antennas. The concept of a multi-layer EBG antenna structure is presented with its application to the design of multi-band antennas using a single radiator. The theoretical prediction of antenna resonances can be achieved based on an effective medium model. Theoretical results have been verified via numerical simulations and measurements which are all in good agreements. Further work includes the improvement of the feeding structure to eliminate the spurious resonance and optimal design to suppress unwanted surface wave radiation. It is anticipated that the proposed layered EBG structure can be used as synthetic dielectric substrates for multi-band antenna design.

A conventional and an EBG enhanced circular polarized photonic patch antenna each integrated with an AFPM have been designed, fabricated and employed as receivers around 5.2GHz. The effect of the SRR EBG structure is that backward radiation is reduced by more than 5dB. A 6dB increase in path gain can be achieved with the proposed EBG antenna (about 2dB contribution) and the subsequent improved packaging technique. A 5dB improvement in harmonic suppression at 10.4GHz also arises from the EBG addition.

A circular polarized two-by-two photonic patch array was designed with the enhancement of metallic spiral EBG elements. Spiral EBG element with via is more compact in size when compared to the traditional mushroom structure, whilst more restricted in bandgap bandwidth. The unwanted surface wave at the antenna resonant frequency is successfully blocked by the spiral EBG structure. Compared to the performance of otherwise identical conventional array antenna without the EBG, overall isolation is significantly improved by more than 5dB at 5.24GHz. The spacing between the radiating patches stays unchanged at around half wavelength in free space, which would otherwise cause high mutual coupling and downgrade the performance of the array. The overall isolation improvement makes the AFPMs work in a less noisy environment. It enables a better system integration to form a photonic array antenna.

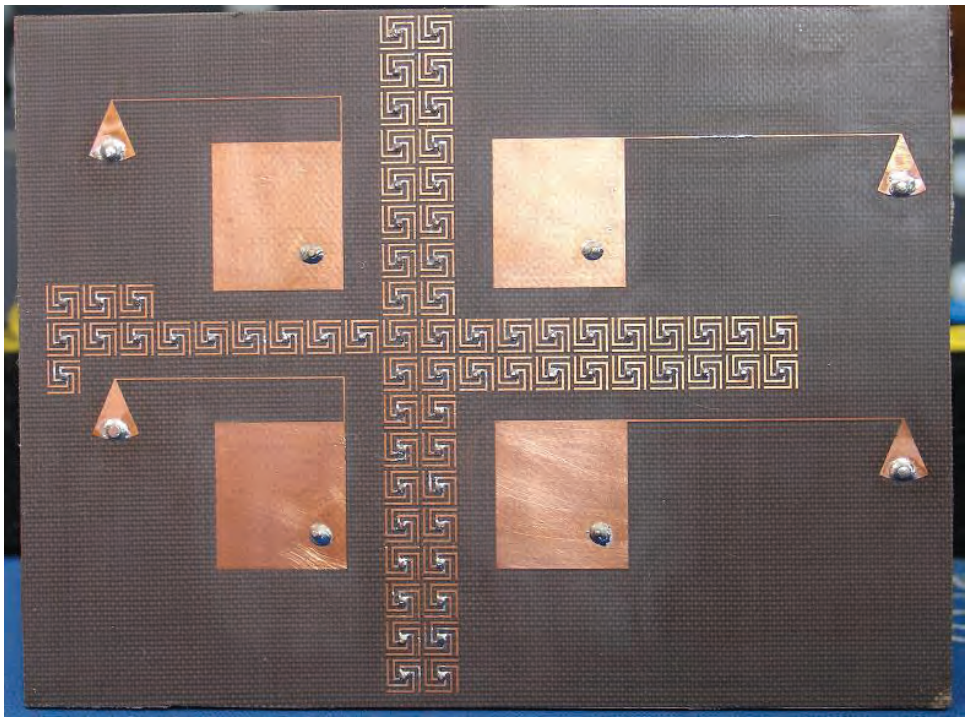

Figure 5.32: Another batch of EBG 2×2 array antenna with mounted AFPM and optical fibre

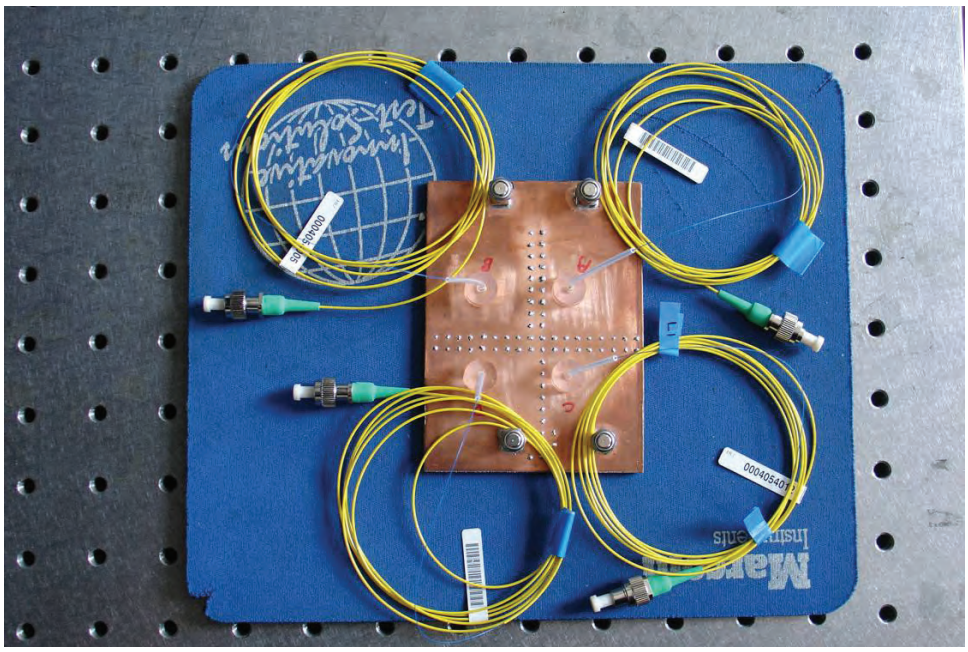

Figure 5.33: The back of the AFPM mounted EBG array antenna

Chapter 6

EBG antenna characterization using a 3D MRTD method

6.1 Introduction

Many of the current commercial EM simulators (e.g. HFSS or CST Microwave Studio) are easy to use and powerful. As seen in previous chapters, these commercial EM modelling software are good at unit-cell approach for pure EBG structures. They are also generally good when dealing with antenna radiation patterns. Indeed, they were able to simulate the combined hybrid structures as proposed. However, ability does not translate to efficiency. As the contrast between the overall hybrid structure and the required mesh size are huge, typically a complete full-wave simulation of the overall structure takes a long time as well as a great deal of computational resources. In other words, the commercial EM simulators are too slow and costly for EBG hybrid antenna applications, although not totally inadequate.

The EBG structure will have slightly different EM characteristics when it is placed very close to the radiator of an antenna. The interactions between the EBG and the antenna will be magnified once the EBG structure is integrated as a part of the hybrid antenna, and even more so when the antenna is not working at frequencies corresponding to the bandgap. These intensified interactions void the stand-alone unit-cell approach,

thus are partially the reason that the EBG behave slightly differently in the multi-layer EBG antenna proposed in previous chapter.

Most of the efforts so far are devoted to developing the algorithm itself and figuring out the update functions, in order to build the 3D simulator from scratch. Although the 3D simulator is still in its infant stage, it is applied to the simulation of the multi-layer EBG antenna aforementioned. The objective here is to try the 3D simulator with this previously tested structure and demonstrate several previously explained theoretical configurations in practice, such as the 3D update equations of the algorithm, the 3D source expansion scheme, the 3D material parameter specification and the 3D PML.

6.2 A patch antenna simulation in the 3D level-one Haar MRTD

Before the multi-layer EBG structure is simulated, it is important to verify the 3D MRTD code with a simple structure. A naturally simplified model would be a one-layer microstrip patch antenna. The first and most important step here is to assign a metallic surface, since other configurations (e.g. PML, source) introduced before have been implemented in the code.

As seen in chapter 4, the 3D simulator currently does not take the conductivity into account. A piece of metal (eg. the patch, its ground plane) is therefore specified by forcing the tangential E field to zero, at the surface. Since the variables representing the E field are actually expanded into wavelet components in MRTD, tangential E field components have to be "shorted" individually. Since the metallic patch is planned to be placed on x-y plane, therefore all the expanded EX and EY components have to be forced to zero in the updating loop for every time step.

The following procedure is used to specify the patch position, size and metallic property.

$$
\begin{aligned}
&for\ i = sX - (3 * patchsize/4) : sX + (patchsize/4)\\
&\quad for\ j = sY - (patchsize/2) : sY + (patchsize/2)\\
&\qquad E_X{}^{\phi\phi\phi}_{k,i,j,sZ+1} = 0;\\
&\qquad E_X{}^{\phi\phi\psi}_{k,i,j,sZ+1} = 0;\\
&\qquad E_X{}^{\phi\psi\phi}_{k,i,j,sZ+1} = 0;\\
&\qquad E_X{}^{\phi\psi\psi}_{k,i,j,sZ+1} = 0;\\
&\qquad E_X{}^{\psi\phi\phi}_{k,i,j,sZ+1} = 0;\\
&\qquad E_X{}^{\psi\phi\psi}_{k,i,j,sZ+1} = 0;\\
&\qquad E_X{}^{\psi\psi\phi}_{k,i,j,sZ+1} = 0;\\
&\qquad E_X{}^{\psi\psi\psi}_{k,i,j,sZ+1} = 0;\\
&\\
&\qquad E_Y{}^{\phi\phi\phi}_{k,i,j,sZ+1} = 0;\\
&\qquad E_Y{}^{\phi\phi\psi}_{k,i,j,sZ+1} = 0;\\
&\qquad E_Y{}^{\phi\psi\phi}_{k,i,j,sZ+1} = 0;\\
&\qquad E_Y{}^{\phi\psi\psi}_{k,i,j,sZ+1} = 0;\\
&\qquad E_Y{}^{\psi\phi\phi}_{k,i,j,sZ+1} = 0;\\
&\qquad E_Y{}^{\psi\phi\psi}_{k,i,j,sZ+1} = 0;\\
&\qquad E_Y{}^{\psi\psi\phi}_{k,i,j,sZ+1} = 0;\\
&\qquad E_Y{}^{\psi\psi\psi}_{k,i,j,sZ+1} = 0;\\
&\quad end\\
&end
\end{aligned}
\tag{6.1}
$$

As in the previous chapter, (sX, sY, sZ) marks the position of a point source, in this model it is set at the center of the domain. A single frequency sine wave at 2.4GHz is assigned to the source. $patchsize$ denotes the number of cells corresponding to the length of the patch, currently 20 cells. With a linear cell size of $\Delta x = 2mm$, the patch dimensions are $40mm \times 40mm$, identical to the patch we intend to use in the latter EBG model. As seen in 6.1, the patch layer is configured to have a z-coordinate of $sZ + 1$ right above the feeding point. Since there is no port structure in this model, this feeding method is used to excite the cavity. Although the point source is set at the center of the

structure, the patch is located slightly off center to be fed at 5 cells ($patchsize/4$) to one edge. k represents the current time step, as this procedure will be embedded into the update loop. The point source is located right underneath the metallic patch.

A 2-cell (4mm) thick Duroid substrate ($\varepsilon_r = 2.2$) is then specified by assigning $\frac{Sc \cdot \eta_0}{\varepsilon_r}$ to every B coefficient except the PML region: $B^{E_{xy}}_{:,:,n}, B^{E_{xz}}_{:,:,n}, B^{E_{yz}}_{:,:,n}, B^{E_{yx}}_{:,:,n}, B^{E_{zx}}_{:,:,n}, B^{E_{zy}}_{:,:,n}$. Sc is the three-dimensional MRTD Courant number, $Sc = \frac{1}{2\sqrt{3}}$. η_0 is the characteristic impedance of free space, $\eta_0 = \sqrt{\frac{\mu_0}{\varepsilon_0}} \approx 377\Omega$.

A metal ground plane is enforced using a similar procedure as in 6.1. This ground plane is configured throughout x-y plane at the bottom of the substrate. A 10-cell PML layer is configured to terminate the 60-cell cube in every direction, which effectively leaves a usable domain size of 40 cells $\times$ 40 cells $\times$ 40 cells. The simulated structure with a 3D E field view is shown in Fig. 6.1. As seen, the patch radiates like 2 slots at the edges along x-direction, which is expected.

An identical structure has been simulated in FDTD. Two different resolutions have been used, a $\Delta x = 2mm$, 60 cells $\times$ 60 cells $\times$ 60 cells one and a $\Delta x = 1mm$, 100 cells $\times$ 100 cells $\times$ 100 cells one. In both FDTD simulations, the PML region are set to be 10-layers thick, leaving an identical usable domain size of 80mm $\times$ 80mm $\times$ 80mm. The $\Delta x = 2mm$ FDTD simulation is shown in Fig. 6.2. To keep the display range from floating around in the Matlab, the figure is fixed to the range of $[-0.1, 0.1]$. In all three simulations (one MRTD, two FDTD), the source is fixed to have a 100 times amplitude of a unit sine wave. As shown, the E field in the $\Delta x = 2mm$ FDTD simulation is noticeably higher than in the MRTD simulation. Bearing in mind that the $\Delta x = 2mm$ FDTD has a Δt twice than the $\Delta x = 2mm$ MRTD, the FDTD at 400 time steps corresponds to the MRTD at 800 time steps. To confirm the difference in results, the time-domain signal at a point 20mm above the patch feeding point was extracted, shown in Fig. 6.3, Fig. 6.4 and Fig. 6.5.

Comparing these three figures, the MRTD result is found to be quite similar to the FDTD with $\Delta x = 1mm$. There are a few minor differences, but deviations are small. However, the FDTD with a cell size of 2mm yields an unacceptable result. The amplitude is somehow 8-10 times larger, the shape of the signal is much more smoother. This is

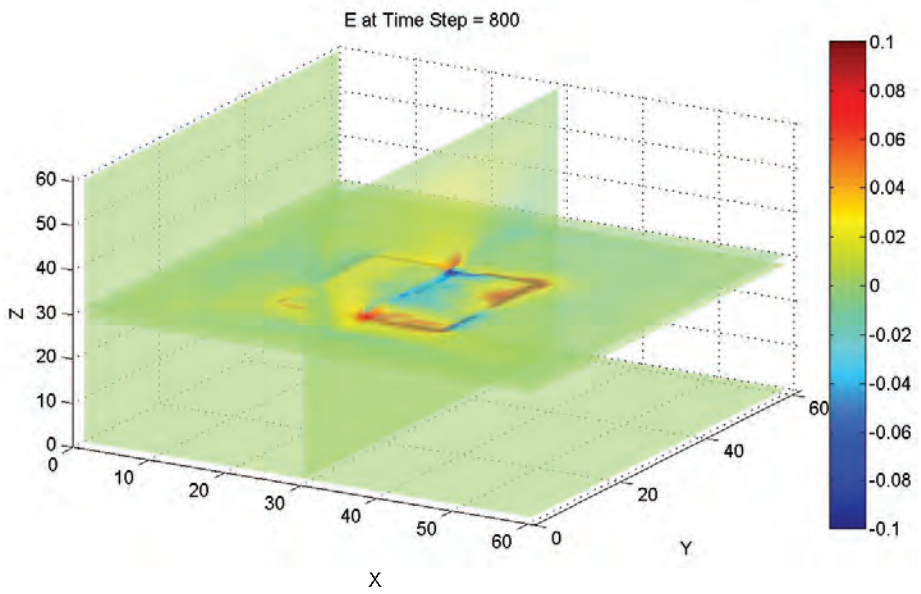

Figure 6.1: 3D MRTD simulation of a simple microstrip patch antenna: 3D view, $\Delta x = 2mm$

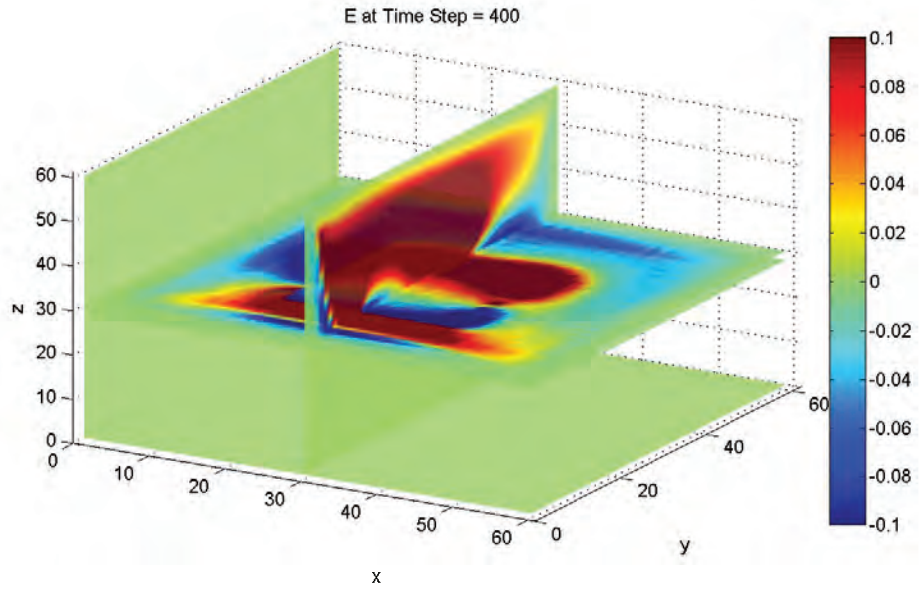

Figure 6.2: 3D FDTD simulation of a simple microstrip patch antenna: 3D view, $\Delta x = 2mm$

due to the inability of the FDTD to properly represent and resolve the substrate with a thickness of two cells. At 2mm spatial resolution, the FDTD cannot account for this 4mm thick substrate accurately. When the resolution is improved to $\Delta x = 1mm$, a 4-cell representation of the substrate in the FDTD makes it perform better, at the cost of 4.63 times of total number of cells needed. In other words, 3.63 times more memory is needed than a $\Delta x = 2mm$ FDTD. The MRTD in this instance uses less memory than the $\Delta x = 1mm$ FDTD but yields a similar result.

Since there is no port structure, input impedance of the antenna is not rigorously defined. Basically the point source can emit an arbitrary signal into the structure. Therefore, the traditional sense of return loss cannot be realized in this simplified model. However, the resonant frequency of the microstrip patch cavity can be found by analyzing the E field inside the structure. In order to do this, the source signal and the total number of time steps are modified in the second simulation of the patch.

The physical structure remains unchanged. Instead of a continuous sine wave, a differentiated gaussian pulse is applied to the point source underneath the patch. The pulse satisfies the following equation.

$$source(k) = \frac{(k-d)\Delta t}{\tau} e^{-\frac{((\frac{(k-d)\Delta t}{\tau})^2 - 1)}{2}} \tag{6.2}$$

where k is index of temporal step. d represents the delay the source experiences before the wave is launched, in this equation $d = \frac{4\tau}{\Delta t}$. $\tau = \frac{1}{f}$, f is the characteristic frequency of this pulse. $\Delta t = \frac{\Delta x}{2\sqrt{3}c_0}$ is the time step, c_0 is the speed of light 3.0×10^8 m/s, $\Delta x = 2mm$ as specified before.

As a Fast Fourier Transform (FFT) will be performed on the extracted signal later, one has to specify the frequency resolution by assigning a proper Δt, f and a long enough maximum k. In this simulation, Δx (therefore Δt) is fixed. The differentiated gaussian is set at 10GHz, and total number of time steps is set at 8000 (so that k is in the range of $k = [1, 8000]$). By doing so, the final frequency resolution after the FFT is set at $\Delta f_{FFT} = \frac{1}{\Delta t \cdot 8000} = 65$MHz. Since the antenna is known to be narrowband, the frequency resolution has to be fine enough in order not to miss the resonance.

The 10GHz differentiated Gaussian pulse is shown in Fig. 6.6. The reason for setting it at 10GHz is that to make the pulse short in duration, so as to observe the field distribution inside the structure after the excitation completes. As seen, the duration of the source is about 450 time steps. The observation cell is chosen to be the one next to the source cell along the y-direction. By extracting the E field at this point, Fig. 6.7 is generated. The part representing the resonating field inside the cavity can then be separated from the part corresponding to the excitation, as shown in the figure. The FFT is applied to convert this extracted resonating signal to frequency domain. The resonance of the cavity is shown in Fig. 6.8. As predicted from the physical size of the antenna, the resonance of the cavity is confirmed at close to 2.4GHz.

6.3 A multi-layer EBG hybrid antenna configuration in the 3D level-one Haar MRTD

The multi-layer EBG antenna is just a few steps in extension from the patch simulated before. First of all, a proper resolution has to be specified. Since a $\Delta x = \Delta y = \Delta z$ cubicle is employed per single cell in the 3D code, the thickness of the dielectric substrate has to be taken into account. In this case, a 1.5mm thick Duroid slab and a 1.5mm RO3210 slab are chosen (1.575mm thick Duroid and 1.27mm thick RO3210 in the manufactured case). A $0.5mm \times 0.5mm \times 0.5mm$ cell size is chosen. Bearing in mind that a 3D MRTD cell has 8 wavelet expanded components to represent a single field variable, it is deemed that two 3-cell configurations of dielectric substrates are sufficient. The top radiating patch has a size of $40mm \times 40mm$, which makes it 80 cells $\times$ 80 cells. EBG elements were set at $19mm \times 19mm$ (38 cells $\times$ 38 cells), placed 4mm (8 cells) apart underneath the Duroid substrate. 3×3 metallic EBG patches are specified. Complete configuration is shown in Fig. 6.9. The dimensions are close to the manufactured antenna described in Chapter 5. The overall domain size is 160 cells $\times$ 160 cells $\times$ 160 cells, terminated by a 10-cell PML layer at every direction.

In Fig. 6.9, the material permittivities are illustrated in a 3D fashion, with every metallic layer labeled in red on a x-y plane slice. There are three metallic layers, from the top:

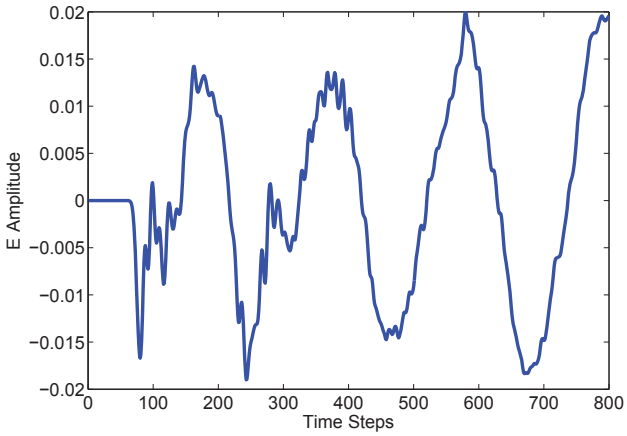

Figure 6.3: Signal extracted at 20mm above the patch, from MRTD simulation, $\Delta x = 2mm$

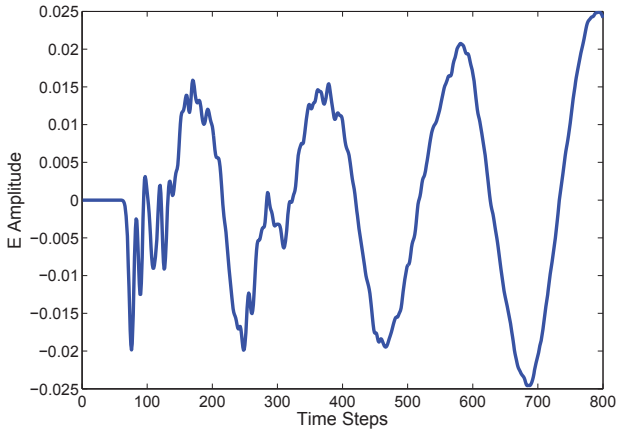

Figure 6.4: Signal extracted at 20mm above the patch, from FDTD simulation, $\Delta x = 1mm$

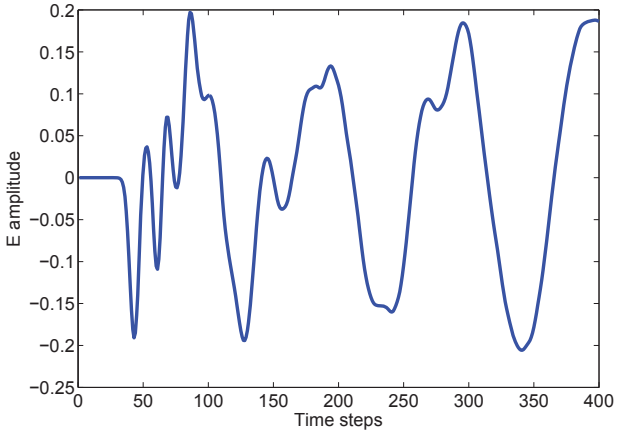

Figure 6.5: Signal extracted at 20mm above the patch, from FDTD simulation, $\Delta x = 2mm$

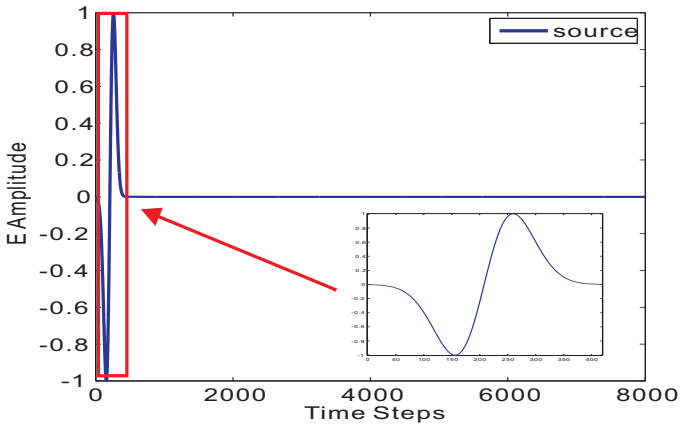

Figure 6.6: The second MRTD patch simulation:10GHz differentiated gaussian pulse

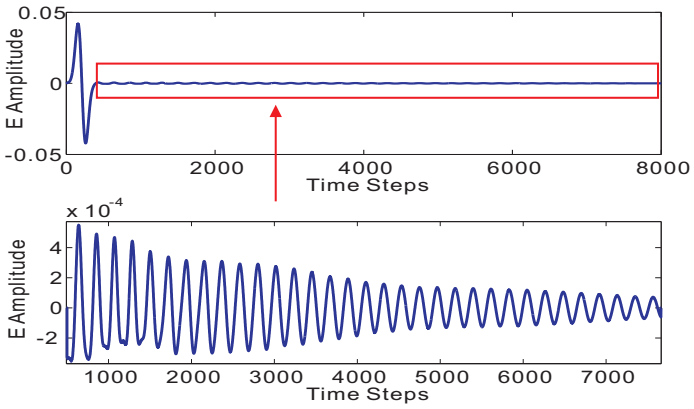

Figure 6.7: The second MRTD patch simulation:E field extracted from observation point next to source

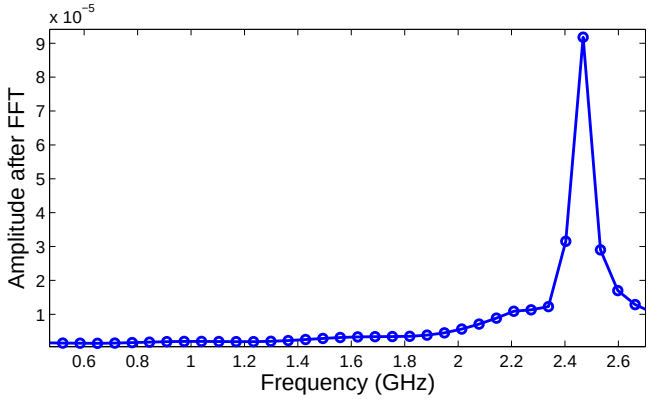

Figure 6.8: Frequency spectrum of the resonant E field inside the cavity

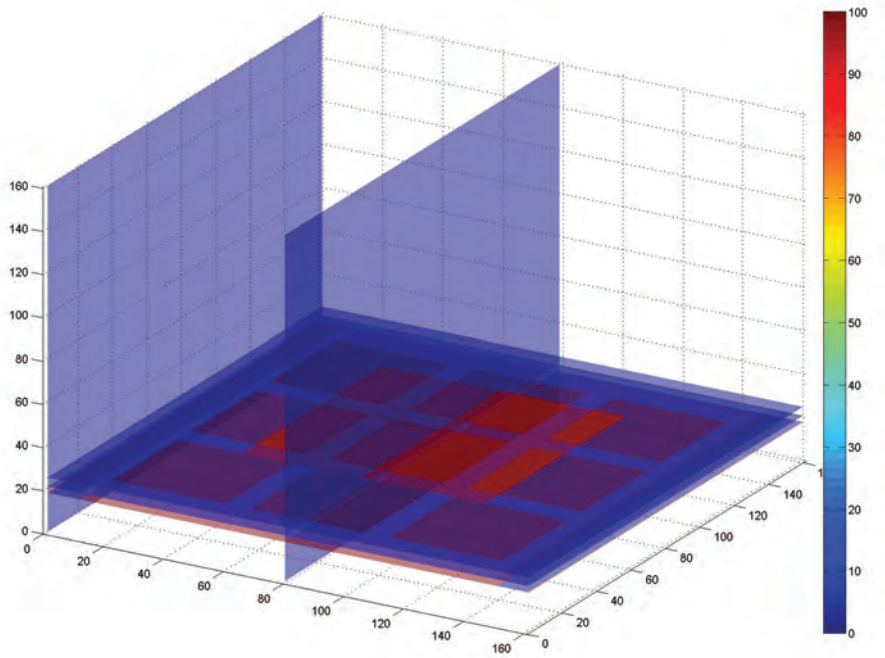

Figure 6.9: 3D MRTD simulation: 3D view

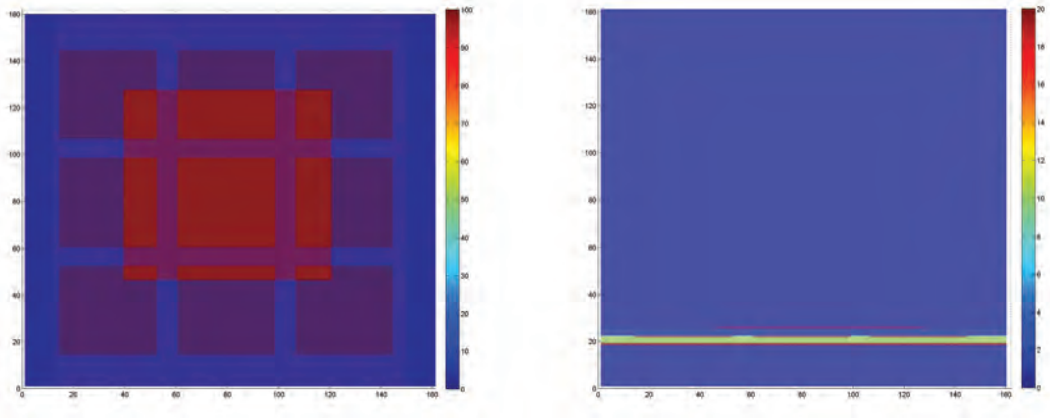

Figure 6.10: 3D MRTD simulation: top view and side view

radiating patch, EBG patch array and a ground plane at the very bottom. Two dielectric slabs are placed in between. In Fig. 6.10, the top view and side view are shown. Two layers of different dielectric slabs can be seen. In both figures the metallic parts are labeled in red artificially for illustration purpose. In the actual 3D code, the metallic boundary is assigned using a procedure similar to 6.1.

Each dielectric layer is configured through the B coefficient to its corresponding dielectric constant. The B coefficient (e.g. $B^{E_{xy}}_{l,m,n}$ in equation C.1) is configured as $B = \frac{c\Delta t}{\Delta x}\frac{\eta_0}{\varepsilon_r}$. Directly underneath the top patch, Duroid substrate is specified. The majority of the domain in Fig. 6.11 is seen filled with material of $\varepsilon_r = 2.2$. The PML regions are visible as gradual varying color regions at the left and right of the domain, as this distribution is derived from $B^{E_{xy}}_{l,m,n}$. Note that, except for the PML regions, coefficients $B^{E_{xy}}_{l,m,n}, B^{E_{xz}}_{l,m,n}, B^{E_{yz}}_{l,m,n}, B^{E_{yx}}_{l,m,n}, B^{E_{zx}}_{l,m,n}, B^{E_{zy}}_{l,m,n}$ are configured with the same permittivity distribution, since the materials specified are isotropic.

At the moment the 3D code only deals with sources that are directly applied onto the structure. It cannot simulate a waveguide or coaxial port in this instance. A Gaussian point source peaked at 10GHz is applied directly underneath the top radiating patch, 10mm to one edge, 30mm to the opposite edge. The source can be described as 100 times a unit modulated Gaussian pulse,

$$source(k) = 100 \cdot e^{-(\frac{(k-d)\Delta t}{\tau})^2} \cdot \sin(2\pi f k \Delta t) \tag{6.3}$$

where k is the temporal step index, as the antenna was simulated for 5000 time steps, $k = [1, 5000]$. d represents the delay the source experiences before the wave is launched, in this equation $d = \frac{2\tau}{\Delta t}$. $\tau = \frac{1}{f}$, $f = 10GHz$ in this simulation. $\Delta t = \frac{\Delta x}{2\sqrt{3}c_0}$ is the time step, C_0 is the speed of light 3.0×10^8 m/s, $\Delta x = 0.5mm$ as specified before. Currently, as the source is set to be centered and modulated at 10GHz, the duration of the pulse is seen to last about 1000 time steps, as shown in Fig. 6.13. Again at the moment the source is considered a hard source, meaning emission only.

6.4 The results

The three-dimensional E-field distribution is shown in Fig. 6.12. As this figure illustrates the field value, the EBG structure underneath the radiating patch can be seen. The shape of the top radiating patch is also obvious, as well as interaction between the EBG patches.

E field at two locations has been extracted and stored along with the simulation: 50 cells above the top patch and 1-cell away (in y-direction) from the feed point. The extracted E field time series are shown in Fig. 6.14 and 6.15.

One can analyze the E field inside the structure to reveal the resonant frequency of the antenna. The current frequency resolution after the FFT is about $\Delta f_{FFT} = \frac{1}{\Delta t \cdot 5000} \approx 0.415$GHz. A meaningful frequency resolution to reveal narrowband features of the EBG would require a more than quadrupled total number of time steps than the presented case. At that scale, the computational efficiency of the Matlab based platform becomes an issue. One would have to convert the MRTD code onto a better platform to improve the efficiency. However, as demonstrated, there are no theoretical difficulties left on the algorithm side for simulating such a structure. The 3D update functions, PML and source expansion are all proven to be complete and correct.

One final note, a FDTD simulation with $\Delta x = 0.25mm$ that takes at least 300 cells $\times$ 300 cells $\times$ 300 cells cannot run on a PC with 4GB memory. The total number of cells requests more memory than the PC can provide. In this sense, the MRTD with $\Delta x = 0.5mm$ has better feasibility comparing to the FDTD, while both are based on the Matlab platform.

6.5 A Comparison between MRTD and FDTD

To demonstrate the superiority of the MRTD over FDTD, in terms of computation time and memory requirement, a comparison is included here. The patch simulations that detailed in Fig. 6.1 and Fig. 6.2 are used as example scenarios in this comparison.

	3D level-one MRTD	3D FDTD	3D FDTD
Cell size Δx (mm)	2	1	2
Time step size Δt (s)	$\frac{1}{c_0\sqrt{3}}$	$\frac{1}{c_0\sqrt{3}}$	$\frac{2}{c_0\sqrt{3}}$
Total domain size (mm^3)	$120 \times 120 \times 120$	100^3	120^3
Total domain size (number of cells)	$60 \times 60 \times 60 = 216K$	$100^3 = 1000K$	$60^3 = 216K$
Usable domain size (mm^3)	$80 \times 80 \times 80$	80^3	80^3
Usable domain size (number of cells)	$40 \times 40 \times 40 = 64K$	$80^3 = 512K$	$40^3 = 64K$
Number of E components per-cell	$(6+1) \times 8 + 1 = 57$	6+1+1=8	6+1+1=8
Number of H components per-cell	$(6+1) \times 8 + 1 = 57$	6+1+1=8	6+1+1=8
Number of material coefficients per-cell	6+6=12	6+6=12	6+6=12
Size of each coefficient matrix	$60^3 = 216K$	$100^3 = 1000K$	$60^3 = 216K$
Overhead variables[*1]	8		
Number of time steps simulated	800	800	400
Memory required in Matlab (MB)[*2]	267	476	110
Computation time required in Matlab (s)[*3]	1610	1430	160
Simulated E-field resolution	good	good	poor

Table 6.1: A comparison between MRTD and FDTD, See notes for ^{*1,2,3}.

As for overhead variables, what is included in the table above does not cover every overhead parameter. Apart from common physical constants like ε_0 and μ_0 which are shared between MRTD and FDTD, because of the source expansion, MRTD has 8 additional matrices with considerable size. The $[E1_k, E2_k, \cdots, E8_k]$ series are time series. Each of them has a matrix size of 1×800 in the illustrated simulation above.

For the total memory measurements, the "Memory" command in Matlab console was utilized before and after (with the matrices stay resident) each specific simulation. The difference in the amount of memory consumed by the Matlab indicates the total memory required. Comparing to the FDTD with a $\Delta x = 1mm$, the MRTD uses 44% less memory, yet yields a similar resolution of the E field.

Two factors explain this memory advantage of MRTD over FDTD. The majority of the reduction comes from algorithmic superiority. First of all, to maintain a comparable

resolution, there is no memory saving on the number of variables representing the E field. As seen in the table above, the MRTD employs many more wavelet components (variables) than the FDTD in every single cell to boost the resolution. In fact, in our simulator, the 3D MRTD uses 57 variables in the single cell to represent various wavelet components of E field. The 3D FDTD employs 8 variables to represents the E field within a cell.

On the other hand, by adding these wavelet components into every single cell, the total number of cells can be greatly reduced. Keeping the usable domain size constant at $80 \times 80 \times 80$, also maintaining a 10-layer PML at each end of the domain, the MRTD needs $216,000$ cells while the FDTD with a $\Delta x = 1mm$ needs 1 million cells. Overall, as the total domain becomes larger and larger and the number of PML layers represent less overall weight, the MRTD tends to use $\frac{1}{8}$ total number of cells of the FDTD with a equivalent resolution. This compensates the hugely denser wavelet components within a single cell, to arrive at a comparable level of memory consumption of E variables as used in a FDTD simulator.

The real saving comes from the coefficient matrices. As shown in the above table, within a single cell, both of the MRTD and the FDTD needs 12 coefficients to represents the tensor fields, 6 for the permittivity ε, 6 for the permeability μ. Every coefficient is a numerical matrix. However, the size of these matrices are vastly different between MRTD and FDTD due to the difference in total number of cells needed. In the illustrated cases, each of the MRTD coefficient occupies 7MB less than its peer in the FDTD. The coefficient savings in computational memory are estimated at about 90MB in the illustrated case. If the computational domain are much larger, the savings resulted from the coefficients would be more obvious.

One may misunderstood this scenario comparison, as we are comparing a MRTD with a total domain size (in terms of number of cells) of 60^3 to a FDTD of 100^3. Why not compare that to a FDTD with a identical domain size? We did, as shown in the third column. Indeed the FDTD scenario with a $\Delta x = 2mm$ uses much less computational memory. But the simulation result is unacceptable, as shown in 6.5. The intensity of the E field is unrealistically high. The critical point is that the FDTD needs a mesh that

is fine enough to yield reasonable results. This is known as a cell size that is $\frac{1}{10}$ of the wavelength, for a common structure. However, this ratio is dependent on the specific structure being simulated. In this patch antenna case, the thickness of the patch substrate indicates a stricter limit. The FDTD with a $\Delta x = 2mm$ just does not meet that limit, hence a poor resolution in the simulated E fields. With a much denser population of wavelet components within every cell, the MRTD is able to yield accurate result with a $\Delta x = 2mm$.

Secondly, the code enhances the memory saving feature by applying several memory management techniques. By assigning a single precision data type to many non-critical variables, the MRTD code uses 4 Bytes on a 1×1 matrix instead of 8 Bytes. Together with several rounds of memory recollection, the required amount of memory is further reduced by about 120MB. These techniques however only reflect the author's skill in Matlab programming, they are not intrinsic benefits that come with the MRTD algorithm.

On the computation time, the measurements are carried out by marking the system time after every 10% of total time steps. To minimize the potential difference in automatic Matlab acceleration during the calculations, the median 10% of each simulation is selected, then multiplied 10 times to arrive at the total time. The MRTD uses slightly longer time than the FDTD with equivalent resolution, 1610 seconds versus 1430 seconds. This difference will drop significantly for simulations of large structures. Overall, there is no clear advantage in terms of computation time, in equivalent resolution simulations.

Noticeably the MRTD uses 10 times longer than the FDTD with a $\Delta x = 2mm$, 1610 seconds versus 160. This is understandable since there are 8 times more update functions hence at least 8 times more computational time, when the total number of cell is the same.

One final remark regarding the multi-layer EBG MRTD simulation. As the simulated domain becomes much larger to have 160^3 cells at $\Delta x = 0.5mm$, the total memory saving becomes huge, comparing to a FDTD with 320^3 cells at $\Delta x = 0.25mm$. In fact, the latter case cannot even be ran on a PC with 4GB memory. The total saving is estimated at about 3GB.

6.6 Conclusions

This chapter demonstrates the basic capability of the proposed 3D MRTD simulator, in its application to a simplified microstrip patch antenna and the aforementioned multi-layer EBG antenna. Three-dimensional PML, source expansion and layered material property specification have been demonstrated. In the patch antenna simulation, results are verified by comparison with FDTD generated ones. Also the resonance of the antenna is confirmed at 2.4GHz. The MRTD are more accurate than FDTD with same cell size. Due to time and resource limit, the multi-layer EBG antenna is presented with preliminary time-domain result extracted from the simulation. The MRTD saves computational memory hence improve feasibility comparing to FDTD with equivalent resolution (half the linear cell size).

Since a coaxial probe exists in the practical antenna, it will be more accurate to include it into future simulations. This requires a way of simulating a waveguide port with a well-defined input impedance. Also, near-field to far-field transformation would be a natural add-on to retrieve far-field radiation patterns. Further, optimization of the EBG antenna can be achieved using this 3D simulator. The cell size specified will affect the simulation. Better spatial resolution can be achieved if the cell size can be reduced to $0.1mm \times 0.1mm \times 0.1mm$. However, reducing the cell size inevitably increases the number of cells needed in a simulation, especially in 3D. The memory required as well as calculation time would be dramatically increased. One has to improve the program's computational efficiency, possibly by migrating the algorithm to a C++ platform. These issues are addressed in next chapter.

Although still at the infant stage, the proposed 3D MRTD simulator does show great numerical capability as well as potentials. It can be used to assist the design and optimization process of the EBG hybrid antennas once complete features are added on. By laying the groundwork of this simulator, further development can be built upon, by other researchers.

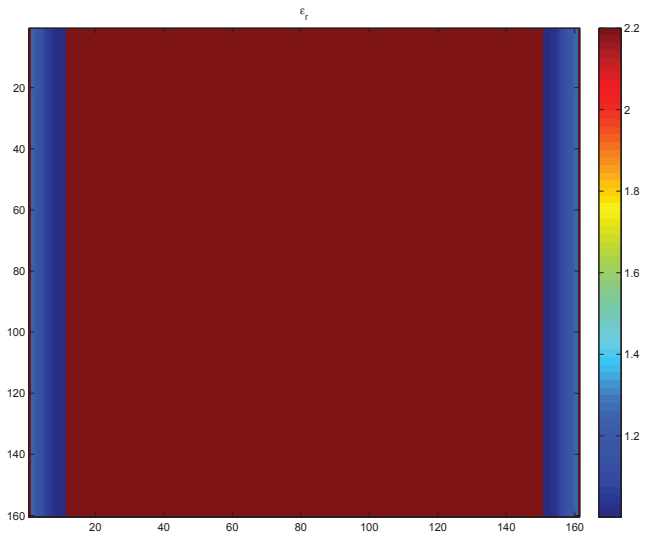

Figure 6.11: 3D MRTD simulation: Permittivity (ϵ_r) distribution underneath the patch layer, top view

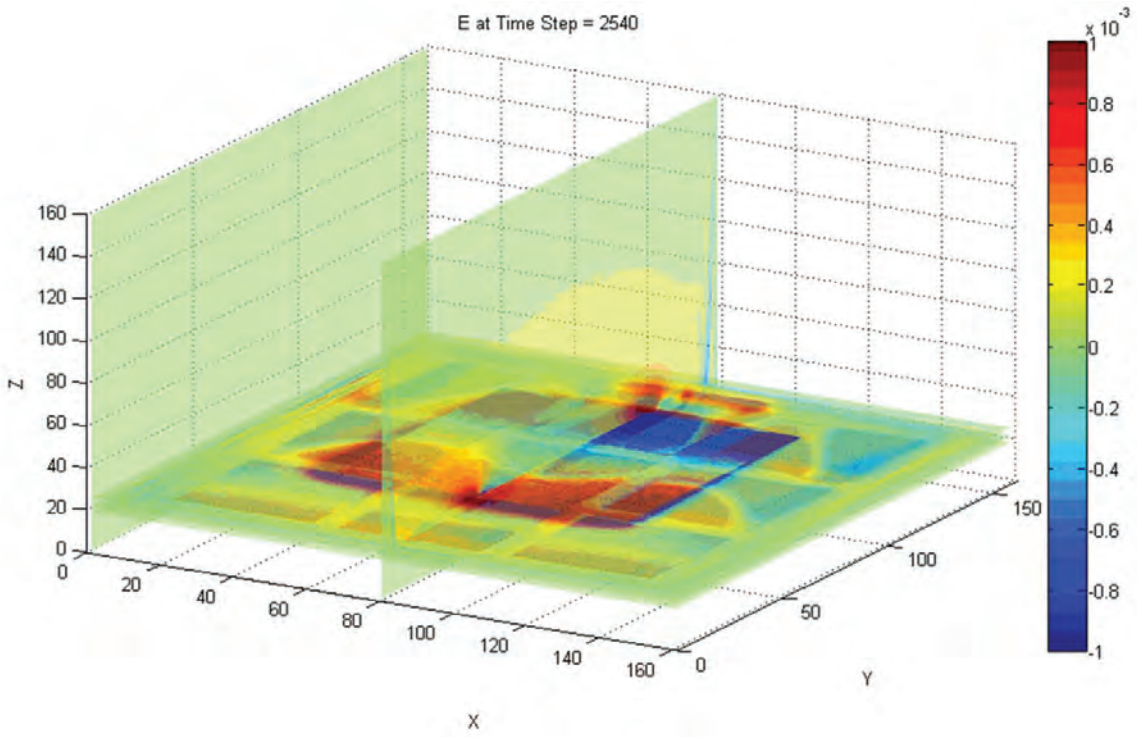

Figure 6.12: 3D MRTD simulation results: 3D E field distribution with a 10GHz source

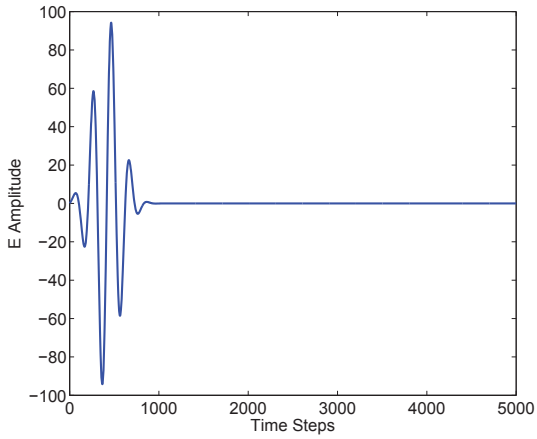

Figure 6.13: 3D MRTD simulation: excitation

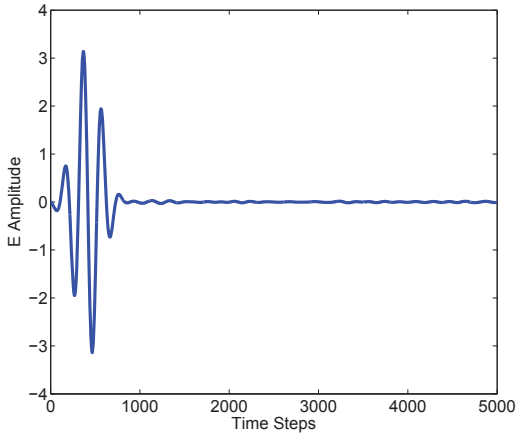

Figure 6.14: 3D MRTD simulation results: E field next to the feeding point, in Duroid layer

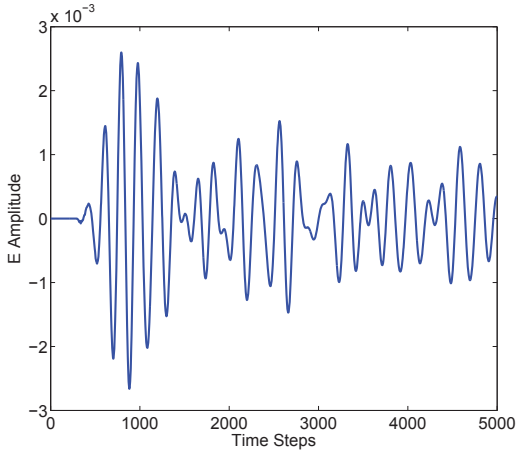

Figure 6.15: 3D MRTD simulation results: E field 50 cells above the top patch

Chapter 7

Conclusions and Future Works

7.1 Conclusions

The level-one Haar wavelet based MRTD algorithm has been successfully developed and employed to build one-dimensional, two-dimensional and three-dimensional electromagnetic simulators. The 1D code was tested using a tri-layer structure with different centerpieces, and then compared with FDTD results. An electrically large 12-shell Luneburg lens structure was studied using the 2D MRTD code, and further verified with results from reference literature. The MRTD simulators yield better resolution, reasonably accurate and steadily stable results over conventional FDTD.

The complete set of 3D level-one Haar MRTD update functions are explained and reported. Also, a precise formulation of the intrinsic PML boundary condition for the level-one Haar based MRTD is presented, which can be further expanded to arbitrary level Haar wavelet basis functions. The proposed intrinsic PML formulation introduces even greater numerical efficiency into the MRTD algorithm. A pseudo subcell source expansion scheme is also developed in 2D and 3D. By constructing several virtual E variables as a middle step, the procedure bypasses a FDTD-like difficult subcell scheme. This pseudo source expansion scheme made it easy to assign a simple excitation or excitations with some shape of geometry. The proposed 3D MRTD simulator, though at infant age, shows good numerical capability in simulating a simple patch antenna and the

multi-layer EBG antenna. It can be used to assist the design and optimization process. Three-dimensional PML, source expansion and layered material property specification have been demonstrated.

One of the trade-offs of the proposed level-1 MRTD scheme appears to be a slow computation speed. After the wavelet expansion, the field variables in the update loops double linearly as the resolution gets higher. Also physically it takes twice the number of temporal steps in MRTD than in an FDTD with the same cell size (at linearly twice the resolution though), since the stability criterion requires half of the FDTD courant number: Δt is fixed at a ratio of $\frac{\Delta x}{2c}$ in stead of $\frac{\Delta x}{c}$ in a 1D scenario. This puts the burden on the speed of the iteration as well as the overall number of steps, which becomes more pronounced in a 3D scenario. The Matlab code of the final 3D simulation introduced in Chapter 6 runs at a speed of roughly 1 time step per minute, on a PC with 3GHz Pentium 4 CPU and 4GB RAM. This issue can only be solved by migrating the algorithm to a much more efficient coding environment, which will be discussed in the section on future works.

Three hybrid EBG antennas have been demonstrated. The concept of a multi-layer EBG antenna structure is presented with its application to the design of multi-band antennas using a single radiator. Theoretical results have been verified via numerical simulations and measurements which are all in good agreement. It is anticipated that the proposed layered EBG structure can be used as synthetic dielectric substrates for multi-band antenna design. A conventional and an EBG enhanced circular polarized photonic patch antenna each integrated with an AFPM have been designed, fabricated and tested. Backward radiation is reduced by more than 5dB due to the surrounding SRR EBG structure. Also, a circular polarized two-by-two photonic patch array was designed with the enhancement of metallic spiral EBG elements. The unwanted surface wave at resonant frequency is successfully blocked by the compact spiral EBG structure. Compared to the performance of otherwise identical conventional array antenna without the EBG, overall isolation is significantly improved by more than 5dB at 5.24GHz. The overall improvements make the AFPMs work in a less noisy environment which enabled a better system integration to form a photonic antenna.

As for these antennas, the manufacturing inconsistency remains an issue for further investigation. Especially for the manually mounted AFPM devices, the problem remains largely unsolved. Although the photonic antenna designs are quite successful in their own context, the difference in mounting procedure and physical difference in AFPM devices made the array beam tuning quite difficult. In particular, because of a defective AFPM (or the way it was mounted), the EBG enhanced array antenna was forced to have other batches of samples fabricated before being deemed acceptable. The accuracy and repeatability of the fabrication procedure should be improved to create better results.

It has been an academically challenging journey, especially for trying to cover two in-depth topics and combining them together. For an engineering student with little background in mathematics other than undergraduate courses, it took a great amount of effort, time as well as patience in working things out, especially during the 9-month period before figuring out the 3D MRTD formulas as well as putting them into working programs. The final 3D simulation of the EBG hybrid antenna is still at its infant stage, leaving issues and extensions to future works. However, the working 1D, 2D and 3D MRTD simulators have been demonstrated with excellent numerical capabilities over conventional means. Together with three proposed EBG hybrid antennas which were designed, fabricated and tested, the overall work marks a successful research outcome with novelty.

7.2 Future Works

There are a few aspects that have not been addressed in this thesis. These additional topics are challenging and interesting, and may be promising directions for future works. As indicated in the Acknowledgement of this thesis, the financial obligation to Queen Mary has been fulfilled. The future works proposed here will not be included in the author's PhD work.

7.2.1 An Efficient algorithm coding platform, Matlab or C++

Although all the MRTD algorithm described in this thesis were programmed with Matlab, Matlab is not the ideal platform for an efficient large-scale simulator. Matlab is good for algorithm prototyping. One particular advantage of Matlab is that it includes a library of many functions, especially display functions (plotting routines) that plot and animate 2D and 3D graphics (extremely handful for visualizing electromagnetic fields). Enforcing these functions sometimes as simple as in one single command, the time span of programming procedure has been shortened considerably. It makes the coding much more focused on the algorithm development itself.

Also, Matlab is specialized in matrix (array) operations, which makes it a platform easier to construct 2D and 3D scenarios upon. For the 2D case, all the field variables can be specified directly as $m \times n$ matrices in Matlab. For 3D scenarios, the variables can be constructed as $l \times m \times n$ arrays. Although the Matlab has a special order in displaying arrays (that it treats the indices as rows and columns, rather than coordinates, hence a vertical x-direction in 2D plot), generally it makes matrix representation easier. Also, there are internal functions that deal with the multiplication and transpose of matrices, which saves a lot of time in algorithm prototyping.

On the other hand, Matlab is less efficient in some other perspectives. It is optimized for matrix operations, and it treats every variable as a matrix. However, the easiness comes at a cost. The memory allocation of a large matrix is by no means efficient. Normally in Matlab, for a large matrix, it is better to pre-allocate memory, to avoid the otherwise tedious dynamic allocation. In the case of pre-allocation, the Matlab assigns a large chunk of continuous virtual memory block to hold the whole matrix. In the case of dynamic allocation, which means the matrix size expands on an ad-hoc basis during calculation, Matlab tends to search for a continuous virtual memory block large enough to hold the new matrix, then initiate the procedure of copying, expanding and releasing (the old).

Occurring in the middle of the a running calculation, the dynamic memory allocation procedure of Matlab drags down the speed, sometimes even stops the calculation since

a continuous large block of memory is hard to come by. One extreme example can be considered here. A program runs with one large matrix and several much smaller ones which are to assist the data manipulation within the large matrix. The large matrix has been allocated 1GB of memory, on a PC with only 1.5GB RAM (the PC can have virtual memory larger than 1.5GB, since the operating system can virtualize space on hard disk to mimic RAM.) One more element row is now being added to expand the size of this matrix, to form a new matrix which would occupy slightly more than 1GB memory. However, this dynamic procedure requires more than 2GB virtual memory to make this transition happen. On a PC with only 1.5GB RAM, the Matlab may deem out of memory and quit itself. Or, the hard disk memory swapping would kick in. Then everything would be inevitably slowed down, since normally the hard disk has a throughput rate less than 5% of that of the physical RAM.

In reality, scenarios like this are not unfounded. For a 32 bit PC with a 32 bit Windows operating system (no matter it is Windows XP, Vista or the new Windows 7), the maximum amount of memory available for all arrays in Matlab is about 1.6GB, or even less if the installed physical RAM is less than that. One can get around this by installing 4GB RAM and utilize the $\backslash 3GB$ switch in windows' boot file, which would increase that threshold to about 2.3GB. When dealing with large scale array (matrix) operations, the amount of memory required by Matlab can easily approach this limit.

On the contrary, by estimating the peak matrix size and assigning a large enough block memory for it initially, in the above scenario, the Matlab program can rely solely on the physical memory without tapping into the hard disk virtual memory scheme. Therefore the pre-allocation is better, in Matlab, comparing to its dynamic memory allocation.

C++ however, has a much better dynamic memory allocation mechanism. C++ allows defining variables on the fly. Basically variables can be defined anywhere in a scope and initialized at the point of definition. Utilizing the constructor, the C++ compiler allocates enough memory on the heap to hold the data for the newly defined variable. However in the aforementioned scenario, a C++ program can simply use a "vector" data type to store the large matrix, in order to prevent the memory reallocation. By definition, a vector in

C++ preserve some storage space so that elements can be added or removed from the end, which makes it easily resized. In case that better ability of data insertion is needed, data types such as "deque" (double-ended queue) or "list" can be employed in C++, which enables element insertion at both ends or anywhere in the list. Best of all, the capacity of variables declared as these three data types is handled automatically.

Being an interpreted language, Matlab programs run much slower than programs of a compiled language, such as C++. Interpreted languages translate the entire program into an intermediate language that is then executed one line at a time by an interpreter. The interpreter stays in the memory all the time which introduces speed and space limitation. On the other hand, the compiled languages translate source codes directly into eventual end files written in machine instructions. The compiled program requires much less space and runs much faster. The fact that the Matlab environment itself is written in C, which is a predecessor and subset of C++, speaks for itself.

Although some elements in Matlab can be considered object-oriented, overall it is still very much a procedure-oriented programming environment. On the contrary, C++ is a Object-Oriented Programming (OOP) language. The debate of which one is better is left to the computing experts to judge. However, by utilizing inheritance and polymorphism (OOP technical terms), one can define a class of coefficient objects and re-appoint this class to all the coefficients, such as $A_{l,m,n}^{E_{xy}}, B_{l,m,n}^{E_{xy}}, C_{l,m,n}^{H_{xy}}, D_{l,m,n}^{H_{xy}}$ etc. Re-use a class will make the definition and initialization much easier.

As the MRTD algorithm itself does not change over platform transition, to migrate the algorithm to a C++ complied form would be fairly easy once the matrix operations are sorted out in C++. The real challenge comes when the display functions are to be incorporated to illustrate the field either statically or through animation. 3D Real-time field animation in C++, as the electromagnetic field calculations are being performed, can be a year-long research topic itself since it involves the shader programming of the video adapter hardware. It is better for someone who has a practical approach and profound knowledge of 3D graphic engine (e. g. engines compatible with OpenGL or DirectX).

7.2.2 An adaptive resolution MRTD algorithm

As shown in Chapter 4 and Appendix C, one of the main achievements in this thesis is the development of a level-one Haar based MRTD code in 3D. As the reader has probably noticed by now, the code is very complicated since field components intertwine with each other, yet it only deals with a single preset resolution. The level-n formulation of an 1D MRTD was explored, however it is very complicated such that a 3D level-n code would be impractical. As the 3D capability was a priority in the author's research, the plan to develop an adaptive resolution algorithm was shelved. Also there is the efficiency issue associated with Matlab. The 3D code requires massive amount of computational resources, a level-n code will have to be built in a more efficient programming environment such as C++ .

Interestingly, if the 3D capability is not required and a C++ based environment is sorted out, a 2D adaptive resolution MRTD is not impossible. One can calculate coefficient arrays associated with several low levels of Haar wavelet, for example level 2 to 5, to expand the field components whenever necessary. Then a unified 2D update function (hopefully not too complicated) can be employed to handle the iterations. There is no need to do sub-gridding, since higher levels of MRTD scheme basically just adds more wavelet expanded field components within one single cell. The PML and source expansion procedure proposed in Chapter 4 can also be easily extended to handle higher levels of Haar wavelets, once the coefficient arrays are figured out.

Although it seems easy, an 2D adaptive resolution algorithm will probably still be a very lengthy project for an experienced programmer who happens to be an electromagnetic expert too.

7.2.3 Far-field projections

As seen in Chapter 6, the 3D MRTD code currently lacks the capability to calculate the far-field pattern. A combination of Near-to-Far-field Transformation (NFT) would make the 3D code much more powerful and complete. However, there are several unsolved

issues with this proposal.

First of all, an NFT would be extremely complicated in the wavelet expansion mode. One has to figure out the mathematical formulas first. According to [66], the simplest form of FDTD far-field projection is proposed by Taflove in [67]. Taflove proposed a single frequency NFT solution by applying a sine wave at an appropriate frequency as the excitation. Fields at arbitrary points outside a virtual current surface surrounding the antenna can be computed using vector potentials. Magnitude and phase information on this equivalent current surface is determined by sampling a steady-state cycle of the sine wave at each measurement point [66]. Then the frequency-domain form of the vector potentials can be used to compute far fields [66]. This simplest FDTD form of far-field projection can not be directly applied to the 3D MRTD scheme. First of all, if a single frequency sine wave is to be applied, the MRTD time-domain method largely lose its broadband appeal, which would compromise its efficiency advantages (one-off broadband simulation). However, time-domain far-field projection methods are somewhat more complicated, even in FDTD, as briefly described in [66]. To make the problem worse, the fields are expanded into wavelet components in MRTD, which have to be recombined to yield the surface currents $\overrightarrow{J}$ and $\overrightarrow{M}$. This is troublesome, as the $\overrightarrow{J}$ and $\overrightarrow{M}$ are required to be defined on the same surface while E and H are spatially apart (would be more messy in an adaptive resolution MRTD). A proper averaging scheme has to be figured out.

Secondly, the efficiency is again an issue. By adding more calculations into the iteration loop of the 3D MRTD, the already slow program would be dragged even slower. C++ migration may improve overall speed, however the side effect of an NFT combination would still be heavy. Alternatively, if one chooses to save the equivalent currents to postprocess the NFT, a significant storage cost shall arise. Also a considerable processing time for transferring large chunks of data from RAM to hard drive has to be accounted for. Based on the current speed of the Matlab based 3D simulator, an NFT combination is just not practical. So the logical step for other researchers would be to convert the algorithm to a C++ based platform first, to add a single frequency NFT afterwards.

Bibliography

[1] A.Haar, "Zur Theorie der orthogonalen Funktionensysteme," Math. Annal., 69, 331-371, 1910.

[2] Michael Krumpholz and Linda P. B. Katehi, "MRTD: New Time-Domain Schemes Based on Multiresolution Analysis", Microwave Theory and Techniques, IEEE Transactions on Volume 44, Issue 4, April 1996 Page(s):555 - 571

[3] Pendry, J.B.; Holden, A.J.; Robbins, D.J.; Stewart, W.J. "Magnetism from conductors and enhanced nonlinear phenomena," Microwave Theory and Techniques, IEEE Transactions on, Volume: 47 Issue: 11, Nov. 1999 Page(s): 2075 -2084

[4] Xiaojing Wang, Yang Hao, "Dual-band operation of an electromagnetic band-gap patch antenna", Microwave and Optical Technology Letters. Volume 49, Issue 10, Date: October 2007, Pages: 2454-2458

[5] C.H. Chuang, C.P. Liu, T.Ismail, X. Wang, Y. Hao, C. Parini, P. G. Huggard, A.B. Krysa, J.S. Roberts and A. J. Seeds, "Integrated Photonic Electromagnetic Band Gap Antenna with Asymmetric Fabry-Perot Modulator transmitting IEEE 802.11a in Wireless-Over-Fiber system", Journal of Lightwave Technology, VOL 26, NO. 15, pp. 2671-2678 August 2008

[6] Yang Hao, Raj Mittra, "FDTD Modelling of Metamaterials: Theory and Applications", Artech House, in press, 2008

[7] Xiaojing Wang, Yang Hao, Peter S. Hall, "Dual-band Resonances of a Patch Antenna on UC-EBG Substrate," The Proceeding of Asia Pacific Microwave Conference 2005 (APMC 2005), DECEMBER 2005

[8] Fan Yang; Rahmat-Samii, Y.; "Reflection phase characterizations of the EBG ground plane for low profile wire antenna applications", IEEE Transactions on Antennas and Propagation, Volume 51, Issue 10, Part 1, Oct. 2003 Page(s):2691 - 2703

[9] Sievenpiper, D.F., "High-Impedance Electromagnetic Surfaces", PhD Thesis, University of California, Los Angeles, 1999

[10] Fan Yang; Rahmat-Samii, Y.; "Microstrip antennas integrated with electromagnetic band-gap (EBG) structures: a low mutual coupling design for array applications", IEEE Transactions on Antennas and Propagation, Volume 51, Issue 10, Part 2, Oct. 2003 Page(s):2936 - 2946

[11] Long Li; Bin Li; Hai-Xia Liu; Chang-Hong Liang; "Locally resonant cavity cell model for electromagnetic band gap structures", IEEE Transactions on Antennas and Propagation, Volume 54, Issue 1, Jan. 2006 Page(s):90 - 100

[12] D. Sievenpiper, "Forward and Backward Leaky Wave Radiation With Large Effective Aperture From an Electronically Tunable Textured Surface, " IEEE Trans. Antennas Propagation., vol. 53, no. 1, pp. 236-247, January 2005.

[13] D. Sievenpiper, J. Schaffner, H. J. Song, R. Loo, and G. Tangonan; "Two-dimensional beam steering reflector using an electrically tunable impedance surface," IEEE Trans. Antennas Propag., vol. 51, no. 10, pp.2713-2722, Oct. 2003.

[14] E. Brennan, A. Gardiner, A. Schuchinsky, V. F. Fusco; "Waves in Anisotropic Metamaterials Comprised of Finite L-C Meshes," IEEE MTT-S International Microwave Symposium, Long Beach California, 2005., 12-17 June 2005.

[15] Fusco, V.F. Schuchinsky, A.G. "2-D Anisotropic Textured Surfaces: Properties and Advanced Antenna Applications," The Second European Conference on Antennas and Propagation, EuCAP 2007, Edinburgh, UK, 2007.

[16] Fei-Ran Yang; Kuang-Ping Ma; Yongxi Qian; Itoh, T.; "A novel TEM waveguide using uniplanar compact photonic-bandgap (UC-PBG) structure", IEEE Transactions on Microwave Theory and Techniques, Volume 47, Issue 11, Nov. 1999 Page(s):2092 - 2098

[17] C.A. Moses, N. Engheta, "Electromagnetic wave propagation in the wire medium:

a complex medium with long thin inclusions", Wave Motion , Volume 34, 2001, Page(s) 301-317

[18] Stefano Maci, "PBG and EBG Background", Lecture slides presented at the European school of Antennas, Antenna Center of Excellence (ACE), April 18, 2005

[19] Sievenpiper, D.; Lijun Zhang; Broas, R.F.J.; Alexopolous, N.G.; Yablonovitch, E.; "High-impedance electromagnetic surfaces with a forbidden frequency band", IEEE Transactions on Microwave Theory and Techniques, Volume 47, Issue 11, Nov. 1999 Page(s):2059 - 2074

[20] Akimasa Hirata, "Accuracy Compensation in Direction Finding Using Patch Antenna Array With EBG Structure", Antennas and Wireless Propagation Letters, Volume 5, 2006 Page(s):1 - 3

[21] Boutayeb, H.; Denidni, T.A.; Mahdjoubi, K.; Tarot, A.-C.; Sebak, A.-R.; Talbi, L.; "Analysis and design of a cylindrical EBG-based directive antenna", IEEE Transactions on Antennas and Propagation, Volume 54, Issue 1, Jan. 2006 Page(s):211 - 219

[22] Bao, X.L.; Ammann, M.J.; Ruvio, G.; John, M.; "High Performance Circularly Polarized Antenna Based on the Fractal EBG structure", 2006 IEEE International Workshop on Antenna Technology Small Antennas and Novel Metamaterials, March 6-8, 2006 Page(s):257 - 260

[23] Li Yang; Zhenghe Feng; "Advanced methods to improve compactness in EBG design and utilization", Antennas and Propagation Society International Symposium, 2004. IEEE Volume 4, 20-25 June 2004 Page(s):3585 - 3588 Vol.4

[24] Jaehoon Kim; Rahmat-Samii, Y.; "Low-profile loop antenna above EBG structure", Antennas and Propagation Society International Symposium, 2005 IEEE, Volume 2A, 3-8 July 2005 Page(s):570 - 573 vol. 2A

[25] Neto, A.; Llombart, N.; Gerini, G.; DeMaagt, P.; "On the Optimal Radiation Bandwidth of Printed Slot Antennas Surrounded by EBGs", IEEE Transactions on Antennas and Propagation, Volume 54, Issue 4, April 2006 Page(s):1074 - 1083

[26] Dan Qu; Shafai, L.; "The performance of microstrip patch antennas over high impedance EBG substrates within and outside its bandgap", IEEE International Symposium on Microwave, Antenna, Propagation and EMC Technologies for Wireless Communications, 2005. (MAPE 2005). Volume 1, 8-12 Aug. 2005 Page(s):423 - 426 Vol. 1

[27] Hossein Mosallaei, Kamal Sarabandi, "Antenna Miniaturization and Bandwidth Enhancement Using a Reactive Impedance Substrate," IEEE Transactions on Antennas and Propagation, VOL.52, NO.9, SEPTEMBER 2004

[28] Constantine A. Balanis, "Antenna Theory: Analysis and Design," John Wiley & Sons, Inc. 1997, ISBN 0-471-59268-4

[29] Levent Sevgi, "EMC and BEM Engineering Education: Physics-Based Modeling, Hands-On Training, and Challenges", IEEE Antennas and Propagation Magazine, Vol 46, No.2, April 2004, Page(s):114 - 119

[30] Kurt L. Shlager and John B. Schneider, "A Survey of the Finite-Difference Time-Domain Literature", www.fdtd.org, June 1999

[31] K. S. Yee, "Numerical solution of initial boundary value problem involving Maxwell's equations in isotropic media", IEEE Trans. Antenna Propagation, vol. 14, pp.302-307, Mar. 1966

[32] John B. Schneider, "Lecture notes by John Schneider.", www.fdtd.org

[33] Constantine A. Balanis, "Advanced Engineering Electromagnetics", John Wiley & Sons, 1989, ISBN 0-471-62194-3

[34] Dogaru, T.; Carin, L.; "Application of Haar-wavelet-based multiresolution time-domain schemes to electromagnetic scattering problems", Antennas and Propagation, IEEE Transactions on Volume 50, Issue 6, June 2002 Page(s):774 - 784

[35] A. Taflove, Computational Electrodynamics: The Finite-Difference Time -Domain Method, Artech, Norwood, MA, 1995

[36] Stephane Mallat, "A Wavelet Tour of Signal Processing", Second Edition, Academic Press, ISBN-13:978-0-12-466606-1

[37] S. Mallat, "Multiresolution representation and wavelets", Ph.D. dissertation, Dept. Math., Univ. Pennsylvania, Philadelphia, PA, 1988

[38] Mattew N.O. Sadiku, Cajetan M. Akujuobi and Raymond C. Garcia, "An Introduction to wavelets in Electromagnetics", IEEE microwave magazine, June 2005

[39] Costas D. Sarris, Linda P. B. Katehi, "An Efficient Numerical Interface Between FDTD and Haar MRTD-Formulation and Applications", IEEE TRANSACTIONS ON MICROWAVE THEORY AND TECHNIQUES, VOL. 51, NO. 4, APRIL 2003

[40] George W. Pan, "Wavelets in Electromagnetics and Device Modeling," John Wiley & Sons, ISBN 0-471-41901-X

[41] Costas D. Sarris and L. P. B. Katehi, "Fundamental Gridding-Related Dispersion Effects in Multiresolution Time-Domain Schemes," IEEE Trans. on Microwave Theory and Techniques, VOL. 49, NO. 12, Dec 2001

[42] Roger F. Harrington, "Field Computation by Moment Methods", IEEE PRESS and Oxford University Press, New York, 1993, ISBN: 0-7803-1014-4

[43] M. Krumpholz and P. Russer, "Two-dimensional FDTD and TLM," Int. J. Num. Modeling., Vol.7, pp.141-153, Feb 1993.

[44] Xingchang Wei, Erping Li and Changhong Liang, "A New MRTD Scheme Based on Coifman Scaling Functions for the Solution of Scattering Problems," IEEE MICROWAVE AND WIRELESS COMPONENTS LETTERS, VOL. 12, NO. 10, OCTOBER 2002

[45] Traian Dogaru and Lawrence Carin, "Multiresolution Time-Domain Using CDF Biorthogonal Wavelets," IEEE TRANSACTIONS ON MICROWAVE THEORY AND TECHNIQUES, VOL. 49, NO. 5, MAY 2001

[46] Nathan Bushyager, John Papapolymerou and Manos M. Tentzeris, "A Composite Cell-Multiresolution Time-Domain Technique for the Design of Antenna Systems Including Electromagnetic Band Gap and Via-Array Structures," IEEE TRANSACTIONS ON ANTENNAS AND PROPAGATION, VOL. 53, NO. 8, AUGUST 2005

[47] Youri V. Tretiakov and Geroge W. Pan, "On Daubechies wavelet based time domain scheme," IEEE Antennas and Propagation Society International Symposium, 2001, Vol. 4, 8-13 July 2001, Page(s): 810-813

[48] Y. W. Cheong, Y. M. Less, K. H. Ra, J. G. Kang, and C. C. Shin, "Wavelet-Galerkin scheme of time-dependent inhomogeneous electromagnetic problem", IEEE Microwave Guided Wave Lett., vol. 9, pp.297-299, Aug 1999.

[49] Y. Meyer, "*ondelettes et Fonctions Splines*", Paris, France: Ecole Polytech., 1986

[50] Masafumi Fuji, Wolfgang J. R. Hoefer, "A Wavelet Formulation of the Finite-Difference Method: Full-Vector Analysis of Optical Waveguide Junctions", IEEE Journal of Quantum Electronics, Vol. 37, No. 8, August 2001

[51] M. Werthen and I. Wolff, "A novel wavelet based time domain simulation approach," IEEE Microwave Guided Wave Lett., vol 6, pp.438-440, Dec.1996.

[52] Xianyang Zhu, Traian Dogaru, and Lawrence Carin, "Three-Dimensional Biorthogonal Multi-Resolution Time-Domain Method and its Application to Electromagnetic Scattering Problems," IEEE Transcations on Antennas and Propagation, Vol. 51, No. 5, May 2003

[53] Leung Tsang, Jin Au Kong, Kuang-Hau Ding, Chi On Ao, "Scattering of Electromagnetic Waves: Numerical Simulations", John Wiley & Sons. Inc. June 2001, ISBN: 0-471-38800-9

[54] Daoxiang Wang, Edward K. N. Yung, R. S. Chen, D. Z. Ding, and W. C. Tang, "On Evaluation of the Green Function for Periodic Structures in Layered Media", IEEE Antenna and Wireless Propagation Letters, VOL 3, 2004.

[55] Jean-Pierre Berenger, "A Perfectly Matched Layer for the Absorption of Electromagnetic Waves", Journal of Computational Physics 114, 185-200, 1994

[56] Zvonimir sipus, Niksa Burum and Tin Komljenovic, "Analysis of Spherical Lens Antennas C Comparison of Two Approaches", 19th International Conference on Applied Electromagnetics and Communications (ICECom 2007), Dubrovnik, Croatia, Sep. 2007

[57] Hal Schrank, John Sanford, "A Luneberg-Lens Update", IEEE Antennas and Propagation Magazine, Vol. 37, No. 1, February 1995

[58] R. K. Luneberg, "Mathematical Theory of Optics", Brown University Press, 1944, pp. 189-212

[59] Tomos L. ap Rhys, "The Design of Radially Symmetric Lenses", IEEE TRAKSACTIOM ox ANTENSAG AND PROPAGATION, VOL. AP-18, NO. 4, JULY 1970

[60] John. R. Sanford, "Scattering by Spherically Stratified Microwave Lens Antennas", IEEE Transcations on Antennas and Propagation, Vol. 42, No. 5, May 1994

[61] A. Das, M. Mjeku, A. Nkansah, and N. J. Gomes, "Effects on IEEE 802.11 MAC throughput in wireless LAN over fiber systems," J. Lightw. Technol. vol. 25, no. 11, pp.3321-3328, Nov. 2007

[62] M. J. Crisp, S. Li, A. Watts, R. V. Penty, and I. H. White, "Uplink and downlink coverage improvements of 802.11g signals using a distributed antenna network," J. Lightw. Technol. vol. 25, no. 11, pp.3388-3395, Nov. 2007

[63] Liu, C., Seeds, A., Chadha, J., Stavrinou, P., Parry, G., Whitehead, M., Krysa, A. and Roberts, J.; "Bi-directional transmission of broadband 5.2 GHz wireless signals over fibre using a multiple-quantum-well asymmetric Fabry-Perot modulator/photodetector", Proc. Opt. Fiber Comm. Conf., Vol. 2, pp 738 - 742 (2003)

[64] Tse S., Izquierdo, B.S., Batchelor, J.C. and Langley, R.J.; "Reduced sized cells for electromagnetic bandgap structures", Electronics Letters, Volume 39, Issue 24, Page(s):1699 - 1701, 27 Nov. 2003

[65] L. Yang, M. Fan, Z. Feng, "A spiral electromagnetic bandgap (EBG) structure and its application in microstrip antenna arrays", Asia-Pacific Microwave Conference Proceedings, 2005. APMC 2005. Volume 3, Page(s): 4-7, Dec. 2005

[66] Andre F. Peterson, Scott L. Ray, Raj Mittra, "Computational Methods for Electromagnetics", IEEE Press, 1998, ISBN 0-7803-1122-1

[67] A. Taflove and M. E. Brodwin, "Numerical solution of steady-state electromagnetic scattering problems using the time-dependent Maxwell's equations," IEEE Trans. Microwave Theory Tech., vol. MTT-23, pp.623-630, Aug. 1975

Appendix A

Mathematical Preliminaries

A few useful mathematical terms are listed here, as preliminaries to facilitate further understanding of various parts in this thesis.

Inner Product: In Euclidean spaces, the inner product is defined as the dot product. Namely, the inner product of $X = [x_1, x_2, \cdots, x_n]$ and $Y = [y_1, y_2, \cdots, y_n]$ is defined as

$$\langle X, Y \rangle = \langle (x_1, x_2, \cdots, x_n), (y_1, y_2, \cdots, y_n) \rangle = \sum_{i=1}^{n} x_i y_i = x_1 y_1 + x_2 y_2 + \cdots + x_n y_n \quad \text{(A.1)}$$

In this thesis, the inner product of two functions are sometimes used. It is defined as such, for two functions f and g on a region Ω,

$$\langle f, g \rangle = \int_{\Omega} f^*(x) g(x) dx \quad \text{(A.2)}$$

where the integration is on the region Ω. The star marks the complex conjugate of a function.

Norm: The Euclidean length of a vector, that is, for a vector $V = [v_1, v_2, \cdots, v_n]$,

$$||V|| = (v_1^2 + v_2^2 + \cdots + v_n^2)^{\frac{1}{2}} \quad \text{(A.3)}$$

Three basic properties of the norm are: 1. $||V|| \geq 0$, and equals 0 if and only if $V = 0$; 2. $||cV|| = |c| \cdot ||V||$ for any number c; 3. $||V + W|| \leq ||V|| + ||W||$, also known as the triangle

inequality.

Orthogonality: In Euclidean spaces, two vectors are orthogonal if their inner product/dot product is zero. In this thesis, the term orthogonality is mainly used between functions. The definition is similar, two functions f and g are orthogonal if their inner product $\langle f, g \rangle$ is zero.

Transpose of a matrix: The transpose of a matrix A is label as A^T. The (i, j) element of A^T is obtained from the (j, i) element of A.

$$[A^T]_{ij} = [A]_{ji} \tag{A.4}$$

Inverse of a matrix: An $n \times n$ matrix P is invertible, if there exists another $n \times n$ matrix Q so that $PQ = QP = I_n$, where ordinary matrix multiplication is used to arrive at the $n \times n$ identity matrix I_n. Q is called the inverse of matrix P.

Fourier Transform: An operation that transforms a time domain function $x(t)$ into its frequency domain representation $X(\omega)$.

$$X(\omega) = \int_{-\infty}^{+\infty} x(t) e^{-j\omega t} dt \tag{A.5}$$

The inverse Fourier transform on the other hand converts to $x(t)$ back from $X(\omega)$.

$$x(t) = \frac{1}{2\pi} \int_{-\infty}^{+\infty} X(\omega) e^{j\omega t} d\omega \tag{A.6}$$

The dual function of a wavelet: For a wavelet function ψ, if there exists a function $\widetilde{\psi} \in L^2(R)$ such that their inner product $\langle \psi_{m,n}, \widetilde{\psi_{m',n'}} \rangle = \delta(m - m')\delta(n - n')$ where δ is the Dirac function, $\widetilde{\psi}$ is called the dual of ψ.

Appendix B

Mathematical Equivalence Between MRTD and FDTD

The level 1 case has been proved in Chapter 4. Here the equivalence is extended to level n Haar wavelets. Again a 1D TM simple case is used to illustrate higher level of Haar MRTD expansion. The goal here is to prove a level-n Haar MRTD with cell size Δx is equivalent to an FDTD with cell size $\frac{1}{2^n}\Delta x$. As long as the level-n MRTD provides 2^n E components after the wavelet expansion, the resolution of it will be considered to be equivalent to an FDTD with cell size $\frac{1}{2^n}\Delta x$. In other words, the emphasis here is to prove that a level-n Haar MRTD expands the E field into 2^n wavelet components.

First of all, the level-1 expansion equation is repeated here.

$$E_z(x,t) = \sum_{k,m=-\infty}^{\infty} [E_{k,m}^{\phi^0} h_k(t)\phi_m^0(x) + E_{k,m}^{\psi^0} h_k(t)\psi_m^0(x)] \tag{B.1}$$

A few simplifications and symbol modifications have been applied, to arrive at a concise form. Here $\psi^{0,0}$ represents the level 1 Haar wavelet function, same as the notation ψ^0 before. The two digit notation form suits better when dealing with higher level wavelet functions.

$$E_z(x,t) = \sum_{k,m} [E_{k,m}^{\phi^0} h_k(t)\phi_m^0(x) + E_{k,m}^{\psi^{0,0}} h_k(t)\psi_m^{0,0}(x)] \tag{B.2}$$

Then, level-2 expansion can be derived as follows:

$$E_z(x,t) = \sum_{k,m}[E_{k,m}^{\phi_0} h_k(t)\phi_m^0(x) + E_{k,m}^{\psi^{0,0}} h_k(t)\psi_m^{0,0}(x) + E_{k,m}^{\psi^{1,0}} h_k(t)\psi_m^{1,0}(x) + E_{k,m}^{\psi^{1,1}} h_k(t)\psi_m^{1,1}(x)] \tag{B.3}$$

There are two wavelets $\psi^{1,0}, \psi^{1,1}$ at level 2. Correspondingly, the equation B.3 has two E components at current level, in addition to the components representing level one expansion. At level 3, there are 4 wavelets $\psi^{2,0}, \psi^{2,1}, \psi^{2,2}, \psi^{2,3}$. At level n, the wavelets will include $\psi^{n-1,0}, \psi^{n-1,1}, \cdots, \psi^{n,2^{n-1}-1}$, in total 2^{n-1} wavelets.

So one can write the level-n Haar wavelet expansion in following form.

$$E_z(x,t) = \sum_{k,m}\sum_{p=0}^{n-1}\sum_{l=0}^{2^{p-1}}[E_{k,m}^{\phi_0} h_k(t)\phi_m^0(x) + E_{k,m}^{\psi^{p,l}} h_k(t)\psi_m^{p,l}(x)] \tag{B.4}$$

The number of E components in equation B.4 can be added up:

$$\begin{aligned} &number\ of\ E\ components = 2 + 2 + 2^2 + \cdots + 2^{n-1} \\ &= 2 + 2(1 + 2 + \cdots + 2^{n-2}) \\ &= 2 + 2(\tfrac{2^{n-1}-1}{2-1}) \\ &= 2 + 2(2^{n-1} - 1) \\ &= 2 + 2^n - 2 \\ &= 2^n \end{aligned} \tag{B.5}$$

So there are 2^n E components after a level-n Haar wavelet expansion of the field. Therefore the equivalence is proved.

Appendix C

Update Functions of 3D Level-one Haar MRTD

As the number of the update equations for the three-dimensional level-one Haar MRTD is so enormous, the complete set is listed here instead of in the text, in order to keep the conciseness. Again, in an update loop, E components are updated first. Then the source expansion procedure is applied to update the E field within the source point. Lastly the H components are updated.

$$
\begin{cases}
{E_{xy}}^{\phi\phi\phi}_{k+1,l,m,n} = A^{E_{xy}}_{l,m,n} {E_{xy}}^{\phi\phi\phi}_{k,l,m,n} + B^{E_{xy}}_{l,m,n} ({H_Z}^{\phi\phi\phi}_{k,l,m,n} - {H_Z}^{\phi\psi\phi}_{k,l,m,n} - {H_Z}^{\phi\phi\phi}_{k,l,m-1,n} + {H_Z}^{\phi\psi\phi}_{k,l,m-1,n}) \\
{E_{xy}}^{\phi\phi\psi}_{k+1,l,m,n} = A^{E_{xy}}_{l,m,n} {E_{xy}}^{\phi\phi\psi}_{k,l,m,n} + B^{E_{xy}}_{l,m,n} ({H_Z}^{\phi\phi\psi}_{k,l,m,n} - {H_Z}^{\phi\psi\psi}_{k,l,m,n} - {H_Z}^{\phi\phi\psi}_{k,l,m-1,n} + {H_Z}^{\phi\psi\psi}_{k,l,m-1,n}) \\
{E_{xy}}^{\phi\psi\phi}_{k+1,l,m,n} = A^{E_{xy}}_{l,m,n} {E_{xy}}^{\phi\psi\phi}_{k,l,m,n} + B^{E_{xy}}_{l,m,n} ({H_Z}^{\phi\phi\phi}_{k,l,m,n} + 3{H_Z}^{\phi\psi\phi}_{k,l,m,n} - {H_Z}^{\phi\phi\phi}_{k,l,m-1,n} + {H_Z}^{\phi\psi\phi}_{k,l,m-1,n}) \\
{E_{xy}}^{\phi\psi\psi}_{k+1,l,m,n} = A^{E_{xy}}_{l,m,n} {E_{xy}}^{\phi\psi\psi}_{k,l,m,n} + B^{E_{xy}}_{l,m,n} ({H_Z}^{\phi\phi\psi}_{k,l,m,n} + 3{H_Z}^{\phi\psi\psi}_{k,l,m,n} - {H_Z}^{\phi\phi\psi}_{k,l,m-1,n} + {H_Z}^{\phi\psi\psi}_{k,l,m-1,n}) \\
{E_{xy}}^{\psi\phi\phi}_{k+1,l,m,n} = A^{E_{xy}}_{l,m,n} {E_{xy}}^{\psi\phi\phi}_{k,l,m,n} + B^{E_{xy}}_{l,m,n} ({H_Z}^{\psi\phi\phi}_{k,l,m,n} - {H_Z}^{\psi\psi\phi}_{k,l,m,n} - {H_Z}^{\psi\phi\phi}_{k,l,m-1,n} + {H_Z}^{\psi\psi\phi}_{k,l,m-1,n}) \\
{E_{xy}}^{\psi\phi\psi}_{k+1,l,m,n} = A^{E_{xy}}_{l,m,n} {E_{xy}}^{\psi\phi\psi}_{k,l,m,n} + B^{E_{xy}}_{l,m,n} ({H_Z}^{\psi\phi\psi}_{k,l,m,n} - {H_Z}^{\psi\psi\psi}_{k,l,m,n} - {H_Z}^{\psi\phi\psi}_{k,l,m-1,n} + {H_Z}^{\psi\psi\psi}_{k,l,m-1,n}) \\
{E_{xy}}^{\psi\psi\phi}_{k+1,l,m,n} = A^{E_{xy}}_{l,m,n} {E_{xy}}^{\psi\psi\phi}_{k,l,m,n} + B^{E_{xy}}_{l,m,n} ({H_Z}^{\psi\phi\phi}_{k,l,m,n} + 3{H_Z}^{\psi\psi\phi}_{k,l,m,n} - {H_Z}^{\psi\phi\phi}_{k,l,m-1,n} + {H_Z}^{\psi\psi\phi}_{k,l,m-1,n}) \\
{E_{xy}}^{\psi\psi\psi}_{k+1,l,m,n} = A^{E_{xy}}_{l,m,n} {E_{xy}}^{\psi\psi\psi}_{k,l,m,n} + B^{E_{xy}}_{l,m,n} ({H_Z}^{\psi\phi\psi}_{k,l,m,n} + 3{H_Z}^{\psi\psi\psi}_{k,l,m,n} - {H_Z}^{\psi\phi\psi}_{k,l,m-1,n} + {H_Z}^{\psi\psi\psi}_{k,l,m-1,n})
\end{cases}
\tag{C.1}
$$

$$
\begin{cases}
E_{xz}{}^{\phi\phi\phi}_{k+1,l,m,n} = A^{E_{xz}}_{l,m,n} E_{xz}{}^{\phi\phi\phi}_{k,l,m,n} + B^{E_{xz}}_{l,m,n}(-H_Y{}^{\phi\phi\phi}_{k,l,m,n} + H_Y{}^{\phi\phi\psi}_{k,l,m,n} + H_Y{}^{\phi\phi\phi}_{k,l,m,n-1} - H_Y{}^{\phi\phi\psi}_{k,l,m,n-1}) \\
E_{xz}{}^{\phi\phi\psi}_{k+1,l,m,n} = A^{E_{xz}}_{l,m,n} E_{xz}{}^{\phi\phi\psi}_{k,l,m,n} + B^{E_{xz}}_{l,m,n}(-H_Y{}^{\phi\phi\phi}_{k,l,m,n} - 3H_Y{}^{\phi\phi\psi}_{k,l,m,n} + H_Y{}^{\phi\phi\phi}_{k,l,m,n-1} - H_Y{}^{\phi\phi\psi}_{k,l,m,n-1}) \\
E_{xz}{}^{\phi\psi\phi}_{k+1,l,m,n} = A^{E_{xz}}_{l,m,n} E_{xz}{}^{\phi\psi\phi}_{k,l,m,n} + B^{E_{xz}}_{l,m,n}(-H_Y{}^{\phi\psi\phi}_{k,l,m,n} + H_Y{}^{\phi\psi\psi}_{k,l,m,n} + H_Y{}^{\phi\psi\phi}_{k,l,m,n-1} - H_Y{}^{\phi\psi\psi}_{k,l,m,n-1}) \\
E_{xz}{}^{\phi\psi\psi}_{k+1,l,m,n} = A^{E_{xz}}_{l,m,n} E_{xz}{}^{\phi\psi\psi}_{k,l,m,n} + B^{E_{xz}}_{l,m,n}(-H_Y{}^{\phi\psi\phi}_{k,l,m,n} - 3H_Y{}^{\phi\psi\psi}_{k,l,m,n} + H_Y{}^{\phi\psi\phi}_{k,l,m,n-1} - H_Y{}^{\phi\psi\psi}_{k,l,m,n-1}) \\
E_{xz}{}^{\psi\phi\phi}_{k+1,l,m,n} = A^{E_{xz}}_{l,m,n} E_{xz}{}^{\psi\phi\phi}_{k,l,m,n} + B^{E_{xz}}_{l,m,n}(-H_Y{}^{\psi\phi\phi}_{k,l,m,n} + H_Y{}^{\psi\phi\psi}_{k,l,m,n} + H_Y{}^{\psi\phi\phi}_{k,l,m,n-1} - H_Y{}^{\psi\phi\psi}_{k,l,m,n-1}) \\
E_{xz}{}^{\psi\phi\psi}_{k+1,l,m,n} = A^{E_{xz}}_{l,m,n} E_{xz}{}^{\psi\phi\psi}_{k,l,m,n} + B^{E_{xz}}_{l,m,n}(-H_Y{}^{\psi\phi\phi}_{k,l,m,n} - 3H_Y{}^{\psi\phi\psi}_{k,l,m,n} + H_Y{}^{\psi\phi\phi}_{k,l,m,n-1} - H_Y{}^{\psi\phi\psi}_{k,l,m,n-1}) \\
E_{xz}{}^{\psi\psi\phi}_{k+1,l,m,n} = A^{E_{xz}}_{l,m,n} E_{xz}{}^{\psi\psi\phi}_{k,l,m,n} + B^{E_{xz}}_{l,m,n}(-H_Y{}^{\psi\psi\phi}_{k,l,m,n} + H_Y{}^{\psi\psi\psi}_{k,l,m,n} + H_Y{}^{\psi\psi\phi}_{k,l,m,n-1} - H_Y{}^{\psi\psi\psi}_{k,l,m,n-1}) \\
E_{xz}{}^{\psi\psi\psi}_{k+1,l,m,n} = A^{E_{xz}}_{l,m,n} E_{xz}{}^{\psi\psi\psi}_{k,l,m,n} + B^{E_{xz}}_{l,m,n}(-H_Y{}^{\psi\psi\phi}_{k,l,m,n} - 3H_Y{}^{\psi\psi\psi}_{k,l,m,n} + H_Y{}^{\psi\psi\phi}_{k,l,m,n-1} - H_Y{}^{\psi\psi\psi}_{k,l,m,n-1})
\end{cases}
\tag{C.2}
$$

$$
\begin{cases}
E_{yz}{}^{\phi\phi\phi}_{k+1,l,m,n} = A^{E_{yz}}_{l,m,n} E_{yz}{}^{\phi\phi\phi}_{k,l,m,n} + B^{E_{yz}}_{l,m,n}(H_X{}^{\phi\phi\phi}_{k,l,m,n} - H_X{}^{\phi\phi\psi}_{k,l,m,n} - H_X{}^{\phi\phi\phi}_{k,l,m,n-1} + H_X{}^{\phi\phi\psi}_{k,l,m,n-1}) \\
E_{yz}{}^{\phi\phi\psi}_{k+1,l,m,n} = A^{E_{yz}}_{l,m,n} E_{yz}{}^{\phi\phi\psi}_{k,l,m,n} + B^{E_{yz}}_{l,m,n}(H_X{}^{\phi\phi\phi}_{k,l,m,n} + 3H_X{}^{\phi\phi\psi}_{k,l,m,n} - H_X{}^{\phi\phi\phi}_{k,l,m,n-1} + H_X{}^{\phi\phi\psi}_{k,l,m,n-1}) \\
E_{yz}{}^{\phi\psi\phi}_{k+1,l,m,n} = A^{E_{yz}}_{l,m,n} E_{yz}{}^{\phi\psi\phi}_{k,l,m,n} + B^{E_{yz}}_{l,m,n}(H_X{}^{\phi\psi\phi}_{k,l,m,n} - H_X{}^{\phi\psi\psi}_{k,l,m,n} - H_X{}^{\phi\psi\phi}_{k,l,m,n-1} + H_X{}^{\phi\psi\psi}_{k,l,m,n-1}) \\
E_{yz}{}^{\phi\psi\psi}_{k+1,l,m,n} = A^{E_{yz}}_{l,m,n} E_{yz}{}^{\phi\psi\psi}_{k,l,m,n} + B^{E_{yz}}_{l,m,n}(H_X{}^{\phi\psi\phi}_{k,l,m,n} + 3H_X{}^{\phi\psi\psi}_{k,l,m,n} - H_X{}^{\phi\psi\phi}_{k,l,m,n-1} + H_X{}^{\phi\psi\psi}_{k,l,m,n-1}) \\
E_{yz}{}^{\psi\phi\phi}_{k+1,l,m,n} = A^{E_{yz}}_{l,m,n} E_{yz}{}^{\psi\phi\phi}_{k,l,m,n} + B^{E_{yz}}_{l,m,n}(H_X{}^{\psi\phi\phi}_{k,l,m,n} - H_X{}^{\psi\phi\psi}_{k,l,m,n} - H_X{}^{\psi\phi\phi}_{k,l,m,n-1} + H_X{}^{\psi\phi\psi}_{k,l,m,n-1}) \\
E_{yz}{}^{\psi\phi\psi}_{k+1,l,m,n} = A^{E_{yz}}_{l,m,n} E_{yz}{}^{\psi\phi\psi}_{k,l,m,n} + B^{E_{yz}}_{l,m,n}(H_X{}^{\psi\phi\phi}_{k,l,m,n} + 3H_X{}^{\psi\phi\psi}_{k,l,m,n} - H_X{}^{\psi\phi\phi}_{k,l,m,n-1} + H_X{}^{\psi\phi\psi}_{k,l,m,n-1}) \\
E_{yz}{}^{\psi\psi\phi}_{k+1,l,m,n} = A^{E_{yz}}_{l,m,n} E_{yz}{}^{\psi\psi\phi}_{k,l,m,n} + B^{E_{yz}}_{l,m,n}(H_X{}^{\psi\psi\phi}_{k,l,m,n} - H_X{}^{\psi\psi\psi}_{k,l,m,n} - H_X{}^{\psi\psi\phi}_{k,l,m,n-1} + H_X{}^{\psi\psi\psi}_{k,l,m,n-1}) \\
E_{yz}{}^{\psi\psi\psi}_{k+1,l,m,n} = A^{E_{yz}}_{l,m,n} E_{yz}{}^{\psi\psi\psi}_{k,l,m,n} + B^{E_{yz}}_{l,m,n}(H_X{}^{\psi\psi\phi}_{k,l,m,n} + 3H_X{}^{\psi\psi\psi}_{k,l,m,n} - H_X{}^{\psi\psi\phi}_{k,l,m,n-1} + H_X{}^{\psi\psi\psi}_{k,l,m,n-1})
\end{cases}
\tag{C.3}
$$

$$
\begin{cases}
E_{yx}{}^{\phi\phi\phi}_{k+1,l,m,n} = A^{E_{yx}}_{l,m,n} E_{yx}{}^{\phi\phi\phi}_{k,l,m,n} + B^{E_{yx}}_{l,m,n}(-H_Z{}^{\phi\phi\phi}_{k,l,m,n} + H_Z{}^{\psi\phi\phi}_{k,l,m,n} + H_Z{}^{\phi\phi\phi}_{k,l-1,m,n} - H_Z{}^{\psi\phi\phi}_{k,l-1,m,n}) \\
E_{yx}{}^{\phi\phi\psi}_{k+1,l,m,n} = A^{E_{yx}}_{l,m,n} E_{yx}{}^{\phi\phi\psi}_{k,l,m,n} + B^{E_{yx}}_{l,m,n}(-H_Z{}^{\phi\phi\psi}_{k,l,m,n} + H_Z{}^{\psi\phi\psi}_{k,l,m,n} + H_Z{}^{\phi\phi\psi}_{k,l-1,m,n} - H_Z{}^{\psi\phi\psi}_{k,l-1,m,n}) \\
E_{yx}{}^{\phi\psi\phi}_{k+1,l,m,n} = A^{E_{yx}}_{l,m,n} E_{yx}{}^{\phi\psi\phi}_{k,l,m,n} + B^{E_{yx}}_{l,m,n}(-H_Z{}^{\phi\psi\phi}_{k,l,m,n} + H_Z{}^{\psi\psi\phi}_{k,l,m,n} + H_Z{}^{\phi\psi\phi}_{k,l-1,m,n} - H_Z{}^{\psi\psi\phi}_{k,l-1,m,n}) \\
E_{yx}{}^{\phi\psi\psi}_{k+1,l,m,n} = A^{E_{yx}}_{l,m,n} E_{yx}{}^{\phi\psi\psi}_{k,l,m,n} + B^{E_{yx}}_{l,m,n}(-H_Z{}^{\phi\psi\psi}_{k,l,m,n} + H_Z{}^{\psi\psi\psi}_{k,l,m,n} + H_Z{}^{\phi\psi\psi}_{k,l-1,m,n} - H_Z{}^{\psi\psi\psi}_{k,l-1,m,n}) \\
E_{yx}{}^{\psi\phi\phi}_{k+1,l,m,n} = A^{E_{yx}}_{l,m,n} E_{yx}{}^{\psi\phi\phi}_{k,l,m,n} + B^{E_{yx}}_{l,m,n}(-H_Z{}^{\phi\phi\phi}_{k,l,m,n} - 3H_Z{}^{\psi\phi\phi}_{k,l,m,n} + H_Z{}^{\phi\phi\phi}_{k,l-1,m,n} - H_Z{}^{\psi\phi\phi}_{k,l-1,m,n}) \\
E_{yx}{}^{\psi\phi\psi}_{k+1,l,m,n} = A^{E_{yx}}_{l,m,n} E_{yx}{}^{\psi\phi\psi}_{k,l,m,n} + B^{E_{yx}}_{l,m,n}(-H_Z{}^{\phi\phi\psi}_{k,l,m,n} - 3H_Z{}^{\psi\phi\psi}_{k,l,m,n} + H_Z{}^{\phi\phi\psi}_{k,l-1,m,n} - H_Z{}^{\psi\phi\psi}_{k,l-1,m,n}) \\
E_{yx}{}^{\psi\psi\phi}_{k+1,l,m,n} = A^{E_{yx}}_{l,m,n} E_{yx}{}^{\psi\psi\phi}_{k,l,m,n} + B^{E_{yx}}_{l,m,n}(-H_Z{}^{\phi\psi\phi}_{k,l,m,n} - 3H_Z{}^{\psi\psi\phi}_{k,l,m,n} + H_Z{}^{\phi\psi\phi}_{k,l-1,m,n} - H_Z{}^{\psi\psi\phi}_{k,l-1,m,n}) \\
E_{yx}{}^{\psi\psi\psi}_{k+1,l,m,n} = A^{E_{yx}}_{l,m,n} E_{yx}{}^{\psi\psi\psi}_{k,l,m,n} + B^{E_{yx}}_{l,m,n}(-H_Z{}^{\phi\psi\psi}_{k,l,m,n} - 3H_Z{}^{\psi\psi\psi}_{k,l,m,n} + H_Z{}^{\phi\psi\psi}_{k,l-1,m,n} - H_Z{}^{\psi\psi\psi}_{k,l-1,m,n})
\end{cases}
\tag{C.4}
$$

$$\begin{cases}
Ezx^{\phi\phi\phi}_{k+1,l,m,n} = A^{Ezx}_{l,m,n} Ezx^{\phi\phi\phi}_{k,l,m,n} + B^{Ezx}_{l,m,n}(HY^{\phi\phi\phi}_{k,l,m,n} - HY^{\psi\phi\phi}_{k,l,m,n} - HY^{\phi\phi\phi}_{k,l-1,m,n} + HY^{\psi\phi\phi}_{k,l-1,m,n}) \\
Ezx^{\phi\phi\psi}_{k+1,l,m,n} = A^{Ezx}_{l,m,n} Ezx^{\phi\phi\psi}_{k,l,m,n} + B^{Ezx}_{l,m,n}(HY^{\phi\phi\psi}_{k,l,m,n} - HY^{\psi\phi\psi}_{k,l,m,n} - HY^{\phi\phi\psi}_{k,l-1,m,n} + HY^{\psi\phi\psi}_{k,l-1,m,n}) \\
Ezx^{\phi\psi\phi}_{k+1,l,m,n} = A^{Ezx}_{l,m,n} Ezx^{\phi\psi\phi}_{k,l,m,n} + B^{Ezx}_{l,m,n}(HY^{\phi\psi\phi}_{k,l,m,n} - HY^{\psi\psi\phi}_{k,l,m,n} - HY^{\phi\psi\phi}_{k,l-1,m,n} + HY^{\psi\psi\phi}_{k,l-1,m,n}) \\
Ezx^{\phi\psi\psi}_{k+1,l,m,n} = A^{Ezx}_{l,m,n} Ezx^{\phi\psi\psi}_{k,l,m,n} + B^{Ezx}_{l,m,n}(HY^{\phi\psi\psi}_{k,l,m,n} - HY^{\psi\psi\psi}_{k,l,m,n} - HY^{\phi\psi\psi}_{k,l-1,m,n} + HY^{\psi\psi\psi}_{k,l-1,m,n}) \\
Ezx^{\psi\phi\phi}_{k+1,l,m,n} = A^{Ezx}_{l,m,n} Ezx^{\psi\phi\phi}_{k,l,m,n} + B^{Ezx}_{l,m,n}(HY^{\phi\phi\phi}_{k,l,m,n} + 3HY^{\psi\phi\phi}_{k,l,m,n} - HY^{\phi\phi\phi}_{k,l-1,m,n} + HY^{\psi\phi\phi}_{k,l-1,m,n}) \\
Ezx^{\psi\phi\psi}_{k+1,l,m,n} = A^{Ezx}_{l,m,n} Ezx^{\psi\phi\psi}_{k,l,m,n} + B^{Ezx}_{l,m,n}(HY^{\phi\phi\psi}_{k,l,m,n} + 3HY^{\psi\phi\psi}_{k,l,m,n} - HY^{\phi\phi\psi}_{k,l-1,m,n} + HY^{\psi\phi\psi}_{k,l-1,m,n}) \\
Ezx^{\psi\psi\phi}_{k+1,l,m,n} = A^{Ezx}_{l,m,n} Ezx^{\psi\psi\phi}_{k,l,m,n} + B^{Ezx}_{l,m,n}(HY^{\phi\psi\phi}_{k,l,m,n} + 3HY^{\psi\psi\phi}_{k,l,m,n} - HY^{\phi\psi\phi}_{k,l-1,m,n} + HY^{\psi\psi\phi}_{k,l-1,m,n}) \\
Ezx^{\psi\psi\psi}_{k+1,l,m,n} = A^{Ezx}_{l,m,n} Ezx^{\psi\psi\psi}_{k,l,m,n} + B^{Ezx}_{l,m,n}(HY^{\phi\psi\psi}_{k,l,m,n} + 3HY^{\psi\psi\psi}_{k,l,m,n} - HY^{\phi\psi\psi}_{k,l-1,m,n} + HY^{\psi\psi\psi}_{k,l-1,m,n})
\end{cases} \tag{C.5}$$

$$\begin{cases}
Ezy^{\phi\phi\phi}_{k+1,l,m,n} = A^{Ezy}_{l,m,n} Ezy^{\phi\phi\phi}_{k,l,m,n} + B^{Ezy}_{l,m,n}(-HX^{\phi\phi\phi}_{k,l,m,n} + HX^{\phi\psi\phi}_{k,l,m,n} + HX^{\phi\phi\phi}_{k,l,m-1,n} - HX^{\phi\psi\phi}_{k,l,m-1,n}) \\
Ezy^{\phi\phi\psi}_{k+1,l,m,n} = A^{Ezy}_{l,m,n} Ezy^{\phi\phi\psi}_{k,l,m,n} + B^{Ezy}_{l,m,n}(-HX^{\phi\phi\psi}_{k,l,m,n} + HX^{\phi\psi\psi}_{k,l,m,n} + HX^{\phi\phi\psi}_{k,l,m-1,n} - HX^{\phi\psi\psi}_{k,l,m-1,n}) \\
Ezy^{\phi\psi\phi}_{k+1,l,m,n} = A^{Ezy}_{l,m,n} Ezy^{\phi\psi\phi}_{k,l,m,n} + B^{Ezy}_{l,m,n}(-HX^{\phi\phi\phi}_{k,l,m,n} - 3HX^{\phi\psi\phi}_{k,l,m,n} + HX^{\phi\phi\phi}_{k,l,m-1,n} - HX^{\phi\psi\phi}_{k,l,m-1,n}) \\
Ezy^{\phi\psi\psi}_{k+1,l,m,n} = A^{Ezy}_{l,m,n} Ezy^{\phi\psi\psi}_{k,l,m,n} + B^{Ezy}_{l,m,n}(-HX^{\phi\phi\psi}_{k,l,m,n} - 3HX^{\phi\psi\psi}_{k,l,m,n} + HX^{\phi\phi\psi}_{k,l,m-1,n} - HX^{\phi\psi\psi}_{k,l,m-1,n}) \\
Ezy^{\psi\phi\phi}_{k+1,l,m,n} = A^{Ezy}_{l,m,n} Ezy^{\psi\phi\phi}_{k,l,m,n} + B^{Ezy}_{l,m,n}(-HX^{\psi\phi\phi}_{k,l,m,n} + HX^{\psi\psi\phi}_{k,l,m,n} + HX^{\psi\phi\phi}_{k,l,m-1,n} - HX^{\psi\psi\phi}_{k,l,m-1,n}) \\
Ezy^{\psi\phi\psi}_{k+1,l,m,n} = A^{Ezy}_{l,m,n} Ezy^{\psi\phi\psi}_{k,l,m,n} + B^{Ezy}_{l,m,n}(-HX^{\psi\phi\psi}_{k,l,m,n} + HX^{\psi\psi\psi}_{k,l,m,n} + HX^{\psi\phi\psi}_{k,l,m-1,n} - HX^{\psi\psi\psi}_{k,l,m-1,n}) \\
Ezy^{\psi\psi\phi}_{k+1,l,m,n} = A^{Ezy}_{l,m,n} Ezy^{\psi\psi\phi}_{k,l,m,n} + B^{Ezy}_{l,m,n}(-HX^{\psi\phi\phi}_{k,l,m,n} - 3HX^{\psi\psi\phi}_{k,l,m,n} + HX^{\psi\phi\phi}_{k,l,m-1,n} - HX^{\psi\psi\phi}_{k,l,m-1,n}) \\
Ezy^{\psi\psi\psi}_{k+1,l,m,n} = A^{Ezy}_{l,m,n} Ezy^{\psi\psi\psi}_{k,l,m,n} + B^{Ezy}_{l,m,n}(-HX^{\psi\phi\psi}_{k,l,m,n} - 3HX^{\psi\psi\psi}_{k,l,m,n} + HX^{\psi\phi\psi}_{k,l,m-1,n} - HX^{\psi\psi\psi}_{k,l,m-1,n})
\end{cases} \tag{C.6}$$

If k= 1,

$$\begin{cases}
E1_k = source(k); \\
E2_k = 0; \\
E3_k = 0; \\
E4_k = 0; \\
E5_k = 0; \\
E6_k = 0; \\
E7_k = 0; \\
E8_k = 0;
\end{cases} \tag{C.7}$$

Else

$$\begin{cases} E1_k = source(k); \\ E2_k = E_Z^{\phi\phi\phi}_{k,sX,sY,sZ} + E_Z^{\phi\phi\psi}_{k,sX,sY,sZ} + E_Z^{\phi\psi\phi}_{k,sX,sY,sZ} + E_Z^{\phi\psi\psi}_{k,sX,sY,sZ} \\ -E_Z^{\psi\phi\phi}_{k,sX,sY,sZ} - E_Z^{\psi\phi\psi}_{k,sX,sY,sZ} - E_Z^{\psi\psi\phi}_{k,sX,sY,sZ} - E_Z^{\psi\psi\psi}_{k,sX,sY,sZ}; \\ E3_k = E_Z^{\phi\phi\phi}_{k,sX,sY,sZ} + E_Z^{\phi\phi\psi}_{k,sX,sY,sZ} - E_Z^{\phi\psi\phi}_{k,sX,sY,sZ} - E_Z^{\phi\psi\psi}_{k,sX,sY,sZ} \\ +E_Z^{\psi\phi\phi}_{k,sX,sY,sZ} + E_Z^{\psi\phi\psi}_{k,sX,sY,sZ} - E_Z^{\psi\psi\phi}_{k,sX,sY,sZ} - E_Z^{\psi\psi\psi}_{k,sX,sY,sZ}; \\ E4_k = E_Z^{\phi\phi\phi}_{k,sX,sY,sZ} + E_Z^{\phi\phi\psi}_{k,sX,sY,sZ} - E_Z^{\phi\psi\phi}_{k,sX,sY,sZ} - E_Z^{\phi\psi\psi}_{k,sX,sY,sZ} \\ -E_Z^{\psi\phi\phi}_{k,sX,sY,sZ} - E_Z^{\psi\phi\psi}_{k,sX,sY,sZ} + E_Z^{\psi\psi\phi}_{k,sX,sY,sZ} + E_Z^{\psi\psi\psi}_{k,sX,sY,sZ}; \\ E5_k = E_Z^{\phi\phi\phi}_{k,sX,sY,sZ} - E_Z^{\phi\phi\psi}_{k,sX,sY,sZ} + E_Z^{\phi\psi\phi}_{k,sX,sY,sZ} - E_Z^{\phi\psi\psi}_{k,sX,sY,sZ} \\ +E_Z^{\psi\phi\phi}_{k,sX,sY,sZ} - E_Z^{\psi\phi\psi}_{k,sX,sY,sZ} + E_Z^{\psi\psi\phi}_{k,sX,sY,sZ} - E_Z^{\psi\psi\psi}_{k,sX,sY,sZ}; \\ E6_k = E_Z^{\phi\phi\phi}_{k,sX,sY,sZ} - E_Z^{\phi\phi\psi}_{k,sX,sY,sZ} + E_Z^{\phi\psi\phi}_{k,sX,sY,sZ} - E_Z^{\phi\psi\psi}_{k,sX,sY,sZ} \\ +E_Z^{\psi\phi\phi}_{k,sX,sY,sZ} - E_Z^{\psi\phi\psi}_{k,sX,sY,sZ} - E_Z^{\psi\psi\phi}_{k,sX,sY,sZ} + E_Z^{\psi\psi\psi}_{k,sX,sY,sZ}; \\ E7_k = E_Z^{\phi\phi\phi}_{k,sX,sY,sZ} - E_Z^{\phi\phi\psi}_{k,sX,sY,sZ} - E_Z^{\phi\psi\phi}_{k,sX,sY,sZ} + E_Z^{\phi\psi\psi}_{k,sX,sY,sZ} \\ +E_Z^{\psi\phi\phi}_{k,sX,sY,sZ} - E_Z^{\psi\phi\psi}_{k,sX,sY,sZ} - E_Z^{\psi\psi\phi}_{k,sX,sY,sZ} + E_Z^{\psi\psi\psi}_{k,sX,sY,sZ}; \\ E8_k = E_Z^{\phi\phi\phi}_{k,sX,sY,sZ} - E_Z^{\phi\phi\psi}_{k,sX,sY,sZ} - E_Z^{\phi\psi\phi}_{k,sX,sY,sZ} + E_Z^{\phi\psi\psi}_{k,sX,sY,sZ} \\ -E_Z^{\psi\phi\phi}_{k,sX,sY,sZ} + E_Z^{\psi\phi\psi}_{k,sX,sY,sZ} + E_Z^{\psi\psi\phi}_{k,sX,sY,sZ} - E_Z^{\psi\psi\psi}_{k,sX,sY,sZ}; \end{cases} \tag{C.8}$$

End

$$\begin{cases} E_Z^{\phi\phi\phi}_{k,sX,sY,sZ} = 0.125 * (E1_k + E2_k + E3_k + E4_k + E5_k + E6_k + E7_k + E8_k); \\ E_Z^{\phi\phi\psi}_{k,sX,sY,sZ} = 0.125 * (E1_k + E2_k + E3_k + E4_k - E5_k - E6_k - E7_k - E8_k); \\ E_Z^{\phi\psi\phi}_{k,sX,sY,sZ} = 0.125 * (E1_k + E2_k - E3_k - E4_k + E5_k + E6_k - E7_k - E8_k); \\ E_Z^{\phi\psi\psi}_{k,sX,sY,sZ} = 0.125 * (E1_k + E2_k - E3_k - E4_k - E5_k - E6_k + E7_k + E8_k); \\ E_Z^{\psi\phi\phi}_{k,sX,sY,sZ} = 0.125 * (E1_k - E2_k + E3_k - E4_k + E5_k - E6_k + E7_k - E8_k); \\ E_Z^{\psi\phi\psi}_{k,sX,sY,sZ} = 0.125 * (E1_k - E2_k + E3_k - E4_k - E5_k + E6_k - E7_k + E8_k); \\ E_Z^{\psi\psi\phi}_{k,sX,sY,sZ} = 0.125 * (E1_k - E2_k - E3_k + E4_k + E5_k - E6_k - E7_k + E8_k); \\ E_Z^{\psi\psi\psi}_{k,sX,sY,sZ} = 0.125 * (E1_k - E2_k - E3_k + E4_k - E5_k + E6_k + E7_k - E8_k); \end{cases} \tag{C.9}$$

$$
\begin{cases}
H_{xy}{}^{\phi\phi\phi}_{k,l,m,n} = C^{H_{xy}}_{l,m,n} H_{xy}{}^{\phi\phi\phi}_{k-1,l,m,n} + D^{H_{xy}}_{l,m,n}(E_Z{}^{\phi\phi\phi}_{k,l,m,n} + E_Z{}^{\phi\psi\phi}_{k,l,m,n} - E_Z{}^{\phi\phi\phi}_{k,l,m+1,n} - E_Z{}^{\phi\psi\phi}_{k,l,m+1,n}) \\
H_{xy}{}^{\phi\phi\psi}_{k,l,m,n} = C^{H_{xy}}_{l,m,n} H_{xy}{}^{\phi\phi\psi}_{k-1,l,m,n} + D^{H_{xy}}_{l,m,n}(E_Z{}^{\phi\phi\psi}_{k,l,m,n} + E_Z{}^{\phi\psi\psi}_{k,l,m,n} - E_Z{}^{\phi\phi\psi}_{k,l,m+1,n} - E_Z{}^{\phi\psi\psi}_{k,l,m+1,n}) \\
H_{xy}{}^{\phi\psi\phi}_{k,l,m,n} = C^{H_{xy}}_{l,m,n} H_{xy}{}^{\phi\psi\phi}_{k-1,l,m,n} + D^{H_{xy}}_{l,m,n}(-E_Z{}^{\phi\phi\phi}_{k,l,m,n} + 3E_Z{}^{\phi\psi\phi}_{k,l,m,n} + E_Z{}^{\phi\phi\phi}_{k,l,m+1,n} + E_Z{}^{\phi\psi\phi}_{k,l,m+1,n}) \\
H_{xy}{}^{\phi\psi\psi}_{k,l,m,n} = C^{H_{xy}}_{l,m,n} H_{xy}{}^{\phi\psi\psi}_{k-1,l,m,n} + D^{H_{xy}}_{l,m,n}(-E_Z{}^{\phi\phi\psi}_{k,l,m,n} + 3E_Z{}^{\phi\psi\psi}_{k,l,m,n} + E_Z{}^{\phi\phi\psi}_{k,l,m+1,n} + E_Z{}^{\phi\psi\psi}_{k,l,m+1,n}) \\
H_{xy}{}^{\psi\phi\phi}_{k,l,m,n} = C^{H_{xy}}_{l,m,n} H_{xy}{}^{\psi\phi\phi}_{k-1,l,m,n} + D^{H_{xy}}_{l,m,n}(E_Z{}^{\psi\phi\phi}_{k,l,m,n} + E_Z{}^{\psi\psi\phi}_{k,l,m,n} - E_Z{}^{\psi\phi\phi}_{k,l,m+1,n} - E_Z{}^{\psi\psi\phi}_{k,l,m+1,n}) \\
H_{xy}{}^{\psi\phi\psi}_{k,l,m,n} = C^{H_{xy}}_{l,m,n} H_{xy}{}^{\psi\phi\psi}_{k-1,l,m,n} + D^{H_{xy}}_{l,m,n}(E_Z{}^{\psi\phi\psi}_{k,l,m,n} + E_Z{}^{\psi\psi\psi}_{k,l,m,n} - E_Z{}^{\psi\phi\psi}_{k,l,m+1,n} - E_Z{}^{\psi\psi\psi}_{k,l,m+1,n}) \\
H_{xy}{}^{\psi\psi\phi}_{k,l,m,n} = C^{H_{xy}}_{l,m,n} H_{xy}{}^{\psi\psi\phi}_{k-1,l,m,n} + D^{H_{xy}}_{l,m,n}(-E_Z{}^{\psi\phi\phi}_{k,l,m,n} + 3E_Z{}^{\psi\psi\phi}_{k,l,m,n} + E_Z{}^{\psi\phi\phi}_{k,l,m+1,n} + E_Z{}^{\psi\psi\phi}_{k,l,m+1,n}) \\
H_{xy}{}^{\psi\psi\psi}_{k,l,m,n} = C^{H_{xy}}_{l,m,n} H_{xy}{}^{\psi\psi\psi}_{k-1,l,m,n} + D^{H_{xy}}_{l,m,n}(-E_Z{}^{\psi\phi\psi}_{k,l,m,n} + 3E_Z{}^{\psi\psi\psi}_{k,l,m,n} + E_Z{}^{\psi\phi\psi}_{k,l,m+1,n} + E_Z{}^{\psi\psi\psi}_{k,l,m+1,n})
\end{cases}
\tag{C.10}
$$

$$
\begin{cases}
H_{xz}{}^{\phi\phi\phi}_{k,l,m,n} = C^{H_{xz}}_{l,m,n} H_{xz}{}^{\phi\phi\phi}_{k-1,l,m,n} + D^{H_{xz}}_{l,m,n}(-E_Y{}^{\phi\phi\phi}_{k,l,m,n} - E_Y{}^{\phi\phi\psi}_{k,l,m,n} + E_Y{}^{\phi\phi\phi}_{k,l,m,n+1} + E_Y{}^{\phi\phi\psi}_{k,l,m,n+1}) \\
H_{xz}{}^{\phi\phi\psi}_{k,l,m,n} = C^{H_{xz}}_{l,m,n} H_{xz}{}^{\phi\phi\psi}_{k-1,l,m,n} + D^{H_{xz}}_{l,m,n}(E_Y{}^{\phi\phi\phi}_{k,l,m,n} - 3E_Y{}^{\phi\phi\psi}_{k,l,m,n} - E_Y{}^{\phi\phi\phi}_{k,l,m,n+1} - E_Y{}^{\phi\phi\psi}_{k,l,m,n+1}) \\
H_{xz}{}^{\phi\psi\phi}_{k,l,m,n} = C^{H_{xz}}_{l,m,n} H_{xz}{}^{\phi\psi\phi}_{k-1,l,m,n} + D^{H_{xz}}_{l,m,n}(-E_Y{}^{\phi\psi\phi}_{k,l,m,n} - E_Y{}^{\phi\psi\psi}_{k,l,m,n} + E_Y{}^{\phi\psi\phi}_{k,l,m,n+1} + E_Y{}^{\phi\psi\psi}_{k,l,m,n+1}) \\
H_{xz}{}^{\phi\psi\psi}_{k,l,m,n} = C^{H_{xz}}_{l,m,n} H_{xz}{}^{\phi\psi\psi}_{k-1,l,m,n} + D^{H_{xz}}_{l,m,n}(E_Y{}^{\phi\psi\phi}_{k,l,m,n} - 3E_Y{}^{\phi\psi\psi}_{k,l,m,n} - E_Y{}^{\phi\psi\phi}_{k,l,m,n+1} - E_Y{}^{\phi\psi\psi}_{k,l,m,n+1}) \\
H_{xz}{}^{\psi\phi\phi}_{k,l,m,n} = C^{H_{xz}}_{l,m,n} H_{xz}{}^{\psi\phi\phi}_{k-1,l,m,n} + D^{H_{xz}}_{l,m,n}(-E_Y{}^{\psi\phi\phi}_{k,l,m,n} - E_Y{}^{\psi\phi\psi}_{k,l,m,n} + E_Y{}^{\psi\phi\phi}_{k,l,m,n+1} + E_Y{}^{\psi\phi\psi}_{k,l,m,n+1}) \\
H_{xz}{}^{\psi\phi\psi}_{k,l,m,n} = C^{H_{xz}}_{l,m,n} H_{xz}{}^{\psi\phi\psi}_{k-1,l,m,n} + D^{H_{xz}}_{l,m,n}(E_Y{}^{\psi\phi\phi}_{k,l,m,n} - 3E_Y{}^{\psi\phi\psi}_{k,l,m,n} - E_Y{}^{\psi\phi\phi}_{k,l,m,n+1} - E_Y{}^{\psi\phi\psi}_{k,l,m,n+1}) \\
H_{xz}{}^{\psi\psi\phi}_{k,l,m,n} = C^{H_{xz}}_{l,m,n} H_{xz}{}^{\psi\psi\phi}_{k-1,l,m,n} + D^{H_{xz}}_{l,m,n}(-E_Y{}^{\psi\psi\phi}_{k,l,m,n} - E_Y{}^{\psi\psi\psi}_{k,l,m,n} + E_Y{}^{\psi\psi\phi}_{k,l,m,n+1} + E_Y{}^{\psi\psi\psi}_{k,l,m,n+1}) \\
H_{xz}{}^{\psi\psi\psi}_{k,l,m,n} = C^{H_{xz}}_{l,m,n} H_{xz}{}^{\psi\psi\psi}_{k-1,l,m,n} + D^{H_{xz}}_{l,m,n}(E_Y{}^{\psi\psi\phi}_{k,l,m,n} - 3E_Y{}^{\psi\psi\psi}_{k,l,m,n} - E_Y{}^{\psi\psi\phi}_{k,l,m,n+1} - E_Y{}^{\psi\psi\psi}_{k,l,m,n+1})
\end{cases}
\tag{C.11}
$$

$$
\begin{cases}
H_{yz}{}^{\phi\phi\phi}_{k,l,m,n} = C^{H_{yz}}_{l,m,n} H_{yz}{}^{\phi\phi\phi}_{k-1,l,m,n} + D^{H_{yz}}_{l,m,n}(E_X{}^{\phi\phi\phi}_{k,l,m,n} + E_X{}^{\phi\phi\psi}_{k,l,m,n} - E_X{}^{\phi\phi\phi}_{k,l,m,n+1} - E_X{}^{\phi\phi\psi}_{k,l,m,n+1}) \\
H_{yz}{}^{\phi\phi\psi}_{k,l,m,n} = C^{H_{yz}}_{l,m,n} H_{yz}{}^{\phi\phi\psi}_{k-1,l,m,n} + D^{H_{yz}}_{l,m,n}(-E_X{}^{\phi\phi\phi}_{k,l,m,n} + 3E_X{}^{\phi\phi\psi}_{k,l,m,n} + E_X{}^{\phi\phi\phi}_{k,l,m,n+1} + E_X{}^{\phi\phi\psi}_{k,l,m,n+1}) \\
H_{yz}{}^{\phi\psi\phi}_{k,l,m,n} = C^{H_{yz}}_{l,m,n} H_{yz}{}^{\phi\psi\phi}_{k-1,l,m,n} + D^{H_{yz}}_{l,m,n}(E_X{}^{\phi\psi\phi}_{k,l,m,n} + E_X{}^{\phi\psi\psi}_{k,l,m,n} - E_X{}^{\phi\psi\phi}_{k,l,m,n+1} - E_X{}^{\phi\psi\psi}_{k,l,m,n+1}) \\
H_{yz}{}^{\phi\psi\psi}_{k,l,m,n} = C^{H_{yz}}_{l,m,n} H_{yz}{}^{\phi\psi\psi}_{k-1,l,m,n} + D^{H_{yz}}_{l,m,n}(-E_X{}^{\phi\psi\phi}_{k,l,m,n} + 3E_X{}^{\phi\psi\psi}_{k,l,m,n} + E_X{}^{\phi\psi\phi}_{k,l,m,n+1} + E_X{}^{\phi\psi\psi}_{k,l,m,n+1}) \\
H_{yz}{}^{\psi\phi\phi}_{k,l,m,n} = C^{H_{yz}}_{l,m,n} H_{yz}{}^{\psi\phi\phi}_{k-1,l,m,n} + D^{H_{yz}}_{l,m,n}(E_X{}^{\psi\phi\phi}_{k,l,m,n} + E_X{}^{\psi\phi\psi}_{k,l,m,n} - E_X{}^{\psi\phi\phi}_{k,l,m,n+1} - E_X{}^{\psi\phi\psi}_{k,l,m,n+1}) \\
H_{yz}{}^{\psi\phi\psi}_{k,l,m,n} = C^{H_{yz}}_{l,m,n} H_{yz}{}^{\psi\phi\psi}_{k-1,l,m,n} + D^{H_{yz}}_{l,m,n}(-E_X{}^{\psi\phi\phi}_{k,l,m,n} + 3E_X{}^{\psi\phi\psi}_{k,l,m,n} + E_X{}^{\psi\phi\phi}_{k,l,m,n+1} + E_X{}^{\psi\phi\psi}_{k,l,m,n+1}) \\
H_{yz}{}^{\psi\psi\phi}_{k,l,m,n} = C^{H_{yz}}_{l,m,n} H_{yz}{}^{\psi\psi\phi}_{k-1,l,m,n} + D^{H_{yz}}_{l,m,n}(E_X{}^{\psi\psi\phi}_{k,l,m,n} + E_X{}^{\psi\psi\psi}_{k,l,m,n} - E_X{}^{\psi\psi\phi}_{k,l,m,n+1} - E_X{}^{\psi\psi\psi}_{k,l,m,n+1}) \\
H_{yz}{}^{\psi\psi\psi}_{k,l,m,n} = C^{H_{yz}}_{l,m,n} H_{yz}{}^{\psi\psi\psi}_{k-1,l,m,n} + D^{H_{yz}}_{l,m,n}(-E_X{}^{\psi\psi\phi}_{k,l,m,n} + 3E_X{}^{\psi\psi\psi}_{k,l,m,n} + E_X{}^{\psi\psi\phi}_{k,l,m,n+1} + E_X{}^{\psi\psi\psi}_{k,l,m,n+1})
\end{cases}
\tag{C.12}
$$

$$
\begin{cases}
H_{yx}{}^{\phi\phi\phi}_{k,l,m,n} = C^{H_{yx}}_{l,m,n} H_{yx}{}^{\phi\phi\phi}_{k-1,l,m,n} + D^{H_{yx}}_{l,m,n}(-E_Z{}^{\phi\phi\phi}_{k,l,m,n} - E_Z{}^{\psi\phi\phi}_{k,l,m,n} + E_Z{}^{\phi\phi\phi}_{k,l+1,m,n} + E_Z{}^{\psi\phi\phi}_{k,l+1,m,n}) \\
H_{yx}{}^{\phi\phi\psi}_{k,l,m,n} = C^{H_{yx}}_{l,m,n} H_{yx}{}^{\phi\phi\psi}_{k-1,l,m,n} + D^{H_{yx}}_{l,m,n}(-E_Z{}^{\phi\phi\psi}_{k,l,m,n} - E_Z{}^{\psi\phi\psi}_{k,l,m,n} + E_Z{}^{\phi\phi\psi}_{k,l+1,m,n} + E_Z{}^{\psi\phi\psi}_{k,l+1,m,n}) \\
H_{yx}{}^{\phi\psi\phi}_{k,l,m,n} = C^{H_{yx}}_{l,m,n} H_{yx}{}^{\phi\psi\phi}_{k-1,l,m,n} + D^{H_{yx}}_{l,m,n}(-E_Z{}^{\phi\psi\phi}_{k,l,m,n} - E_Z{}^{\psi\psi\phi}_{k,l,m,n} + E_Z{}^{\phi\psi\phi}_{k,l+1,m,n} + E_Z{}^{\psi\psi\phi}_{k,l+1,m,n}) \\
H_{yx}{}^{\phi\psi\psi}_{k,l,m,n} = C^{H_{yx}}_{l,m,n} H_{yx}{}^{\phi\psi\psi}_{k-1,l,m,n} + D^{H_{yx}}_{l,m,n}(-E_Z{}^{\phi\psi\psi}_{k,l,m,n} - E_Z{}^{\psi\psi\psi}_{k,l,m,n} + E_Z{}^{\phi\psi\psi}_{k,l+1,m,n} + E_Z{}^{\psi\psi\psi}_{k,l+1,m,n}) \\
H_{yx}{}^{\psi\phi\phi}_{k,l,m,n} = C^{H_{yx}}_{l,m,n} H_{yx}{}^{\psi\phi\phi}_{k-1,l,m,n} + D^{H_{yx}}_{l,m,n}(E_Z{}^{\phi\phi\phi}_{k,l,m,n} - 3E_Z{}^{\psi\phi\phi}_{k,l,m,n} - E_Z{}^{\phi\phi\phi}_{k,l+1,m,n} - E_Z{}^{\psi\phi\phi}_{k,l+1,m,n}) \\
H_{yx}{}^{\psi\phi\psi}_{k,l,m,n} = C^{H_{yx}}_{l,m,n} H_{yx}{}^{\psi\phi\psi}_{k-1,l,m,n} + D^{H_{yx}}_{l,m,n}(E_Z{}^{\phi\phi\psi}_{k,l,m,n} - 3E_Z{}^{\psi\phi\psi}_{k,l,m,n} - E_Z{}^{\phi\phi\psi}_{k,l+1,m,n} - E_Z{}^{\psi\phi\psi}_{k,l+1,m,n}) \\
H_{yx}{}^{\psi\psi\phi}_{k,l,m,n} = C^{H_{yx}}_{l,m,n} H_{yx}{}^{\psi\psi\phi}_{k-1,l,m,n} + D^{H_{yx}}_{l,m,n}(E_Z{}^{\phi\psi\phi}_{k,l,m,n} - 3E_Z{}^{\psi\psi\phi}_{k,l,m,n} - E_Z{}^{\phi\psi\phi}_{k,l+1,m,n} - E_Z{}^{\psi\psi\phi}_{k,l+1,m,n}) \\
H_{yx}{}^{\psi\psi\psi}_{k,l,m,n} = C^{H_{yx}}_{l,m,n} H_{yx}{}^{\psi\psi\psi}_{k-1,l,m,n} + D^{H_{yx}}_{l,m,n}(E_Z{}^{\phi\psi\psi}_{k,l,m,n} - 3E_Z{}^{\psi\psi\psi}_{k,l,m,n} - E_Z{}^{\phi\psi\psi}_{k,l+1,m,n} - E_Z{}^{\psi\psi\psi}_{k,l+1,m,n})
\end{cases}
\tag{C.13}
$$

$$
\begin{cases}
H_{zx}{}^{\phi\phi\phi}_{k,l,m,n} = C^{H_{zx}}_{l,m,n} H_{zx}{}^{\phi\phi\phi}_{k-1,l,m,n} + D^{H_{zx}}_{l,m,n}(E_Y{}^{\phi\phi\phi}_{k,l,m,n} + E_Y{}^{\psi\phi\phi}_{k,l,m,n} - E_Y{}^{\phi\phi\phi}_{k,l+1,m,n} - E_Y{}^{\psi\phi\phi}_{k,l+1,m,n}) \\
H_{zx}{}^{\phi\phi\psi}_{k,l,m,n} = C^{H_{zx}}_{l,m,n} H_{zx}{}^{\phi\phi\psi}_{k-1,l,m,n} + D^{H_{zx}}_{l,m,n}(E_Y{}^{\phi\phi\psi}_{k,l,m,n} + E_Y{}^{\psi\phi\psi}_{k,l,m,n} - E_Y{}^{\phi\phi\psi}_{k,l+1,m,n} - E_Y{}^{\psi\phi\psi}_{k,l+1,m,n}) \\
H_{zx}{}^{\phi\psi\phi}_{k,l,m,n} = C^{H_{zx}}_{l,m,n} H_{zx}{}^{\phi\psi\phi}_{k-1,l,m,n} + D^{H_{zx}}_{l,m,n}(E_Y{}^{\phi\psi\phi}_{k,l,m,n} + E_Y{}^{\psi\psi\phi}_{k,l,m,n} - E_Y{}^{\phi\psi\phi}_{k,l+1,m,n} - E_Y{}^{\psi\psi\phi}_{k,l+1,m,n}) \\
H_{zx}{}^{\phi\psi\psi}_{k,l,m,n} = C^{H_{zx}}_{l,m,n} H_{zx}{}^{\phi\psi\psi}_{k-1,l,m,n} + D^{H_{zx}}_{l,m,n}(E_Y{}^{\phi\psi\psi}_{k,l,m,n} + E_Y{}^{\psi\psi\psi}_{k,l,m,n} - E_Y{}^{\phi\psi\psi}_{k,l+1,m,n} - E_Y{}^{\psi\psi\psi}_{k,l+1,m,n}) \\
H_{zx}{}^{\psi\phi\phi}_{k,l,m,n} = C^{H_{zx}}_{l,m,n} H_{zx}{}^{\psi\phi\phi}_{k-1,l,m,n} + D^{H_{zx}}_{l,m,n}(-E_Y{}^{\phi\phi\phi}_{k,l,m,n} + 3E_Y{}^{\psi\phi\phi}_{k,l,m,n} + E_Y{}^{\phi\phi\phi}_{k,l+1,m,n} + E_Y{}^{\psi\phi\phi}_{k,l+1,m,n}) \\
H_{zx}{}^{\psi\phi\psi}_{k,l,m,n} = C^{H_{zx}}_{l,m,n} H_{zx}{}^{\psi\phi\psi}_{k-1,l,m,n} + D^{H_{zx}}_{l,m,n}(-E_Y{}^{\phi\phi\psi}_{k,l,m,n} + 3E_Y{}^{\psi\phi\psi}_{k,l,m,n} + E_Y{}^{\phi\phi\psi}_{k,l+1,m,n} + E_Y{}^{\psi\phi\psi}_{k,l+1,m,n}) \\
H_{zx}{}^{\psi\psi\phi}_{k,l,m,n} = C^{H_{zx}}_{l,m,n} H_{zx}{}^{\psi\psi\phi}_{k-1,l,m,n} + D^{H_{zx}}_{l,m,n}(-E_Y{}^{\phi\psi\phi}_{k,l,m,n} + 3E_Y{}^{\psi\psi\phi}_{k,l,m,n} + E_Y{}^{\phi\psi\phi}_{k,l+1,m,n} + E_Y{}^{\psi\psi\phi}_{k,l+1,m,n}) \\
H_{zx}{}^{\psi\psi\psi}_{k,l,m,n} = C^{H_{zx}}_{l,m,n} H_{zx}{}^{\psi\psi\psi}_{k-1,l,m,n} + D^{H_{zx}}_{l,m,n}(-E_Y{}^{\phi\psi\psi}_{k,l,m,n} + 3E_Y{}^{\psi\psi\psi}_{k,l,m,n} + E_Y{}^{\phi\psi\psi}_{k,l+1,m,n} + E_Y{}^{\psi\psi\psi}_{k,l+1,m,n})
\end{cases}
\tag{C.14}
$$

$$
\begin{cases}
H_{zy}{}^{\phi\phi\phi}_{k,l,m,n} = C^{H_{zy}}_{l,m,n} H_{zy}{}^{\phi\phi\phi}_{k-1,l,m,n} + D^{H_{zy}}_{l,m,n}(-E_X{}^{\phi\phi\phi}_{k,l,m,n} - E_X{}^{\phi\psi\phi}_{k,l,m,n} + E_X{}^{\phi\phi\phi}_{k,l,m+1,n} + E_X{}^{\phi\psi\phi}_{k,l,m+1,n}) \\
H_{zy}{}^{\phi\phi\psi}_{k,l,m,n} = C^{H_{zy}}_{l,m,n} H_{zy}{}^{\phi\phi\psi}_{k-1,l,m,n} + D^{H_{zy}}_{l,m,n}(-E_X{}^{\phi\phi\psi}_{k,l,m,n} - E_X{}^{\phi\psi\psi}_{k,l,m,n} + E_X{}^{\phi\phi\psi}_{k,l,m+1,n} + E_X{}^{\phi\psi\psi}_{k,l,m+1,n}) \\
H_{zy}{}^{\phi\psi\phi}_{k,l,m,n} = C^{H_{zy}}_{l,m,n} H_{zy}{}^{\phi\psi\phi}_{k-1,l,m,n} + D^{H_{zy}}_{l,m,n}(E_X{}^{\phi\phi\phi}_{k,l,m,n} - 3E_X{}^{\phi\psi\phi}_{k,l,m,n} - E_X{}^{\phi\phi\phi}_{k,l,m+1,n} - E_X{}^{\phi\psi\phi}_{k,l,m+1,n}) \\
H_{zy}{}^{\phi\psi\psi}_{k,l,m,n} = C^{H_{zy}}_{l,m,n} H_{zy}{}^{\phi\psi\psi}_{k-1,l,m,n} + D^{H_{zy}}_{l,m,n}(E_X{}^{\phi\phi\psi}_{k,l,m,n} - 3E_X{}^{\phi\psi\psi}_{k,l,m,n} - E_X{}^{\phi\phi\psi}_{k,l,m+1,n} - E_X{}^{\phi\psi\psi}_{k,l,m+1,n}) \\
H_{zy}{}^{\psi\phi\phi}_{k,l,m,n} = C^{H_{zy}}_{l,m,n} H_{zy}{}^{\psi\phi\phi}_{k-1,l,m,n} + D^{H_{zy}}_{l,m,n}(-E_X{}^{\psi\phi\phi}_{k,l,m,n} - E_X{}^{\psi\psi\phi}_{k,l,m,n} + E_X{}^{\psi\phi\phi}_{k,l,m+1,n} + E_X{}^{\psi\psi\phi}_{k,l,m+1,n}) \\
H_{zy}{}^{\psi\phi\psi}_{k,l,m,n} = C^{H_{zy}}_{l,m,n} H_{zy}{}^{\psi\phi\psi}_{k-1,l,m,n} + D^{H_{zy}}_{l,m,n}(-E_X{}^{\psi\phi\psi}_{k,l,m,n} - E_X{}^{\psi\psi\psi}_{k,l,m,n} + E_X{}^{\psi\phi\psi}_{k,l,m+1,n} + E_X{}^{\psi\psi\psi}_{k,l,m+1,n}) \\
H_{zy}{}^{\psi\psi\phi}_{k,l,m,n} = C^{H_{zy}}_{l,m,n} H_{zy}{}^{\psi\psi\phi}_{k-1,l,m,n} + D^{H_{zy}}_{l,m,n}(E_X{}^{\psi\phi\phi}_{k,l,m,n} - 3E_X{}^{\psi\psi\phi}_{k,l,m,n} - E_X{}^{\psi\phi\phi}_{k,l,m+1,n} - E_X{}^{\psi\psi\phi}_{k,l,m+1,n}) \\
H_{zy}{}^{\psi\psi\psi}_{k,l,m,n} = C^{H_{zy}}_{l,m,n} H_{zy}{}^{\psi\psi\psi}_{k-1,l,m,n} + D^{H_{zy}}_{l,m,n}(E_X{}^{\psi\phi\psi}_{k,l,m,n} - 3E_X{}^{\psi\psi\psi}_{k,l,m,n} - E_X{}^{\psi\phi\psi}_{k,l,m+1,n} - E_X{}^{\psi\psi\psi}_{k,l,m+1,n})
\end{cases}
\tag{C.15}
$$